Inaugural dissertation

for

obtaining the doctoral degree

of the

Combined Faculty of Mathematics, Engineering and Natural Sciences

of the

Ruprecht - Karls - University

Heidelberg

Presented by

M.Sc. Violeta Pancakova

Born in Krāslava

Oral examination on 28.04.2025

Protein export and cytoadhesion in *Plasmodium falciparum*: structure-functional analysis of KAHRP and proteomic discovery of novel export pathway components

Referees:

Prof. Dr. Michael Lanzer

Prof. Dr. Ulrich Schwarz

Summary

In 2023, an estimated 263 million malaria cases and 597,000 deaths occurred across 83 countries, with *Plasmodium falciparum* being the deadliest malaria parasite (World Health Organization, 2024). A key driver of *Plasmodium falciparum* virulence is cytoadhesion, mediated by antigens such as PfEMP1, presented on knobs formed on infected red blood cells (iRBCs). These knobs depend on the knob-associated histidine-rich protein (KAHRP, PfIT_020006800), exported alongside other parasite proteins that remodel iRBCs. This study focuses on two major virulence factors: knob assembly and protein export.

Using alanine scanning, I identified the β-sheet structured region of KAHRP (amino acids 136 to 190) as essential for knob formation, with alanine substitutions disrupting knob assembly and resulting in a knobless phenotype. In contrast, mutations in the histidine-rich region (HRR, amino acids 60 to 116) did not affect knob density or shape, and lipid-binding assays confirmed no interaction between HRR and common iRBC lipids, even in the presence of Zn^{2+}. Although largely unstructured, the β-sheet core of KAHRP is crucial for knob formation and structural integrity.

To investigate protein export, I employed stevor-miniTurbo biotin ligase fusion proteins with wild-type or altered PEXEL motifs to arrest export at distinct stages: ER (RLWAQ construct stevor1-80^{50W}), PV (RLLEQ construct stevor1-80^{51E}), or allow normal export (RLLAQ). These constructs identified proteins interacting with the PEXEL motif or PEXEL-exported proteins, elucidating the molecular machinery of the export pathway. Mass spectrometry revealed several novel, potential interaction partners, and Split-GFP assay confirmed the interaction with SEC12, a guanine nucleotide exchange factor (PF3D7_1116400) involved in COPII vesicle transport, suggesting protein trafficking via vesicular transport from ER to Golgi complex – a poorly studied organelle in *Plasmodium*. Another confirmed interaction partner, a liver-stage antigen 3 (LSA-3, PF3D7_0220000), conferred its localization and function in the PV.

This data emphasizes the importance of the Golgi complex as a potential site for post-translational modifications of PEXEL proteins. It further underscores the need to investigate the functional contributions of LSA-3, which has primarily been studied in immune contexts, to export machinery. This study also reveals the importance of β-sheet structured region of KAHRP in knob assembly. These findings provide a foundation for understanding the molecular details of protein export and cytoadhesion, to open avenues for creating therapeutic interventions that disrupt *Plasmodium falciparum* virulence.

Zusammenfassung

Im Jahr 2023 gab es in 83 Ländern schätzungsweise 263 Millionen Malariafälle und 597.000 Todesfälle, wobei *Plasmodium falciparum* der tödlichste Malariaparasit ist (Weltgesundheitsorganisation, 2024). Ein wichtiger Faktor für die Virulenz von *Plasmodium falciparum* ist die Zytoadhäsion, die durch Antigene wie PfEMP1 vermittelt wird, die sich auf "Knobs" (Knubbeln) auf infizierten Erythrozyten befinden. Diese Knobs hängen von dem Knob-associated histidine-rich Protein (KAHRP, PfIT_020006800) ab, das zusammen mit anderen Parasitenproteinen exportiert wird, die die infizierten Erythrozyten umgestalten. Diese Studie konzentriert sich auf zwei wichtige Virulenzfaktoren: den Aufbau der Knobs und den Proteinexport.

Mit Hilfe eines Alanin-Scans habe ich die β-Faltblatt-strukturierte Region von KAHRP (Aminosäuren 136 bis 190) als essentiell für die Knob-Bildung identifiziert. Alanin-Substitutionen in dieser Region unterbrachen die Knob-Bildung und führten zu einem Phänotyp ohne Knobs. Im Gegensatz dazu hatten Mutationen in der histidinreichen Region (HRR, Aminosäuren 60 bis 116) keine Auswirkungen auf die Knob-Dichte oder -Form. Lipidbindungsversuche bestätigten zudem keine Interaktion zwischen der HRR und gängigen Lipiden der infizierten Erythrozyten, selbst in Gegenwart von Zn^{2+}. Obwohl die HRR weitgehend unstrukturiert ist, erwies sich der β-Faltblatt-Kern von KAHRP als entscheidend für die Knob-Bildung und die strukturelle Integrität.

Um den Proteinexport zu untersuchen, habe ich stevor-miniTurbo-Biotin-Ligase-Fusionsproteine mit Wildtyp- oder modifizierten PEXEL-Motiven eingesetzt, um den Export in verschiedenen Stadien zu stoppen: im endoplasmatischen Retikulum (ER, RLWAQ-Konstrukt stevor1-80^{50W}), in der parasitophoren Vakuole (PV, RLLEQ-Konstrukt stevor1-80^{51E}), oder um den normalen Export zu ermöglichen (RLLAQ). Diese Konstrukte identifizierten Proteine, die mit dem PEXEL-Motiv oder PEXEL-exportierten Proteinen interagieren, wodurch die molekulare Maschinerie des Exportwegs weiter aufgeklärt wurde. Die Massenspektrometrie ergab mehrere neue potenzielle Interaktionspartner, und ein Split-GFP-Assay bestätigte die Interaktion mit SEC12, einem Guanin-Nukleotid-Austauschfaktor (PF3D7_1116400), der am COPII-Vesikeltransport beteiligt ist. Dies deutet darauf hin, dass die Proteine über den vesikulären Transport vom ER zum Golgi-Komplex transportiert werden – einer bislang wenig untersuchten Organelle in *Plasmodium*. Ein weiterer bestätigter Interaktionspartner, das Liver Stage Antigen 3 (LSA-3, PF3D7_0220000), zeigte eine Lokalisierung und Funktion in der PV.

Diese Daten unterstreichen die Bedeutung des Golgi-Komplexes als potenziellen Ort für posttranslationale Modifikationen von PEXEL-Proteinen. Sie zeigen außerdem die Notwendigkeit auf, die funktionellen Beiträge von LSA-3, das bisher vor allem in immunologischen Kontexten untersucht wurde, zur Exportmaschinerie zu analysieren. Diese Studie hebt zudem die zentrale Rolle der β-Faltblatt-strukturierten Region von KAHRP beim Aufbau der Knobs hervor. Die Ergebnisse bilden eine

Grundlage für das Verständnis der molekularen Details des Proteinexports und der Zytoadhäsion und eröffnen Wege für die Entwicklung therapeutischer Ansätze, die die Virulenz von *Plasmodium falciparum* stören könnten.

Acknowledgments

First and foremost, I would like to express my deepest gratitude to Professor Michael Lanzer for granting me the opportunity to conduct my PhD project in his lab and for his support in guiding the projects toward their objectives.

I am sincerely thankful to Professor Ulrich Schwarz, Dr. Markus Ganter, Dr. Victoria Ingham, and Dr. Camilo Aponte-Santamaría for their invaluable advice during project meetings. Their insights and expertise greatly enriched the course of my research.

I extend my heartfelt thanks to Professor Matthias Mayer and Professor Dr. Nina Papavasiliou for their readiness to join my PhD defense committee.

Sincere thank you to Dr. Markus Ganter, Dr. Yannik Voß, and Marta Machado for their generous help in troubleshooting multiple experiments and for sharing key reagents essential to the success of these projects.

To my lab members, thank you for your constant support, engaging scientific discussions, and camaraderie. Special thanks to Dr. Jessica Kehrer, Dr. Marianne Papagrigorakes, Soria Gasparini, and Katharina Scholz for your friendship and support. You brought light and cheer to this journey and equipped me with bullet-proof protocols.

Thank you to Miriam Griesheimer for her empathy, understanding, and unwavering support in every situation, and to Sandra Niebel for her constant positivity and gentle reminders to take it easy.

A heartfelt thank you to the students I had the privilege of working with: Fabian Kropp, Laura Andacic, Björn Schwortschik, and Lea Ahrens. Your contributions and the lessons I learned from you were invaluable.

I am grateful to the electron microscopy core facility and its members, particularly Sebastian Weber, who trained me in SEM, and Larissa Eis, for her prompt and reliable assistance.

My gratitude also goes to the infectious diseases imaging platform and its members, especially Dr. Sylvia Olberg and Dr. Vibor Laketa, for their exceptional training and scientific support.

The core facility for mass spectrometry and proteomics played an integral role in my work. Thank you to Sabine Merker and Dr. Thomas Ruppert for conducting the mass spectrometry experiments and for your guidance in analyzing the data.

I am deeply grateful to my lifelong friends Anita, Agnese, and Laura for a lifetime of adventures that shaped my path to this point and to my family for holding together despite the distance.

Finally, my greatest thanks go to Dr. Karl Sutanto, who has been my rock throughout this PhD journey and beyond. Thank you for your emotional support, for finding the TOTO dimer nucleic acid stain, for our McDonald's runs after late lab nights, for being my ultimate scientific consultant, and, of course, for proofreading this thesis.

Table of contents

1. Introduction

1.1 Impact, treatment, and lifecycle of *Plasmodium falciparum*

1.1.1 Global effect

In 2023, malaria affected an estimated 263 million individuals across 83 endemic countries, resulting in 597,000 deaths. The WHO African Region bears the majority of the global burden, accounting for 94% of malaria cases (246 million) and 95% of malaria deaths (569,000). Children under the age of five are particularly vulnerable, representing approximately 76% of all malaria-related fatalities in this region. While global malaria cases fluctuated between 227 million and 248 million annually from 2000 to 2019, a steady increase has been observed since 2020 (World Health Organization, 2024).

1.1.2 The fife cycle of *Plasmodium falciparum*

The *Plasmodium falciparum* lifecycle is a complex process involving both the human host and the *Anopheles* mosquito vector (Figure 1). Infection in human begins with a bite of an infected female *Anopheles* mosquito, injecting motile sporozoites into the skin. These sporozoites travel via the bloodstream to the liver, where they invade hepatocytes and undergo asexual replication within a parasitophorous vacuole (Aravind et al., 2003; Cowman et al., 2016). Over approximately 10 days, sporozoites proliferate extensively, eventually forming thousands of merozoites that are released into the bloodstream in vesicles known as merosomes (Baer et al., 2007).

When in the bloodstream, merosomes rupture, releasing the merozoites to infect erythrocytes and initiate the asexual blood stage (Sturm et al., 2006). Each cycle of replication lasts around 48 hours, during which the parasite progresses through the ring, trophozoite, and schizont stages. The schizont stage culminates in the production of ~16–20 daughter merozoites through a process known as schizogony. Rupture of the infected erythrocytes releases merozoites, which invade new red blood cells, continuing the cycle and rapidly increasing the parasite population (White et al., 2014). This stage of the lifecycle is directly associated with the clinical symptoms of malaria, such as fever, chills, and anemia, as the parasite disrupts the host's red blood cell population (Church et al., 1997).

While most merozoites repeat the asexual cycle, a subset differentiates into gametocytes, the sexual transmission stage of the parasite. Over approximately 10–15 days, gametocytes mature through five morphological stages into male (microgametes) and female (macrogametes) forms (Aravind et al., 2003; White et al., 2014). These gametocytes are taken up by a mosquito during a blood meal, where sexual reproduction occurs in the mosquito midgut. The fusion of the male and female gametes produces a zygote, which develops into a motile ookinete. The ookinete crosses the mosquito midgut wall and forms an oocyst, within which thousands of sporozoites are produced over a 17-day sporogonic cycle. The sporozoites migrate to the mosquito's salivary glands, and infect another human host upon the next blood meal, and perpetuate the lifecycle (Cowman et al., 2016).

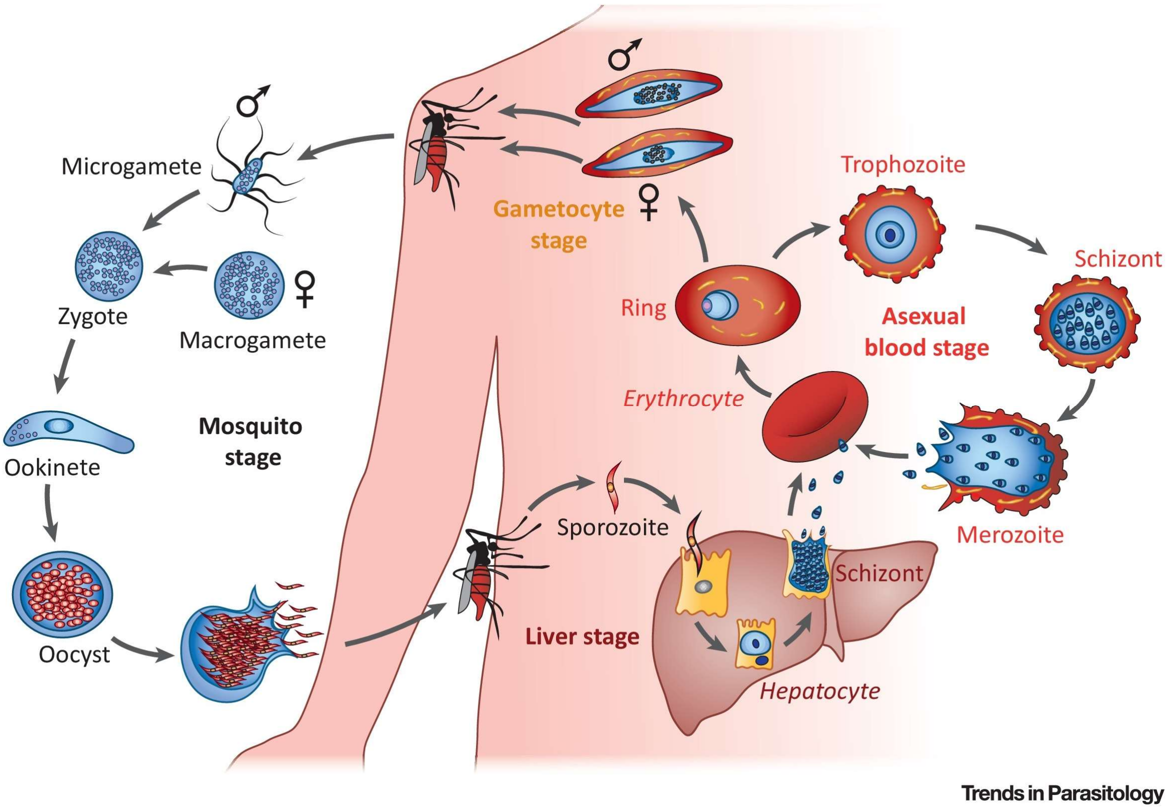

Figure 1. *Plasmodium falciparum* life cycle.
(Maier et al., 2019)

1.1.3 Malaria control strategies

Efforts to combat *Plasmodium falciparum* malaria have been braced by significant interventions recommended by the World Health Organization (WHO). In October 2023, WHO endorsed a second malaria vaccine, R21/Matrix-M (R21), to complement the rollout of the first vaccine, RTS,S/AS01 (RTS,S), which began in July 2022, ensuring sufficient vaccine supply to protect children in high-risk areas. To enhance vector control, WHO introduced two new types of insecticide-treated mosquito nets (ITNs) in March 2023: pyrethroid–chlorfenapyr nets, combining a pyrethroid and a pyrrole insecticide for increased mosquito lethality, and pyrethroid–pyriproxyfen nets, which include an insect growth regulator to disrupt mosquito development and reproduction. These dual-active ingredient nets demonstrated 20–50% greater malaria control compared to standard pyrethroid-only nets in trials conducted across 17 sub-Saharan African countries between 2019 and 2022, particularly in areas with insecticide resistance (Bayili et al., 2017; Camara et al., 2018; Mosha et al., 2022; N'Guessan et al., 2016; Ngufor et al., 2017; Tiono et al., 2018; Tungu et al., 2021). Long-standing preventive strategies such as intermittent preventive treatment in pregnancy (IPTp-SP) with sulfadoxine–pyrimethamine and seasonal malaria chemoprevention (SMC) for young children in highly seasonal regions remain central to malaria control efforts. SMC is currently implemented in 19 countries across the Sahel and other seasonal zones in sub-Saharan Africa. Additionally, WHO supports the deployment of rectal artesunate as a pre-referral medication for severe malaria in young children (World Health Organization, 2024).

1.1.4 *Plasmodium falciparum* treatment strategies and drug resistance mechanisms

Treatment of *Plasmodium falciparum* malaria primarily relies on artemisinin-based combination therapies (ACTs), which combine an artemisinin derivative with a partner drug to target the parasite at multiple stages (Blasco et al., 2017). Artemisinin derivatives, such as artesunate, artemether, and dihydroartemisinin (DHA), are highly effective against asexual blood stages, reducing parasite biomass by up to 10,000-fold every 48 hours. These drugs act by undergoing reductive scission of their endoperoxide bridge through interaction with Fe^{2+}-heme, producing reactive species that alkylate biomolecules, causing oxidative stress and cellular damage (Dondorp et al., 2009).

The degradation and detoxification of host hemoglobin (Hb) is a critical process targeted by many antimalarial drugs in asexual blood stage parasites. Among these, 4-aminoquinolines such as chloroquine (CQ) and amodiaquine (AQ) are believed to exert their effects by binding to the growing surfaces of hemozoin crystals, thereby disrupting the incorporation and detoxification of free heme (Roepe, 2009).

Clinically used antimalarial drugs also target other parasite-specific processes, such as cytosolic folate synthesis, the mitochondrial electron transport chain essential for pyrimidine biosynthesis, and protein synthesis within the apicoplast (Blasco et al., 2017).

However, resistance to these therapies has emerged, particularly in Southeast Asia. Partial resistance to artemisinin, characterized by delayed parasite clearance after treatment, is linked to mutations in the *P. falciparum Kelch13* (*Pfkelch13*) gene, which encodes a protein essential for artemisinin's action. Mutations in the *Pfkelch13* propeller domain have driven independent resistance events in Southeast Asia, resulting in a drug-selective sweep of resistant parasites, while remaining rare in Africa (Straimer et al., 2015).

Resistance to ACT partner drugs has also been documented. For piperaquine (PPQ), resistance is associated with increased copy numbers of *plasmepsin 2/3* genes, as well as mutations in the chloroquine resistance transporter (*PfCRT*) (Amato et al., 2017; Witkowski et al., 2017). Mefloquine resistance is linked to increased copy numbers of the *pfmdr1* gene, which encodes an ABC transporter in the digestive vacuole membrane, reducing susceptibility to mefloquine and the aryl-amino alcohol lumefantrine (World Health Organization, 2020). Additionally, resistance to sulfadoxine-pyrimethamine (SP), is associated with mutations in *dihydrofolate reductase* (*dhfr*) and *dihydropteroate synthase* (*dhps*) (Maiga et al., 2016). The widespread global use of chloroquine (CQ) in earlier years led to the selection of a limited number of mutant *pfcrt* alleles containing between four and nine point mutations, causing CQ resistance (Callaghan et al., 2015; Ecker et al., 2012).

1.1.5 *Plasmodium falciparum* genome flexibility and rapid diagnostic tests

Rapid diagnostic tests (RDTs) for *P. falciparum* malaria primarily target the histidine-rich protein 2 (HRP2) antigen, making them ineffective in detecting parasites that lack HRP2 expression. At high parasite densities, HRP3, a homolog of HRP2, may cross-react with the antibodies used in HRP2-based tests. However, parasites lacking both HRP2 and HRP3 evade detection entirely by these RDTs, of which approximately 448.5 million were sold in 2023. In some regions of Djibouti, Eritrea, and Peru, the prevalence of parasites with dual *pfhrp2* and *pfhrp3* deletions has reached up to 80% among symptomatic patients. Currently, no WHO-prequalified RDTs exist that can detect and differentiate between *P. falciparum* and *P. vivax* without relying on HRP2 (World Health Organization, 2024).

1.1.6 Vector resistance to insecticides

Currently, Plasmodium falciparum malaria is spread globally by over 70 species of Anopheles mosquitoes (Sinka et al., 2012). *Anopheles stephensi* is a highly efficient vector for both *Plasmodium falciparum* and *Plasmodium vivax*, playing a major role in malaria transmission in rural and urban areas due to it's ability to adapt to the local urban environment, and breed in human-made water storage containers (World Health Organization, 2024).

Most prequalified insecticide-treated nets (ITNs) are treated with pyrethroids; however, the widespread development of resistance has necessitated the incorporation of additional compounds. One such compound is PBO, a synergist that enhances the killing efficacy of pyrethroids against resistant mosquitoes. In 2023, WHO recommended two new types of dual active ingredient ITNs: pyrethroid–chlorfenapyr nets, which combine a pyrethroid with a pyrrole insecticide for increased lethality, and pyrethroid–pyriproxyfen nets, which include an insect growth regulator to disrupt mosquito development and reproduction (Bayili et al., 2017; Camara et al., 2018; Mosha et al., 2022; N'Guessan et al., 2016; Ngufor et al., 2017; Tiono et al., 2018; Tungu et al., 2021).

Indoor residual spraying (IRS) remains another vital vector control strategy, with five prequalified insecticide classes: pyrethroids, carbamates, organophosphates, neonicotinoids, and meta-diamides. Although DDT, an organochlorine, is still used in some countries, it is being phased out due to the lack of prequalified products. Preventive rotation of insecticide classes is recommended to mitigate resistance, but IRS usage has declined in recent years, largely due to cost (World Health Organization, 2024).

Between 2018 and 2023, insecticide resistance was confirmed in 57 of 66 malaria-endemic countries reporting data, with pyrethroid resistance observed in 55 countries. Insecticide resistance is based on mosquito mortality rates, with a threshold of less than 98% indicating resistance (World Health Organization, 2024).

1.2 Cytoadhesion and KAHRP

1.2.1 Rearrangement of the red blood cell

The remodeling of the red blood cell (RBC) during *Plasmodium falciparum* infection begins early in the parasite lifecycle. Maurer's clefts, membranous structures associated with protein export, are fully developed at 6–8 hours post-infection (hpi) (Mundwiler-Pachlatko and Beck, 2013). Parasite knobs, which are essential for cytoadherence, begin to appear around 16 hpi (Gruenberg et al., 1983). These modifications coincide with significant changes in the iRBC membrane composition. Experimental data suggest that the iRBC membrane undergoes lipid rearrangement facilitated by parasite-driven transport mechanisms. For instance, phosphatidylcholine, comprising approximately 30% of the lipidome in uninfected RBC microvesicles, is reduced by half in iRBC microvesicles. Conversely, phosphatidylserine content increases from around 15% to approximately 30% in iRBC vesicles (Gulati et al., 2015).

As the iRBC undergoes structural remodeling, homeostasis must be maintained to prevent premature lysis and ensure parasite survival throughout its 48-hour lifecycle. Homeostasis is achieved through a delicate balance of cell volume, pH, ion transport, hemoglobin consumption, and membrane potential. New permeation pathways (NPPs) are activated around 20 hpi, facilitating the migration of nutrients, waste products, Na^+, K^+, and anions across the cell membrane. As K^+ concentrations decrease and Na^+ concentrations increase, the overall efflux of KCl slightly exceeds NaCl influx, leading to a reduction in cell water volume (Mauritz et al., 2009). This triggers short-term acidification, with the intracellular pH of iRBCs dropping to approximately 6.8–7.0, about 0.4 units lower than uninfected cells (Friedman et al., 1979; Voigt et al., 2000).

Around the same time that NPPs are activated, the parasite begins consuming hemoglobin, a process that peaks at approximately 30 hpi. Hemoglobin digestion generates amino acids, which are exported via NPPs, mitigating colloid-osmotic pressure buildup within the iRBC. This mechanism prevents premature swelling and hemolysis, ensuring uninterrupted parasite development (Mauritz et al., 2009). These interdependent processes highlight the intricate balance between iRBC remodeling and homeostasis during *Plasmodium* infection, enabling the parasite to modify its host while sustaining a viable intracellular environment.

Protein export is the cornerstone of *Plasmodium falciparum's* ability to remodel iRBCs. Through the *Plasmodium* translocon of exported proteins (PTEX), the parasite delivers a suite of effector proteins into the iRBC cytosol and membrane, enabling profound structural and functional alterations necessary for its survival (Beck et al., 2014; Ho et al., 2018). These exported proteins drive processes such as nutrient uptake, membrane permeability changes, and, crucially, the formation of parasite-specific structures like knobs (Elsworth et al., 2014).

Knob formation, facilitated by exported proteins such as knob-associated histidine-rich protein (KAHRP), is a critical step in iRBC remodeling (Sanchez et al., 2021; Waller et al., 2002). Knobs serve as anchoring points for erythrocyte membrane protein 1 (PfEMP1), a major virulence factor that mediates cytoadhesion by binding to endothelial receptors like intercellular adhesion molecule 1 (ICAM-1) and CD36 (Beck and Ho, 2021; Smith et al., 2013). This cytoadhesion enables iRBCs to evade splenic clearance by sequestering in the microvasculature. While essential for immune evasion, this adaptation has severe consequences for the host, contributing to the obstruction of blood flow and inflammation, hallmarks of cerebral malaria, placental malaria, and other severe complications (Fried and Duffy, 1996; Taylor et al., 2013).

Protein export and cytoadhesion are intricately linked processes that together define the parasite's capacity to remodel its host environment. Protein export not only facilitates the structural reorganization required for knob formation but also ensures the delivery of functional mediators of cytoadhesion like PfEMP1. These processes work in concert to support parasite survival, immune evasion, and pathogenesis, making them critical focal points for understanding malaria's molecular mechanisms and clinical outcomes (Elsworth et al., 2014; Ho et al., 2018; Smith et al., 2013).

1.2.2 Cytoadhesion in the pathogenesis of severe malaria

During the cell remodelling process, iRBCs develop protrusions on the surface of the iRBC called knobs. Knobs contribute to the adhesive properties of iRBC, creating a structural interface where (EMP1) is located and acts as adhesin binding to the endothelium membrane receptors. This facilitates sequestration of iRBC in microvasculature causing the main symptoms of severe malaria.

Every *Plasmodium falciparum* strain contains 60 *var* gene paralogs that encode EMP1 proteins with variations, which allow iRBC to bind to various receptors expressed on the endothelial cell surface. In cerebral malaria, the expressed EMP1 adhesin molecule has been described to bind Endothelial Protein C Receptor (EPCR) or to be a dual binder, binding EPCR and ICAM-1 and containing a CIDRα1 or a specific DBLβ3 domain (Adams et al., 2021; Jespersen et al., 2016). These EMP1 variants enable firm adhesion with endothelial receptor ICAM-1, leading to the iRBC internalization in an ICAM-1-dependent manner into the endothelial cell. This results in increased permeability of the blood-brain barrier, causing brain swelling (Adams et al., 2021; Lennartz et al., 2017).

Placental malaria occurs in pregnant women and causes maternal anemia, low birth weight, preterm delivery, and stillbirth. Here, too, the main cause is the cytoadhesion in combination with a specific EMP1 receptor, which binds to a glycosaminoglycan called chondroitin sulfate A (CSA), a ligand expressed on the surface of the placental syncytiotrophoblasts, which are responsible for nutrient and gas exchange on the outer surface of placental villi. The adherent iRBCs accumulate on the surface of syncytiotrophoblasts inducing local immune response and inflammation (Lucchi et al., 2008). Due to the sequestration and inflammation, the nutrient and oxygen transfer to the fetus is impaired leading to low birth weight, neurodevelopmental impairments, and stillbirth. The inflammation, immune dysregulation, and anemia lead to complications in pregnancy (Dimasuay et al., 2017; Fried and Duffy, 1996). Placental malaria is commonly the most severe during the first pregnancy, even with preexisting immunity against *Plasmodium falciparum*; this appears to be due to a lack of antibodies against VAR2CSA. Even though VAR2CSA expression is not restricted to pregnant women, the antibodies to VAR2CSA have been detected only in women who suffered from placental malaria, but not in men, children, or women who have not been pregnant (Beeson et al., 1999; Duffy et al., 2006; Fried et al., 1998; Maubert et al., 1999).

Cytoadhesion and sequestration in renal capillaries can cause acute kidney injury in up to 40% of adult patients with *Plasmodium falciparum* infection (Koopmans et al., 2015). iRBC sequestration in the liver causes inflammation and prevents normal bilirubin metabolism causing yellowing of the skin and eyes (Anand and Puri, 2005; Nacher et al., 2001). Sequestrated cells activate clotting cascade and can deplete clotting factors, which lead to bleeding or clotting abnormalities (Angchaisuksiri, 2014; Francischetti et al., 2008).

Overall, these findings underscore how diverse *Plasmodium falciparum* EMP1 variants exploit distinct receptor-ligand interactions to cause tissue-specific damage—whether in the brain, placenta, liver, or kidneys. Given the extensive diversity of *var* genes encoding numerous EMP1 variants, targeting each individual variant represents a significant therapeutic challenge. Instead, a more effective strategy may be to target the underlying mechanisms that enable EMP1 function, particularly the knob structures that cluster and stabilize EMP1 on the red blood cell membrane. A greater understanding of knob formation, composition, and dynamics could yield therapies that disrupt EMP1 display en masse, thereby reducing cytoadhesion, local inflammation, and the subsequent organ dysfunction characteristic of severe malaria.

1.2.3 Immune evasion mechanisms

In malariaendemic areas, children under the age of 5 are most prone to death as they require multiple exposures to develop immunity. This is due to the multiple immune evasion mechanisms *Plasmodium* employs. First and foremost, the majority of the time, the parasite is protected by the host erythrocytes, which, during the erythrocyte maturation process, shed major histocompatibility complex (MHC) class I and, therefore, do not present internal antigens to the immune cells (Imai et al., 2015; Liu et al., 2024). Secondly, parasites reduce the exposure time to the immune system by rapidly invading the hepatocyte and RBC. Furthermore, the parasite controls the parasitic protein expression on the surface of iRBC, determining the antigens exposed to the host immune system. To avoid natural clearance of remodelled, infected RBCs, parasitized cells cluster in rosettes and sequester in capillaries, avoiding splenic clearance.

Multiple proteins expressed on the surface of the iRBC are involved in the immune evasion processes. EMP1 is a well-studied variant surface antigen, it is encoded in each parasite by 60 variant antigen (*var*) genes that contribute to immune evasion. Only one *var* gene is actively transcribed and expressed at the time through a process called mutually exclusive expression, which silences the transcription of other *var* genes (Scherf et al., 1998). Switching to express another EMP1 variant on the iRBC surface makes the antibodies developed against the previously expressed EMP1 ineffective.

A few smaller variant surface antigens, such as RIFIN and STEVOR, contribute to the *Plasmodium falciparum* evasion mechanism. RIFINs are encoded by approximately 150 genes and STEVOR by 30-40 genes, and the partially conserved N-terminal domain of RIFINs and certain STEVOR proteins is displayed on the surface of infected erythrocytes (Bachmann et al., 2015; Bultrini et al., 2009; Wichers et al., 2019).

Multiple parasite proteins expressed on the iRBC surface, as well as host factors, contribute to rosetting, a phenomenon where iRBC binds to uninfected RBCs, forming a cluster of cells. This cluster contributes to the obstruction of microvascular blood flow and protects the iRBC from splenic clearance. From *Plasmodium* proteins, EMP1 N-terminal DBL1α1domain is associated with rosetting (Vigan-Womas et al., 2012). STEVOR proteins have also been reported to mediate rosetting, which protects merozoites against neutralizing antibodies during the invasion process (Niang et al., 2014). RIFIN proteins are suggested to play an accessory role in rosetting (Goel et al., 2015; Kyes et al., 1999). Among human RBC factors, various molecules have been suggested as potential receptors involved in rosetting, including blood group A and B carbohydrates, heparan sulfate (HS)-like compounds, and complement receptor 1 (CR1), which are widely acknowledged to play a significant role in this phenomenon (McQuaid and Rowe, 2020; Rowe et al., 1997).

Under normal physiological conditions, the lifespan of RBCs is approximately 120 days. The spleen filters out old, damaged, or abnormal RBCs to prevent hemolysis and inflammation and maintain the functionality of circulating RBCs that have to traverse capillaries narrower than their size (Paradkar and Gambhire, 2021). RBCs enter the red pulp through the splenic artery, and to return to the blood flow, they must squeeze through slits in splenic venules of 0.25-1.2 µm in width, 0.9 -3.2 µm in length and around 5 µm in depth (Deplaine et al., 2011; Moreau et al., 2023). Reactive oxygen species (ROS) react with RBC membrane and proteins, leading to cross-linking of spectrin and hemoglobin and aggregation, causing RBCs to lose their flexibility (Fortier et al., 1988; Snyder et al., 1983). These RBCs can no longer squeeze through the narrow slits in the spleen causing them to be filtered out and phagocytosed by macrophages in the red pulp (Klei et al., 2020).

The anion transport protein band 3 is a membrane integral protein. It interacts with ankyrin to serve as an anchor point for the membrane skeleton. As the RBC ages, it accumulates oxidized proteins, including band 3, which results in band 3 clusters, that disrupt the membrane skeleton linkage to the membrane. (Paradkar and Gambhire, 2021). The band 3 cluster is exposed to the auto-antibodies that ensure the clearance of senescent RBCs (Arese et al., 2005; Badior and Casey, 2018; Hornig and Lutz, 2000). Old, damaged, and infected RBCs can be detected by the change of surface antigen composition, such as excess of clustered band 3 and Phosphatidylserine (PS), leading to opsonization or direct phagocytosis (Li et al., 2024).

The formation of knobs on the surface of *Plasmodium falciparum*-infected RBCs is a critical adaptation that allows the parasite to evade immune clearance. By altering membrane flexibility, the parasite renders iRBCs more rigid and susceptible to removal by the spleen. In artemisinin-treated patients, parasites can be cleared from RBCs through a process called pitting, where the infected RBC passes through the splenic slit, and the parasite is physically removed (Buffet et al., 2011). However, cytoadherent iRBCs avoid this fate by sequestering in capillaries, where knobs and EMP1 facilitate adhesion to endothelial cells. This sequestration mechanism, supported by knob structures that stabilize EMP1, effectively prevents splenic filtration and represents a crucial strategy for immune evasion in *Plasmodium falciparum*-mediated malaria.

In conclusion, *Plasmodium falciparum* employs a range of sophisticated immune evasion strategies, leveraging both its ability to manipulate host cell biology and its extensive repertoire of variant surface antigens. The parasite's capacity to avoid immune detection by residing within RBCs, regulate antigen exposure through mutually exclusive gene expression, and utilize mechanisms like rosetting and sequestration highlights its adaptability. Knob structures play a central role in immune evasion by stabilizing EMP1 and facilitating cytoadherence, allowing iRBCs to avoid splenic clearance. Understanding these mechanisms is critical for developing therapies that target the parasite's immune evasion tactics, potentially disrupting its ability to evade host defenses and cause severe disease.

1.2.4 Functional role of knobs in infected erythrocyte

When the host RBCs are infected, they go through a remodelling process during which parasite proteins are exported into the iRBC cytosol and membrane, creating a parasite-controlled interface between the parasite and host cell surroundings. In this process, iRBCs develop protrusions that display, on average, 3 EMP1 adhesin molecules, and this complex is referred to as knobs (Gruenberg et al., 1983; Sanchez et al., 2019; Wiser, 2023). Knobs give iRBCs their cytoadhesive properties causing the main symptoms in severe malaria.

Although EMP1 plays an important role in cytoadhesion, the knobs enable effective interaction between EMP1 and endothelial receptors. KAHRP knock-out (KO) parasites do not produce knobs but express EMP1 on the iRBC surface, yet significantly fewer KAHRP-KO parasite iRBCs can cytoadhere under physiological sheer stress when compared to WT parasite iRBCs. The average wall shear stress required to detach 50% of adherent parasitized cells was 0.33 Pa for the 3D7 KAHRP-KO lines whereas it was 0.95 Pa for the WT 3D7 line. (Crabb et al., 1997). Parasite clones with spontaneous Chromosome 2 end deletion around 100 kB from the telomere lack the KAHRP gene and are, therefore, knobless, also have reduced EMP1 expression by approximately 50% on the iRBC surface compared to WT knobby iRBCs (Horrocks et al., 2005). Another study shows, that when various KAHRP regions were disrupted with the rest of Chromosome 2 end genes intact, EMP1 was expressed on the surface of the iRBC to an equivalent amount as in WT parasite-infected cells, yet the cytoadhesion properties of the KAHRP knock-out line were reduced by up to 80% (Rug et al., 2006). These findings underscore that while EMP1 is necessary for cytoadhesion, the structural component of the knob is crucial for maintaining adhesion strength and effective sequestration under shear stress.

The knob structure is supported by a 50-100 nm wide, 20-50 nm high spiral structure underlying the iRBC membrane (Sanchez et al., 2021; Watermeyer et al., 2016). The spiral is anchored in the membrane via EMP1 and integrated into the membrane skeleton. Electron microscopy using Ni^{2+}-NTA-5 nm gold nanoprobes on the inner leaflet of the iRBC membrane identified the histidine-rich region of KAHRP in the knob spiral (Sanchez et al., 2021). KAHRP is essential for knob development, as KAHRP knock-out parasite lines do not develop knobs and cannot efficiently adhere under the shear forces of blood flow (Crabb et al., 1997; Glenister et al., 2002). Less drastic changes, such as selectively removing C-terminal regions of KAHRP, still reduce adhesiveness by 50% at a loss of 3' repeat region or 80% at the disruption of 5' repeats (Rug et al., 2006). In addition, KAHRP has been shown to play a part in the infected erythrocyte membrane rigidification contributing 51% of the overall increase of membrane rigidity when comparing iRBC to uninfected RBC membrane (Glenister et al., 2002). Single-molecule localization microscopy determined that approximately 60 KAHRP molecules are involved per knob. (Sanchez et al., 2021). Although the main spiral component has not been identified so far, it is assumed that the KAHRP protein does not support the spiral structure on its own due to its disordered nature but plays a role in binding the interaction partners.

1.2.5 KAHRP structure and functional domains

Knobs are distinctive membrane protrusions that arise on *Plasmodium falciparum*–infected erythrocytes, enhancing the rigidity of the red cell membrane and facilitating parasite sequestration in the microvasculature by providing anchor sites for adhesive ligands. Seminal work in the late 1970s and early 1980s demonstrated that knob-positive parasite lines produce an 80–89 kDa protein absent in knob-negative lines (Hadley et al., 1983; Kilejian, 1979), and this factor was subsequently identified as the KAHRP. Although KAHRP's (PfIT_020006800) predicted molecular mass is approximately 62.7 kDa, it runs at a higher apparent molecular weight on SDS-PAGE, which has been attributed to the unusually high content of histidine and lysine residues (Pologe et al., 1987; Rug et al., 2006). The protein's sequence begins with a signal peptide and a *Plasmodium* export element (PEXEL) motif that direct cleavage of its N terminus in the endoplasmic reticulum, enabling the export of KAHRP into the host erythrocyte cytosol. Once cleaved, the protein exposes a new N terminus containing an ~60-residue histidine-rich region (HRR) characterized by three discrete histidine repeats—one each of 7, 6, and 9 residues in length, and alternating Gln-His sequence (Pologe et al., 1987). Predictions from AlphaFold Monomer v2.0 suggest that the segment following this histidine-rich stretch contains three β-strands constituting a β-sheet, followed by two short α-helices. Beyond this structured domain, KAHRP transitions into a predominantly disordered region but retains two critical repeat domains, commonly designated the 5′ and 3′ repeats. The 5′ repeat, residues 370–438, consists of multiple iterations of a 13-amino-acid consensus sequence Asp-Gly-Glu-Gly-Glu-Lys-Lys-Lys-Ser-Lys-Lys-His-Lys and has been closely tied to the protein's interactions with host skeletal components (Pologe et al., 1987; Rug et al., 2006). Slightly further downstream, the 3′ repeat region begins near residue 540 and encompasses four approximate repeats of a 10-amino-acid motif (Thr/Ser)-Lys-Gly-Ala-Thr-Lys-Glu-Ala-Ser-Thr (Pologe et al., 1987).

The protein's overall architecture thus features an N-terminal signal and export sequence, a histidine-rich region, a partially ordered core with identifiable β-sheet and α-helices, and two major repeat domains called 5′ and 3′ repeats. Deletions or significant alterations within these repeat regions have been shown to disrupt KAHRP's capacity to bind to other proteins, and affect cytoadhesion properties, underlining the importance of both the histidine-rich segment and the extended repeats in establishing KAHRP's pivotal role in knob formation and iRBC cytoadherence (Rug et al., 2006; Waller et al., 1999). Notably, parasites lacking the *kahrp* gene fail to form knobs and cannot efficiently adhere under the shear forces of blood flow, underscoring the protein's essential function in building the knob scaffold and anchoring key parasite ligands for immune evasion and vascular sequestration (Crabb et al., 1997).

1.2.6 KAHRP localization and knob architecture

Knobs appear as electron-dense protrusions on the surface of infected erythrocytes and have long been associated with the presence of KAHRP and an underlying scaffold of host cytoskeletal proteins. Early microscopic analyses using immunogold labeling of KAHRP provided direct evidence of its enrichment in these dense structures: for instance, immunoelectron microscopy in knob-positive parasite lines showed discrete accumulations of gold-labeled KAHRP at the knobs, whereas knob-negative parasites lacked this signal (Culvenor et al., 1987; Pologe et al., 1987). These findings helped clarify that knobs themselves possess a characteristically dense staining under transmission electron microscopy (TEM), potentially reflecting the high concentration of proteins in localized membrane domains. Indeed, an earlier study proposed that the "electron-dense cups," later identified as knobs, are formed when KAHRP binds to components of the erythrocyte skeletal network—bands 1, 2, 4.1, and 5—thereby creating focal membrane protrusions (Leech et al., 1984). More recent advancements in sample preparation and imaging techniques have provided further insight into the spatial organization of KAHRP within knobs. For example, electron tomography of detergent-insoluble skeletal extracts from infected erythrocytes has shown that knobs are built upon a well-defined, spiral-like skeleton coated by an electron-dense layer, and these spiral elements physically link to the red cell cytoskeleton (Watermeyer et al., 2016). Building on these three-dimensional electron tomography data, super-resolution fluorescence and single-molecule localization microscopy revealed that KAHRP not only accumulates at knob sites but also undergoes dynamic relocalization within the infected cell; early in the ring stage, it associates with structures such as ankyrin bridges, and later in parasite development it concentrates at the remodeled actin junctions (Sanchez et al., 2021). Findings from previous studies indicate that parasite-regulated changes in binding affinity are necessary to explain the relocalization of KAHRP from actin junctions to ankyrin. It has been suggested that these changes may be mediated by post-translational modifications, like tyrosine phosphorylation of KAHRP (Jäger et al., 2021).

Taken together, these observations from classical TEM, immunogold electron microscopy, electron tomography, and advanced super-resolution methods present a unified picture of KAHRP as a principal component of the electron-dense knob scaffold—one that, through its strong association with host proteins, both initiates and stabilizes the protrusions necessary for effective cytoadherence and immune evasion.

1.2.7 KAHRP interactions with the host cytoskeletal network

1.2.7.1 KAHRP binds to spectrin in multiple sites

A hallmark of KAHRP function is its affinity for self and other proteins (Figure 2). GST-KAHRP polypeptides were observed to self-associate in solution, forming structures resembling previously characterized knobs (Oh et al., 2000). This self-associative property of KAHRP complements its ability to interact with host cytoskeletal components. Through peptide-based mapping, researchers found that a 5' region, a segment spanning residue 370–441 in KAHRP is essential for its attachment to the N-5 fragment of α -spectrin (Pei et al., 2005). Cell-based experiments reveal that introducing the N-5 α-spectrin region into infected erythrocytes can misdirect KAHRP from its usual knob location, indicating the importance of KAHRP–spectrin binding for proper knob assembly (Pei et al., 2005). Fluorescent polarization binding assay using a KAHRP segment spanning the 5′ repeats and the region between the 5′ and 3′ repeats showed binding to the spectrin α-chain repeats 12-16 and to the β-chain repeats 10-14 (Cutts et al., 2017). This finding indicates that the KAHRP 5′ repeat domain can engage with the spectrin dimer at several points, including the region near ankyrin's binding site at β-chain repeats 14–15 and the α-chain N-5 fragment, which is associated with spectrin tetramerization (Ipsaro et al., 2009).

1.2.7.2 Ankyrin R uniquely engages with KAHRP in the ring stage

Among several malaria proteins known to interact with the membrane skeleton (EMP1, EMP3, RESA), KAHRP stands out as the only one clearly shown to bind ankyrin R (Weng et al., 2014). This association hinges on a 79-residue fragment of KAHRP (termed K1D) shortly upstream from the 5' repeat region and a subregion D3 in ankyrin R's membrane-binding domain. Erythrocytes resealed with the D3 peptide of ankyrin R when infected with parasites lack normal KAHRP–ankyrin R interactions at the membrane and display diffused localization of KAHRP in RBC cytoplasm rather than its concentrated presence at the membrane, illustrating the necessity of that interaction for proper knob architecture (Weng et al., 2014).

Time-resolved analyses have revealed that KAHRP's interaction with ankyrin and the C-terminus of β-spectrin is transient, occurring predominantly during the early ring stage of parasite development. As the parasite progresses to the trophozoite stage, KAHRP relocates to actin junctional complexes, displaying a strong spatial correlation with actin and the N-terminus of β-spectrin, highlighting a dynamic repositioning essential for knob assembly (Sanchez et al., 2021).

1.2.7.3 Knob formation relies on KAHRP's actin-binding dynamics

Multiple studies have demonstrated that KAHRP can bind to actin and may help organize or stabilize actin-rich sites within infected erythrocytes. Early evidence for a direct KAHRP–actin interaction came from experiments using recombinant KAHRP fragments: one such fragment, designated “Fragment II” and containing a central domain of KAHRP and following 5’ repeat region, was shown to form stable complexes with both spectrin and actin *in vitro* (Kilejian et al., 1991). Later work applied a slow-speed sedimentation method to full-length KAHRP, confirming that KAHRP binds F-actin independently of Native RBCs contain short actin filaments of about 33 to Native RBCs contain short actin filaments of about 33 to 37 nm in length, capped and stabilized by tropomodulin, tropomyosin, and adducin (Gokhin and Fowler, 2016). In *Plasmodium falciparum*–infected RBCs, the parasite mines these actin filaments, forming localized actin networks that link Maurer’s clefts and other parasite-derived structures to the RBC membrane (Cyrklaff et al., 2011; Gokhin and Fowler, 2016). By binding to these actin filaments, KAHRP may foster effective clustering of parasite adhesion ligands, such as PfEMP1, at the membrane surface. This actin-based tethering is proposed to work in tandem with KAHRP’s additional contacts to spectrin, creating a multivalent anchoring mechanism for knobs.

Recent microscopy analyses also corroborate KAHRP’s dynamic relationship with RBC actin. Super-resolution imaging demonstrated that KAHRP relocates from ankyrin early in the ring stage to the remodeled actin junctions in later trophozoite stages (Sanchez et al., 2021). Such observations suggest that KAHRP–actin binding can be transient or developmentally regulated, allowing knobs to form at sites of cytoskeletal remodeling.

37 nm in length, capped and stabilized by tropomodulin, tropomyosin, and adducin (Gokhin and Fowler, 2016). In *Plasmodium falciparum*–infected RBCs, the parasite mines these actin filaments, forming localized actin networks that link Maurer’s clefts and other parasite-derived structures to the RBC membrane (Cyrklaff et al., 2011; Gokhin and Fowler, 2016). By binding to these actin filaments, KAHRP may foster effective clustering of parasite adhesion ligands, such as PfEMP1, at the membrane

surface. This actin-based tethering is proposed to work in tandem with KAHRP's additional contacts to spectrin, creating a multivalent anchoring mechanism for knobs.

Recent microscopy analyses also corroborate KAHRP's dynamic relationship with RBC actin. Super-resolution imaging demonstrated that KAHRP relocates from ankyrin early in the ring stage to the remodeled actin junctions in later trophozoite stages (Sanchez et al., 2021). Such observations suggest that KAHRP–actin binding can be transient or developmentally regulated, allowing knobs to form at sites of cytoskeletal remodeling. other skeletal components (Oh et al., 2000). These findings highlight actin as a key host target for KAHRP, in addition to the well-documented spectrin and ankyrin interactions.

1.2.7.4 KAHRP does not bind protein 4.1

Several investigations have addressed whether KAHRP physically associates with red cell protein 4.1, a key component of the spectrin–actin junctional complex. A slow-speed sedimentation approach that successfully demonstrated the binding of KAHRP to spectrin and F-actin did not detect meaningful binding to purified protein 4.1 (Oh et al., 2000). This finding stands in contrast to other parasite proteins such as MESA (also called PfEMP2), which have been shown to form stable complexes with band 4.1 in infected erythrocytes (Lustigman et al., 1990; Waller et al., 2003). In the case of KAHRP, most functional data instead underscore strong interactions with α -spectrin, β -spectrin, and ankyrin R, as well as a capacity to bind actin (Kilejian et al., 1991; Oh et al., 2000; Weng et al., 2014). Despite the lack of direct biochemical evidence of binding, super-resolution imaging confirmed KAHRP colocalization with protein 4.1 with a positive yet lower cross-correlation coefficient than that of tropomyosin or actin (Sanchez et al., 2021).

Overall, biochemical and imaging data show that KAHRP interacts with spectrin (including its α-chain N-5 region and repeats 12-16, and the β-chain repeats 10-14) as well as F-actin, indicating a multivalent capacity to engage various skeletal components. Additionally, KAHRP binds ankyrin R through a 79-residue fragment (K1D) in KAHRP and the D3 subdomain in ankyrin's membrane-binding domain.

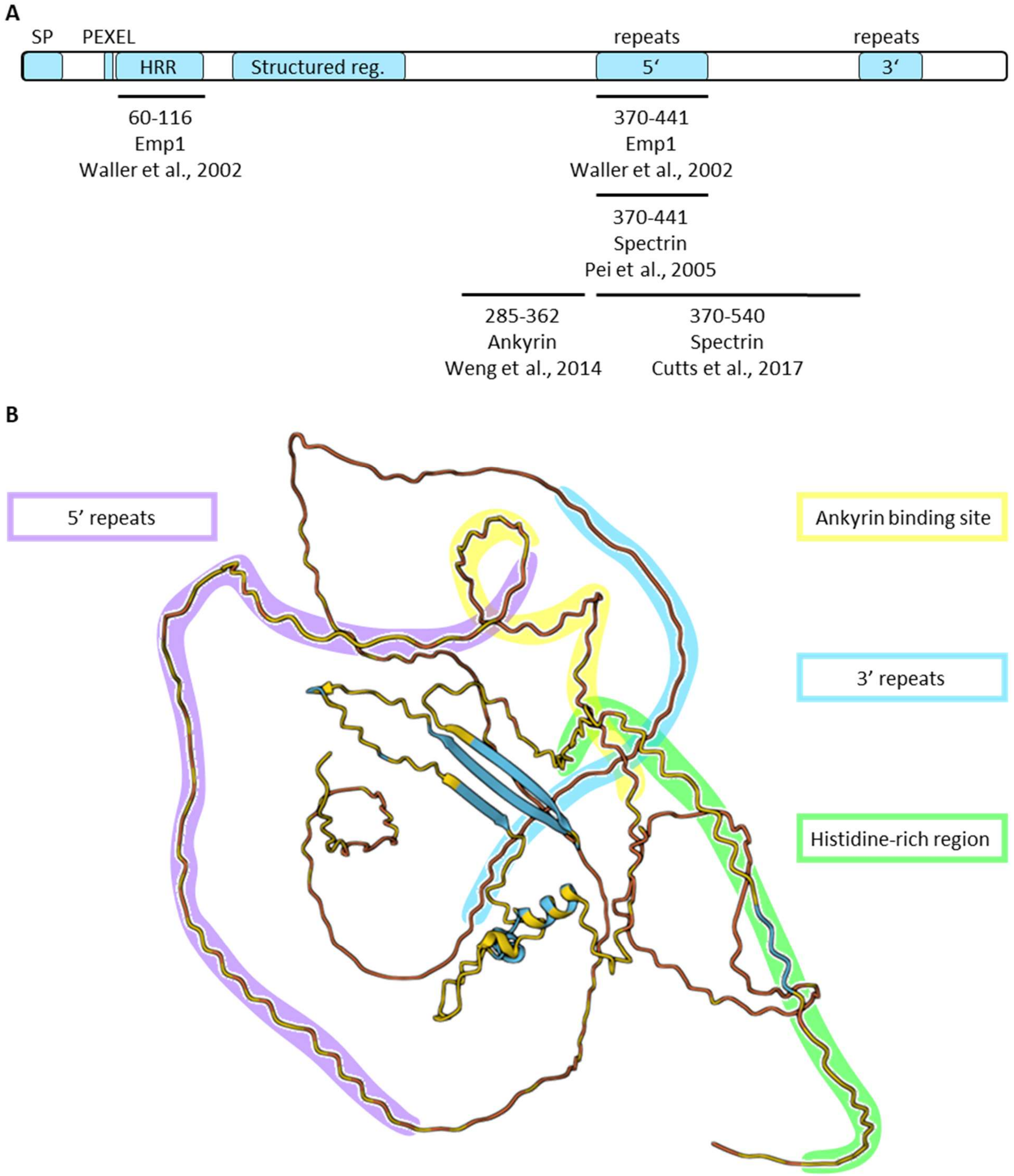

Figure 2. Knob-associated histidine rich protein.
(A) KAHRP domains and identified interaction partners. (B) KAHRP 3D structure prediction with AlphaFold Monomer v2.0. with prediction confidence: ▮ very high (pLDDT > 90), ▮ confident (90 > pLDDT > 70), ▮ low (70 > pLDDT > 50), ▮ very low (pLDDT < 50).

However, results regarding a direct KAHRP–protein 4.1 interaction remain inconclusive; while co-localization has been reported, *in vitro* assays have shown no affinity. Recent computational and imaging studies support a model in which KAHRP transitions from initially associating with ankyrin, spectrin, and actin complexes to ultimately concentrating at remodelled actin junctions, where knobs fully develop. A particle-based simulation suggested that KAHRP may occupy spectrin, ankyrin, and actin binding sites in the ring stage (1–24 hours post-invasion) to facilitate a diffusion gradient toward the membrane before relocating to actin-dense regions in the trophozoite stage (24–36 hours) (Jäger et al., 2021). Despite these insights, precisely which regulatory events trigger such repositioning remains unknown.

1.2.8 PfEMP1 binds KAHRP and the erythrocyte membrane skeleton

PfEMP1, the major cytoadherence ligand on *Plasmodium falciparum*–infected erythrocytes, interacts directly with KAHRP through specific regions on both molecules. The most extensively characterized sites on KAHRP include its histidine-rich segment (residues ~61–116) and the 5' repeat domain, each of which can bind the cytoplasmic region of PfEMP1 (Waller et al., 1999). Biochemical assays with recombinant KAHRP fragments showed that removing the histidine-rich or 5' repeats disrupts PfEMP1 binding, whereas altering the 3' repeats has little effect (Waller et al., 1999). Further work indicated that these contacts are largely electrostatic, owing to KAHRP's abundance of basic residues and PfEMP1's acidic cytoplasmic tail (Voigt et al., 2000).

Subsequent domain-mapping studies refined this interaction model by analyzing how the histidine-rich region and 5' repeats of KAHRP bind different segments of PfEMP1's cytoplasmic portion, known as VARC (Waller et al., 2002). The VARC domain, which encompasses multiple subfragments (A, B1, B2, B3, and C), appears to be engaged in a stepwise manner: the histidine-rich region first associates with VARC B3, then proceeds to VARC C, whereas the 5' repeats bind VARC B2 before ultimately attaching to VARC A. This sequential, multi-step "entwining" mechanism suggests that KAHRP progressively wraps around VARC to form an especially stable KAHRP–PfEMP1 complex. By establishing high-affinity, multi-domain contacts, KAHRP may help to cluster PfEMP1 in knobs, thereby promoting robust cytoadherence under the shear conditions encountered in human microvasculature (Waller et al., 2002).

The cytoplasmic tail of PfEMP1 also engages with components of the host membrane skeleton. According to structural analysis, the recombinant constructs of the cytoplasmic tail of PfEMP1, referred to as the acidic terminal segment (ATS), was reported to have broad affinity for various spectrin domains but showed some residue-specific bias toward domain 17 of α -spectrin (Cutts et al., 2017). This repeat lies near the skeletal junction complex, close to where spectrin connects with actin filaments. PfEMP1 can also associate with the host actin through its cytoplasmic domain. An *in vitro* binding assay demonstrated that purified PfEMP1 (expressed as GST-VARCD) co-sediments with both F-actin and spectrin–actin–protein 4.1 complexes, while showing no measurable affinity for protein 4.1 or ankyrin alone (Oh et al., 2000). This result indicates that PfEMP1's actin-binding capability does not depend on protein 4.1 or other membrane components but, rather, arises directly from the recognition of the filamentous actin.

1.2.9 Complementary parasite proteins in membrane skeleton remodeling

In addition to KAHRP and PfEMP1, several other parasite proteins contribute to the intricate rearrangement of the red blood cell membrane skeleton, playing complementary roles in stabilizing the modified structure and facilitating parasite survival and immune evasion.

PfEMP3 is a membrane-associated protein that has been shown to account for roughly 15% of the overall increase in membrane rigidity in *Plasmodium falciparum*–infected erythrocytes, as determined by micropipette aspiration (Glenister et al., 2002). A specific 60-residue fragment (FIa1, spanning residues 38–97) of PfEMP3 binds to a site near the C terminus of α -spectrin, fragment from repeat 17 until C-terminus, exactly where spectrin attaches to actin and protein 4.1R, forming the actin junction (Pei et al., 2007b). This interaction was confirmed by *in vitro* binding assays, which showed that introducing the recombinant FIa1 fragment disrupts the spectrin–actin–4.1R ternary complex and lowers erythrocyte shear resistance (Pei et al., 2007b). Additionally, erythrocytes resealed with growing concentrations of FIa1 fragment showed increasing decay of deformability (Pei et al., 2007b). Collectively, these findings suggest that PfEMP3 alters the local cytoskeletal organization, thereby affecting local membrane stiffness and aiding membrane skeletal rearrangement.

Mature Parasite-Infected Erythrocyte Surface Antigen (MESA), also referred to as PfEMP2, localizes to the cytoplasmic side of the infected RBC membrane and binds to protein 4.1 (Coppel et al., 1988; Lustigman et al., 1990). Parasite lines that form knobs display increased MESA membrane attachment, implying a potential contribution to knob assembly (Coppel et al., 1988). Interestingly, the MESA erythrocyte cytoskeleton-binding (MEC) motif is also found in at least six additional parasite proteins, all of which can bind RBC inside-out vesicles and two coprecipitate protein 4.1R in inside-out vesicle lysates (Kilili and LaCount, 2011). This suggests a level of functional redundancy where other MEC domain-containing proteins may compensate for MESA's role in the membrane skeleton. Moreover, protein 4.1 undergoes heightened phosphorylation in infected erythrocytes, and band 4.1's increased phosphorylation is known to decrease its affinity for spectrin (Eder et al., 1986; Lustigman et al., 1990). These modifications may modulate the cytoskeletal network in ways that indirectly support knob architecture, even though MESA deletion by itself does not compromise cytoadherence (Magowan et al., 1995).

Ring-infected erythrocyte surface antigen (RESA) is predominantly involved in stiffening the RBC membrane during the early (ring) stages. Studies have demonstrated that a 108-amino-acid segment of RESA (residues 663–770) specifically interacts with repeat 16 of the β-spectrin chain, located near the site where spectrin dimers associate to form tetramers (Pei et al., 2007a). This interaction plays a crucial role in stabilizing the spectrin tetramer, preventing its dissociation into individual dimers, both within resealed erythrocytes with the $RESA_{663\text{-}770}$ fragment and in solution. The presence of this RESA fragment enhances the erythrocyte's resilience against mechanical stress and thermal damage. Additionally, experiments with resealed erythrocytes containing the $RESA_{663–770}$ fragment have shown that these cells exhibit increased resistance to invasion by *Plasmodium falciparum* merozoites (Pei et al., 2007a).

The study of knobs and KAHRP underscores the remarkable complexity and specificity of *Plasmodium falciparum's* adaptations for survival and immune evasion within the host. Knobs, supported by the structural and functional versatility of KAHRP, integrate multiple interactions with the host cytoskeleton, providing a robust scaffold for PfEMP1 clustering and effective cytoadhesion under physiological shear stress. Despite significant advances in understanding these processes, the interaction of parasite and host proteins in knob assembly and function remains only partially understood. This work highlights the importance of unraveling these mechanisms to inform targeted therapeutic strategies that could disrupt cytoadherence and mitigate severe malaria pathology.

1.2.10 Membrane skeleton

The red blood cell (RBC) cytoskeleton is primarily composed of spectrin tetramers, which organize into a hexagon-like network. On average, six spectrin tetramers connect at approximately 35,000 actin junctions, each actin protofilament measuring just 36 nm in length (Lux, 2016; Mohandas and Gallagher, 2008). Each spectrin tetramer consists of two dimers joined head-to-head, giving them a predicted length of roughly 200 nm (Brown et al., 2015; Lux, 2016; Machnicka et al., 2014). Their measured length is, however, much shorter, experimental findings place the end-to-end distance within a 50–100 nm range (Lux, 2016; Mohandas and Gallagher, 2008). Despite these measurements, the precise length distribution of spectrin tetramers remains unclear due to the limitations of sample preparation techniques for microscopy, which often stretch the spectrin chains (Jäger et al., 2021). The tight coiling of spectrin strands contributes to the formation of a dense jelly-like layer beneath the plasma membrane (Boal, 1994; Heinrich et al., 2001; Picart et al., 2000; Stokke et al., 1985).

The red blood cell (RBC) membrane skeleton relies on the spectrin–actin network for shear elasticity, while the plasma membrane contributes bending rigidity, forming a mechanically resilient composite (Lim H. W. et al., 2002). This stability depends on numerous links between the cytoskeleton and the membrane, established primarily through two types of protein complexes. At spectrin ends, actin junctional complexes connect the cytoskeleton through protein 4.1 and p55 to the membrane via interactions with glycophorin C and D (Lux, 2016). At the midpoints of spectrin tetramers, ankyrin complexes provide additional attachment points by binding anion exchanger 1 (AE1), also referred to as band 3 (Lux, 2016; Mohandas and Gallagher, 2008). Band 3, one of the most abundant proteins in

RBCs with approximately 1.2 million copies per cell, is essential for these connections and is distributed across the two complexes and the membrane itself (Lux, 2016).

Junctional complexes within the red blood cell cytoskeleton undergo continuous turnover, as evidenced by actin monomer exchange and the presence of uncapped actin filaments (Gokhin et al., 2015; Nowak et al., 2021; Pan et al., 2018). This dynamic regulation is mediated by two critical capping proteins: adducin, which caps the fast-growing barbed ends, and tropomodulin, which stabilizes the slow-growing pointed ends. Additionally, tropomyosin binds along the sides of actin filaments, enhancing their stability and supporting the overall integrity of the cytoskeleton (Matsuoka et al., 2000).

1.2.11 Application of CRISPR-Cas9 in *Plasmodium falciparum*

The first contribution to the CRISPR Cas9 technology was published in 1987 (Ishino et al., 1987) where they described a class of interspaced short sequence repeats (SSRs) in *E. coli*. Only in 2002 were CRISPR-associated genes (*Cas*) discovered (Jansen et al., 2002). Subsequent years elucidated the functional role of Cas9 in creating double-stranded breaks (DSBs) in DNA, guided by CRISPR RNAs (crRNAs) and the programmability of CRISPR Cas9 to cleave a specific DNA sequence when provided with a guide RNA (gRNA) (Doudna and Charpentier, 2014; Jinek et al., 2012).

A functional complex is created by combining Cas9 endonuclease with crRNA that is complementary to a palindromic repeat and the target DNA sequence, and tracrRNA complementary and annealing to the palindromic repeat sequence in crRNA. The complex will then cleave DNA by introducing DSBs in the target DNA sequence if it is followed by a protospacer adjacent motif (PAM). This complex has been simplified for applications in genetic editing, combining the crRNA and tracrRNA into a single-guide RNA molecule. The DSB is introduced by simultaneously cleaving the DNA strand complementary to the sgRNA with the Cas9 HNH nuclease domain, while the complementary strand is cleaved by the Cas9 RuvC domain (Jinek et al., 2012).

The DSB is further repaired via one of the two pathways: (1) Non-Homologous End Joining (NHEJ), where the ends are joined by ligase to repair the break. This mechanism often results in small insertions or deletions at the ligation site, leading to mutations or gene disruption (Dueva and Iliakis, 2013). *Plasmodium* lacks proteins required for NHEJ, such as Ku 70/80 and DNA ligase 4 (Kirkman et al., 2014), and this mechanism is, therefore, unavailable in the asexual culture. (2) Homology-directed repair (HDR) is mediated by general recombination mechanisms that rely on homologous chromosomes in a diploid genome or sister chromatids during the DNA replication process. The DSB is first recognized by the Mre11-Rad50-Xrs2 (MRX) complex, which binds to the dsDNA ends and initiates 5’-to-3’ resection with the help of Sae2 nuclease, which removes a small oligonucleotide (Mimitou and Symington, 2008; Zhu et al., 2008). Two homologues to the proteins in this complex have been identified in *Plasmodium*, gene PF3D7_0107800 encodes for a homologue of Mre11 and PF3D7_0605800 encodes a homologue of Rad50 (Lee et al., 2014). Next, an extensive tract of ssDNA is generated by Exo1 nuclease or Sgs1 helicase in complex with Dna2 endonuclease. Homologues to Exo1 and Sgs1 proteins are described in *Plasmodium* generated by genes PF3D7_0725000 and PF3D7_0918600 respectively (Cejka et al., 2010; Mimitou and Symington, 2008). The newly created 3’ ssDNA strand is protected from degradation by heterotrimeric replication protein A (RPA) (Bhattacharyya et al., 2005). In yeast model, RPA is further displaced by Rad52, which delivers ATP-bound Rad51 recombinase. Rad51 forms nucleoprotein filament and catalyzes the pairing of the ssDNA to the complementary sequence, forming a displacement loop (D loop). Although *Plasmodium* expresses Rad51 homolog PF3D7_1107400 and two RPA homologs PF3D7_0409600 and PF3D7_0904800, they lack the N-terminal domain necessary for the interaction with Rad52, and there are no discovered Rad52 homologs (Bhattacharyya et al., 2005; Gopalakrishnan and Kumar, 2013; Voss et al., 2002). The 3’ ssDNA strand is extended by polymerase δ-dependent DNA synthesis(Lee et al., 2014; Mimitou and Symington, 2008). In *Plasmodium falciparum* SNPs have been inserted in the sequence up to 900 bp from the site of DSB (McNamara et al., 2013).

For the purpose of mutation introduction, the DSB is repaired using a synthetic linear ssDNA (PCR product) or circular dsDNA (episomal plasmid) as a template for HDR. Asexual stages of *Plasmodium falciparum* are haploid and lack the homologous sequence (Calhoun et al., 2017). Furthermore, the first S-phase in *Plasmodium falciparum* has been determined to start no earlier than 24 hours post-infection (hpi), hindering parasite genome-based HDR in the first 24 hours of the asexual cycle (Arnot et al., 2011; Ganter et al., 2017; Russo et al., 2009) . These qualities make *Plasmodium falciparum* an especially attractive target organism for CRISPR Cas9 mutagenesis.

Compared to other methods of genomic DNA (gDNA) mutagenesis, CRISPR Cas9 has many advantages in ease and application robustness. For example, zinc finger nucleases (ZNFs), are enzymes, the sequence of which is customized to target a specific DNA sequence. These enzymes encode for the FokI endonuclease domain, which is only active in a heterodimer, where one protein would bind upstream and another downstream of the DSB site. ZNFs, therefore, require the design and expression of two proteins in the parasite to target 24 bases determining the site of the DSB (Porteus and Carroll, 2005; Urnov et al., 2010) Similarly, transcription activator-like effector nucleases (TALENs) use the same FokI catalytic domain and require the simultaneous expression of two proteins in the cell to achieve catalytic activity. However, the specificity of the restriction site is determined by 30-40 bp, making this technique more precise. Engineering and testing ZNF or TALEN enzymes is time-consuming and cost-consuming compared to CRISPR Cas9 technology, which requires only a DNA template for HDR and a sgRNA to determine the 20 bp specificity of the DSB in the cell with the Cas9 enzyme.

Finding a suitable guide for a restriction site is one of the challenges faced when using CRISPR Cas9 technology in *Plasmodium falciparum*. Following the guide, Cas9 requires a 5’-NGG-3’ PAM sequence.

82% of the *Plasmodium falciparum* genome is composed of A+T base pairs, which limits the potential guide design and subsequent DSB site (Videvall, 2018; Weber, 1987). Other Cas enzymes, such as Cas12, which requires a 5’-TTTV-3’ PAM sequence, could be considered for genetic manipulation of *Plasmodium falciparum* (Webi et al., 2024).

1.2.12 Gap of knowledge

Despite over four decades of research on knobs and KAHRP, the molecular mechanisms driving knob assembly remain poorly understood. Targeting key components of the spiral scaffold, such as KAHRP or the adhesin PfEMP1, offers a promising strategy to disrupt knob formation or function, potentially reducing the severity of malaria symptoms and improving patient outcomes. To advance this effort, it is critical to identify and characterize the functional roles of proteins involved in knob architecture. Recent advancements in in situ protein modeling have made three-dimensional structural predictions more accessible, enabling a deeper exploration of KAHRP’s regions beyond those commonly studied.

KAHRP is predominantly a disordered protein, but it contains a predicted structured region spanning residues 136–246. This region includes a β-sheet followed by two short α-helices, forming a domain that has been rarely addressed in prior studies. In this work, I investigated the potential contribution of this structured region to knob assembly by employing alanine scanning mutagenesis. Additionally, I focused on the HRR, which has been mostly studied in the context of its interaction with PfEMP1. Although both the HRR and the 5’ repeat region are known to bind PfEMP1, the fact that there are approximately 60 KAHRP molecules but only three PfEMP1 molecules per knob suggests that the HRR may have additional, unexplored functions (Sanchez et al., 2021; Waller et al., 2002). To explore this hypothesis, I am using alanine scanning to test the HRR's role in knob assembly and assessing its ability to interact with the infected RBC membrane.

Moreover, multiple studies suggest that after its export, KAHRP initially associates with multiple membrane skeleton components during the ring stage before being redirected toward actin junctions and away from ankyrin in later stages. This dynamic relocalization is potentially influenced by changes in binding forces caused by post-translational modifications, such as phosphorylation. To investigate this, I created a mutant substituting a potentially phosphorylated tyrosine at position 193 with phenylalanine, aiming to determine if this modification affects knob assembly.

By targeting these two regions—the structured domain and the HRR—this study aims to uncover previously unidentified roles of KAHRP in knob assembly and further our understanding of this critical structure.

1.3 Protein export

1.3.1 Export sequences

Protein export in *Plasmodium falciparum* relies on a remarkable diversity of export signals and sequences, reflecting the parasite's ability to adapt its trafficking machinery to a wide range of protein architectures. Canonical PEXEL motifs provide a well-defined pathway for directing proteins into the host erythrocyte, involving specific sequence recognition, cleavage, and translocation through the parasitophorous vacuole membrane (PVM). Beyond this canonical system, *Plasmodium* employs non-canonical PEXEL sequences and distinct mechanisms for PEXEL-negative exported proteins (PNEPs). PNEPs lack the conserved PEXEL motif and instead depend on other structural features, such as transmembrane (TM) domains, N-terminal signal peptides, or a combination of both. These variations in export signals highlight the versatility of the parasite's export machinery in ensuring the delivery of effector proteins to their functional destinations, crucial for host cell remodeling and parasite survival.

1.3.1.1 PEXEL-mediated export

PEXEL motif, defined as RxLxE/Q/D, is a conserved sequence that guides proteins into the host erythrocyte. It facilitates their co-translational entry into the endoplasmic reticulum (ER), followed by a critical cleavage event after the leucine residue (RxL↓xE), enabling subsequent export through the PVM (Boddey et al., 2010; Russo et al., 2010). This cleavage event, performed by the aspartyl protease plasmepsin V (PMV), exposes a new N-terminus, which is often N-acetylated, further stabilizing the export-competent protein (Chang et al., 2008).

While co-translational entry into the ER is a well-established mechanism for PEXEL proteins, evidence also supports post-translational ER entry for a subset of these proteins. Specifically, the incorporation of PfSec62, an essential component of post-translational ER translocons, into the PfSec61-PfSPC25-PMV complex suggests that some PEXEL proteins are translocated into the ER after their synthesis. Interestingly, not all PEXEL proteins depend on PfSec62 for ER entry, as demonstrated in the study by Marapana et al., though the underlying reasons for this variability remain unclear (Marapana et al., 2018). This distinction between co-translational and post-translational ER entry reflects the nuanced and flexible nature of protein trafficking within *Plasmodium falciparum*.

Following the PEXEL motif, the spacer region plays an essential role in the export process. This downstream region, composed of approximately 20–50 amino acids, is necessary for efficient export and determines the protein's ability to engage the PTEX machinery. Spacer length and amino acid composition significantly influence export efficiency; for example, truncation experiments have shown a marked ~80% reduction in export efficiency when the spacer is shortened to three amino acids (Gilson et al., 2023). These observations highlight the importance of spacer regions in optimizing the export process.

1.3.1.2 Non-canonical PEXEL-mediated export

While canonical PEXEL sequences are well-documented, non-canonical PEXEL/HT motifs expand the versatility of the export system. Non-canonical motifs deviate from the standard RxLxE/Q/D configuration, yet some are still functional in specific export contexts. For instance, experiments using reporter constructs such as REX3 and GBP demonstrated varying tolerances for substitutions at key PEXEL positions. In REX3 green fluorescent reporter (GFP) reporters, replacing leucine at position 3 with isoleucine (REX3-RQISE-GFP) allowed efficient export, while substitutions of arginine at position 1 with lysine or histidine (REX3-KQLSE-GFP and REX3-HQLSE-GFP) reduced export efficiency by approximately 50%. Conversely, the GBP reporter exhibited a broader tolerance for non-canonical variants: efficient export was observed when arginine at position 1 was replaced by lysine or histidine (GBP-KILAE-GFP and GBP-HILAE-GFP), and when leucine at position 3 was replaced by isoleucine (GBP-RIIAE-GFP). Importantly, immunoblot analyses confirmed the correct cleavage and N-acetylation of these variants, including K.L.E., R.I.E., and H.L.E. sequences (Schulze et al., 2015).

However, not all proteins can tolerate non-canonical modifications. For instance, KAHRP, a protein critical for knob formation and cytoadherence, is unable to accommodate non-canonical PEXEL/HTs, underscoring the importance of sequence specificity for certain exported proteins (Schulze et al., 2015). These findings highlight the nuanced requirements for export mediated by canonical and non-canonical PEXEL motifs, reflecting the diversity of *Plasmodium* protein trafficking mechanisms.

1.3.1.3 Export signals driving PNEP translocation

Unlike PEXEL-containing proteins, the precise molecular triggers for the export of PNEPs remain enigmatic. These proteins represent a structurally diverse group within the *Plasmodium falciparum* exportome, relying on alternative signals for trafficking into the host erythrocyte. Notably, some PNEPs feature an N-terminal signal peptide, others possess internal TM domains, and certain proteins exhibit both structural elements. These variations suggest that distinct export mechanisms might operate within the PNEP class, accommodating diverse protein architectures (Grüring et al., 2012; Heiber et al., 2013).

PNEPs such as MSRP6 and MSRP7, which lack transmembrane domains, rely on classical N-terminal signal peptides for their export. Experiments using murine dihydrofolate reductase (mDHFR) fusion constructs demonstrated that the export of MSRP6 and MSRP7 required protein unfolding during translocation. When unfolded, the proteins trafficked efficiently into the host erythrocyte. However, the addition of the folate analog WR99210 blocked unfolding and arrested these proteins at the PVM, as shown through fluorescence microscopy (Heiber et al., 2013). These results highlight that the N-terminal signal peptide alone is sufficient to direct these soluble PNEPs through a translocation-dependent mechanism, bypassing the need for transmembrane domains.

In contrast, PNEPs such as REX2 require both an internal TM domain and N-terminal signal peptide for efficient export. Protease protection assays showed that the C-terminal region of REX2 was translocated into the parasitophorous vacuole (PV) in an unfolded state, with its TM domain interacting transiently with the parasite plasma membrane (PPM). Additional experiments using mDHFR-tagged REX2 constructs revealed that blocking protein unfolding prevented its export over PMV, indicating that REX2 crosses PVM via the *Plasmodium* translocon of exported proteins (PTEX) complex (Grüring et al., 2012). Reporter constructs with only the TM domain of REX2 were shown to reach the PV or PVM but were not exported across the PVM. In contrast, constructs containing both the TM domain and N-terminal signal peptide of REX2 successfully translocated via PTEX, indicating that both elements are required for the protein to engage with PTEX and complete translocation into the host erythrocyte. This highlights the cooperative role of these domains in the export process.

Protein export in *Plasmodium falciparum* showcases an intricate system accommodating canonical and non-canonical PEXEL motifs as well as PNEPs with distinct structural signals. PEXEL motifs enable ER entry and export, while non-canonical variants highlight functional diversity in export pathways. PNEPs, on the other hand, leverage combinations of N-terminal signal peptides and transmembrane domains for efficient trafficking. Experiments with reporter constructs have demonstrated the essential roles of these structural elements in engaging the PTEX machinery. The reliance on different motifs and signals reflects the parasite's evolutionary adaptability, providing insights into its strategies for host cell manipulation and survival.

1.3.2 Mechanism of protein export

1.3.2.1 Key early events in plasmodium protein export

Exported proteins in *Plasmodium falciparum* are directed into the ER as the first step in their journey to the host erythrocyte (Figure 3). These proteins are inserted into the ER through one of two pathways: co-translational translocation via the Sec61 translocon or post-translational translocation mediated by Sec62, depending on the specific features of the exported protein (Marapana et al., 2018; Matthews et al., 2019). Co-translational translocation is the predominant route, where the signal sequence or TM domain directs proteins into the ER lumen as they are being synthesized (de Koning-Ward et al., 2016).

1.3.2.1.1 Co-translational translocation of PEXEL proteins into the ER

The co-translational translocation of PEXEL-containing proteins begins with their entry into the ER via the PfSec61-PfSPC25-PMV translocon. Marapana et al. (2018) employed stable isotope labeling of amino acids in cell culture (SILAC) and LC-MS/MS to identify proteins interacting with PMV, an aspartyl protease responsible for PEXEL cleavage. Using *Plasmodium falciparum* strains expressing HA-tagged PMV, they demonstrated that PMV co-immunoprecipitated specifically with PfSPC25 and Sec61, but not SPC21, a key component of the classical signal peptidase complex. This result revealed that the PfSec61-PfSPC25-PMV complex functions distinctly from the Sec61-SPC21 complex, which processes signal peptide-containing proteins. Cleavage-incompetent EMP3 competitively inhibited PEXEL protein export, which accumulated in ER. In contrast, secretion of proteins with a signal peptide remained unaffected, highlighting the specificity of the PMV-associated machinery for PEXEL-mediated translocation.

Once inside the ER, PEXEL-containing proteins undergo processing by PMV. PMV cleaves the PEXEL motif at the leucine residue (RxL↓xE), exposing a new N-terminus, which is often N-acetylated. This modification is critical for subsequent export (Boddey et al., 2010; Russo et al., 2010). Using synthetic peptides mimicking the PEXEL motif, Russo et al. (2010) demonstrated that PMV cleaves specifically at the leucine residue. Mutation of this leucine residue abolished cleavage and export competence, as observed through mass spectrometry and protein localization studies (Russo et al., 2010). Further evidence of the critical role of precise PEXEL cleavage was demonstrated by a reporter protein with glutamic acid instead of lysine in the fifth position of the PEXEL motif, which was miscleaved. Instead of being processed at the PEXEL site, cleavage occurred after the signal peptide, resulting in the protein being trapped in the ER and failing to undergo export (Gabriela et al., 2022). This underscores the necessity of accurate PEXEL motif recognition and processing for successful protein trafficking.

The interplay between the PEXEL motif and signal peptides provides further insights into the specificity of PMV. Boddey et al. (2010) showed that in proteins with both a signal peptide and a PEXEL motif, PMV cleaves the PEXEL motif first, before the signal peptide is identified. This sequence-specific cleavage is essential, as demonstrated in experiments where a reporter protein with the PEXEL motif replaced by a signal peptide was successfully translocated into the ER but failed to be exported into the host erythrocyte (Hasan et al., 2023). These findings highlight that PEXEL cleavage by PMV is a prerequisite for export competence, underscoring the specialized role of PMV in guiding PEXEL proteins through the secretory pathway.

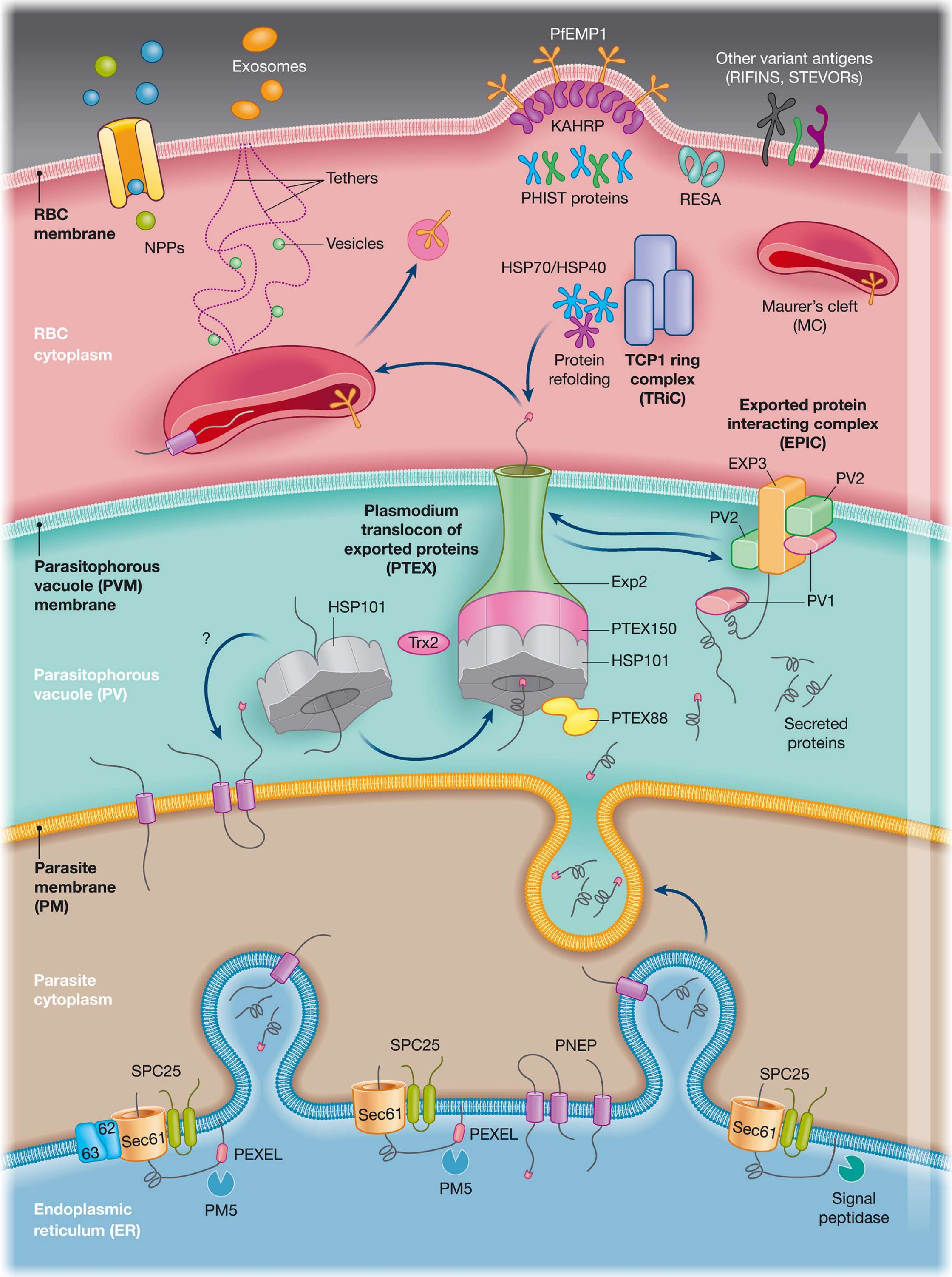

Figure 3. Protein export overview (Matthews et al., 2019).

1.3.2.1.2 Post-translational translocation of PEXEL Proteins via the PfSec61-PfSPC25-PMV-Sec62 complex

A subset of exported proteins in *Plasmodium falciparum* utilizes a specialized post-translational translocation mechanism, mediated by a distinct ER translocon complex involving PfSec62. Unlike the co-translational pathway, this route bypasses the immediate insertion requirement and relies on the unique interaction of PEXEL-containing proteins with the PfSec62-PfSec61-PfSPC25-PMV complex. Knockdown of PfSec62 led to a significant reduction in the levels of specific PEXEL-containing proteins, such as PfEMP3, KAHRP1–69, and HYP1, resulting in their accumulation in the parasite cytosol. Notably, this effect was not observed in classical signal peptide-dependent secretory proteins like MSP1, underscoring the specificity of this post-translational machinery for PEXEL proteins (Marapana et al., 2018).

Further studies suggest that the subset of PEXEL proteins dependent on Sec62 might possess distinct structural features, such as a recessed signal sequence or an absence of a detectable hydrophobic domain at their N-termini, which could differentiate them from proteins utilizing the co-translational pathway (Matthews et al., 2019). Although direct experimental confirmation is pending, these characteristics may reflect unique adaptations that facilitate interaction with the post-translational translocation machinery.

Validation of the PfSec62-associated complex's role was strengthened by crosslinking studies using dithiobis(succinimidyl propionate) (DSP), which stabilized interactions between PMV, PfSec62, and Sec61. Reciprocal immunoprecipitation experiments confirmed these interactions, highlighting the formation of a dedicated machinery for the post-translational translocation of specific PEXEL-containing proteins (Marapana et al., 2018).

1.3.2.1.3 The essential role of HSP101 in PEXEL protein trafficking

Following PMV cleavage, exported proteins travel through intermediate steps before reaching the PTEX translocon at the PVM. HSP101, a member of the ClpB/HSP100 ATPase family, is an ATP-driven molecular motor responsible for unfolding proteins to translocate them across the PVM through PTEX translocon. HSP101 essentiality has been demonstrated in both *Plasmodium falciparum* and P. berghei. Knockdown of HSP101 in *Plasmodium falciparum* led to an arrest in protein export, with cargo accumulating in the PV and parasite growth stalling at the trophozoite stage (Beck et al., 2014; de Koning-Ward et al., 2009). Similar genetic knockdown experiments in P. berghei confirmed that HSP101 is critical for parasite survival (Matthews et al., 2013; Matz et al., 2013).

In addition to its role at the PVM, HSP101 is active in the ER, where it binds PEXEL-containing proteins, potentially stabilizing them for trafficking to PTEX. Gabriela et al. (2022) demonstrated dual localization of HSP101 in both the ER and PV, building on earlier findings by Russo et al. (2010), where PMV pull-downs consistently identified HSP101 and an ER-resident HSP70 as associated proteins, indicating HSP101's presence and functional role in the ER. Immunoprecipitation assays further confirmed its interaction with PEXEL proteins before they engage with PTEX (Gabriela et al., 2022). Structural studies by Ho et al. (2018) showed that HSP101 operates through an ATP-dependent threading mechanism, with pore loops in its hexameric structure sequentially gripping and passing unfolded cargo through the PTEX channel.

1.3.2.1.4 Role of secretory pathway in Plasmodium protein export

Exported proteins use the standard secretory pathway for trafficking from the ER to the PV or the PPM. Evidence for this comes from experiments using Brefeldin A, which inhibits protein transport from ER to Golgi complex by preventing the assembly of COPI coat and vesicle transport (Helms and Rothman, 1992). The addition of Brefeldin A disrupts ER-to-Golgi transport, causing exported proteins like KAHRP to accumulate in the ER (Wickham et al., 2001). Immunofluorescence showed that these proteins failed to exit the ER when Brefeldin A was applied, highlighting the reliance of exported proteins on the secretory pathway (Chang et al., 2008).

1.3.2.1.5 Unique routes for PNEP trafficking to the PV

The transport of PNEPs from the ER to the PV involves distinct mechanisms that diverge from those of PEXEL-containing proteins and showcase the complexity of *Plasmodium*'s export machinery. Following their exit from the ER, PNEPs utilize the standard secretory pathway, with soluble PNEPs being directly released into the PV, while membrane-bound PNEPs first integrate into the PPM via vesicular fusion (Grüring et al., 2012; Mesén-Ramírez et al., 2016; Wickham et al., 2001). Grüring et al., (2012) demonstrated that the transmembrane domains of PNEPs mediate their initial insertion into the ER or its membrane, followed by vesicular transport to the PPM. Using protease protection assays and reporter constructs, they provided evidence that PNEPs, such as REX2, are embedded into the PPM before undergoing further processing.

Mesén-Ramírez et al., (2016) further elucidated the transport of PNEPs by proposing a two-step model for membrane-bound proteins. Once at the PPM, these proteins are subjected to ATP-dependent extraction into the PV. This extraction is crucial for making membrane-bound PNEPs accessible for translocation across the PVM. By contrast, soluble PNEPs bypass this step, being secreted directly into the PV. These findings collectively highlight the sequential and distinct pathways utilized by soluble and membrane-bound PNEPs, reflecting the intricacy and specificity of protein trafficking within *Plasmodium*'s export system.

1.3.2.2 The *Plasmodium* translocon of exported proteins (PTEX) machinery

1.3.2.2.1 EXP2 is the central channel of PTEX

EXP2 forms the central pore of the PTEX complex, enabling the translocation of unfolded proteins across the PVM. Structural studies, including cryo-electron microscopy (cryo-EM), have shown that EXP2 assembles into a ring-like structure, creating a channel through which proteins pass. EXP2 formed pores play a dual role as a part of both a protein translocon and a nutrient channel (Bullen et al., 2012; Ho et al., 2018). Its structural conformation and interaction with other PTEX components, such as HSP101 and PTEX150, are critical for maintaining PTEX function and stability (Ho et al., 2018). Functionally, EXP2 facilitates the export of unfolded substrates driven by the ATP-dependent motor activity of HSP101. As shown in crosslinking studies, EXP2 oligomer builds a pseudo-seven-fold-symmetric funnel-shaped channel, that goes through PVM (Ho et al., 2018).

Several studies have confirmed the essentiality of EXP2 through genetic and experimental knockdown approaches. Mutagenesis experiments in *Plasmodium falciparum* revealed that specific regions of EXP2 are critical for maintaining its channel properties (Ho et al., 2018). EXP2 knockdown via conditional expression systems led to severe defects in protein export, with exported proteins accumulating within the PV. Parasite growth was arrested at the trophozoite stage, underscoring the critical role of EXP2 in parasite survival (Garten et al., 2018; Ho et al., 2018). Similarly, genetic knockouts of EXP2 in *Plasmodium* berghei were lethal, demonstrating its indispensability across different *Plasmodium* species (Matthews et al., 2013; Matz et al., 2013).

1.3.2.2.2 Role of PTEX150 in Plasmodium protein export

PTEX150 is a large, globular protein primarily functioning as the structural backbone of PTEX. Cryo-EM) studies have revealed its location adjacent to the central EXP2 pore, where it interacts extensively with other PTEX components, particularly EXP2 and HSP101 (Bullen et al., 2012; Ho et al., 2018). Functionally, PTEX150 supports the protein export process by stabilizing the interactions between EXP2 and HSP101. It creates a protected pathway for substrate threading by maintaining the funnel-shaped conformation of the EXP2-PTEX150 complex. A proteomic analysis revealed that truncation of the PTEX150 C-terminus reduced the association of other PTEX subunits, highlighting its role in complex stability despite no impact on parasite growth, protein export, or permeability pathways (Elsworth et al., 2016).

Knockdown and knockout studies have unequivocally established the essentiality of PTEX150 for *Plasmodium* survival. Conditional knockdown of PTEX150 in *Plasmodium falciparum* led to an accumulation of exported proteins within the PV, indicating a failure in protein export. Parasite growth was arrested at the trophozoite stage, emphasizing the critical role of PTEX150 in maintaining parasite viability (Elsworth et al., 2014). Genetic knockout of PTEX150 was unsuccessful in *Plasmodium falciparum* and P. berghei, further underscoring its essentiality across different *Plasmodium* species (de Koning-Ward et al., 2009).

1.3.2.2.3 The mechanistic and structural basis of PTEX activity

Recent advances in understanding the PTEX translocon have provided crucial insights into its structure, assembly, and function in facilitating protein export in *Plasmodium falciparum*. As a central machinery for translocating both PEXEL and PNEP proteins across the PVM, PTEX integrates multiple components—EXP2, PTEX150, and HSP101—each contributing uniquely to the translocation process. This section explores studies that elucidate the structural organization, dynamic interactions, and mechanistic roles of PTEX components, shedding light on the sequential and coordinated steps involved in protein export.

Studies utilizing DHFR constructs fused to PEXEL and PNEP proteins have demonstrated that these proteins are translocated across the PVM in an unfolded state. By treating parasites with WR99210, a folate analog that stabilizes the folded state of DHFR, researchers observed that export of the fusion proteins was arrested at the PVM. Fluorescence microscopy confirmed that the proteins accumulated at the PVM instead of entering the host cytosol. These findings indicate that unfolding is a prerequisite for successful translocation through the PTEX machinery, emphasizing the role of ATP-driven unfolding by HSP101 in facilitating export (Grüring et al., 2012; Heiber et al., 2013).

Knockdown studies revealed that the assembly of the PTEX150-EXP2 subcomplex is independent of HSP101. Even after HSP101 knockdown, PTEX150 and EXP2 remained part of a large >1236 kDa complex, though it lacked most HSP101. In contrast, knockdown of either PTEX150 or EXP2 disrupted the integrity of the >1236 kDa complex entirely, emphasizing the foundational role of PTEX150 and EXP2 in maintaining PTEX structure, independent of HSP101 (Gabriela et al., 2022).

EXP2 and PTEX150 form a stable subcomplex within the PTEX machinery, providing a docking platform for HSP101 (Gabriela et al., 2022; Ho et al., 2018). Structural studies revealed that PTEX150 forms a heptameric assembly of hook-like structures (PTEX150 S668–D823) that interlock with the EXP2 channel. These hooks, labeled a–g, oligomerize into a flange-like structure that fits seamlessly into the mouth of the EXP2 pore. Each hook rests in the groove between adjacent EXP2 body domains, with their tips curling into the pore. Additionally, a vertical ring of heptameric H2 helices from PTEX150 line the mouth of the EXP2 funnel, bridging the hexameric HSP101 and the heptameric EXP2 central pores. This arrangement creates a continuous and protected conduit for the translocation of unfolded cargo from HSP101 through EXP2, highlighting PTEX150's role as a structural adaptor connecting these components (Ho et al., 2018).

While EXP2 and PTEX150 remain static, HSP101 dynamically migrates with exported proteins. HSP101 localizes to both the PV and the parasite's ER during the ring and trophozoite stages, interacting specifically with PEXEL proteins in the ER, regardless of their processing status. This suggests that HSP101 may recognize and chaperone PEXEL proteins from the ER to the PV, underscoring its specificity for the EXP2-PTEX150 subcomplex (Gabriela et al., 2022).

HSP101 operates as a molecular motor in the PTEX complex, unfolding and translocating cargo proteins across the PVM in a cyclic process. Its NBD2 pore loops are divided into an "active hand" (Protomers 4–6) and a "passive hand" (Protomers 1–3). The active hand grasps the unfolded cargo, spiraling it downward into the PTEX150-EXP2 funnel while the passive hand maintains a firm grip to prevent backsliding. The active hand then resets, moving upwards to grasp the next region of the unfolding protein, repeating this process until the cargo is completely translocated into the erythrocyte cytosol (Ho et al., 2018; Matthews et al., 2019).

PTEX translocon exists in two distinct conformational states: an extended "engaged" state measuring 195 Å and a more compact "resetting" state measuring 175 Å. While the structures of PTEX150 (S668–D823) and EXP2 remain largely unaltered between these states, the height difference arises from an HSP101 hexamer, which alternates between states in a hinge-like swinging motion. This structural flexibility in HSP101 allows it to transition between gripping and releasing unfolded cargo during the translocation process (Ho et al., 2018).

1.3.2.2.4 PTEX88's contribution to export mechanisms and virulence

PTEX88, initially identified in co-immunoprecipitation experiments as part of the PTEX complex alongside HSP101, PTEX150, and EXP2, is considered an accessory protein rather than a core component. Pull-down assays using HA-tagged HSP101 and PTEX150 in *Plasmodium falciparum* revealed PTEX88 among the proteins co-precipitated with these core PTEX components, suggesting its association with the PTEX machinery (de Koning-Ward et al., 2009).

Functional studies on PTEX88 have shown that it is dispensable for general protein export. Knockout experiments in *Plasmodium berghei* confirmed that PTEX88-deficient parasites were viable and capable of normal protein export. The localization of multiple exported proteins, including PEXEL-containing and PNEPs, remained unaffected in PTEX88-deficient mutants, as observed through immunofluorescence analysis (Matz et al., 2013). Similarly, in *Plasmodium falciparum*, knockdown of PTEX88 using a glmS ribozyme knock-down system showed no significant impairment in the export of a range of proteins, including RESA, STEVOR, SBP1, KAHRP, RIF50, and PfEMP1 (Chisholm et al., 2016).

Despite its non-essential role in general protein export, PTEX88 appears to have a specific function in cytoadherence and tissue sequestration. *P. berghei* parasites lacking PTEX88 failed to sequester in the brain, leading to reduced cerebral complications in infected mice (Matz et al., 2013). In *Plasmodium falciparum*, knockdown of PTEX88 resulted in a marked reduction in cytoadherence to CD36 without affecting the surface presentation of PfEMP1, indicating that PTEX88 may influence sequestration pathways beyond PfEMP1-mediated interactions (Chisholm et al., 2016). These findings suggest that while PTEX88 is not critical for survival or protein export, it plays a significant role in parasite virulence and tissue-specific sequestration.

1.3.2.2.5 Contribution of TRX2 to protein export

Thioredoxin 2 (TRX2) was identified alongside PTEX88 as an accessory protein of the PTEX complex through co-immunoprecipitation studies involving HA-tagged PTEX150 and HSP101 (de Koning-Ward et al., 2009). TRX2 is thought to contribute to the redox environment necessary for PTEX functionality by reducing disulfide bonds in exported proteins, a process critical for their proper folding after translocation.

Knockout studies in *P. berghei* revealed that TRX2-deficient parasites are viable, though they display minor growth and virulence defects. These parasites exhibited delayed trophozoite development, fewer nuclei per schizont, and a slight reduction in blood-stage propagation rates, suggesting a role for TRX2 in optimizing parasite growth and export efficiency (Matz et al., 2015). Absence of TRX2 leads to minor changes in growth rate and virulence (Matz et al., 2015).

1.3.2.2.6 Emerging contributors in Plasmodium protein export

In addition to well-studied accessory proteins like PTEX88 and TRX2, other proteins such as HSP70-x, Pf113, and PV1 have been implicated in supporting the PTEX machinery, suggesting a broader network of interactions essential for *Plasmodium* protein export.

HSP70-x, a parasite-specific chaperone, was identified in association with both exported protein-interacting complex (EPIC) and PTEX machinery through mass spectrometry of PV1 immunoprecipitation native DPS crosslinked PTEX50 immunoprecipitation respectively (Batinovic et al., 2017; Elsworth et al., 2016). While its specific role remains less defined than other PTEX components, HSP70-x is hypothesized to contribute to the folding and stabilization of exported proteins as they transit through the PVM.

Mass spectrometry of DPS cross-linked PTEX150 immunoprecipitated Pf113 and PV1 (Batinovic et al., 2017; Elsworth et al., 2016). The interaction was confirmed by reverse immunoprecipitation of Pf113 and PV1 (Elsworth et al., 2016). Additionally PV1 immunoprecipitated HSP101 and EXP2 (Batinovic et al., 2017). Pf113 was identified as a GP1-anchored protein associated with PTEX in the PV, while PV1 is a PV-resident protein (Sanders et al., 2005). While Pf113 does not appear to directly mediate protein translocation, its consistent presence in the PTEX complex and localization to the PV imply a supporting role, possibly in stabilizing PTEX or coordinating with other accessory proteins. Knockdown experiments revealed that while PV1 is not essential for parasite viability, it plays a critical role in host cell remodeling. Depletion of PV1 led to reduced adhesion of infected erythrocytes to CD36 and altered cellular deformability, highlighting its importance in virulence-related pathways (Batinovic et al., 2017). PV1 also appears to be a component of EPIC, reinforcing its role in export function (Batinovic et al., 2017).

In summary, the PTEX translocon operates as a highly coordinated machinery for protein export in *Plasmodium falciparum*. EXP2 and PTEX150 form a static subcomplex that establishes the structural framework and serves as a docking platform for the dynamic HSP101 motor. HSP101 unfolds and translocates cargo proteins in a cyclic manner, utilizing its ATP-driven activity to drive them through a protected conduit formed by PTEX150 and EXP2. The complex exhibits conformational flexibility, transitioning between "engaged" and "resetting" states to accommodate cargo translocation.

Knockdown studies highlight the independent assembly and structural integrity of the EXP2-PTEX150 subcomplex, underscoring its essential role in the export process. Additionally, HSP101 interacts with PEXEL proteins in the ER, suggesting a potential role in recruiting and stabilizing exported proteins prior to their engagement with the PTEX machinery. A diverse range of accessory proteins, including PTEX88, TRX2, HSP70-x, Pf113, and PV1, further underscores the complexity and adaptability of the PTEX machinery.

1.3.2.3 Protein export beyond PTEX: mechanisms and pathways

1.3.2.3.1 Export from PTEX to Maurer's Clefts

After exiting the PTEX translocon, exported proteins traverse the erythrocyte cytoplasm, ultimately reaching Maurer's clefts or other destinations. Electron microscopy studies suggest that proteins destined for the erythrocyte plasma membrane, such as PfEMP1, first, transit the cytoplasm towards Maurer's clefts as chaperone-associated transport complexes rather than in vesicles (de Koning-Ward et al., 2016; Knuepfer et al., 2005a, 2005b). Studies utilizing solubility assays, fluorescence photobleaching, and immunogold electron microscopy have demonstrated that these proteins exist in complexes during their transit to Maurer's clefts, supporting the hypothesis of a vesicle-independent transport mechanism (Knuepfer et al., 2005a, 2005b).

Further evidence of complex-mediated transport comes from J-dots, small structures containing parasite-encoded Hsp40 proteins and HSP70-x, which may assist in trafficking PfEMP1 to Maurer's clefts (Külzer et al., 2012, 2010; McMillan et al., 2013).

1.3.2.3.2 Maurer's Cleft's structure and function

Maurer's clefts are flattened membranous structures with a complex morphology and distinct subdomains (Hanssen et al., 2008). Electron tomography has revealed that these clefts are tethered to the PVM during early development and connected to the red blood cell membrane via stalk-like actin filaments. These filaments likely facilitate protein transfer between the clefts and the erythrocyte membrane (Cyrklaff et al., 2011; Hanssen et al., 2008; Rug et al., 2014; Tilley et al., 2008).

Proteins within Maurer's clefts, such as REX1, SBP1, and MAHRP1, are organized into discrete subdomains, demonstrated by 3D-SIM imaging. PfEMP1 and MAHRP1 occupy distinct regions, while REX1 occupies peripheral areas. This compartmentalization likely reflects specialized roles in protein trafficking (McMillan et al., 2013). Inducible knockdown of REX1, a Maurer's cleft-resident protein, leads to stacked and interconnected clefts, indicating its role in maintaining cleft structure and severing lamellae into discrete cisternae (de Koning-Ward et al., 2016). Disruption of PfPTP1, a protein suggested to link Maurer's clefts to the host actin cytoskeleton, results in cleft disorganization and impaired trafficking of virulence factors like PfEMP1 and STEVOR to the erythrocyte surface (Rug et al., 2014).

1.3.2.3.3 Protein export from Maurer's Clefts to the erythrocyte surface

Forward trafficking of proteins from Maurer's clefts to the erythrocyte membrane may involve either vesicle-mediated or chaperone-mediated mechanisms. Electron-dense vesicles (EDVs), approximately 80–100 nm in size, have been identified in the erythrocyte cytoplasm, often near the clefts (Cyrklaff et al., 2011; McMillan et al., 2013; Trelka et al., 2000). These vesicles, labeled with antibodies against PfEMP1 and PfEMP3, appear during the early trophozoite stage, coinciding with PfEMP1 delivery to the erythrocyte surface (de Koning-Ward et al., 2016; McMillan et al., 2013; Trelka et al., 2000; Wickham et al., 2001). EDVs have been proposed to function in PfEMP1 transport to the erythrocyte surface, where they fuse with the membrane, as evidenced by immunogold labeling and electron microscopy (de Koning-Ward et al., 2016; McMillan et al., 2013).

Additionally, 25 nm vesicle-like structures (VLS) have been observed, but their role in trafficking remains unclear as they do not label with known Maurer's cleft protein markers or exported proteins EMP1 and EMP3 (de Koning-Ward et al., 2016; Hanssen et al., 2008; McMillan et al., 2013).

Actin filaments also play a critical role in bridging Maurer's clefts and the erythrocyte membrane. Disruption of actin filaments by deleting or mutating proteins like PfPTP1 or SBP1 leads to impaired trafficking and reduced cytoadherence, emphasizing the importance of cytoskeletal dynamics in protein export (Blisnick et al., 2000; Rug et al., 2014).

The export of virulence factors and other proteins beyond PTEX involves a complex interplay of chaperone-mediated transport, vesicular pathways, and cytoskeletal linkages. Maurer's clefts serve as central hubs for organizing and forwarding proteins to the erythrocyte membrane. These findings underscore the intricate mechanisms *Plasmodium* parasites utilize to remodel their host cells and ensure effective protein export, with significant implications for parasite virulence and host-pathogen interactions.

1.3.2.4 Gaps in understanding protein export pathways

Despite significant advances in understanding the mechanisms of protein export in *Plasmodium falciparum*, critical gaps remain that limit a comprehensive picture of this complex process. Notably, the exact identity of the enzyme responsible for acetylating the newly exposed N-terminus after PEXEL cleavage remains elusive, as does the full complement of accessory proteins that guide exported proteins through the erythrocyte cytoplasm. Further study is required on how accessory proteins like HSP70-x, TRX2, and other unidentified factors contribute to protein stability and processing in the PV before PTEX translocation. The coordination of ER-derived post-translational modifications with the PTEX machinery, as well as the specific cues directing PEXEL and non-PEXEL proteins to the PTEX translocon, remain to be clarified. Addressing these gaps, particularly by identifying and characterizing additional proteins involved in these pathways, could illuminate new therapeutic targets to disrupt parasite virulence and survival.

To address the extensive complexity of the *Plasmodium* protein export pathway, I designed an experimental approach leveraging fusion proteins whose export is selectively arrested at different stages, including the ER, PV, and during normal export. This strategy was intended to unravel the distinct molecular interactions occurring at each stage. I created episomally expressed fusion proteins tagged with miniTurbo biotin ligase to biotinylate and identify interaction partners of proteins arrested at specific checkpoints. By capturing these interactions, I aimed to uncover novel players in the export process.

To confirm the interactions, I employed a split GFP assay, a robust method for validating physical interactions between proteins in live cells. This dual approach of biotin labeling and split GFP complementation allowed me to not only discover new interaction partners but also confirm their functional relevance with high confidence.

Through these methods, my aim was to identify and characterize novel PEXEL interaction partners, addressing critical gaps in our understanding of the *Plasmodium* protein export system. This work focused on elucidating unresolved processes, particularly those bridging the ER and PTEX, to advance our mechanistic understanding of protein export in *Plasmodium*.

2. Materials and Methods

2.1 Materials

2.1.1 Equipments

Equipment	Company
Analytical scales	Sartorius, Göttingen, Germany
Autoclave 2540 EL	Tuttnauer, Breda, The Netherlands
Autoclave ABT 120-5DM	Kern & Sohn, Balingen, Germany
Blot scanner C-DiGit	Li-cor, Bad Homburg, Germany
Centrifuge Biofuge fresco	Thermo Fisher Scientific, Dreieich, Germany
Centrifuge Biofuge pico	Thermo Fisher Scientific, Dreieich, Germany
Centrifuge J2-MC	Beckman Coulter, Krefeld, Germany
Centrifuge Megafuge 1.0 R	Heraeus, Hanau, Germany
Centrifuge Sorvall RC5B Plus	Thermo Fisher Scientific, Dreieich, Germany
Confocal microscope Leica SP8	Leica Microsystems, Wetzlar, Germany
Critical Point Dryer EM CPD300	Leica Microsystems, Wetzlar, Germany
DC120 Zoom Digital Camera	Kodak, Rochester, NY, USA
Electrophoresis power supply EPS 1001	Amersham (GE Healthcare), München, Germany
Electrophoresis power supply EPS 3501	Amersham (GE Healthcare), München, Germany
Electrophoresis power supply Power Pac 200	Bio-Rad, München, Germany
Electrophoresis power supply Power Pac 300	Bio-Rad, München, Germany
Freezer -20°C LGex 3410 MediLine	Liebherr, Biberach, Germany
Freezer -80°C HERAfreeze	Thermo Fisher Scientific, Dreieich, Germany
Fridge LKexv 3910 MediLine	Liebherr, Biberach, Germany
Gas burner gasprofi 1 micro	WLD-TEC
Gene Pulser II Electroporation System	Bio-Rad, München, Germany
Heating block NeoBlock Mono I	NeoLab, Heidelberg, Germany
Ice machine	Ziegra, Isernhagen, Germany
Incubator Heraeus B12/UB12	Thermo Fisher Scientific, Dreieich, Germany
Light optical microscope Axio Lab.A1	Zeiss, Jena, Germany
Liquid nitrogen tank MVE Cryosystem 6000	Thermo Fisher Scientific, Dreieich, Germany
Magnetic sorter VarioMACS	Miltenyi Biotec, Bergisch Gladbach, Germany
Magnetic stirrer COMBIMAG RCH	IKA, Staufen, Germany

Equipment	**Company**
Magnetic stirrer HR 3001	Heidolph, Schwabach, Germany
Magnetic stirrer RCT	IKA, Staufen, Germany
Microscope UltraVIEW VoX	PerkinElmer, Inc., Shelton, CT, USA
Microwave oven R940/94ST	Sharp, Hamburg, Germany
MiliQ water system Purist ultrapure	Rephile, Germany
Mini-PROTEAN Tetra Vertical Electrophoresis Cell	Bio-Rad, München, Germany
Nanodrop One spectrophotometer	Thermo Fisher Scientific, Dreieich, Germany
pH meter pH 7110	WTW, Weilheim, Germany
Pipetman Gilson P2, P20, P200, P1000	Gilson, Limburg an der Lahn, Germany
Pipetus Forty / Standard	Hirschmann, Eberstadt, Germany
Printer hp LaserJet 1300	Hewlett Packard, Heidelberg, Germany
Q Exactive HF Orbitrap LC-MS/MS System	Thermo Fisher Scientific, Dreieich, Germany
Rotor JA20.2, JA20.1	Beckman instruments, Palo Alto, CA, USA
Rotor SS-34; GS-3 , SM24	DuPont Instruments, Bad Homburg, Germany
Scanning electron microscope Leo 1530	Carl Zeiss Microscopy Deutschland GmbH, Oberkochen, Deutschland
Shaker incubator Innova 4000	New Brunswick, Wesseling-Berzdorf, Germany
Shaker incubator Innova 4300	New Brunswick, Wesseling-Berzdorf, Germany
Shaker KS 501 digital	IKA, Staufen, Germany
Sonicator Sonoplus HD 2070	Bandelin, Berlin, Germany
Spectrophotometer UVIKON 923	Kontron instruments, Munich, Germany
Sputter Coater EM ACE600	Leica Microsystems, Wetzlar, Germany
Sterile work bench Herasafe	Thermo Fisher Scientific, Dreieich, Germany
Sterile work bench SterilGard Class II	The Baker company, Sanford, ME, USA
Stop watch	Roth, Karlsruhe, Germany
Thermal cycler ABI 7500 Real-Time PCR System	Applied Biosystems, Foster City, CA, USA
Thermocycler Labcycler	Sensoquest, Göttingen, Germany
Trans-Blot® SD Semi-Dry Transfer Cell	Bio-Rad, München, Germany
UltiMate 3000 HPLC	Thermo Fisher Scientific, Dreieich, Germany
UV chamber GS Gene linker	Bio-Rad, München, Germany
UV table TFX-35M	Vilber Lourmat, Eberhardzell, Germany
Vortex Genie 2	Scientific Industries, Bohemia, NY, USA

Equipment	Company
Waterbath 7A	Julabo, Seelbach, Germany

2.1.2 Consumables

Consumable	Producer
96-well V/bottom plates, clear	Greiner Bio-One, Frickenhausen, Germany
Aluminium foil	Roth, Karlsruhe, Germany
Centrifuge bottles	Thermo Fisher Scientific, Dreieich, Germany
Centrifuge tubes, conical bottom	Corning Inc., Corning, NY, USA
Cover slips	Roth, Karlsruhe, Germany
Cryovials	Nalgene®, Wiesbaden, Germany
Cuvettes	Sarstedt, Nümbrecht, Germany
Disposable glass pasteur pipettes, 150 mm, 230 mm	Corning, NJ, USA
Electroporation cuvettes Gene Pulser	Bio-Rad, München, Germany
Eppendorf LoBind tubes	Sigma-Aldrich, Darmstadt, Germany
Eppendorf tubes	Sarstedt, Nümbrecht, Germanx
Filter systems 500 ml (0.2 µL)	Corning, Kaiserslautern, Germany
Filter tips P20, P200, P1000	Greiner Bio-One, Frickenhausen, Germany
Filters Millex GS (0.2 µm)	Merck Millipore, Darmstadt, Germany
Gel Releasers	Bio-Rad, München, Germany
Glassware	Corning Inc., Corning, NY, USA
Gloves TouchNTuff	Ansell, München, Germany
Immersion oil	Zeiss, Jena, Germany
MACS CS column	Miltenyi Biotec, Bergisch Gladbach, Germany
Microscopic cover glasses, round, 12 mm	Epredia, Inc., Kalamazoo, MI, USA
Mini-PROTEAN Combs, 15-well, 1.5 mm, 40 µl	Bio-Rad, München, Germany
Mini-PROTEAN® Spacer Plates with 1.5 mm	Bio-Rad, München, Germany
Mini-PROTEAN® Short Plates	Bio-Rad, München, Germany
Object slides	Marienfeld, Lauda-Königshofen, Germany
Parafilm	Bemis, Londonerry, UK
PCR softtubes 0.25 mL	Biozym Scientific, Hessisch Oldendorf, Germany
PCR strip tubes & domed caps	BioMedical Instruments, Zoellnitz, Germany

Consumable	Producer
Petri dishes, 100 mm/140 mm diameter	Greiner Bio-One, Frickenhausen, Germany
Pipette tips	Corning incorporation, Bodenheim, Germany
Plastic pipettes (1 mL; 2 mL; 5 mL; 10 mL; 25 mL; 50mL)	Corning incorporation, Bodenheim, Germany
PVDF membrane	Bio-Rad, München, Germany
ReproSil-Pur 200 C18-AQ	Dr. A. Maisch HPLC GmbH, Ammerbuch, Germany
SEM Specimen pins, 12.5mm diameter	Gloor Instruments AG, Kloten, Switzerland
Sterile filtration devices	Corning incorporation, Bodenheim, Germany
Strep-Tactin®XT 4Flow® 5 mL	IBA Lifesciences GmbH, Göttingen, Germany
Thermo well PCR	Corning incorporation, Bodenheim, Germany
Transfer pipettes	Sarstedt, Nümbrecht, Germany
Ultra centrifugal filter Amicon® Ultra, 3 kDa MWCO, 0.5 mL	Merck, Darmstadt, Germany
WesternSure® Pen	Li-Cor Biosciences, NE, USA

2.1.3 Chemicals

The chemicals used in this study were sourced from the specified companies or obtained from Sigma-Aldrich (Burlington, MA, USA), Merck (Darmstadt, Germany), Honeywell Fluka (Charlotte, NC, USA), BIORON Diagnostics (Römerberg, Germany), c.c.pro (Oberdorla, Germany), AppliChem (Darmstadt, Germany), Jacobus Pharmaceuticals (Princeton, NJ, USA), Thermo Fisher Scientific (Dreieich, Germany), Serva Electrophoresis (Heidelberg, Germany), Roche (Basel, Switzerland), or Roth (Karlsruhe, Germany). Orders were placed either directly with the vendors or through the Heidelberg Medical Facility, as noted.

2.1.4 Kits

Kit	Producer
BM chemiluminescence blotting substrate POD	Roche, Mannheim, Germany
DNeasy Blood & Tissue Kit	Qiagen, Hilden, Germany
In-Fusion® HD Cloning Kit	Clontech Laboratories, USA
Plasmid Maxi Kit	Qiagen, Hilden, Germany
QIAquick Gel Extraction Kit	Qiagen, Hilden, Germany
Strep-Tactin®XT 4Flow® 5 mL	IBA Lifesciences GmbH, Göttingen, Germany
SuperScript III First-Strand Synthesis SuperMix	Thermo Fisher Scientific, Dreieich, Germany

2.1.5 Buffers and solutions

Buffer/ medium/ solution	Composition
Albumax I	5% (w/v) Albumax I in RPMI 1640 with 25 mM HEPES and L-Glutamine (Gibco) Filter sterilized
Biotin stock 100x	5 mM Biotin in RPMI 1640 with 25 mM HEPES and L-Glutamine (Gibco) Filter sterilized
Blocking buffer	3% BSA in PBS, pH7.4
Blocking buffer (lipid strip assay)	1 % milk in PBS, pH7.4
Blocking Solution (WB)	5% (w/v) skimmed milk in PBS, pH7.4
Buffer BXT	100 mM Tris/HCl, pH 8.0 150 mM NaCl 1 mM EDTA 50 mM biotin add PI before use
Buffer W	100 mM Tris/HCl, pH 8.0 150 mM NaCl 1 mM EDTA add PI before use
Complete Medium	5% Human A Serum 0.25% Albumax I 0.2 µg/ml Gentamycin 0.2 mM Hypoxanthine in RPMI 1640 with 25 mM HEPES and L-Glutamine (Gibco)
Cytomix	120 mM KCl 0.15 mM CaCl2 10 mM K2HPO4/KH2PO4, pH 7.6 25 mM HEPES/2 mM EGTA, pH 7.6 5 mM MgCl2 in ddH2O Adjusted to pH 7.6 with KOH Filter sterilized
DNA loading buffer 6x	60% Glycerol 60 mM EDTA 0.25% Bromophenol Blue
DSM1	10 mM DSM1 20% DMSO (v/v)

Buffer/ medium/ solution	Composition
Elution buffer	30 mM Biotin 2.0 % SDS 150 mM NaCl 50 mM Tris, pH 7.5 add PI before use
Fixing solution (IFA)	4% paraformaldehyde 0.0075% glutaraldehyde in PBS, pH7.4
Fixing solution (SEM)	1% glutaraldehyde 0.1 M cacodylate buffer, pH 7.2
Freezing Solution	6.2 M Glycerol 0.14 M Na-Lactate 0.5 mM KCl in ddH2O adjusted to pH 7.2 with 0.5 M NaHCO3 Filter sterilized
Gelatine flotation solution	0.7 % gelatine in RPMI 1640 with 25 mM HEPES and L-Glutamine (Gibco) Filter sterilized
Laemmli buffer 4x	3% (w/v) SDS 250 mM Tris pH 6.8 20% Glycerol 0.1% Bromophenol blue 3% 2-mercaptoethanol
LB agar	1% (w/v) tryptone/peptone 0.5% (w/v) yeast extract 0.5% (w/v) NaCl 1.5 % agar in ddH2O, autoclaved
LB medium	1% (w/v) tryptone/peptone 0.5% (w/v) yeast extract 0.5% (w/v) NaCl in ddH2O, autoclaved
MACS buffer	2 mM EDTA 0.5% (w/v) BSA in 1x PBS, pH 7.4 autoclaved
Membrane stripping butter	2% SDS 100 mM β-Mercaptoethanol in PBS, pH7.4
PBS	1 tablet of phosphate-buffered saline, pH 7.4 (Sigma-Aldrich) in 200 ml ddH2O

Buffer/ medium/ solution	**Composition**
PBST	0.1 % Tween-20 in PBS, pH7.4
Permeabilization-Quenching Buffer	0.1% Triton-100 100 mM Glycine in PBS, pH7.4
Poly-l-lysine	0.1 % Poly-l-lysine in H_2O
Protease Inhibitors (PI)	0.002% (w/v) Leupeptin 0.005% (w/v) Aprotinin 100 µM PMSF
RIPA buffer	50 mM Tris pH 7.5 150 mM NaCl 2 mM EDTA 1.0 % NP40 0.5% sodium deoxycholate 0.1% SDS add PI before use
RNA Running Buffer (20x)	0.4 M MOPS 40 mM NaOAc 5 mM EDTA, pH 8.0 In 500 ml ddH_2O
SB medium	3.5 % Tryptone/Peptone 3.0 % Yeast Extract 0.5 % NaCl In ddH_2O, autoclaved
SDS-PAGE Running Buffer	25 mM Tris 250 mM Glycine 0.1% (w/v) SDS
SDS-PAGE Transfer Buffer	39 mM Tris 48 mM Glycine 0.038% (w/v) SDS
SOC Medium	2.0 % Tryptone/Peptone 0.5 % Yeast Extract 0.05 % NaCl 0.5 % $MgSO_4 \times 7 H_2O$ 20 mM D-Glucose Filter sterilized
Solvent A	0.1% formic acid 1% acetonitrile
Solvent B	0.1% formic 89.9% acetonitrile
Sorbitol Lysis Solution	5% (w/v) D-sorbitol in ddH_2O, autoclaved

Buffer/ medium/ solution	**Composition**
TAE Buffer, 1x	4 mM Tris-Acetate 1 mM EDTA, pH 8
TE Buffer	10 mM Tris/HCl, pH 8 1 mM EDTA in ddH2O Filter sterilized
Thawing Solution I	12% NaCl in ddH2O, autoclaved
Thawing Solution II	1.6% NaCl in ddH2O, autoclaved
Thawing Solution III	0.9% NaCl 0.2% Glucose In ddH2O Filter sterilized
W1 buffer	2.0 % SDS 150 mM NaCl 50 mM Tris pH 7.5 add PI before use
W2 buffer	150 mM NaCl 50 mM Tris pH 7.5 add PI before use
WR99210 Stock	10 mM WR99210 20% DMSO (v/v)
WR99210 Working Solution	20 µM WR99210 in RPMI 1640 with 25 mM HEPES and L-Glutamine
Zn buffer	200 µM ZnCl in PBS, pH7.4

2.1.6 Biological material

2.1.6.1 *E. coli* strains

***E. coli* strains**	**Origin**
E. coli PMC 103	Provided by Prof. Alan Cowman (Doherty et al., 1993)
E. coli Rosetta™(DE3) Competent Cells	Merck KGaA, Darmstadt, Germany
E. coli XL10 Gold	Agilent Technologies, Böblingen, Germany

2.1.6.2 *P. falciparum* strains

***P. falciparum* strains**	**Origin**
P. falciparum 3D7	The Netherlands (D Walliker et al., 1987)
P. falciparum IT	Isolated from an infected human blood sample collected by M. Friedman, Medical Research Council Labs Clinic, Fajara, Gambia, 1976.
P. falciparum IT KAHRP Y193F	Generated by Violeta Pancakova in this work
P. falciparum IT KAHRP HIS1	Generated by Violeta Pancakova in this work
P. falciparum IT KAHRP HIS2	Generated by Violeta Pancakova in this work
P. falciparum IT KAHRP HIS3	Generated by Violeta Pancakova in this work
P. falciparum IT KAHRP ga15	Generated by Violeta Pancakova in this work
P. falciparum IT KAHRP ga16	Generated by Violeta Pancakova in this work
P. falciparum IT KAHRP ga17	Generated by Violeta Pancakova in this work
P. falciparum IT KAHRP ga18	Generated by Violeta Pancakova in this work

2.1.6.3 Antibodies

Antibodies and Conjugate	**Source**	**Dilution**	**Company**
Anti-HA 3F10, monoclonal	Mouse	1:500	Roche, Basel, Switzerland
Anti-His	Mouse	1:500	Roche, Mannheim, Germany
Anti-KAHRP, polyclonal	Rabbit	1:500	Costum-made, Eurogentec
Anti-mouse-Alexa 488	Goat	1:1000	Invitrogen - Thermo Fisher Scientific, Dreieich
Anti-mouse-POD	Goat	1:10,000	Jackson ImmunoResearch, Suffolk, UK
Anti-rabbit-POD	Goat	1:10,000	Jackson ImmunoResearch, Suffolk, UK
Streptavidin-Alexa 594	Conjugate	1:500	Thermo Fisher Scientific, Dreieich, Germany
Streptavidin-PE	Conjugate	1:1000	Thermo Fisher Scientific, Dreieich, Germany
Streptavidin-POD	Conjugate	1:2,000	Roche, Mannheim, Germany

2.1.6.4 Enzymes

Enzymes	Company
EuroTaq Polymerase	BioCat, Heidelberg, Germany
Phusion Polymerase	Fermentas, Germany
Restriction Enzymes	New England Biolabs, Frankfurt am Main, Germany
T4 Ligase	Thermo Fisher Scientific, Dreieich, Germany

2.1.6.5 Fluoroscent dyes

Fluoroscent Dyes	Company
Hoechst 33342	Thermo Fisher Scientific, Dreieich, Germany

2.1.6.6 Markers and loading dyes

Markers and loading dyes	Company
GeneRuler 1 Kb plus DNA ladder	Ambion - Thermo Fisher Scientific,Dreieich, Germany
RNA Gel Loading Dye (2x)	Ambion - Thermo Fisher Scientific, Dreieich,Germany

2.1.6.7 Plasmids

Plasmids	Origin
pUF1-Cas9	Provided by Dr. Jose-Juan Lopez-Rubio, Montpellier, France
pL6-B	Provided by Dr. Jose-Juan Lopez-Rubio, Montpellier, France
pL6-eGFP	Provided by Dr. Jose-Juan Lopez-Rubio, Montpellier, France
pL6-Y193F	Generated by Violeta Pancakova for this work
pL6-guide11	Generated by Violeta Pancakova for this work
pDC2-cam-co.Cas9-U6-hDHFR (pDC2)	Provided by Dr. Markus Ganter
pDC2-hDHFR-g11-HIS1	Generated by Violeta Pancakova for this work
pDC2-hDHFR-g11-HIS2	Generated by Violeta Pancakova for this work
pDC2-hDHFR-g11-HIS3	Generated by Violeta Pancakova for this work
pDC2-hDHFR-g11-ga15	Generated by Violeta Pancakova for this work
pDC2-hDHFR-g11-ga16	Generated by Violeta Pancakova for this work
pDC2-hDHFR-g11-ga17	Generated by Violeta Pancakova for this work
pDC2-hDHFR-g11-ga18	Generated by Violeta Pancakova for this work

Plasmids	**Origin**
pET18-HRR	Custom-made by GenScript Biotech Corporation, Rijswijk, Netherlands
pARL-BSD-GFP11	Generated by Prof. Jude Przyborski
pARL-DHFR-GFP1-10	Generated by Prof. Jude Przyborski
pARL-DHFR-STEVOR1-80^{50W}-GFP	Generated by Dr. Sophia Deil
pARL-DHFR-STEVOR1-80^{51E}-GFP	Generated by Dr. Sophia Deil
pARL-DHFR-STEVOR1-80-GFP	Generated by Dr. Sophia Deil
pARL-DHFR-STEVOR1-80^{50W}-miniTurbo	Generated by Violeta Pancakova for this work
pARL-DHFR-STEVOR1-80^{51E}-miniTurbo	Generated by Violeta Pancakova for this work
pARL-DHFR-STEVOR1-80-miniTurbo	Generated by Violeta Pancakova for this work
pARL-DHFR-STEVOR1-80^{50W}-GFP1-10	Generated by Violeta Pancakova for this work
pARL-DHFR-STEVOR1-80^{51E}-GFP1-10	Generated by Violeta Pancakova for this work
pARL-DHFR-STEVOR1-80-GFP1-10	Generated by Violeta Pancakova for this work
pARL-DHFR-PF3D7_0220000-GFP11	Generated by Violeta Pancakova for this work
pARL-DHFR-PF3D7_0422100-GFP11	Generated by Violeta Pancakova for this work
pARL-DHFR-PF3D7_1013300-GFP11	Generated by Violeta Pancakova for this work
pARL-DHFR-PF3D7_1116400-GFP11	Generated by Violeta Pancakova for this work
pARL-DHFR-PF3D7_1116800-GFP11	Generated by Violeta Pancakova for this work
pARL-DHFR-PF3D7_1201000-GFP11	Generated by Violeta Pancakova for this work
pARL-DHFR-PF3D7_1323500-GFP11	Generated by Violeta Pancakova for this work
pARL-DHFR-PF3D7_1419400-GFP11	Generated by Violeta Pancakova for this work

All the plasmids used in this study are described in Appendix I.

2.1.6.8 Computer tools, software and databases

Computer tools, software and databases	**Origin**
Benchling biology software	Benchling, Inc., San Francisco, CA, USA, http://www.benchling.com/
Biorender	Science Suite Inc., Toronto, ON, Canada, https://www.biorender.com/
ChatGPT	OpenAI, San Francisco, CA, USA, https://openai.com/index/chatgpt/
FIJI Image Analysis	http://fiji.sc/Fiji
Grammarly	Grammarly Inc., San Francisco, CA, USA, https://www.grammarly.com/
human protein database UP0005640_9606, June 2020, 20,531 sequences	https://www.uniprot.org/proteomes/UP000005640
ImageJ	https://imagej.nih.gov/ij/
MS Office	Microsoft Corporation, CA, USA
Perseus version 1.6.13.0	https://maxquant.net/perseus/
PlasmoDB	http://plasmodb.org/plasmo/
Plasmodium falciparum protein database UP000001450, November 2021, 5,380 sequences	https://www.uniprot.org/proteomes/UP000001450
Proteome Discoverer 2.5 with Sequest HT	Thermo Fisher Scientific, Dreieich, Germany
Scaffold	https://www.proteomesoftware.com/products/scaffold-5
UniProt	https://www.uniprot.org/ [112]
ZEISS SmartSEM	Zeiss, Jena, Germany

2.1.6.9 Oligonucleotide list

P 1	**GGACTAGTGAAGTGCTCTAATAACGTAAG**
P 2	**AGTCCTTAAGTTGTGCTAAAGTTCTCTTATTTC**
P 3	**ATAAGAATGCGGCCGCAGAAAAAGATTCCCTCTTG**
P 4	**TCCCCGCGGCACAATCGTGGCTTTTGTG**
P 5	**TAAGTATATAATATTCAGGTTCACCAACAAGTACAGTTTTAGAGCTAGAA**
P 6	**TTCTAGCTCTAAAACTGTACTTGTTGGTGAACCTGAATATTATATACTTA**
P 7	**AGAACTTTAGCACAAAAACAGCATGAACATCATCAC**
P 8	**AGGGAATCTTTTTCTCAGTGCAAAAATGTTCGGACC**

P 9	**GCGAAGAATGTCCGGCTACCGTGAATGATTATAG**
P 10	**GCGAAGAATGTCCGTTTACCGTGAATGATTATAG**
P 11	**GCTATGACCATGATTACGCC**
P 12	**CCAATAGATAAAATTTGTAGAG**
P 13	**TATTCAGGTTCACCAACAAGTACA**
P 14	**AAACTGTACTTGTTGGTGAACCTG**
P 15	**AAGCACCGACTCGGTGCCAC**
P 16	**AGAACTTTAGCACAAAAGCAACATGAAGCTGCTG**
P 17	**AGAACTTTAGCACAAAAGCAACATGAACATCATCAC**
P 18	**AGTCAGAATTCGAAGTGCTCTAATAACGTAAG**
P 19	**AGTCGACGTCCACAATCGTGGCTTTTGTG**
P 20	**AACATATGTTAAATATTTATTTCTC**
P 21	**AGGGTTATTGTCTCATGAGCGG**
P 22	**ATCGCCTAGGACCACAGCATCCTCTTTTCTTC**
P 23	**AAAACCCAGGTTTTTCGTGAAGC**
P 24	**CAATTACAACCTCAACAACTC**
P 25	**TTCATGAGCTTTTGATCCATCTG**
P 26	**GGGAAGATAATGGACATTCG**
P 27	**GAACACGTTTTCATTATATTTCC**
P 28	**ATGAAGGACAACAAAATACTGG**
P 29	**TTTGGATTTTTCATTATCAGACG**
P 30	**ATGGCGCCAGGTAGTACTGG**
P 31	**GTGTTTTTATTGAGCCCCC**
P 32	**GCTGCTGCAGCTGCCGC**
P 33	**ATGCGCGCTACCCGTATGATGTTCCGGATTAC**
P 34	**CCCCCCGGGTTACTTTTCGGCAGACCGCAGACTG**
P 35	**TAATATCCGTTAATAATAAATACACGCAGTC**
P 36	**CACAACATACACATTTTTACAG**
P 37	**CCGCTCGAGATGACAAATAGTAATTACAAATC**
P 38	**CCGCTCGAGATGTATCATGTTACTCGCTC**
P 39	**CCGCTCGAGATGAAAATATATAGGAAAAAGAGTAC**
P 40	**CCGCTCGAGATGAGAAAAATAATACCTCTTTTG**
P 41	**CCGCTCGAGATGAATGAAATGAAAGTTTCC**
P 42	**CCGCTCGAGATGACAAGAAGATATTTAAAGTATTATAT**
P 43	**CCGCTCGAGATGAATATTTTTAAAAGATATATATTTTTTTTATG**
P 44	**CCGCTCGAGATGTACAGTGCTTTAAGGTC**
P 45	**CCGCTCGAGATGAATAATTATTTTTTAAGGAAAGAAAAT**

P 46	**CCGCTCGAGATGAAGAGGAAGAATATCCATG**
P 47	**CCGCTCGAGATGAGAATAATAATATTAGCCTTGTTG**
P 48	**ATCGCCTAGGTTTTGATTTTTGCGTTCTAC**
P 49	**ATCGCCTAGGTAGAACCCTTTTATTTGAGAC**
P 50	**ATCGCCTAGGTGCTGCTTTTATTTTGTTTTTATAAAAC**
P 51	**ATCGCCTAGGATGGCCTACAGTCG**
P 52	**ATCGCCTAGGTAATTCGTCCATGTCCATG**
P 53	**ATCGCCTAGGGGTCTTAGATAAGTTTATAACC**
P 54	**ATCGCCTAGGTCTATGTAATTTATGTTGTCTG**
P 55	**ATCGCCTAGGATCTTCATTGTTGAAATATTTAATTATC**
P 56	**ATCGCCTAGGTGTTGATTCCTGTATGGG**
P 57	**ATCGCCTAGGTTTCTCTGGTATCTCCA**
P 58	**ATCGCCTAGGATTGTCGTCCTCTTCTTCG**
P 59	**GTTTTACCATATGAAAGTGAAGAAG**
P 60	**ATCTTCATTTCCAATAATGGATTTAG**
P 61	**GATGAAGAATGAAGAAAGTAAATATTTCC**
P 62	**TCAAAATTGACGTTAGACCCTTC**
P 63	**ATGCGCGCAGCAAAGGAGAAGAACTTTTCAC**
P 64	**CCCCCCGGGTTACTTTTCGTTGGGATCTTTCG**
P 65	**ATGAAGATGTATAACCTTAAAATG**
P 66	**CTTATGTAATCCCAGCAGC**

2.2 Methods

2.2.1 Molecular methods

2.2.1.1 Preparation of electro-competent PMC 103 *E. coli* bacteria

To prepare electro-competent PMC 103 *E. coli* cells, a starter culture was initiated by inoculating 10 mL of SB medium with bacterial cells obtained from a frozen glycerol stock. The culture was incubated overnight at 37 °C while shaking at 200 rpm. After approximately 16 hours, 6 mL of the overnight culture were used to inoculate 600 mL of SB medium, followed by incubation at 37 °C with shaking at 200 rpm for 3.5 hours.

Cells were harvested by centrifugation at 6,000 × g for 15 minutes at 4 °C, and the supernatant was discarded. All subsequent steps were performed on ice and using pre-chilled solutions. The bacterial pellet was resuspended 600 ml volume of sterile distilled water and centrifuged at 6,000 × g for 15 minutes at 4 °C. This washing step was repeated twice to ensure thorough removal of media components. Next, the pellet was resuspended in 600 ml volume of sterile 10% (v/v) glycerol in distilled water and centrifuged again under the same conditions. After discarding the supernatant, the final pellet was resuspended in 1.2 mL of sterile 10% (v/v) glycerol.

The prepared cell suspension was divided into 50 µL aliquots, transferred to pre-chilled 1.5 mL microcentrifuge tubes, snap-frozen in a liquid nitrogen, and then stored at -80 °C until use.

2.2.1.2 Transformation of electro-competent PMC 103 *E. coli* bacteria

Electroporation was employed to introduce plasmid DNA into PMC 103 *E. coli* cells. Fifty-microliter aliquots of electro-competent cells were thawed on ice and gently combined with 150 µL of sterile 10% (v/v) glycerol in ddH$_2$O to protect the cells from osmotic stress during the procedure. To this suspension, up to 10 µL of plasmid DNA was added, and the mixture was transferred into a pre-chilled electroporation cuvette. Electroporation was performed at 2,500 V, inducing transient membrane pores to facilitate DNA uptake.

Immediately after electroporation, 1 mL of pre-warmed SOC medium was added to the cuvette to stabilize and nourish the transformed cells. The suspension was transferred to a sterile 15 mL centrifuge tube and incubated at 37 °C for 1 hour with shaking at 200 rpm to promote recovery and the expression of the antibiotic resistance marker. The bacterial culture was then either pelleted or directly plated onto LB agar plates containing the appropriate selective antibiotic. Plates were incubated overnight at 37 °C to allow colony development.

2.2.1.3 Transformation of chemocompetent *E. coli* cells

Two chemocompetent *E. coli* strains were used for distinct applications. XL10-Gold ultracompetent cells were employed to transform the In-Fusion cloning mix, while Rosetta (DE3) cells were used to express the HRR peptide.

For the transformation of XL10-Gold ultracompetent cells, a heat shock protocol was used. Aliquots of 40 µL of cells were thawed on ice and gently agitated every 2 minutes. To enhance transformation efficiency, 1.2 µL of β-mercaptoethanol was added, followed by a 10-minute incubation on ice. Alliquots of 50 µl of Rosetta (DE3) cells were thawed on ice, and the subsequent transformation steps for both XL10-Gold and Rosetta (DE3) cells were identical.

Plasmid DNA was added to the cells and mixed gently, and the suspension was incubated on ice for 30 minutes. Heat shock was carried out by exposing the cells to 42 °C for 30 seconds, then immediately cooling on ice for 2 minutes. Recovery was facilitated by adding 1 mL of pre-warmed SOC medium to the transformed cells, which were then transferred to a 15 mL Falcon tube and incubated at 37 °C with shaking at 200 rpm for 1 hour.

After the recovery step, the cells were pelleted by centrifugation at 1 500 × g for 8 minutes. The supernatant was discarded, leaving approximately 100 µL of medium to resuspend the pellet. The resuspended cells were plated onto LB agar plates pre-warmed and supplemented with 100 µg/mL ampicillin or 100 µg/ml Kanamycin. Plates were incubated overnight at 37 °C, or alternatively, for two days at room temperature to facilitate colony formation.

2.2.1.4 Plasmid DNA isolation from bacteria

Plasmid DNA was extracted from bacterial cultures using the Plasmid Maxi Kit (Qiagen) following the manufacturer's protocol. A single bacterial colony was inoculated into 3 mL of SB medium containing 100 µg/mL ampicillin and incubated at 37 °C with shaking at 200 rpm for 6–8 hours. The resulting starter culture was diluted 1:1,000 in 400 mL of fresh SB medium supplemented with 100 µg/mL ampicillin and incubated overnight at 37 °C with shaking at 200 rpm.

The overnight culture was harvested by centrifugation at 6,000 × g for 15 minutes at 4 °C. The bacterial pellet was resuspended in the provided resuspension buffer and lysed by incubation with lysis buffer for 5 minutes at room temperature. Lysis was halted by adding a chilled neutralization buffer, and the suspension was incubated on ice for 20 minutes. The lysate was clarified by centrifugation at 15,000 × g for 30 minutes at 4 °C, and the supernatant containing plasmid DNA was applied to a pre-equilibrated column. The plasmid DNA was applied to the column matrix via gravity flow.

After binding, the column was washed multiple times to remove contaminants, and plasmid DNA was eluted with the elution buffer. The eluted DNA was precipitated using isopropanol and pelleted by centrifugation at 15,000 × g for 30 minutes at 4 °C. The pellet was washed with chilled on ice 70% ethanol and centrifuged again under the same conditions for 20 minutes. The supernatant was carefully removed, and the DNA pellet was air-dried at room temperature. The dried DNA was resuspended in 50–150 µL of ddH_2O and stored at -20 °C for further use.

2.2.1.5 Polymerase chain reaction (PCR)

DNA amplification was carried out using either EconoTaq DNA Polymerase for general identification and amplification purposes or Phusion High-Fidelity DNA Polymerase for applications requiring high accuracy, such as sequencing or cloning. The choice of polymerase was based on the intended downstream application.

The following PCR reaction mix and thermocycling conditions were applied:

Reaction mix	
DNA template	1 µl
10x buffer	5 µl
2 mM dNTPs	5 µl
50 mM $MgCl_2$	2.5 µl
50 µM forward primer	1 µl
50 µM reverse primer	1 µl
DNA Polymerase	1 µl
ddH_2O	33.5 µl
Final volume	50 µl

Thermocycling conditions			
Initial denaturation	94 °C	10 min	
Denaturation	94 °C	45 sec	x30
Annealing	x °C*	45 sec	
Elongation	68 °C	1 min/kb	
Final elongation	68 °C	10 min	
Hold	4 °C		

*x= T_m of primers – 5 °C

The PCR products were subsequently analyzed via agarose gel electrophoresis to confirm amplification and verify the size of the fragments.

2.2.1.6 Agarose gel electrophoresis

Agarose gel electrophoresis is used to separate DNA molecules based on their size and charge. Gels with agarose concentrations ranging from 0.8% to 2% were prepared, depending on the desired resolution. Agarose was dissolved in 1X Tris-acetate-EDTA (TAE) buffer by heating the mixture in a microwave until fully melted. Once cooled to approximately 55–56 °C, ROTI®GelStain was added at a 1:10,000 dilution to stain the DNA. The molten agarose was poured into a gel cast, and a comb was inserted to form wells. The gel was left at room temperature to solidify completely.

Once solidified, the gel was placed into an electrophoresis chamber filled with 1X TAE buffer. DNA samples were prepared by mixing with 6X DNA loading dye and loaded into the wells alongside a 1 kb Plus DNA Ladder used as a molecular size marker. Electrophoresis was conducted at room temperature using a constant voltage of 90–140 V, depending on the gel size and desired separation time.

After electrophoresis, DNA bands were visualized under UV light using a transilluminator. Images of the separated DNA bands were captured using a DC120 Zoom Digital Camera (Kodak).

2.2.1.7 RNA gel electrophoresis

RNA gel electrophoresis was conducted using a 0.7% agarose gel to assess RNA integrity. To prepare the gel, 0.28 g of Biozym SeaKem LE Agarose was dissolved in 2 mL of 20X RNA running buffer and 30 mL of distilled water by heating in a microwave until fully melted. Once cooled to approximately 55 °C, 8 mL of formaldehyde was added to maintain RNA in its denatured state, along with ROTI®GelStain for visualization. The gel mixture was poured into a casting tray and allowed to solidify at room temperature.

RNA samples were prepared by mixing with RNA loading buffer (Ambion, Thermo Fisher Scientific) and heating at 65 °C for 3 minutes to ensure proper denaturation. The samples were then loaded into the wells of the solidified gel. Electrophoresis was carried out at a constant voltage of 60 V using RNA running buffer.

Following electrophoresis, RNA bands were visualized under UV light and documented using a DC120 Zoom Digital Camera (Kodak).

2.2.1.8 DNA extraction and purification from agarose gel

The DNA fragments were isolated and purified from agarose gels using the QIAquick Gel Extraction Kit (Qiagen), following the manufacturer's protocol. Desired DNA bands were excised from the gel and transferred to microcentrifuge tubes. The gel slices were dissolved in QG buffer at a ratio of 1:3 (w/v) by incubating at 50 °C until thoroughly melted, typically for 10 minutes. Isopropanol was subsequently added to facilitate DNA precipitation.

The resulting solution was applied to a QIAquick spin column and centrifuged at 17,000 × g for 15 seconds at room temperature, allowing the DNA to bind to the column membrane. The bound DNA was washed with PE buffer to remove impurities and contaminants. Finally, the DNA was eluted from the column using 20–30 µL of sterile distilled water. Purified DNA samples were stored at -20 °C for further applications.

2.2.1.9 Determination of DNA concentration using nanodrop spectrophotometer

The concentration and purity of DNA samples were measured using a Nanodrop One spectrophotometer (Thermo Fisher Scientific). Prior to measurement, the instrument was initialized and blanked with 1–2 µL of nuclease-free water to ensure accuracy.

For each sample, 1–2 µL of DNA solution was pipetted onto the measurement pedestal, and the sample arm was lowered to form a liquid column. The spectrophotometer recorded absorbance values at 260 nm (for nucleic acids), 280 nm (for protein contamination), and 230 nm (for organic contaminants), and calculated the DNA concentration in ng/µL based on the 260 nm absorbance.

The purity of the DNA was assessed using the A260/A280 and A260/A230 ratios. Samples with A260/A280 ratios of approximately 1.8 and A260/A230 ratios above 2.0 were considered pure. After each measurement, the pedestal was cleaned with lint-free tissue and nuclease-free water to avoid cross-contamination.

2.2.1.10 Restriction enzyme digestion of DNA

Restriction enzyme digestion was used to cleave DNA at specific recognition sites. The reactions were prepared using restriction enzymes and their corresponding reaction buffers, provided by New England Biolabs (NEB), in accordance with the manufacturer's recommendations. For double-enzyme reactions, buffer selection and enzyme concentrations were optimized using the NEB Double Digest Finder to ensure compatibility.

The digestion reactions were set up in final volumes of either 10 µL or 50 µL, depending on the experimental requirements. DNA quantities used for the reactions were 1 µg for smaller volumes, such as control digest, or 10 µg for larger preparations, e.g., for cloning. To reach the final reaction volume, variable amounts of nuclease-free water were added, calculated based on the volume of other reaction components required for the desired concentration.

The reaction mixtures were incubated at the optimal temperature specified for each enzyme, typically 37 °C, for a duration of 1 to 4 hours. PCR products and vectors were generally digested for 1 hours for analytical purposes, while reactions intended for cloning purposes were incubated for up to 4 hours. After digestion, the samples were either directly analyzed using agarose gel electrophoresis or subjected to subsequent processing steps such as gel extraction or ligation.

The following reaction mix was used:

Components	Control digest	Cloning digest
DNA	1 µg	10 µg
Enzymes	5 U each	20 U each
Buffer	1 µl	5 µl
ddH_2O	x µl	x µl
Total volume	10 µl	50 µl

2.2.1.11 T4 mediated DNA ligation

DNA fragments and vectors previously digested with the appropriate restriction enzymes were purified using the QIAquick Gel Extraction Kit (Qiagen). The purified DNA fragments were ligated using T4 DNA ligase (New England Biolabs) following the manufacturer's protocol. The ligation reaction mixture, typically containing a molar ratio of an insert to a vector of 3:1, was prepared in a final volume of 10 µl suitable for downstream transformation.

The reaction was incubated overnight at 16 °C to facilitate the ligation process. The ligated DNA was subsequently transformed into electrocompetent *E. coli* PMC 103 cells using electroporation the following day.

The following reaction mix was used:

Components	
Insert DNA	3:1 molar ratio over vector
Vector DNA	100 ng
5x T4 DNA Ligase Buffer	2 µl
T4 DNA Ligase	1 µl
ddH_2O	x µl
Total volume	10 µl

2.2.1.12 In-Fusion cloning

In-Fusion cloning is used to insert DNA fragments without introducing restriction sites, for precise integration and to avoid addition of amino acids in the resulting protein sequence. This method was used to clone guide sequences under the U6 promoter for guide RNA transcription or to insert recodonized templates between homology regions.

To create the guides, primers with reverse complementary sequences and specific overhangs for the insertion site were annealed. The recodonized template was amplified using PCR, and the corresponding vectors were digested with appropriate restriction enzymes. The In-Fusion cloning reaction was prepared using 100 ng of vector DNA and a 2:1 molar ratio of insert to vector.

The following reaction mix was used:

Components	
Insert DNA	2:1 molar ratio over vector
Vector DNA	100 ng
5x In-Fusion Mix	2 µl
ddH_2O	x µl
Total volume	10 µl

The reaction mixture was briefly vortexed to ensure thorough mixing and incubated at 50 °C for 15 minutes. Following incubation, the reaction was immediately placed on ice to stabilize the products until transformation into XL10-Gold ultracompetent cells.

2.2.1.13 DNA sequencing

DNA sequencing was outsourced to Eurofins Genomics Europe Shared Services GmbH (Ebersberg, Germany). Samples were prepared and submitted according to the provider's specifications. The samples were sent as follows:

Sequencing sample	Sample volume and concentration
Plasmid DNA	20 µl, 100 ng/µl
Purified PCR product	20 µl, 1-10 ng/µl
Full plasmid sequencing	20 µl, 30 ng/µl

The raw data were analyzed following sequencing, and sequence alignments were conducted using the Electronic Lab Notebook software Benchling.

2.2.1.14 Total RNA extraction from *P. falciparum*

RNA was extracted from *Plasmodium falciparum* parasites cultured at the trophozoite and schizont stages with 3–5% parasitemia. To release parasites from erythrocytes, 36 mL of culture was used, the parasites were pelleted by centrifugation at 900 × g for 2 minutes at 4 °C, with the brake reduced to 130 × g. The supernatant was discarded, and the pellet was resuspended in 10 mL of freshly prepared ice-cold 0.2% saponin in PBS. After a 3-minute incubation on ice, the sample was centrifuged at 3,000 × g for 8 minutes at 4 °C.

The pellet was washed with ice-cold PBS and centrifuged again under the same conditions. After discarding the supernatant, 1–2 mL of TRIzol reagent was added to the pellet, mixed thoroughly by vortexing, and frozen at -80 °C overnight. The samples were thawed at 37 °C and transferred to 1.5 mL Eppendorf tubes. For phase separation, 200 µL of chloroform per 1 mL of TRIzol was added, followed by vigorous hand shaking, a 3-minute incubation at room temperature, and centrifugation at 10,500 × g for 30 minutes at 4 °C.

The upper aqueous phase, containing RNA, was carefully collected into fresh 1.5 mL LoBind tubes. To precipitate the RNA, 500 µL of isopropanol per 1 mL of TRIzol was added, and the mixture was incubated at -80 °C for at least 30 minutes. The precipitate was recovered by centrifugation at 10,500 × g for 10 minutes at 4 °C, washed with cold 70% ethanol, and centrifuged again under the same conditions. The RNA pellet was air-dried at room temperature to remove residual ethanol and dissolved in 30 µL of ribonuclease-free water.

RNA concentration was measured using spectrophotometry, and the samples were stored at -80 °C. The integrity of the extracted RNA were verified using denaturing agarose gel electrophoresis on a 0.7% agarose gel.

2.2.1.15 cDNA synthesis from parasite RNA

Complementary DNA (cDNA) synthesis from RNA extracted from *P. falciparum* was performed using the SuperScript III First-Strand Synthesis SuperMix (Thermo Fisher Scientific) according to the manufacturer's protocol. The process began with combining the following components for the reaction in a 0.2 mL microcentrifuge tube.

Components	
RNA	Up to 5 µg
50 µM Oligo$(dT)_{20}$	1 µl
Annealing Buffer	1 µl
RNase/DNase-free water	x µl
Total volume	8 µl

The reaction mixture was then incubated at 65 °C for 5 minutes in a thermal cycler, followed by immediate cooling on ice for at least 1 minute. The tube contents were briefly centrifuged to collect the reaction mix.

Next, 10 µL of 2X First-Strand Reaction Mix and 2 µL of SuperScript III/RNaseOUT Enzyme Mix were added to the tube while on ice. The reaction mixture was vortexed briefly to ensure thorough mixing, and the contents were collected by brief centrifugation. The tube was incubated for 50 minutes at 50°C.

The reaction was terminated by heating at 85 °C for 5 minutes and subsequently chilled on ice. The synthesized cDNA was either stored at -20 °C for future use or used immediately in downstream PCR reactions.

2.2.1.16 Genomic DNA isolation from *P. falciparum* parasites

Genomic DNA from *Plasmodium falciparum* parasites was extracted after separating them from host erythrocytes. For this purpose, 14 mL of trophozoite- and schizont-stage culture with a parasitemia level of at least 5% was transferred to a 15 mL centrifuge tube and centrifuged at 900 × g for 2 minutes at room temperature. The supernatant was discarded, and the pellet was washed with PBS and centrifuged again under the same conditions.

The genomic DNA isolation was performed using the DNeasy Blood & Tissue Kit (Qiagen) following the manufacturer's instructions. iRBCs were lysed with 200 µL of AL buffer and 20 µL of proteinase K, followed by vortexing and incubation at 56 °C for 10 minutes. Subsequently, 200 µL of 99% ethanol was added to the lysate, and the mixture was vortexed thoroughly before being loaded onto a DNeasy spin column. The column was centrifuged at 6,000 × g for 1 minute, and the flow-through was discarded.

The column was washed sequentially with 500 µL of AW1 buffer and 500 µL of AW2 buffer, with centrifugations at 6,000 × g for 1 minute and 17,000 × g for 3 minutes, respectively. After the final wash, the column was transferred to a clean 1.5 mL microcentrifuge tube. Genomic DNA was eluted by applying 50 µL of nuclease-free water to the membrane, incubating at room temperature for 1 minute, and centrifuging at 6,000 × g for 1 minute. The resulting genomic DNA solution was stored at -20 °C for further use.

2.2.2 Microbiology methods, biochemistry

2.2.2.1 Peptide expression in Rosetta (DE3) cells

The expression of the HRR peptide was performed in Rosetta (DE3) cells to optimize expression conditions and produce a high yield of HRR peptide for further analysis. A single Rosetta (DE3) colony transformed with the plasmid of interest was selected from an LB agar plate and used to inoculate 20 mL of LB medium supplemented with 100 µg/mL ampicillin. This pre-culture was grown overnight at 37 °C with shaking.

The next day, the overnight culture was diluted to an optical density at 600 nm (OD_{600}) of 0.2 in a fresh 20 mL LB medium containing 100 µg/mL ampicillin. The diluted culture was incubated at 37 °C until it reached an OD_{600} of 0.4. At this point, a pre-induction (t_0) sample was taken by normalizing the sample volume to 1 mL at an OD_{600} of 1 (calculated as volume = $1/OD_{600}$). Protein expression was induced by adding isopropyl β-D-1-thiogalactopyranoside (IPTG) to a final concentration of 1 mM. Post-induction samples were collected at 4 hours (t_1) and 18 hours (t_2) after IPTG addition.

For Western blot (WB) analysis, the collected samples were prepared as follows: cell pellets were harvested by centrifugation at 16,100 × g for 2 minutes in 1.5 mL microcentrifuge tubes and washed by resuspending in 300 µL of phosphate-buffered saline (PBS) supplemented with protease inhibitors (PI). The samples were centrifuged again, and the supernatant was discarded. The resulting pellets were resuspended in 37.5 µL of PBS containing PI and subjected to three freeze-thaw cycles to lyse the cells. The samples were then mixed with 4x Laemmli buffer, sonicated for 10 seconds at 10% amplitude in mode 2, and boiled at 95 °C for 5 minutes using Sonoplus HD 2070 ultrasonic homogenizer (Bandelin). Prepared samples were either used immediately or stored at -80 °C for later analysis.

For large-scale HRR peptide production, the culture volume was expanded to 400 mL. Following induction with 1 mM IPTG for 4 hours, the cells were harvested by centrifugation at 6,000 × g for 15 minutes at 4 °C. The pellet was resuspended in 4 mL of Buffer W and lysed using a sonicator in 30-second intervals at 40% amplitude in mode 5 for 15 minutes. The efficiency of lysis was monitored by measuring the OD_{590} of the lysate, aiming for 80–90% cell lysis. The lysate was pre-cleared by centrifugation at 16,100 × g for 15 minutes at 4 °C and prepared for further purification steps.

2.2.2.2 Purification of HRR peptide using Strep-Tactin® Superflow® gravity column

The HRR peptide was purified using a 5 mL Strep-Tactin®XT 4Flow® (IBA Lifesciences) following the manufacturer's protocol.

The column was first equilibrated by adding two column volumes (CV) of Buffer W to establish optimal binding conditions. After equilibration, the pre-cleared cell lysate, containing the HRR peptide, was applied to the column, allowing the protein to bind to the Strep-Tactin® resin.

Subsequently, the column was washed five times with one CV of Buffer W to remove unbound or non-specifically bound proteins. The HRR peptide was then eluted by applying six 0.5 CV of Buffer E. The eluate was collected in 0.5 CV fractions to maximize protein recovery.

To assess the quality and yield of the purified HRR peptide, 20 µL samples from each collected fraction were analyzed using SDS-PAGE and Western blot.

2.2.2.3 Peptide concentration

The purified protein fractions were analyzed using SDS-PAGE to evaluate the purity of the HRR peptide and Western blot to confirm its identity. Fractions displaying only the HRR peptide band were pooled for further concentration.

The pooled fractions were concentrated using a 0.5 mL Amicon® Ultra centrifugal filter unit with a 3 kDa molecular weight cutoff (Merck). The sample was loaded into the filter tube and centrifuged at 16,100 × g for 15 minutes. After centrifugation, the flowthrough was discarded, and additional sample was added to the filter. The remaining sample within the filter unit was resuspended gently before repeating the process. This cycle was continued until the HRR peptide reached the desired concentration of 2.5 mg/mL.

Once the target concentration was achieved, the concentrated peptide was re-evaluated using SDS-PAGE and Western blot to confirm its purity and identity.

2.2.2.4 Membrane protein extraction from *P. falciparum*

Parasites were isolated from *Plasmodium falciparum* cultures at the trophozoite and schizont stages using a 36 mL culture with a parasitemia of 5%. The iRBCs were purified using a magnetic-activated cell sorting (MACS) system. After purification, 5 µL of iRBCs, corresponding to 5×10^7 cells, were aliquoted, and resuspended in 500 µL of ddH_2O supplemented with PI.

The suspension was subjected to 3–4 freeze-thaw cycles by alternating between liquid nitrogen and a 37 °C water bath to lyse the cells. Following lysis, the sample was centrifuged at 16,100 x g for 1 minute at 4 °C. The supernatant was discarded, and the pellet was resuspended in ddH_2O with PI. This washing step was repeated once more. The supernatant was discarded, and the pellet was resuspended in 50 µL of 1x Laemmli buffer. The suspension was sonicated using three sets of eight impulses at 10% amplitude in mode 2 to ensure complete disruption of the sample. The sonicated material was then centrifuged at 16,100 × g for 10 minutes at room temperature, and the supernatant was used as the membrane protein sample.

For SDS-PAGE and Western blot analysis, 10 µL of the sample was used to represent 10^7 parasites.

2.2.2.5 SDS-polyacrylamide gel electrophoresis (SDS-PAGE) of proteins

Protein samples were analyzed using SDS-PAGE to separate proteins based on their molecular weight. Prior to electrophoresis, samples were mixed with Leamli buffer and heated to 95 °C for 5 minutes to denature the proteins. PageRuler Plus Prestained Protein Ladder (10–250 kDa) was used as the molecular weight marker and was loaded alongside the samples for size reference.

Proteins were resolved on self-prepared polyacrylamide gels. The percentage of acrylamide in the gel was chosen based on the resolution required for the protein of interest. Gels were run in a Tris-Glycine SDS running buffer with a constant voltage of 200 V and a current of 60 mA. Electrophoresis typically lasts 45 to 60 minutes, depending on the gel porosity and resolution needed. The following gels were cast as indicated below:

Resolving gel

	10%	12%	15%
ddH$_2$O	3.96 mL	3.35 mL	2.3 mL
1.5 M tris pH 8.6	2.50 mL	2.50 mL	2.50 mL
10% SDS	100 µl	100 µL	100 µL
30% acrylamide	3.33 mL	4.00 mL	5.00 mL
10% APS	100 µL	100 µL	100 µL
TEMED	6 µL	6 µL	6 µL
Total volume	10 mL	10 mL	10 mL

Stacking gel

	5%
ddH$_2$O	3.46 mL
1 M tris pH 6.8	630 µL
10% SDS	50 µL
30% acrylamide	830 µL
10% APS	50 µL
TEMED	5 µL
Total volume	5 mL

2.2.2.6 Coomassie Blue staining for protein visualization

Protein bands were visualized on SDS-PAGE gels using Coomassie blue staining. Following electrophoresis, the gels were immersed in Coomassie staining solution and incubated for 5–10 minutes with gentle shaking at room temperature (100 rpm). After staining, the solution was discarded, and the gels were rinsed multiple times with distilled water to remove excess stain.

The gels were then transferred to distilled water for de-staining, which was performed under gentle shaking (100 rpm) at room temperature. The de-staining process continued overnight or until the background was sufficiently clear and the protein bands were distinctly visible.

2.2.2.7 Western Blot by semi-wet protein transfer

Proteins separated by SDS-PAGE were transferred onto an Immun-Blot PVDF membrane (Bio-Rad) using the Trans-Blot® SD Semi-Dry Transfer Cell (Bio-Rad). The PVDF membrane was activated by soaking in methanol for at least 30 seconds. The PVDF membrane and six Whatman papers were cut to match the gel size and equilibrated in transfer buffer for 5 minutes, along with the freshly run SDS-PAGE gel. In the transfer chamber, three pre-soaked Whatman papers were layered first, followed by the PVDF membrane and the SDS-PAGE gel. Another three Whatman papers were placed on top. Bubbles were carefully removed from the sandwich using a roller before closing the chamber.

The semi-wet transfer was performed at 230 mA and 15 V for 1 hour.

After the transfer, the PVDF membrane was blocked overnight at 4 °C in 5% milk dissolved in PBS with gentle agitation. The following day, the membrane was incubated with the primary antibody, diluted in 1% BSA, for 1 hour at room temperature on a roller. The membrane was then washed three times, each for 5 minutes, with PBST (0.1% Tween-20 in PBS) and subsequently blocked for 30 minutes in 5% milk. Secondary antibody incubation, also diluted in 1% BSA, was performed for 30 minutes at room temperature on a roller, followed by another set of three 5-minute washes with PBST.

Before visualization, the protein ladder was marked on the membrane using a LICOR WesternSure Pen. The membrane was then incubated for 5 minutes in freshly prepared developing solution (2 mL of solution A mixed with 20 µL of solution B, BM chemiluminescence blotting substrate POD, Roche). The chemiluminescent signal was captured using a LiCor C-DiGit Blot Scanner, and the resulting images were analyzed and processed with Image Studio software.

2.2.2.8 Western Blot membrane stripping

To remove bound antibodies from a Western blot membrane for reprobing, the membrane was incubated in stripping buffer for 30 minutes at room temperature with gentle agitation on a roller. Following incubation, the membrane was washed five times, each for 10 minutes, with PBST to thoroughly remove residual stripping buffer and antibodies. The membrane was then prepared for subsequent reprobing.

2.2.2.9 Protein concentration measurement using Bradford Assay

Protein concentrations were determined using the Bradford assay with the Bio-Rad Dye Reagent Concentrate (Bio-Rad), following the manufacturer's instructions. Bovine Serum Albumin (BSA) dissolved in ddH_2O was used as the standard. A standard curve was prepared using five BSA concentrations: 0, 1, 2.5, 5, and 10 µg of BSA were added to ddH2O aliquots of 800 µL. Each standard concentration was prepared in duplicate.

To each standard or sample dilution, 200 µL of Bio-Rad dye reagent concentrate was added, and the mixtures were vortexed briefly to ensure thorough mixing. The samples were incubated at room temperature for 5 minutes to allow color development. Absorbance was then measured at 595 nm using a spectrophotometer.

Protein concentrations in the samples were calculated based on the absorbance readings of the standard curve prepared with the BSA standard readings. Dilutions of the protein samples were prepared when needed to ensure their concentrations fell within the linear range of the standard curve.

2.2.2.10 Lipid interaction assay

The lipid interaction assay was conducted under two experimental conditions: using PBS as the buffer or PBS supplemented with 200 µM Zn^{2+} (Zn buffer) in all steps. The HRR peptide sample was thawed on ice and centrifuged at 16,100 × g for 5 minutes to remove any precipitates. The supernatant was transferred to a clean microcentrifuge tube, and the peptide concentration was determined using the Bradford assay. The protein was diluted as needed to a final concentration of 2 µg/mL in 5 mL of PBS for membrane incubation, and 0.5 mg/mL in 10 µL for spot application.

A membrane was placed flat on a petri dish, and 1 µL spots of 0.5 mg/mL HRR peptide (0.5 µg per spot), primary antibody, and secondary antibody were applied to the open membrane. These spots were allowed to dry completely before the membrane was transferred to a Falcon tube. The membrane was then incubated with 10 mL of blocking solution (1% milk in PBS) on a roller at room temperature for 1 hour to prevent nonspecific binding.

After blocking, the solution was discarded, and the membrane was incubated with 2 µg/mL HRR peptide diluted in PBS or Zn buffer for 1 hour on a roller at room temperature. The membrane was then washed three times with PBST (PBS containing 0.1% Tween-20), each wash lasting 5 minutes on a roller. Following this, the membrane was incubated with a 1:500 dilution of anti-His primary antibody for 1 hour at room temperature on a roller. The membrane was washed again three times with PBST for 5 minutes each.

A 30-minute blocking step was performed, after which the membrane was incubated with a 1:10,000 dilution of anti-mouse secondary antibody for 1 hour at room temperature on a roller. The membrane was then washed three more times with PBST for 5 minutes each.

To visualize the results, the membrane was incubated for 5 minutes in freshly prepared developing solution (2 mL of solution A mixed with 20 µL of solution B, BM chemiluminescence blotting substrate POD, Roche). The chemiluminescent signal was captured using a LiCor C-DiGit Blot Scanner.

2.2.2.11 Mass spectrometry sample preparation

P. falciparum 3D7 parasites were transfected to express stevor amino acids 1-80 in fusion with miniTurbo biotin ligase. Biological replicates were generated by culturing transfected or WT parasites using RBCs from three different donors, with each replicate corresponding to a separate donor.

The purified iRBCs were lysed in 1 mL of RIPA buffer by performing four freeze-thaw cycles using liquid nitrogen and a 37 °C water bath. The lysate was sonicated in mode 2 with two sets of 8 impulses at 50% intensity. After sonication, the lysate was centrifuged at 16,100 × g for 10 minutes, and the supernatant (SN) was collected for subsequent incubation with streptavidin beads. The pellet was discarded.

Fifty microliters of well-mixed Pierce™ Streptavidin Magnetic Beads were transferred into a tube and collected by placing the tube in a magnetic stand. The supernatant was discarded, and the beads were washed with 500 µL of W2 buffer. The iRBC lysate was incubated with the streptavidin beads overnight on a rotating shaker at 4 °C to allow biotinylated proteins to bind.

After incubation, the beads were separated from the lysate by magnetic collection, and the supernatant was discarded. The beads were washed twice with 500 µL of W1 buffer for 8 minutes on a rotator, followed by one wash with 500 µL of W2 buffers for 8 minutes on a rotator. The bound proteins were eluted from the beads using 50 µL of elution buffer by boiling at 95 °C for 5 minutes. The supernatant containing the eluted proteins was stored at -80 °C.

Ten microliters of the eluate were used for SDS-PAGE analysis and another 10 µL for Western blotting to confirm the enrichment of biotinylated proteins in the purified sample. Following confirmation, an additional 10 µL of the eluate was loaded onto a new SDS-PAGE gel, which was run until the smallest proteins migrated approximately 1 cm into the gel. The gel was subsequently processed for in-gel protein digestion and peptides were sent for mass spectrometry analysis to identify biotinylated proteins.

2.2.2.12 In-gel tryptic digestion and LC-MS/MS analysis

After SDS-PAGE, Coomassie-stained protein bands were excised using a scalpel, split into two slices, and processed according to previously described methods. Briefly, gel pieces were subjected to reduction, alkylation, and digestion with trypsin. The resulting peptides were extracted, concentrated using a vacuum centrifuge, and dissolved in 15 µL of 0.1% trifluoroacetic acid (TFA).

Peptides were analyzed using nanoflow liquid chromatography-tandem mass spectrometry (LC-MS/MS) on an Ultimate 3000 liquid chromatography system coupled to an Orbitrap QE HF mass spectrometer (Thermo Fisher Scientific). Separation was performed on an in-house packed analytical column (75 µm × 200 mm) containing 1.9 µm Reprosil-Pur AQ C18 material (Dr. Maisch, Germany). The mobile phase solvents were prepared as follows: solvent A consisted of 0.1% formic acid and 1% acetonitrile, and solvent B consisted of 0.1% formic acid and 89.9% acetonitrile.

Peptides from a single gel lane were combined and separated using two gradient options. In the first, a 60-minute linear gradient was applied, starting at 3% solvent B and increasing to 23% over 50 minutes, then to 38% over the subsequent 10 minutes, followed by a washout phase at 95% solvent B. In the second, a 25-minute gradient was used, starting at 3% solvent B, increasing to 23% over 21 minutes, then to 38% over the following 4 minutes, with a final washout at 95% solvent B.

The mass spectrometer operated in data-dependent acquisition mode, alternating between MS and MS/MS scans. Full MS spectra (m/z 400–1600) were acquired at a resolution of 60,000 (m/z 400), while up to 15 precursor ions were selected for MS/MS analysis with a normalized collision energy of 27 and an isolation width of 1.4 m/z.

MS/MS spectra were searched against the *Plasmodium falciparum* protein database (UP000001450, November 2021, 5,380 sequences), a human protein database (UP0005640_9606, June 2020, 20,531 sequences), and a customized contaminant database (Proteome Discoverer 2.5 with Sequest HT (Thermo Fisher Scientific)). Search parameters included a fragment ion mass tolerance of 0.02 Da, a parent ion mass tolerance of 10 parts per million (ppm), and trypsin as the specified enzyme. Carbamidomethylation of cysteine was set as a fixed modification, while oxidation (methionine), deamidation (asparagine and glutamine), acetylation (protein N-terminus), and methionine loss (protein N-terminus) were specified as variable modifications.

Peptide quantification was performed using the precursor ion quantifier node with the summed abundance method for protein abundance calculations.

2.2.2.13 Mass spectrometry data processing

MS/MS data were analyzed and processed using Perseus software (version 1.6.13.0). Protein abundances were transformed into $\log_2(x)$ values to facilitate statistical analysis. Proteins absent in all three replicates of at least one group were excluded. Additionally, within each group, proteins detected in only one of the three biological replicates were discarded. Common contaminants, such as keratin and hemoglobin (specific to infected red blood cells), were also filtered out.

For proteins present in only two of three replicates within a group, the missing value in the third replicate was imputed using a normal distribution derived from the values in the other two replicates. To account for variability in sample concentrations, data normalization was performed. This was achieved by comparing the average protein abundance in each sample to the average protein abundance across all samples.

A multiple-sample analysis of variance (ANOVA) test was conducted to compare all experimental groups, including the wild-type (WT) 3D7 control group and WT 3D7 control incubated with biotin. Proteins identified as significantly different by ANOVA were used for further analyses, including Principal Component Analysis (PCA) to assess group clustering and Pearson correlation analysis to evaluate relationships between pairs of mutant experimental groups.

2.2.3 Parasitology

2.2.3.1 *In vitro* cultivation of *Plasmodium falciparum*

Intraerythrocytic stages of *Plasmodium falciparum* were maintained in continuous blood culture following the standard protocols established by Trager and Jensen (2005). Parasites were cultured at 37 °C in complete RPMI 1640 medium under a controlled atmosphere consisting of 5% O_2, 3% CO_2, 92% N_2, and 95% relative humidity. The medium was supplemented with Albumax and high concentrations of hypoxanthine for transfected parasites under selective drug pressure.

Human A+ erythrocytes were used to achieve a hematocrit of 2–4%, with parasitemia levels maintained between 0.1% and 5% unless specified otherwise for experimental purposes. The medium was replaced at least every two days or more frequently as needed to prevent the accumulation of toxic metabolites. Parasite cultures were monitored regularly by preparing methanol-fixed, Giemsa-stained thin blood smears to assess parasitemia, defined as the percentage of infected erythrocytes. When necessary, a fraction of the culture was transferred to a new plate with new media and erythrocytes to dilute the parasitemia.

For standard culture maintenance, 14 mL or 36 mL of medium was used in 100 mm or 140 mm petri dishes, respectively. These conditions ensured optimal growth and viability of the parasites.

2.2.3.2 Heat inactivation of human serum for parasite growth medium

Human serum used for cell culture medium preparation was sourced from the blood bank in Heidelberg and stored at -20 °C until processing. Prior to inactivation, A+ human serum bags were thawed at room temperature and transferred into a sterile flask. To facilitate clotting, the serum was treated with 30 mM calcium chloride, prepared from a 1 M sterile stock solution in ddH_2O. The serum was then aliquoted into 50 mL centrifuge tubes.

The aliquots were incubated in a 37 °C water bath to allow coagulation and subsequently stored overnight at 4 °C. The following day, the samples were centrifuged at 2,600 × g for 60 minutes at room temperature to remove coagulated proteins. The clarified serum was then heat-inactivated by incubation in a 56 °C water bath for 30 minutes.

After inactivation, the serum aliquots were stored at -20 °C until further use in cell culture media preparation.

2.2.3.3 Morphological examination of parasites and determination of parasitemia

Parasite cultures were monitored regularly using Giemsa-stained thin blood smears to evaluate the morphological stages of *Plasmodium falciparum* and determine parasitemia. Thin smears were prepared by placing approximately 20 µL of settled erythrocytes onto a microscope slide and spreading the sample thinly across the surface. The smears were allowed to air dry at room temperature before fixation in absolute methanol for at least 30 seconds. After fixation, the slides were air-dried again.

The smears were stained using a 10% Giemsa solution prepared in ddH_2O. The slides were incubated in the staining solution for 5-10 minutes, depending on the desired staining intensity. After staining, the slides were carefully rinsed with water, dried gently using tissue paper, and examined under a light microscope using an oil immersion objective at 100X magnification.

The different asexual stages of *P. falciparum* were identified and assessed for morphological alterations, referencing established literature examples. For parasitemia determination, the number of infected red blood cells and total red blood cells were counted across ten consecutive microscopic fields, amounting to approximately 1,000 total cells. Parasitemia was expressed as the percentage of infected cells relative to the total erythrocyte count. This method provided insights into parasite development and culture health.

2.2.3.4 Synchronization of *Plasmodium falciparum* parasites with d-sorbitol

Synchronization of *Plasmodium falciparum* cultures to the ring stage was performed using 5% D-sorbitol, following the method of Lambros and Vanderberg (1979). This procedure exploits the differential permeability of erythrocyte membranes. Mature-stage parasites (late trophozoites and schizonts) induce structural modifications in the erythrocyte membrane that render it permeable to sorbitol, causing osmotic lysis, while uninfected erythrocytes and ring-stage-infected erythrocytes remain intact.

To synchronize the culture, parasite-infected RBCs were harvested and centrifuged at 900 × g for 2 minutes at room temperature. The supernatant was discarded, and the pellet was resuspended in 10 mL of pre-warmed 5% D-sorbitol solution. The suspension was incubated at 37 °C for 5 minutes to selectively lyse mature stages of the parasite iRBCs. Following incubation, the cells were centrifuged at 900 × g for 2 minutes, and the supernatant containing lysed mature stages was discarded.

The resulting pellet, containing synchronized ring-stage parasites and uninfected erythrocytes, was washed once with pre-warmed complete RPMI 1640 media. After a subsequent centrifugation step, the pellet was resuspended in 14 mL of complete RPMI culture medium pre-warmed to 37 °C and transferred to a culture dish for further incubation. Parasitemia levels and parasite stages were evaluated after at least one hour recovery using Giemsa-stained thin blood smears.

For tighter synchronization, this process was repeated after a 4–12 hour interval, depending on the specific requirements of the experiment, as only parasites younger than 18 hours post-invasion survive the initial sorbitol treatment.

2.2.3.5 Magnetic purification of late-stage parasite infected RBCs

Late intraerythrocytic stages of *Plasmodium falciparum*, such as trophozoites and schizonts, were purified using the Magnetic Activated Cell Sorting (MACS) system. This technique leverages the paramagnetic properties of hemozoin crystals, which are formed in the food vacuoles of mature parasite stages during hemoglobin catabolism. These properties enable the selective retention of late-stage parasite-infected erythrocytes within a magnetic field, while uninfected erythrocytes and early-stage parasites flow through the system.

For purification, the MACS column was equilibrated by washing twice with pre-warmed (37 °C) MACS buffer and then inserted into the VarioMACS separator. Parasite cultures were resuspended in MACS buffer and loaded onto the column. The flow rate was carefully adjusted to approximately one drop a second to ensure optimal separation. Once the culture had passed through the column, the column was washed with additional MACS buffer until the flow-through appeared clear, indicating the removal of uninfected erythrocytes and early-stage parasite iRBCs.

The column was then removed from the magnetic separator, and the retained late-stage infected erythrocytes were eluted by washing the column with 10–12 mL of MACS buffer into a 15 mL falcon tube. The eluted cells were collected by centrifugation at 900 × g for 2 minutes at room temperature. The resulting pellet was resuspended in the appropriate solution, depending on the downstream experimental application, such as culture medium or a specific buffer.

2.2.3.6 Gelatine flotation for knobby iRBC selection

Gelatine flotation was employed as a synchronization and selection method for late-stage *Plasmodium falciparum* parasites, particularly those with high knob densities. This method relies on the slower sedimentation of late-stage parasitized erythrocytes, which possess knobs, in a heated gelatine solution.

For this protocol, parasite cultures were centrifuged at 900 x g for 2 minutes at room temperature to pellet the cells. The pellet was resuspended in 10 pellet volumes of a pre-warmed 0.7% gelatine solution and incubated at 37 °C for 1 hour. This process enabled the separation of uninfected erythrocytes, ring-stage parasites, and knobless parasitized erythrocytes from knobby late-stage parasite iRBCs, including trophozoites (24–36 hours post-invasion) and schizonts (36–48 hours post-invasion).

2.2.3.7 Transfection of *P. falciparum*

2.2.3.7.1 Preparation of DNA

Approximately 100 µg of each transfection plasmid DNA was precipitated by combining 1 volume of DNA solution with 1/10 volume of 3M sodium acetate, and 2.5 volumes of 100% ethanol. The mixture was incubated at -20 °C for at least 30 minutes. The precipitated DNA was then centrifuged at 16,100 × g for 30 minutes at 4 °C. The resulting pellet was washed with 0.5 mL of 70% ethanol, followed by another centrifugation step at 16,100 × g for 15 minutes. In sterile conditions, the pellet was air-dried, resuspended in 30 µL of sterile TE buffer, and stored at -20 °C until use. Before the transfection 370 µL of sterile cytomix was mixed with the 30 µL of plasmid DNA solution.

2.2.3.7.2 Preparation of parasite culture

Ring-stage *P. falciparum* parasites with a parasitemia of 3–5% were used for transfection. The parasites were synchronized one cycle prior to transfection using sorbitol treatment.

2.2.3.7.3 Transfection

The parasite culture was centrifuged at 900 × g for 2 minutes, and the supernatant was discarded. A volume of 200 µL of the packed iRBC pellet was mixed with the prepared 400 µL plasmid DNA in cytomix by gentle pipetting, and transferred into an electroporation cuvette. The electroporation was performed using the Gene Pulser II Electroporator (Bio-Rad) system set at 0.310 kV and 950 µF. Following electroporation, the sample was transferred to a 14 ml culture dish supplemented with 500 µL of fresh erythrocytes.

2.2.3.7.4 Selection under drug pressure

One day after transfection, drug selection was initiated with 5 nM WR99210, 5µM blasticidin S deaminase (*BSD*), 1.5 µM DSM1, or a combination of two, depending on the selection markers of the transfected plasmids. The culture medium and drug were exchanged for fresh for seven consecutive days. After the initial selection phase, the medium was changed every 2–3 days, and the culture was supplemented weekly with 100 µL of fresh erythrocytes. Selection continued for 3–5 weeks until parasites became visible in blood smears.

Once parasite growth was observed, the drug pressure was removed from CRISPR Cas9-produced mutants as the integration events were expected to have taken place, while transfectants with episomal plasmids were kept under drug pressure the entire cultivation time to ensure the retention of episomal plasmids. Part of the transfected culture was cryopreserved, and the remaining culture was cultivated for further characterization.

2.2.3.8 Selecting monoclonal parasite lines by limiting dilution

In parasites altered by CRISPR-Cas9 technology, where the mutation was integrated into the genomic DNA (gDNA), clonal parasite populations were isolated once the desired mutation or integration post-transfection was confirmed. Limiting dilution method was used to obtain monoclonal parasite lines. In 96-well plate, clonal parasite line cultures were maintained at 2% hematocrit, with an initial seeding of approximately 0.25–0.5 parasites per well. Parasite clones were identified by examining Giemsa-stained blood smears after 2 weeks of growth.

To prepare accurate dilutions, the parasitemia of the parental culture was assessed by . The total number of parasites was calculated, assuming 0.5 mL of packed erythrocytes with 100% hematocrit contained approximately 5×10^9 cells. Based on this calculation, a concentrated suspension containing 10^6 parasites per mL was prepared in complete RPMI 1640 media. Serial 1:10 dilutions were performed in 10 ml volume to reduce the concentration to 10^1 parasites per mL. This was followed by two consecutive 1:2 dilutions to create working suspensions of 5 and 2.5 parasites per mL. These suspensions were mixed with fresh erythrocytes (200 µL per 10 mL of suspension) to achieve a final hematocrit of 2%, ensuring proper mixing through repeated inversions.

in a 96-well plate 100 µL of seed culture was pipetted per well, providing a calculated seeding density of 0.25–0.5 parasites per well. The cultures were maintained in transfection medium without drug selection, and the medium was exchanged every 2–3 days. The presence of parasites in wells was monitored after 2 weeks and positive wells were selected by microscopic examination of Giemsa-stained smears.

Once parasite growth was verified, the cultures from positive wells were transferred to larger plates to expand parasite populations. Expanded cultures were cryopreserved or utilized for further analysis.

2.2.3.9 Cryopreservation and thawing of *P. falciparum* parasites

For cryopreservation, *P. falciparum* ring-stage cultures with a parasitemia of at least 1% were used, as early ring stages exhibit greater membrane elasticity, allowing them to survive the freeze-thaw cycle. Cultures were transferred to 15 mL centrifuge tubes and centrifuged at 900 × g for 2 minutes at room temperature. The supernatants were carefully discarded, and the resulting pellets were gently resuspended in 166 µL of freezing solution, followed by a 5-minute incubation at room temperature. An additional 660 µL of freezing solution was added dropwise with gentle mixing. The suspensions were aliquoted into cryogenic vials at a volume of 500 - 600 µL and frozen initially at -80 °C. For long-term storage, vials were transferred to liquid nitrogen tanks (-196 °C).

Thawing starts by warming the cryovials in a 37 °C water bath until the contents were completely liquid. The thawed suspension was transferred to a 15 mL centrifuge tube, and 200 µL of pre-warmed Thawing Solution I was added dropwise with gentle mixing. After a 5-minute incubation, 9 mL of pre-warmed at 37°C Thawing Solution II was added gradually while continuously mixing. The sample was centrifuged at 900 × g for 2 minutes at RT, and the supernatant was discarded. Subsequently, 7 mL of pre-warmed Thawing Solution III was added dropwise, mixed gently, and centrifuged again under the same conditions.

The final pellet was resuspended in 14 mL of complete RPMI medium pre-warmed to 37 °C and transferred to a 100 mm petri dish containing 500 µL of fresh erythrocytes. Cultures were monitored for revival after one ful cycle of 48 h, and the medium was exchanged, or cultures were diluted as needed to maintain appropriate parasitemia levels. Parasites were considered ready for experimental use after a minimum of 7 days.

2.2.3.10 Biotinylation assay

For the biotinylation assay, *Plasmodium falciparum* parasites were cultured in 36 mL culture to reach 5% parasitemia, at the ring stage. Synchronization to the ring stage was achieved using sorbitol treatment. The culture was supplemented with biotin to a final concentration of 50 µM to initiate biotin ligase activity and allowed to grow under standard conditions for 18 hours (overnight). On the following day, mature-stage iRBCs were purified using MACS and collected parasites were used to prepare mass spectrometry samples.

2.2.4 Microscopy

2.2.4.1 Immunofluorescence assay (IFA) sample preparation

Young trophozoite-stage parasites were purified using the MACS system from a 36 mL culture with a parasitemia of 5–10%. After purification, the samples were centrifuged at 900 × g for 2 minutes, and the erythrocytes were washed with PBS. Fixation was performed by incubating the samples in a Fixing Solution (4% paraformaldehyde and 0.0075% glutaraldehyde) for 30 minutes at 37 °C with shaking at 200 rpm. Following fixation, the cells were treated with a permeabilization-quenching solution (0.1% Triton X-100 and 100 mM glycine) for 15 minutes at room temperature with continuous rotation.

Subsequent steps were carried out at room temperature under gentle rotation. The samples were blocked for 1 hour in 3% BSA prepared in PBS, which also served as the antibody dilution buffer. After blocking, the samples were incubated with the primary antibody diluted in the blocking buffer for 1 hour. Unbound primary antibodies were removed by washing the samples three times in the blocking buffer, with each wash lasting 15 minutes. Secondary antibody staining was then performed for 1 hour in the dark, followed by another series of three washes in PBS. During the final wash, Hoechst dye was added at a concentration of 5 µM to stain the nuclei.

The stained cells were resuspended in PBS and stored at 4 °C until imaging. Fluorescence imaging was conducted using a Leica SP8 confocal microscope.

2.2.4.2 Split-GFP assay

Parasites were transfected with two plasmids: one encoding the bait protein fused to GFP1-10 and the other encoding a selected mass-spectrometry hit (MSH) fused to GFP11.

A 14 mL mixed parasite culture at 5% parasitemia was collected by centrifugation at 900 × g for 2 minutes, and the supernatant was discarded. The live parasites were resuspended in 5 µM Hoechst dye prepared in complete RPMI 1640 medium and incubated for 5 minutes to stain the parasite nuclei. After incubation, the cells were centrifuged again under the same conditions, and the pellet was resuspended in fresh complete RPMI 1640 medium.

The stained and prepared cells were directly imaged by spinning disc confocal microscopy.

2.2.4.3 Fluorescence microscopy

2.2.4.3.1 Leica SP8 microscope

Immunofluorescence imaging was conducted using point laser scanning confocal microscopy on a Leica SP8 microscope equipped with an HC PL APO CS2 63x/1.4 N.A. oil immersion objective.

Multichannel images were acquired sequentially to minimize spectral overlap using HyD detectors in standard mode.

Fluorescent signals were captured with laser excitation set at 488 nm and a spectral detection window between 500 and 550 nm for Alexa 488 or GFP. For Phycoerythrin (PE) imaging, a 561 nm laser was used with a spectral detection window between 570 and 590 nm. Brightfield images were acquired simultaneously using a transmitted light photomultiplier tube (PMT) detector.

2.2.4.3.2 Spinning disk confocal microscopy

Spinning disk confocal microscopy was conducted using a PerkinElmer UltraVIEW VoX microscope equipped with a Yokogawa CSU-X1 spinning disk head and a Nikon TiE microscope body. Imaging was performed with an Apo TIRF 60x/1.49 N.A. oil immersion objective, enabling high-resolution visualization. Multichannel images were acquired sequentially using solid-state lasers with excitation wavelengths of 405 nm and 488 nm, paired with corresponding emission filters to optimize signal detection.

2.2.4.4 Scanning electron microscopy (SEM) sample preparation

2.2.4.4.1 Coverslip cleaning

Round 12 mm coverslips were cleaned to prepare them for SEM sample coating. Coverslips were placed in a 50 mL tube and washed with double-distilled water (ddH_2O) by gentle inversion, followed by decanting the liquid. Fresh ddH_2O was added, and the coverslips were sonicated for 15 minutes, with the water subsequently decanted. This washing and sonication process was repeated twice more. After cleaning, the coverslips were incubated in 0.1 M HCl solution in ddH_2O while rotating at room temperature for 1 hour. The coverslips were then washed three additional times with ddH_2O and stored in 99% ethanol until further use.

2.2.4.4.2 Poly-l-lysine slide coating

Pre-cleaned 12 mm round coverslips stored in 99% ethanol were transferred into multi-well plates, with a piece of Whatman filter paper placed underneath each coverslip. The coverslips were dried at 56 °C. A droplet of 0.1% poly-L-lysine solution in ddH_2O was then applied to the center of each coverslip and dried at 56 °C for 30 minutes to 1 hour. The filter paper was carefully removed before proceeding with sample application.

2.2.4.4.3 SEM sample preparation

Late-stage iRBCs were purified using MACS system. The purified cells were washed in a microcentrifuge tube with 1 mL of 0.1 M cacodylate buffer (pH 7.2) and centrifuged. The iRBCs were then fixed in 1 mL of 1% glutaraldehyde (GA) in cacodylate buffer for 30 minutes at room temperature with gentle rotation. After fixation, the sample was washed once with cacodylate buffer.

The fixed cells were resuspended in 1% GA in cacodylate buffer and loaded onto poly-L-lysine-coated coverslips. The coverslips were incubated at 4 °C for 5–10 minutes, allowing cells to adhere. Excess cells were gently washed off using cacodylate buffer, leaving a thin, transparent layer of adhered cells on the coverslip. To stabilize the sample, 1% GA in cacodylate buffer was added to the coverslips, which were then stored at 4 °C overnight.

The following day, the coverslips were washed twice with 0.1 M cacodylate buffer and then incubated in 1% osmium tetroxide (OsO_4) in cacodylate buffer for 1 hour at 4 °C. The samples were washed twice with cacodylate buffer and twice with ddH_2O to remove residual OsO_4. Dehydration was performed using sequentiall acetone dilutions in ddH_2O: 25%, 50%, 75%, 95%, and 100%, with each step lasting 10 minutes. After the final acetone wash, critical point drying was conducted using CPD300 (Leica) by replacing acetone with CO_2.

The dried coverslips were mounted onto 12.5 mm pins using silver glue. The mounted samples were further sputtered with a 5 nm coat of gold-palladium mix in Sputter Coater EM ACE600 (Leica). The prepared samples were then ready for SEM imaging.

2.2.4.5 Scanning electron microscopy (SEM)

SEM was utilized to evaluate the shape of knobs and density on iRBCs. The analysis was conducted using a Leo 1530 high-resolution scanning electron microscope equipped with a secondary electrons 2 (SE2) detector. The Electron High Tension (EHT) was set to 2 kV and individual cell images were captured at a magnification of 12,000x.

2.2.4.6 Image processing

All images were processed and analyzed using ImageJ software, with identical settings applied to all samples within the same experiment.

2.2.5 Scientific writing and figures

ChatGPT and Grammarly were used to improve text clarity, structure, and grammar throughout the thesis. Benchling biology software and Biorender tool were used to create schematic figures.

3. Results

3.1 KAHRP role in knob assembly

To identify KAHRP role in knob assembly, I introduced multiple mutations and analyzed the resulting knob phenotype. The mutations were introduced in the genomic locus of the KAHRP gene in the *Plasmodium falciparum* IT parasite line using CRISPR Cas9 genome editing technology. We targeted the HRR – the region from amino acid 61 to 116, and the alpha-fold predicted beta-sheet structured region from amino acid 136 to 190.

3.1.1 Y193F mutation does not affect knob formation

The tyrosine in amino acid position 193 of the KAHRP protein was predicted to be phosphorylated and, therefore, was mutated to phenylalanine. Due to the structural similarity between tyrosine and phenylalanine, with the exception of the carboxyl group, which results in the lack of ability for phenylalanine to be phosphorylated, phenylalanine supports the structural role of tyrosine.

To introduce Y193F mutation in the KAHRP protein, I used CRISPR Cas 9 genome editing technology to replace 453 nucleic acids in the genomic locus of the *KAHRP* gene with a genetically engineered construct (geneart). Geneart encodes a part of the KAHRP protein with an identical amino acid sequence except for the intended mutation but has changed codons and, therefore, has a different DNA sequence (Figure 4A). I used a three-plasmid system to introduce Y193F mutation, where the guide, Cas9, and template were each on a separate episomal plasmid (Figure 4B).

In the template plasmid, geneart is flanked by homology regions 1 and 2 (HR1 and HR2), creating a rescue template for double-strand break reparation. To clone the template carrying plasmid, I first extracted DNA from the *Plasmodium falciparum* IT line and amplified HR1 and HR2 using primer pairs P 1 and P 2, P 3 and P 4 respectively. The created HR1 insert was flanked by SpeI and AflII restriction sites, and the HR2 insert was flanked by NotI and SacII restriction sites. pL-6-B vector and inserts were digested accordingly to clone both HRs one after the other into the same plasmid in two restriction and T4 ligation cycles, creating plasmid pL-6-B-HR. Further, I amplified the geneart and introduced Y193F mutation by performing overlap extension PCR with primers P 7 to P 10, and cloned the geneart into the plasmid using an In-Fusion cloning mix to eliminate the restriction sites between HRs and the geneart. Correct insertion and sequence were confirmed by sequencing using primers P 11 and P 12 binding upstream (forward) and downstream (reverse) from multiple cloning site (MCS).

The guide was introduced into a separate plasmid under the U6 promoter. I annealed the primers P 5 and P 6, creating the guide insert DNA fragment, and then inserted the guide into the BtgZI digested pL-6_eGFP

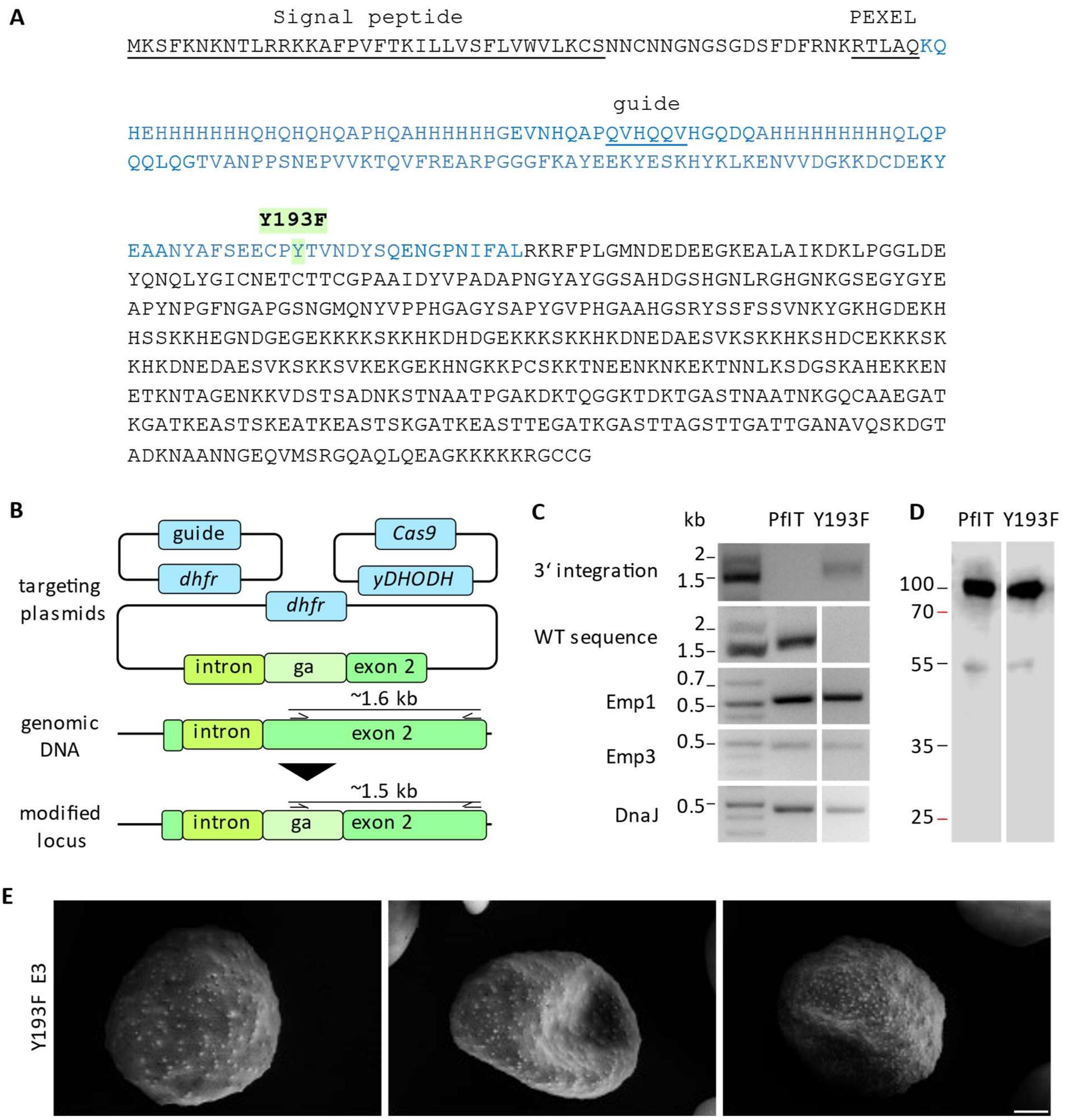

Figure 4. Introduction and analysis of Y193F mutation.

(A) Placement of Y193F mutation in KAHRP protein. The segment of the KAHRP protein encoded by the genetically engineered construct replacing the native genomic sequence is in blue. The guide region is underlined, and the tyrosine undergoing the Y193F mutation is highlighted in green. (B) Cloning strategy for genomic sequence replacement. Part of the genomic KAHRP sequence is replaced by a genetically engineered sequence carrying Y193F mutation (ga). The guide and Cas9 for CRISPR-Cas9 genome editing technology are encoded in two additional plasmids. Arrows indicate primer pair binding sites used to confirm 3' integration or the presence of wild-type (WT) sequence. (C) Genotyping of Y193F clone E3. PCRs were performed using genomic DNA (gDNA) of the *P. falciparum* IT line (PfIT) or Y193F monoclonal mutant line. The presence of Chromosome 2 end genes Emp1, Emp3, and DnaJ was confirmed. (D) Western blot analysis. Membrane proteins were extracted from the *P. falciparum* IT line (PfIT) and the Y193F E3 mutant line. Samples of 10^7 iRBCs were loaded per well, and anti-KAHRP antibody was used to visualize the KAHRP protein. (E) Scanning electron microscopy images show the knob density and shape in the Y193F E3 clone. Scale bar = 1 µm.

plasmid. The guide for Cas9 targeting recognizes KAHRP genomic sequence in the replacement region but not in the recodonized geneart.

I transfected *Plasmodium falciparum* IT line parasites with three plasmids simultaneously and clonally diluted them to create clonal lines of parasites stemming from a single transfected parasite. I further genotyped the clonal lines and selected one line to work with further. To ensure integration, I performed PCR confirming 3' integration using a primer pair, where the forward primer P 23 binds in the region of Y193F mutation, and reverse primer P 22 is reverse-complementary to the C-terminus of the KAHRP gene. To confirm that there is no WT parasite contamination in the selected clones, I performed PCR with a primer pair where the forward primer P 24 binds to the WT sequence to be replaced by the recodonized geneart, and the KAHRP C-terminus reverse primer P 22. Mutant Y193F clone E3 was positive for geneart integration and negative for WT sequence (Figure 4C). Chromosome 2 end is prone to breakage (Calhoun et al., 2017), this is enhanced by double-strand break and repair at the KAHRP gene located 90 kb from Chromosome 2 end. Therefore, I confirmed the presence of Chromosome 2 end genes *EMP1*, *EMP3,* and *DnaJ* located between the *KAHRP* gene and the telomere using primers P 26 to P 31. I further sequenced the integrated template using P 25, one additional mutation was observed that substitutes asparagine at position 202 by serine.

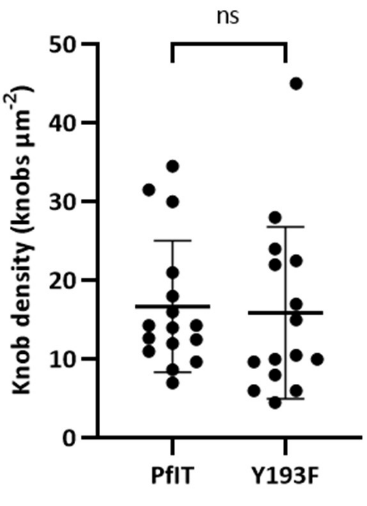

Figure 5. Mutation Y193F does not affect iRBC knob density.

The late-stage iRBCs were enriched by magnetic purification and further imaged with a scanning electron microscope. Knob density was counted per square µm in 16 cells of *P. falciparum* IT line (n=16) and 15 Y193F mutant iRBCs (n=15).

To confirm KAHRP expression, I extracted membrane proteins from the Y193F mutant E3 line and the parental line *Plasmodium falciparum* IT. I then performed Western Blot to analyze 10^7 late-stage iRBC using an anti-KAHRP antibody to identify the KAHRP protein. KAHRP in the Y193F E3 mutant line was equally abundant and of the same size as in the parental IT line (Figure 4D).

To assess knob shape and density, I performed scanning electron microscopy (SEM) of the whole late-stage iRBCs (Figure 4E). The cells are covered densely in small knobs, similar to the *Plasmodium falciparum* IT line (WT in Figure 8). There is no significant difference in knob density between the Y193F mutant iRBCs and the parental *Plasmodium falciparum* IT line (Figure 5). We, therefore, conclude that this amino acid plays no crucial role in knob assembly.

3.1.2 KAHRP alanine screening reveals the importance of beta-sheet region in knob formation

To further analyze KAHRP's role in knob assembly, we targeted the histidine-rich region of KAHRP protein containing three stretches of 6-9 consecutive histidines, and the alpha fold predicted beta-sheet structured region (Figure 3A and C) for alanine screening. To mutagenize these regions, I replaced 6-10 consecutive amino acids with alanines (Figure 6A) using CRISPR Cas9 genome editing technology.

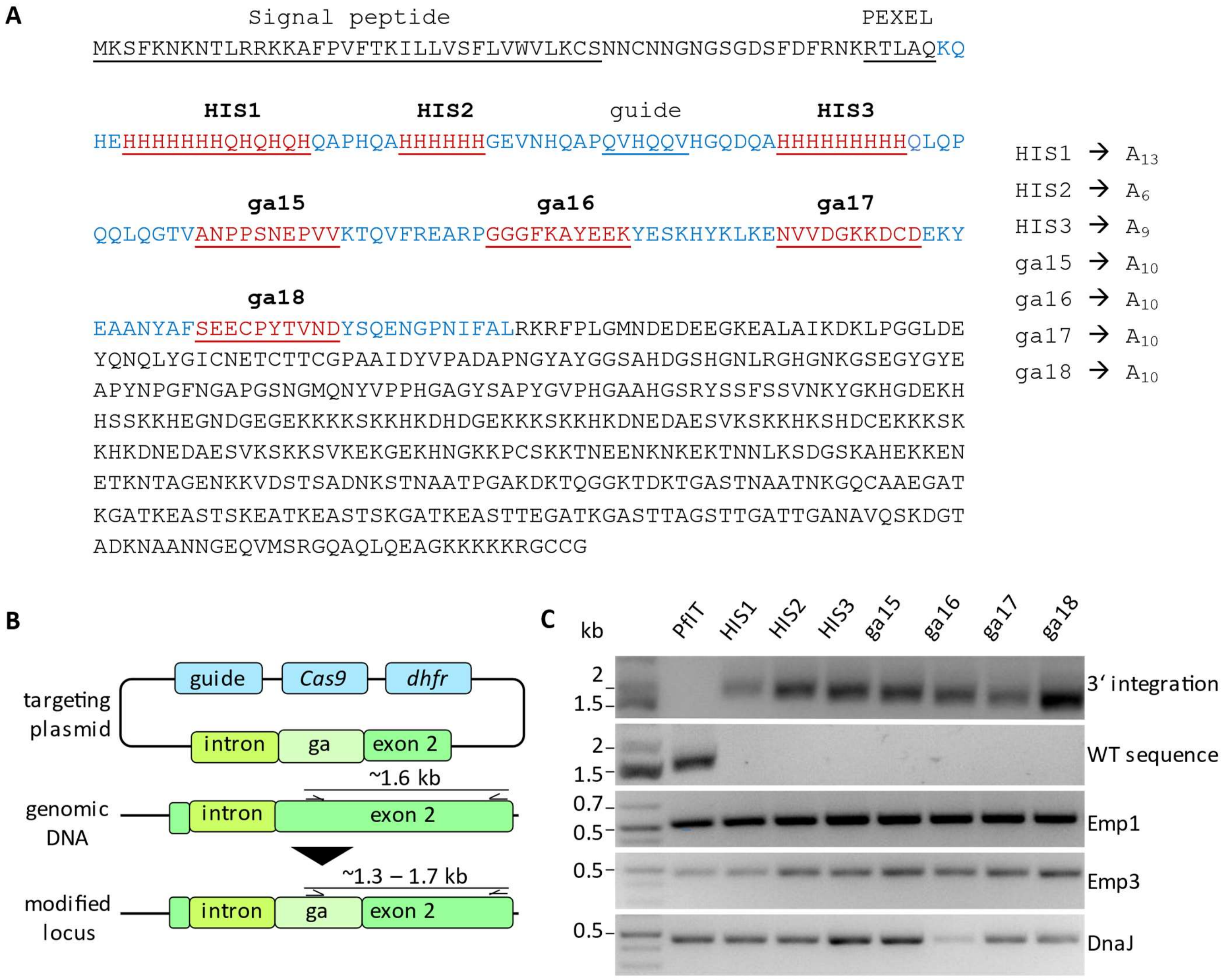

Figure 6. Alanine screening mutation integration.
(A) Map of alanine screening mutation sites. In blue the protein part encoded by the geneart sequence is, the mutation sites are underlined in red. The same guide was used to introduce any alanine screening mutation, underlined in blue. (B) Cloning strategy. CRISPR-Cas9 genome editing technology was utilized with a single plasmid carrying guide, Cas9, and template. Arrows represent primer pairs that detect wild-type (WT) sequence or 3' integration. The length of the 3' integration PCR varies depending on the position of the alanine site in the gene. (C) Genotyping of alanine screening mutant monoclonal lines. PCR fragments of various lengths demonstrate 3' integration according to the distance between the introduced alanine fragment and the end of the *KAHRP* gene. WT sequence PCRs confirm the absence of WT sequence in mutants. The presence of Chromosome 2 end is confirmed with PCR amplification of *Emp1*, *Emp3*, and *DnaJ* genes.

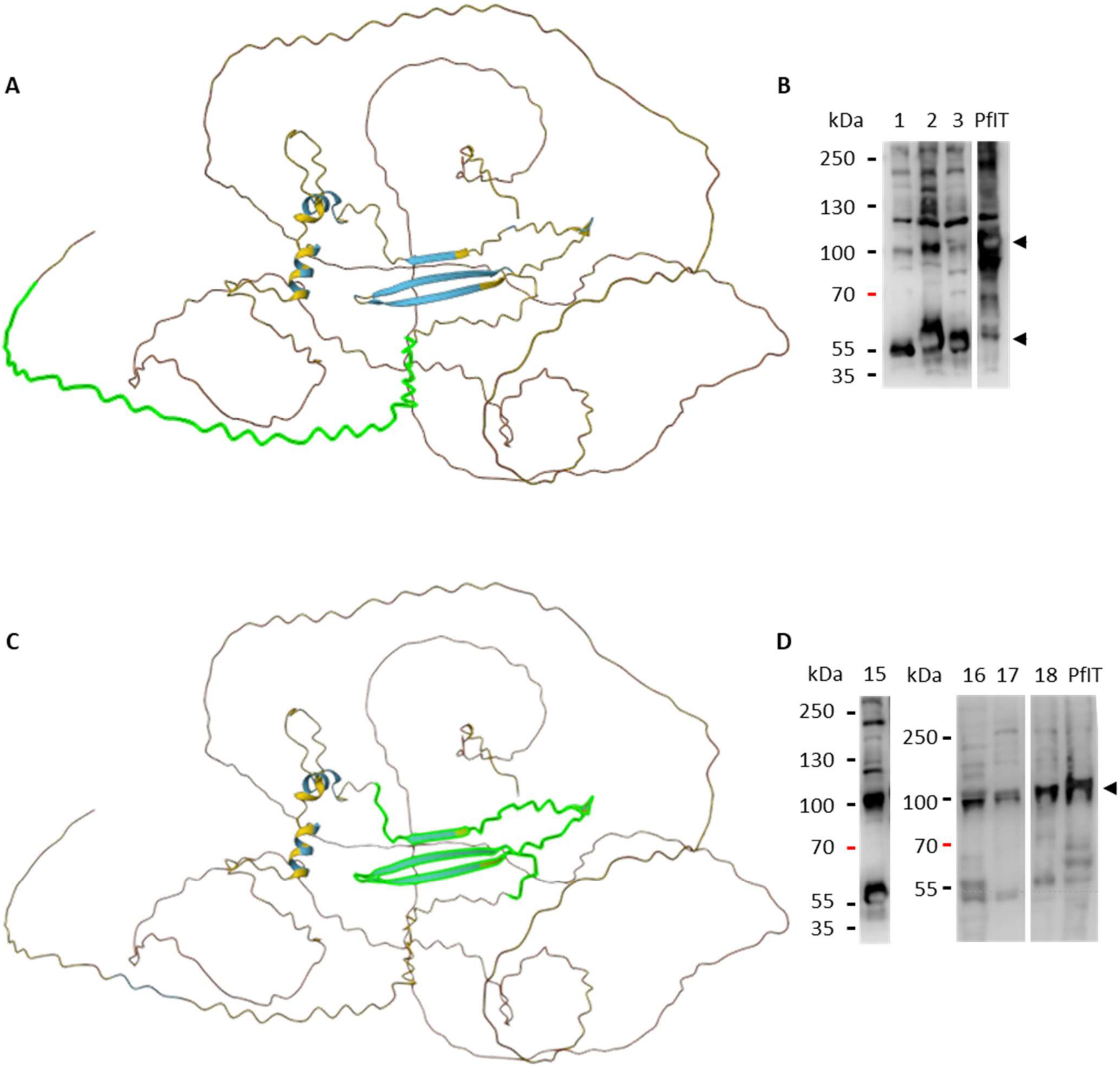

Figure 7. Alpha fold protein structure prediction and mutant WB analysis.
(A) Alpha fold KAHRP protein structure prediction with HRR highlighted in green. (B) Western blot of HRR mutants HIS1, HIS2, HIS3 and parental IT line. Arrowheads indicate KAHRP bands at expected position (~100 kDa) and a band most abundant in mutants (~55 kDa). (C) Alpha fold KAHRP structure prediction with beta sheet region highlighted where mutations ga15, ga16, ga17 and ga18 were introduced. (D) Western blot of mutants ga15, ga16, ga17, ga18 and parental IT line. The arrowhead indicates KAHRP band. Alpha fold prediction colors indicate 🟦 very high confidence (pLDDT > 90), 🟦 confident (90 > pLDDT > 70), 🟨 low confidence (70 > pLDDT > 50), 🟧 very low confidence (pLDDT < 50).

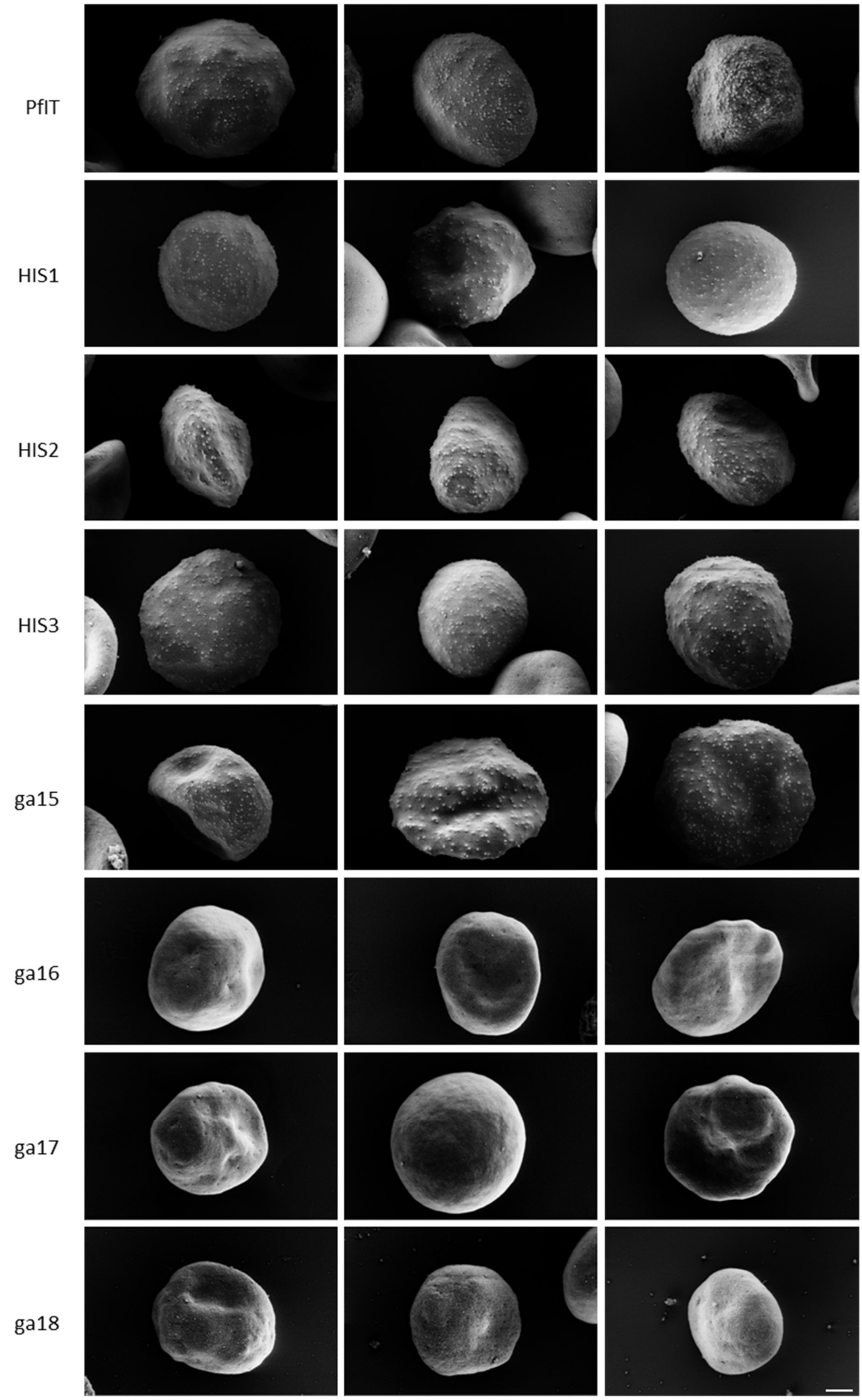

Figure 8. Alanine screening mutant knob phenotype analysis using scanning electron microscopy. P. falciparum IT line (PfIT) compared to the mutant lines. Scale bar represents 1 µm.

To introduce alanine screening mutations, I used pDC2-cam-co.Cas9-U6-hDHFR (further called pDC2) vector where all necessary elements for CRISPR Cas9 mutagenesis could be inserted: guide, Cas9 expression cassette, and a rescue template (Figure 6B). The change from a three-plasmid system to a single plasmid increased the efficacy of mutation integration.

pDC2 vector already possesses Cas9 expression cassette. Therefore, I only cloned the template and the guide into the vector. First, I introduced the guide into the pDC2 vector by annealing primers P 13 and P 14, and performing T4 ligation of annealed insert and BbsI digested pDC2 vector. The created plasmid was sequenced to confirm guide insertion using P 15 which is reverse-complement to the downstream sequence from the guide integration site.

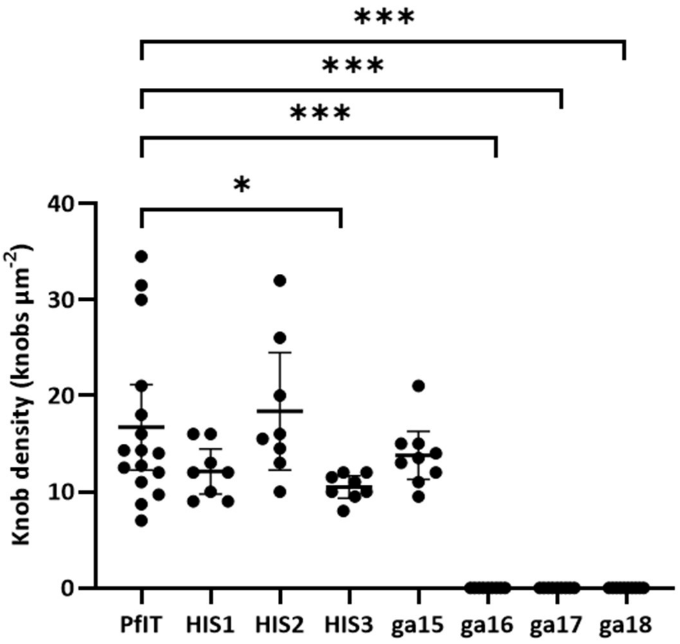

Figure 9. Knob density in alanine screening mutant iRBCs. Magnetically enriched late-stage iRBCs were imaged by SEM and knobs were counted per µm² in parental line P. falciparum IT (n=16) and mutant iRBCs HIS1 (n=9), HIS2 (n=9), HIS3 (n=9), ga15 (n=10), ga16 (n=10), ga17 (n=10), ga18 (n=11). "*" indicate $0.01 < p < 0.05$, "***" indicate $p < 0.0001$.

I transfected every alanine-screening plasmid into the *Plasmodium falciparum* IT line. Further, I clonally diluted the parasites to select monoclonal parasite lines, each stemming from a single parasite. For genotyping purposes, I performed multiple PCRs to confirm the correct integration of the template (Figure 6C). To detect 3' integration, I performed PCR using a primer pair where the forward primer P 32 annealed to the DNA sequence of alanine stretch, and the reverse primer P 22 was reverse-complimentary to the C-terminus of the KAHRP gene. Due to the alanine positioning in mutants, the PCR fragments are of different sizes, from 1.7 kb in the HIS1 mutant to 1.3 kb in the ga18 mutant. The PCRs to test WT parasite contamination and chromosome 2 end breakage were performed as described for the Y193F mutant. All alanine screening clones were positive for 3' integration and negative for WT DNA. Furthermore, PCRs of *EMP1*, *EMP3*, and *DnaJ* genes located between telomere and *KAHRP* gene were positive, indicating intact Chromosome 2 end. One clone was further selected for analysis and sequenced using a reverse primer P 25 that is reverse complementary to the *KAHRP* genomic sequence shortly downstream of HR2.

To confirm that mutations did not affect KAHRP expression, I purified membrane proteins and performed western blots with 10^7 parasites per sample (Figure 3B and D). I observed that while in mutants ga16, ga17, and ga18, KAHRP was presented at the expected size of 100 kDa, mutants display no knobs on the iRBC surface, indicating that parasites with the disrupted beta-sheet region in KAHRP cannot produce knobs (Figure 8). The significance of the difference between the WT and ga16, ga17, and ga18 groups was confirmed by knob density measurement (Figure 9).

Four mutations have been introduced in the region of KAHRP, which was predicted by AlphaFold to be structured and contain three beta strands. The mutations were genotypically confirmed, and KAHRP protein expression was unaffected, as confirmed by western blot. Out of four mutations in this region, three—ga16, ga17, and ga18—resulted in the knobles phenotype, while mutation ga15 did not alter knob density or shape.

3.1.3 Histidine-rich region analysis by alanine screening

When analyzing the mutants of HRR by western blot, mutants HIS1, HIS2, and HIS3, as well as a mutant of structured region ga15, presented a band of around 55 kDa in addition to the expected 100 kDa KAHRP band. The changing proportion between 100 kDa and 55 kDa KAHRP was reflected in the percentage of knobby versus knobless parasites in SEM samples. In the *Plasmodium falciparum* IT line SEM sample, 79% of cells present knobs. In the ga15 sample, only 13 % of cells present knobs. This percentage reduces to below 10% in mutants HIS1 (8%), HIS2 (3%), and HIS3(5%). Knob shape and density represented that of the parental IT line (Figure 8).

Due to abnormal KAHRP size and percentage of the knobby cells in HIS1, HIS2, and HIS3 mutants, I separated knobby iRBCs from not knobby late-stage iRBCs and compared two groups by western blot (Figure 10A). To enrich knobby parasites, I performed a gelatine flotation assay of mature stage parasite culture (“knobs+” group). The remaining cells were subjected to MACS purification to select the late-stage parasite iRBCs (“knobs-“ group). WT parasites were subjected to the same procedure (PfIT).

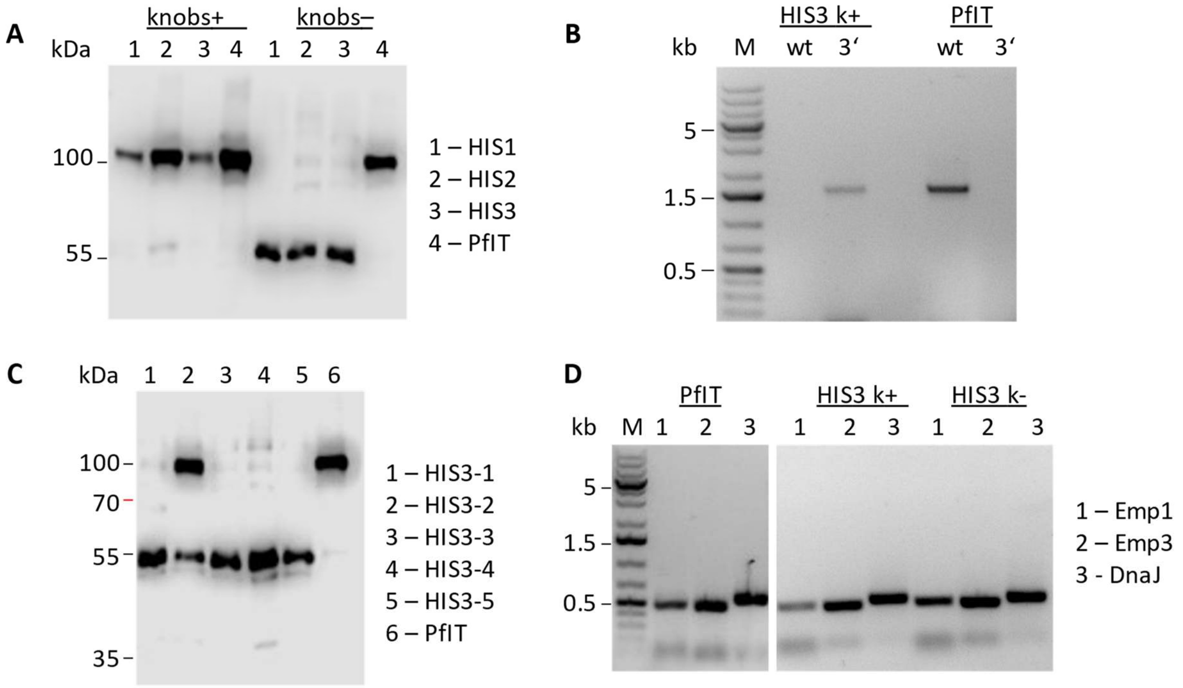

Figure 10. Analysis of populations observed in histidine rich region mutants.
(A) Western blot analysis: Protein samples obtained from parasites selected by gelatin flotation (knobs+) and MACS purification of parasites of cells excluded by gelatin flotation (knobs-). Anti-KAHRP antibody reveals bands at 100 kDa and around 55 kDa. (B) Agarose gel electrophoresis: PCR fragments of 3' integration and wild-type (WT) sequence PCR are depicted. Genomic DNA (gDNA) from the HIS3 mutant population with knobs (HIS3 k+) and *P. falciparum* IT (PfIT) were used as a template for the PCR reactions. (C) HIS3 clone reevaluation: Five HIS3 mutant clones assessed in Western blot reveal KAHRP bands of 55 kDa; in addition, HIS3 clone 2 has the expected 100 kDa KAHRP band. (D) Agarose gel with PCR amplified chromosome 2 end genes *Emp1*, *Emp3*, and *DnaJ*. gDNA extracted from *P. falciparum* IT line (PfIT), HIS3 knobby population (HIS3 k+), and knobless population (HIS3 k-) used as a template.

I analyzed the KAHRP protein using western blot and the cell surface using SEM. Knobs+ group in all mutants presented nearly exclusively the 100 kDa KAHRP band, the same as the WT IT line. The knobles group mutants presented almost exclusively 55 kDa band, except for the parental IT line, where KAHRP still runs at 100 kDa (Figure 10A). SEM confirmed the knob status of selected populations (Figure 11). The difference in knob density between knob positive and negative groups was significant with $p<0.0001$ in all mutants, but not in WT (Figure 12A). HIS1, HIS2, and HIS3 mutants confirmed the knobby versus knobless population split. At the same time, WT parasite iRBCs were knobby in both groups, supporting the expectation that purified late-stage iRBCs would have knobs.

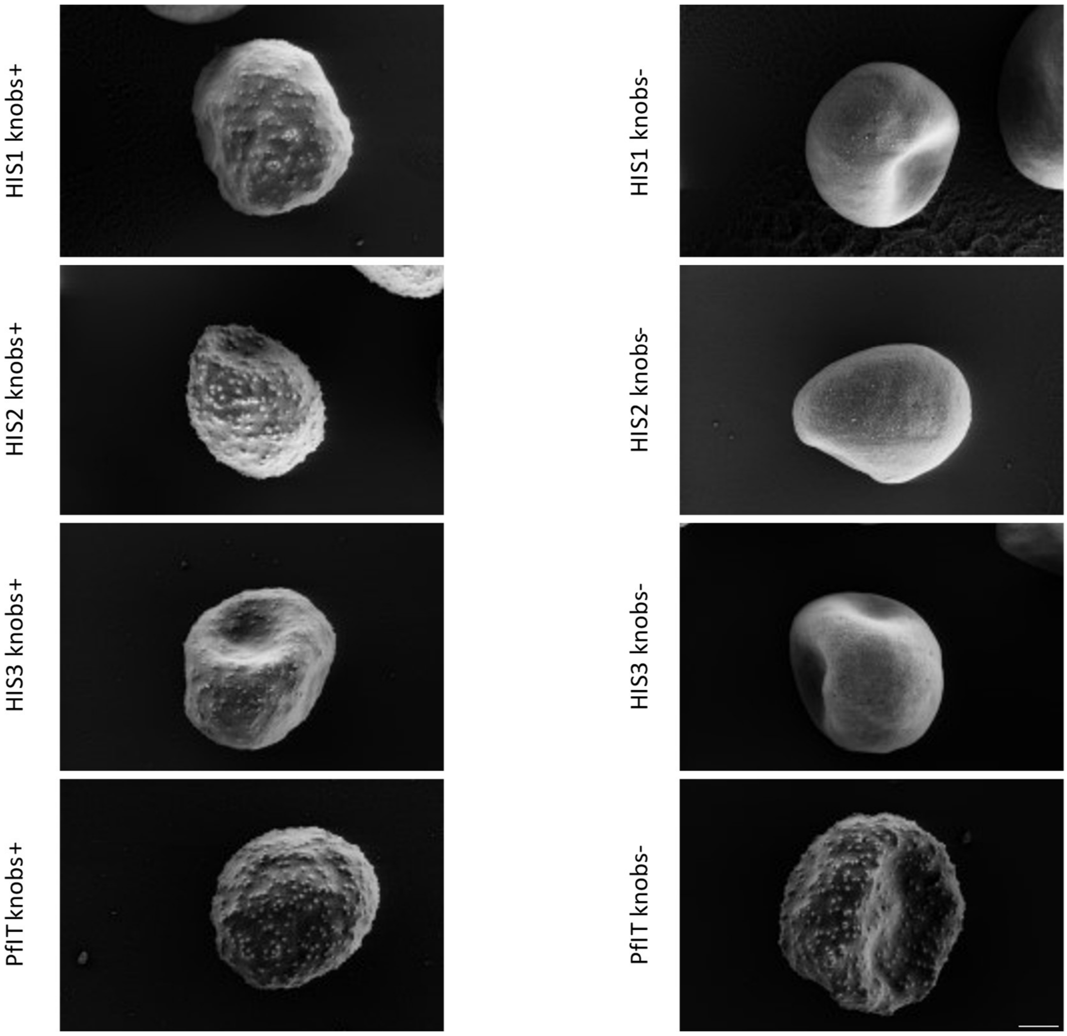

Figure 11. SEM imaging of populations in HIS mutation cultures.
SEM pictures of knob enriched (knobs+) versus late stage purified iRBC population (knob-) in HRR alanine screening mutants and P. falciparum IT line. Scale bar represents 1 µm.

We hypothesized that HIS mutant lines may have two populations due to parasite genome instability or unexpected plasmid integration. I extracted genomic DNA from the two populations of HIS3 mutant to confirm that the knobby parasites have mutant KAHRP sequence integrated and no WT KAHRP sequence in the integration site by performing 3' integration PCR and WT PCR with the gDNA extracted from each population (Figure 10B). Knobby parasites had a mutant sequence and no WT sequence. The knobby and the knobless population also had three tested chromosome 2 end genes, indicating chromosome 2 end stability (Figure 10D).

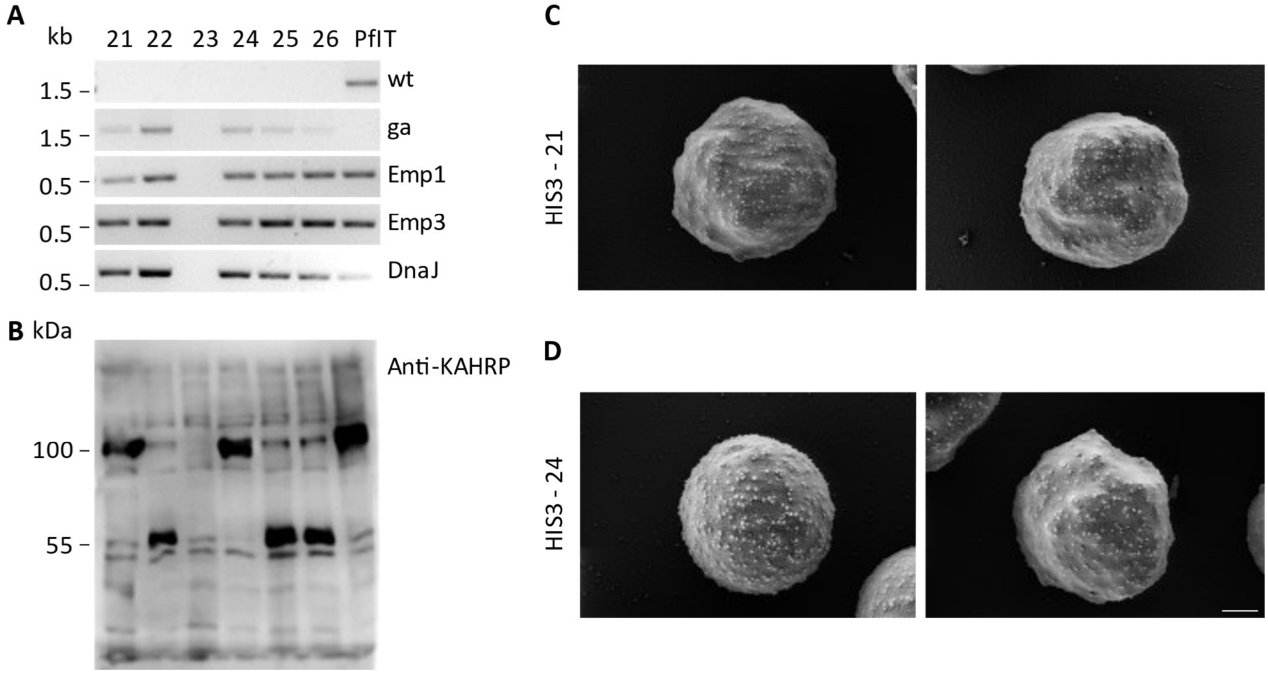

Figure 13. HIS3 mutant new clone selection.
(A) Genotyping of six HIS3 clones selected from HIS3-2 line (21-26). PCR fragments are depicted in agarose gel, gDNA of each clone and *P. falciparum* IT line (PfIT) was used as PCR template. (B) Western blot with anti-KAHRP antibody reveals KAHRP bands representing differing masses in six clones selected from HIS3-2 line. (C and D) SEM pictures of HIS3-21 and HIS3-24 clones. Scale bar is 1 µM.

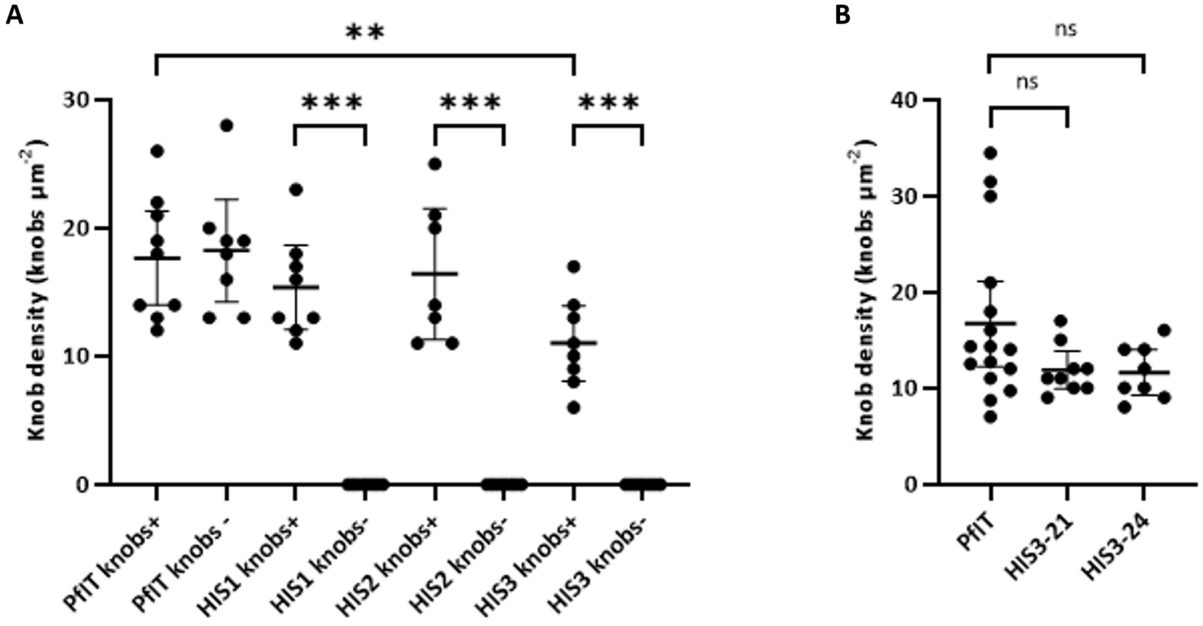

Figure 12. Knob density in populations of HIS mutants.
(A) Knobby late-stage parasites were selected from the mixed population by gelatin flotation (knobs+), and the remaining cells were used for the enrichment of late-stage iRBCs using magnetic purification (knobs-). The iRBCs were imaged using SEM and knob density was counted in *P. falciparum* IT knobs+ group (n=9) and knobs- group (n=8), HIS1 knobs+ group (n=8) and knobs- group (n=8), HIS2 knobs+ group (n=7) and knobs- group (n=8), and HIS3 knobs+ group (n=8) and knobs- group (n=8). (B) The knob density was counted in *P. falciparum* IT line (n=16) and mutant HIS3 clones 21 (n=9) and 24 (n=8). “**” indicate 0.0001 < p < 0.01, “***” indicate p < 0.0001, ns non-significant.

I further compared all previously selected HIS3 clones in western blot. Only the clone HIS3-2, which was used for all experiments representing HIS3 mutant, had the KAHRP band running at 100 kDa in addition to the 55 kDa band (Figure 10C). This clone was further subjected to repeated clonal dilution. Among six new clones, two were selected with a KAHRP band present only at 100 kDa; three clones had only a 55 kDa band, and one clone had no KAHRP expression and no chromosome 2 end genes, meaning that chromosome 2 end was missing in this clone (Figure 13A and B). Clones 21 and 24 were further sequenced, and the correct integration of HIS3 mutation was confirmed. SEM revealed that knob phenotype is similar to that of WT iRBCs in clones 21 and 24 (Figure 13. C and D). Knob density in HIS3 clone 21 and 24 iRBCs does not significantly differ from the knob density in WT iRBCs (Figure 12B).

Upon mutation of HRR of KAHRP, it was confirmed by sequencing that the WT KAHRP gene was disrupted and repaired with the template introducing the wanted mutation. The monoclonal lines, however, proved to be unstable, although the chromosome 2 end retained the genes between KAHRP and the telomere. A 55 kDa band recognized by the anti-KAHRP antibody appeared in mutant parasites, potentially indicating a secondary rescue template integration site. The mutants HIS1, HIS2, and HIS3 that expressed 100 kDa KAHRP band displayed phenotypically unaltered knobs and retained normal knob density compared to the WT iRBCs.

3.1.4 Histidine-rich region function

To identify potential HRR functions, I performed a literature review identifying the functions of other histidine-rich proteins. Human histidine-rich glycoprotein (HRG) exhibits antibacterial and antifungal effects by binding and destabilizing the membranes in the presence of 50 µM Zn2+ or at low pH (Poon et al., 2011). This leads to bacteria and fungi releasing cytoplasmic contents. HRR was crucial for this function, as HRG with the HRR domain absent did not exhibit this activity (Rydengård et al., 2008, 2007). Since Zn2+ concentration in RBCs is between 152.9 and 229.3 µM (Sayama et al., 1998), I hypothesized that the HRR region of KAHRP could interact with Zn2+ ions and the RBC membrane.

To test HRR-lipid interaction, I produced an HRR peptide. The HRR sequence with the additional 5 amino acids flanking the N-terminus and 4 amino acids – C-terminus – was fused to a linker connecting HRR to Strep-tag II for peptide purification purposes (Figure 14A). I confirmed peptide expression by a western blot. The peptide was expressed already before the induction; however, the band was gone after the overnight induction, suggesting that the peptide is degrading upon a longer induction period (Figure 14B).

The induction culture was upscaled to 400 ml volume, and after a 4-hour induction period, the harvested cells were lysed, and the precleared lysate was used for peptide purification using the Strep-Tactin®XT

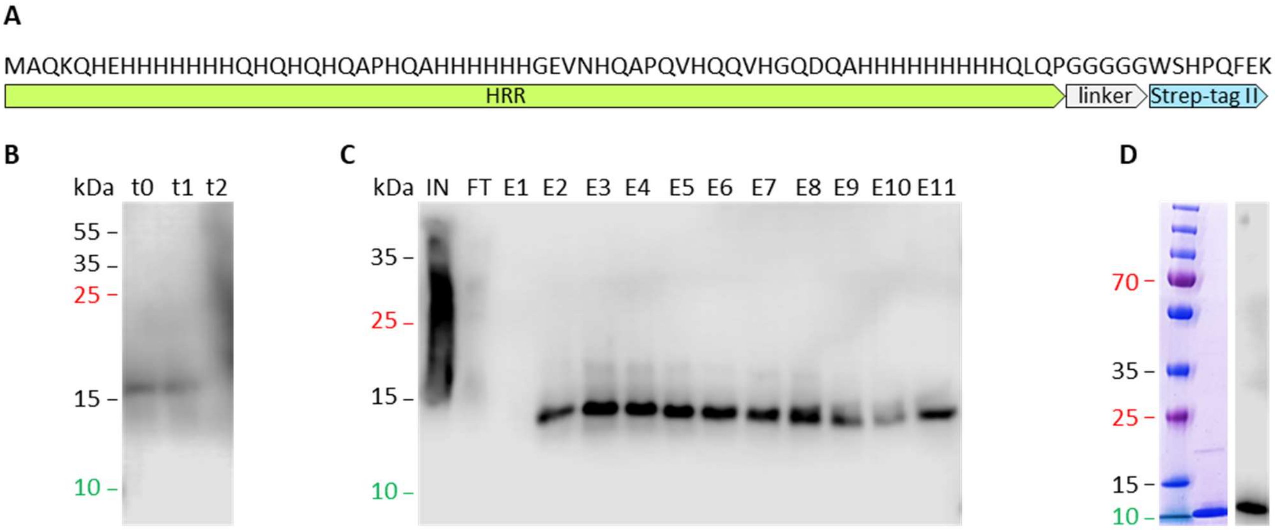

Figure 14 . Histidine-rich region expression.
(A) Peptide design, HRR is expressed in fusion with Strep-tag II. (B) Western blot shows protein expression before induction (t0), 4h after IPTG induction (t1), and 18h post-induction (t2). (C) Western blot of the fractions collected in the peptide purification steps using Strep-Tactin®XT 4Flow® column, IN – input sample, FT – flow-through fraction, E1-11 – elution fractions. (D) SDS-PAGE and Western blot of concentrated HRR sample from elution fractions.

4Flow® column. Histidine signal was observed in the input sample but not in the flow-through fraction, indicating that the column was not over-saturated. Elution fractions 2-11 presented HRR signal and were collected for protein concentration (Figure 14C). I concentrated the HRR peptide to 2.5 mg/ml and tested 10 µg by SDS-PAGE and western blot to confirm protein purity (Figure 14D).

Knob formation in *Plasmodium falciparum* starts as early as 16 hours post-infection (hpi). Before that, at 6-8 hpi Maurer's clefts are fully formed, and transportation channels between the parasite and iRBC membrane are established. In the process of iRBC remodeling, iRBC membrane lipid content is changed by the parasite, as evidenced in the comparison between the microvesicles produced by iRBC compared to the RBC membrane (Gulati et al., 2015). To identify HRR-lipid interaction, I performed a lipid-protein interaction assay using Membrane lipid strips, which represent 9 out of 27 detected lipids and approximately 70 % of the total microvesicle membrane lipid content determined in Gulati et al., (2015).

To determine potential interactions, I performed the assay in PBS buffer (Figure 15A) and PBS supplemented by 200 µM Zn^{2+} (Figure 15B). No interaction between HRR and lipids was detected under either condition. The positive control of spotted 0.5 µg HRR disappeared from the strip incubated with 200 µM Zn^{2+}, indicating HRR interaction with Zn^{2+} ions in the buffer. This, however, did not result in HRR interaction with presented lipids.

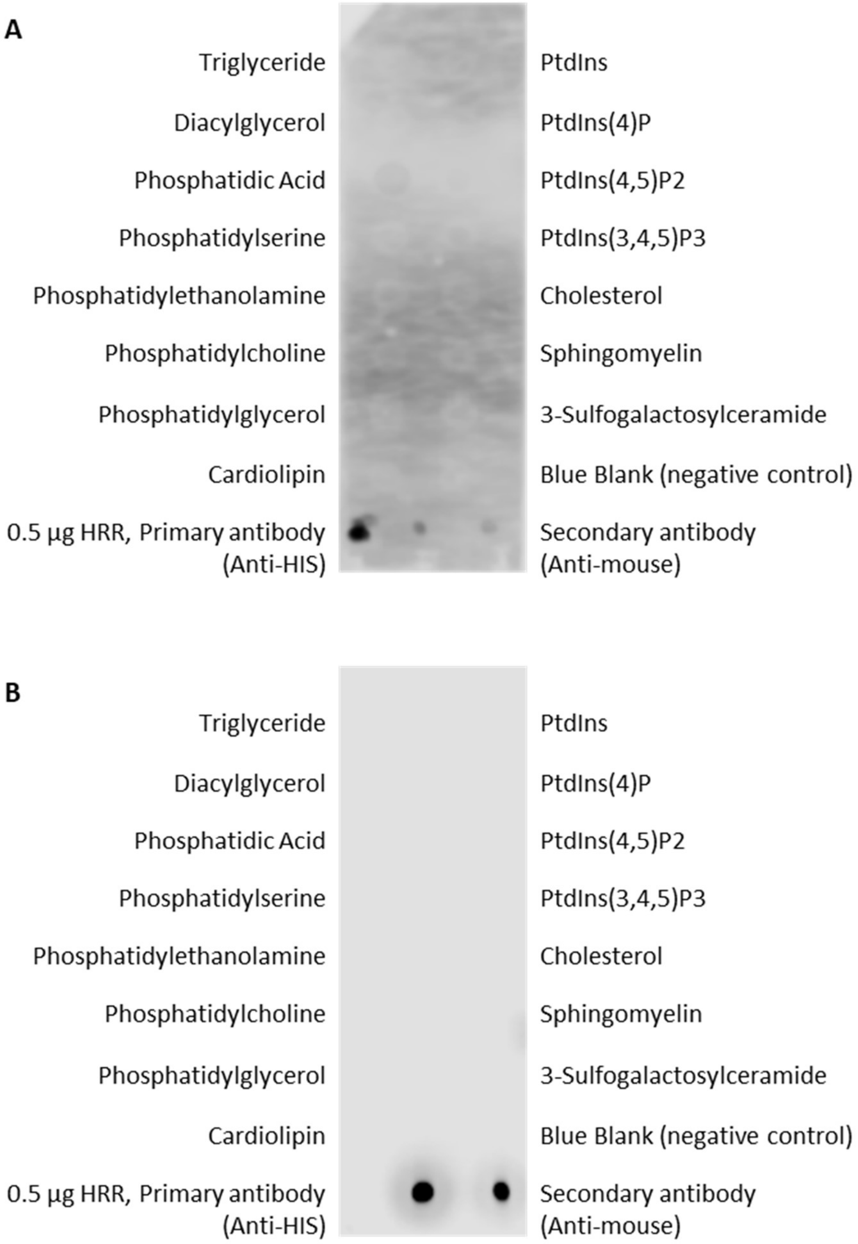

Figure 15. Histidine-rich region interaction with lipids.
(A) HRR interaction with membrane lipids on Eschelon membrane lipid strips in PBS buffer compared to (B) HRR-lipid interaction in buffer supplemented by 200 µM Zn^{2+}.

3.2 Identifying PEXEL interaction partners in the protein export pathway

3.2.1 Arrest phenotype mutants express functional stevor-miniTurbo

Mutations introduced in the PEXEL motif of stevor protein may result in protein export arrest (Deil, 2014). We selected two arrest phenotypes conferred by mutations L50W and A51E – amino acids before and after the PEXEL cleavage site. The fusion protein consisting of the first 80 amino acids of Stevor protein carrying mutated PEXEL motif fused to GFP – stevor1-80^{50W}-GFP – was described to have export arrest at the ER, where the main GFP signal was observed. In addition, the PEXEL element is not cleaved, and the protein remains at its full size of 42.4 kDa. Stevor1-80^{51E}-GFP signal was observed in PV, and the PEXEL motif was cleaved, but the new N-terminus was not acetylated, leading to a protein size of 38.9 kDa. This is compared to stevor1-80-GFP with the WT PEXEL motif, which is exported to RBC, the PEXEL element is cleaved and acetylated. We aimed to identify PEXEL motif processing proteins by identifying stevor1-80 (WT PEXEL motif) interaction partners and missing interactions in arrest phenotypes. To this end, I used biotin ligase miniTurbo to label proteins in close proximity to baits (stevor1-80, stevor1-80^{50W}, and stevor1-80^{51E}) being exported and identified the interaction partners using mass spectrometry.

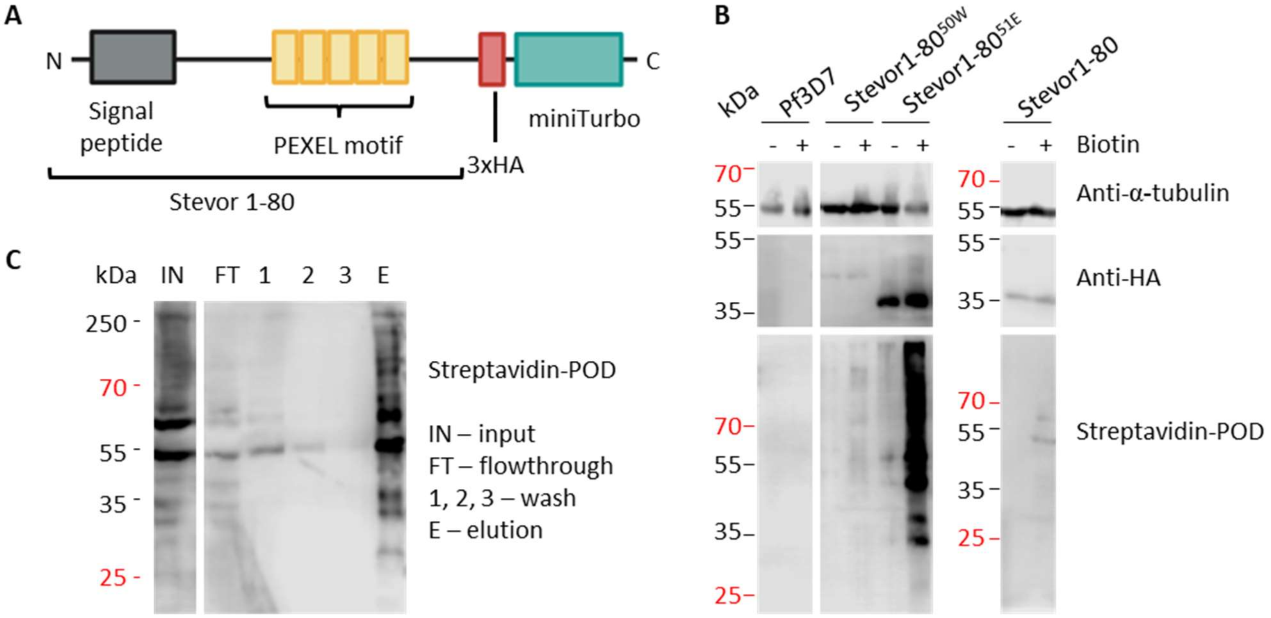

Figure 16 . Stevor-miniTurbo Construct Design and Mutant Analysis.
(A) MiniTurbo biotin ligase was cloned to replace GFP in the Stevor mutant constructs Stevor1-80^{50W}, Stevor1-80^{51E}, and wild-type Stevor1-80 previously utilized in Sophia Deil's work (2014). (B) Western blot analysis of mutants expressing Stevor1-80^{50W}, Stevor1-80^{51E}, and Stevor1-80 compared to the parental *P. falciparum* 3D7 line (3D7). Anti-α-tubulin antibody served as a loading control, anti-HA was used to visualize miniTurbo fusion proteins, and streptavidin-POD was used to visualize biotinylated proteins. "Biotin +" or "–" indicates biotin supplementation in the culture. (C) Biotinylated protein enrichment from Stevor1-80^{50W} parasite lysate using magnetic streptavidin beads. "IN" represents parasite lysate input, "FT" indicates flow-through, "1, 2, and 3" denote wash fractions, and "E" stands for the elution fraction.

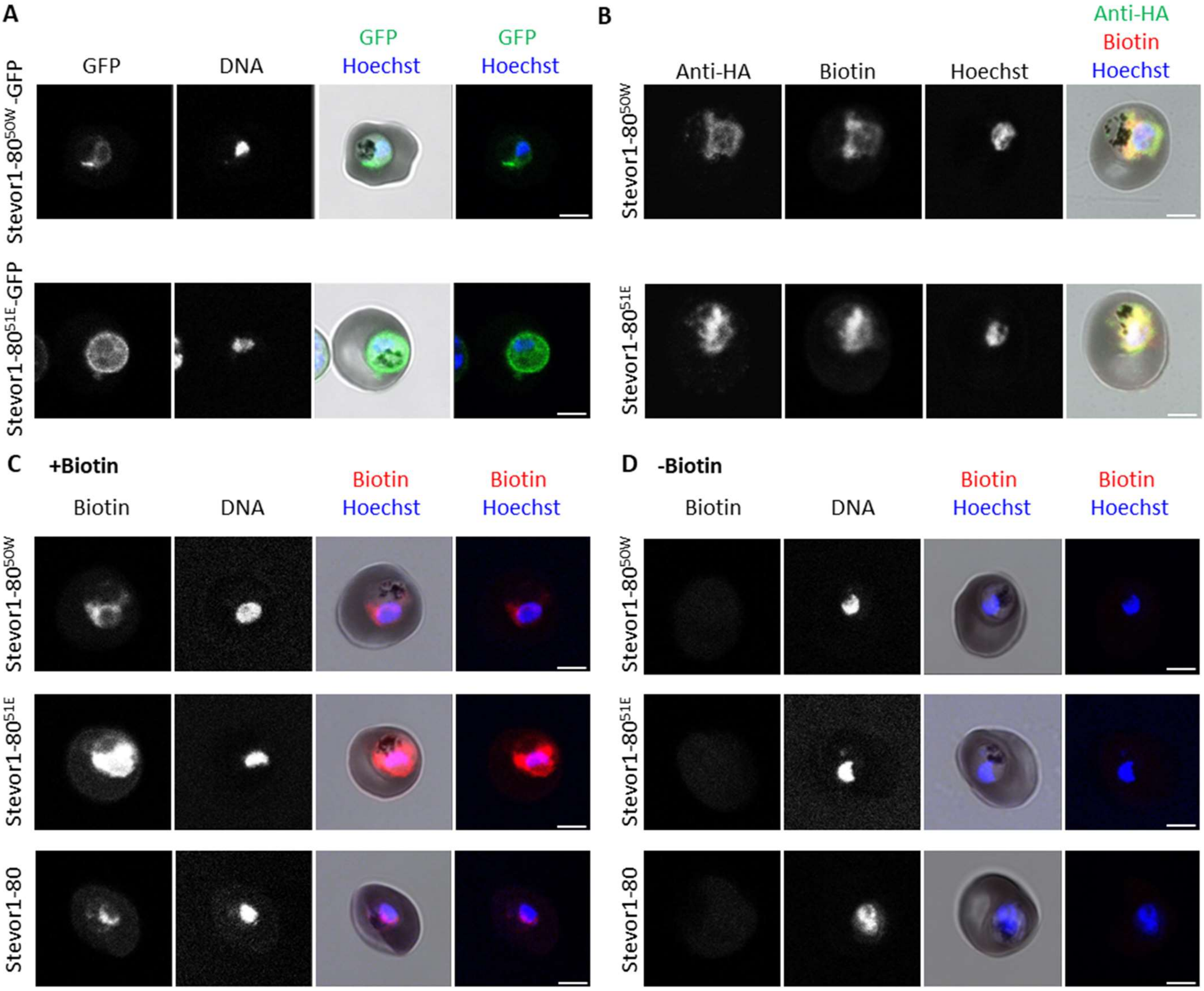

Figure 17 . Fluorescent imaging of transfected parasites.
(A) Export pattern of Stevor1-80^{50W} and Stevor1-80^{51E} GFP fusion proteins, (B) Immuno-fluorescence assay (IFA) images visualizing miniTurbo fusion protein (Anti-HA) and biotinylation pattern (Biotin). (C) IFA images of iRBCs when culture is supplemented with biotin compared to (D) IFA images of biotinylation patterns without biotin supplementation. Scale bar = 3 µm.

To introduce miniTurbo in the already existing stevor mutant plasmids, I amplified HA-tagged miniTurbo using P 33 and P 34 primer pair. I restricted the inserts and the pARL1 vectors containing stevor1-80, stevor1-80^{50W}, and stevor1-80^{51E} previously described by S. Deil (2014) with BssHII and XmaI to remove the GFP and ligated the amplified HA-tagged miniTurbo insert using T4 ligase (Figure 16A). To confirm correct insertion, plasmids were sequenced with primers P 35 and P 36 complementary to the upstream (forward) or downstream (reverse) sequence around MCS. I then transfected the *Plasmodium falciparum* 3D7 parasite line with the created plasmids, and stevor fusion proteins were expressed from episomal plasmids.

To confirm protein expression, I extracted proteins from transfected parasite iRBCs and the parental *Plasmodium falciparum* 3D7 line iRBCs. A western blot performed with the anti-HA antibody shows stevor1-80^{50W} fusion protein with a PEXEL motif that is unprocessed at 42.4 kDa, and stevor1-80^{51E} and stevor1-80 with PEXEL element cleaved at 38.9 kDa as expected (Figure 16B). Streptavidin-POD visualizes a biotinylation increase in mutant cultures supplemented by 50 µM biotin compared to unsupplemented complete RPMI media. The biotinylation pattern in WT 3D7 culture does not increase. Anti-α-tubulin antibody is used as a loading control. Biotinylated proteins were further enriched by streptavidin magnetic beads (Figure 16C). The elution fractions of three biological replicates of each mutant were submitted to mass spectrometry analysis.

The GFP fusion proteins present a clear export arrest phenotype, with stevor1-80^{50W} localizing to ER and stevor1-80^{51E} localizing to PV (Figure 17A). I performed an immunofluorescence assay to identify the export phenotype of miniTurbo fusion proteins to compare the fusion protein's anti-HA signal to the biotinylation pattern in iRBCs (Figure 17B). The HA and biotinylation patterns were similar and mostly colocalizing. Next, I compared biotinylation in cultures with complete RPMI media and biotin-supplemented complete media (Figures 10C and D). No signal was visible in the absence of supplementary biotin. Mutant stevor1-80^{50W} displays biotinylation in ER similar to the same arrest phenotype of GFP fusion protein. Mutant stevor1-80^{51E} presents a biotinylation signal in PV and a weak signal in RBC in addition to ER. This deviates from GFP fusion protein localization, with most of the signal being in the PV. Similarly, in stevor1-80 iRBCs, the biotinylation signal is observed in ER and RBC, while the GFP fusion protein was observed mostly in the RBC compartment (Deil, 2014)We concluded that the biotinylation process starts at the beginning of the protein export pathway, leading to the signal being in the ER. We also concluded that biotinylated proteins may spread beyond the compartment where the miniTurbo fusion protein resides.

To identify PEXEL interacting partners, the biotinylated proteins were identified by mass spectrometry performed by Sabine Merker at the core facility for mass spectrometry and proteomics (CFMP, Heidelberg), and I analyzed the output data. Five groups, three biological replicates each, were compared: stevor1-80^{50W}, stevor1-80^{51E,} and stevor1-80 incubated with supplementary 50 µM biotin, and parental *Plasmodium falciparum* 3D7 line incubated with or without supplementary biotin ("Pf3D7 +Biotin" and "Pf3D7 -Biotin"). After sample normalization, I performed the analysis of variance (ANOVA) significance test comparing five groups, obtaining 220 significant proteins out of 243 identified hits. ANOVA significant proteins were used for principal component analysis. The groups are well separated, and biological replicates of the same group are highly similar, suggesting high reproducibility of samples in each group (Figure 18A). Among the ANOVA significant proteins, I identified several proteins known to play a role in protein export, including exported protein 3 (Exp3), translocon component PTEX88, and PMV (Figure 18B).

I further compared groups of interest stevor1-80^{50W} and stevor1-80^{51E} to a group with WT PEXEL motif stevor1-80 using a t-test to identify significant proteins. Significant hits are visualized with a false discovery rate of 0.05 (Figure 19A and B). Multiple known export mediating proteins, including HSP101, PMV, and Exp3, were identified among the significant hits. Volcano plots did not present any specific cluster of export-mediating proteins.

To select proteins of interest, I analyzed 190 significant proteins in comparing group stevor1-80^{50W} and stevor1-80^{51E} to group stevor1-80 (Table 1). Using gene ontology cellular component data, I excluded proteins that have known localization other than ER, Golgi complex (GC), or PV. I further researched the proteins that localize to ER, GC, PV, or with their localization unknown to exclude all proteins described in connection to protein export.

We selected eight mass spectrometry hits (MSHs) of interest and two control proteins (HSP101 and PMV) that were significant in the analysis. As an additional control for further experiments, I used PTEX150, a part of the translocon complex; however, it remained insignificant among hits in this experiment.

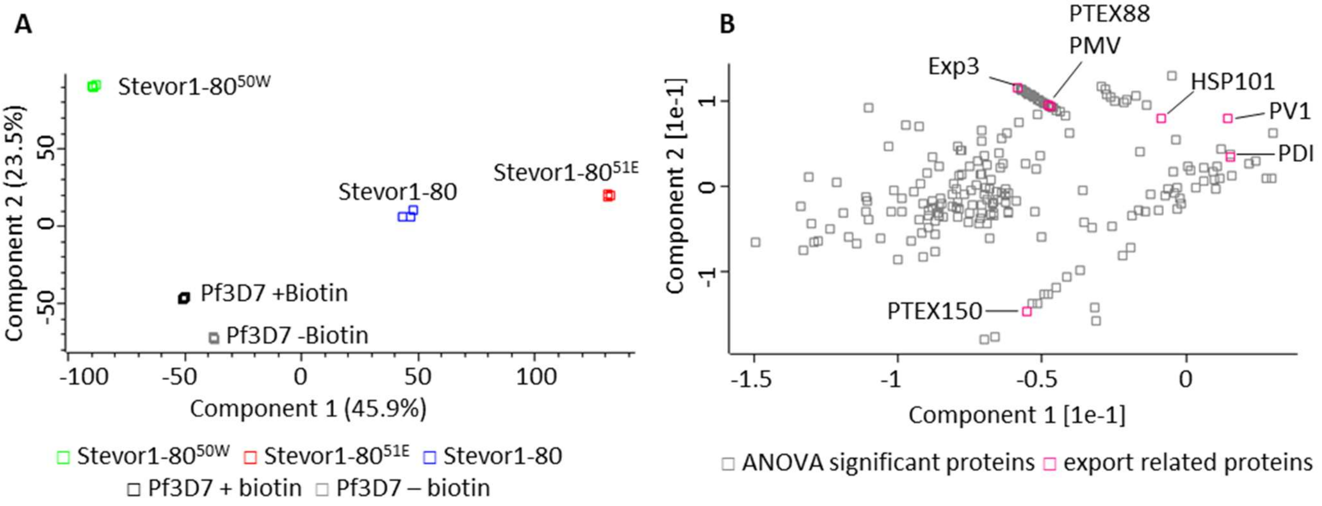

Figure 18 . Principal component analysis (PCA) of mass spectrometry groups.
(A) Group distribution according to calculated Components 1 and 2, squares represent biological replicates. (B) ANOVA significant protein distribution according to calculated Components 1 and 2. Pink squares indicate *P. falciparum* export-related proteins. "Exp3" Exported protein 3, "PTEX88" Translocon component PTEX88, "PMV" Plasmepsin V, "PDI" Protein disulfide-isomerase, "PV1" Parasitophorous vacuolar protein 1, "PTEX150" Translocon component PTEX150, "HSP101" Heat shock protein 101.

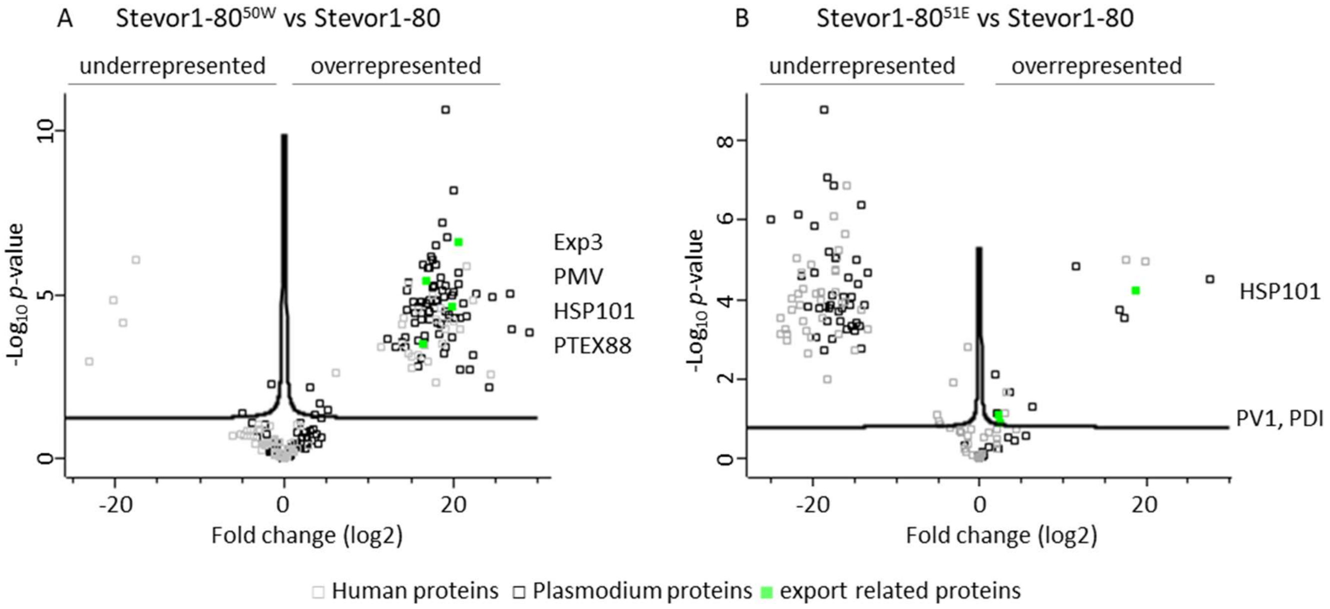

Figure 19 . Comparison of mutant export arrest groups to WT stevor group.
(A) Stevor1-80^{50W} group comparison to Stevor1-80 group. (B) Stevor1-80^{51E} group comparison to Stevor1-80. Proteins above solid lines are high-confidence significant interactors (FDR=0.01), proteins above dashed lines are low-confidence significant interactors (FDR=0.05). Exp3 – Exported protein 3, PTEX88 – Translocon component PTEX88, PMV – Plasmepsin V, PDI – Protein disulfide-isomerase, PV1 – Parasitophorous vacuolar protein 1, HSP101 – Heat shock protein 101.

Table 1. Mass spectrometry hits.

Mass spectrometry hits that are significantly upregulated or downregulated in groups stevor1-80^{50W} and stevor1-80^{51E} compared to group stevor1-80 and candidates selected for interaction confirmation.

PlasmoDB or Uniprot ID	**Stevor1-80^{50W}**			**Stevor1-80^{51E}**			**Selected candidate number**
	Fold change Log2	**p-value**	**Significance group with ++FDR<0.01 +FDR<0.05**	**Fold change Log2**	**p-value**	**Significance group with ++FDR<0.01 +FDR<0.05**	
PF3D7_0102800	19.07	3.32E-05	++	0.00	1.00E+00		
PF3D7_0102900	0.61	5.76E-01		-18.29	8.41E-08	++	
PF3D7_0103900	1.45	3.84E-01		-17.86	1.36E-04	++	
PF3D7_0106300	15.38	7.38E-05	++	0.00	1.00E+00		
PF3D7_0107500	20.73	4.95E-05	++	0.00	1.00E+00		
PF3D7_0108300	-0.94	5.36E-01		-14.53	4.27E-05	++	
PF3D7_0202400	-0.05	9.76E-01		-19.26	1.61E-04	++	
PF3D7_0207500	18.44	3.07E-06	++	0.00	1.00E+00		
PF3D7_0207600	-1.69	4.24E-01		-16.40	8.47E-05	++	
PF3D7_0209800	17.15	1.46E-05	++	0.00	1.00E+00		
PF3D7_0220000	17.51	8.94E-07	++	0.00	1.00E+00		1
PF3D7_0301600	16.59	2.88E-04	++	0.00	1.00E+00		
PF3D7_0302500	16.88	1.75E-05	++	0.00	1.00E+00		
PF3D7_0310400	4.47	2.25E-01		-18.13	1.72E-04	++	
PF3D7_0311600	2.05	2.31E-01		-15.78	2.85E-05	++	
PF3D7_0316400	19.18	3.81E-04	++	0.00	1.00E+00		
PF3D7_0317600	1.83	7.96E-02		-17.50	1.36E-07	++	
PF3D7_0318300	14.47	7.62E-06	++	0.00	1.00E+00		
PF3D7_0401800	24.57	1.21E-05	++	0.00	1.00E+00		
PF3D7_0412400	-3.78	7.88E-02		-20.63	1.51E-04	++	
PF3D7_0422100	5.17	3.23E-02	+	-18.52	1.58E-04	++	2
PF3D7_0501200	18.05	1.44E-05	++	0.00	1.00E+00		
PF3D7_0505700	4.40	5.61E-02	+	-13.40	2.14E-05	++	
PF3D7_0507100	-0.76	7.74E-01		-17.71	9.84E-04	++	
PF3D7_0510100	15.84	2.24E-05	++	0.00	1.00E+00		
PF3D7_0520800	3.82	1.78E-01		-14.50	4.82E-04	++	
PF3D7_0526700	2.52	1.52E-01		-15.45	8.46E-05	++	
PF3D7_0532300	2.74	3.91E-01		-21.78	7.67E-07	++	
PF3D7_0608800	-1.25	4.30E-01		-17.72	7.57E-05	++	
PF3D7_0624000	19.55	5.32E-05	++	0.00	1.00E+00		

PlasmoDB or Uniprot ID	**Stevor1-80^{50W}**			**Stevor1-80^{51E}**			**Selected candidate number**
	Fold change Log2	**p-value**	**Significance group with ++FDR<0.01 +FDR<0.05**	**Fold change Log2**	**p-value**	**Significance group with ++FDR<0.01 +FDR<0.05**	
PF3D7_0628200	24.27	6.86E-03	++	0.00	1.00E+00		
PF3D7_0629200	20.24	4.91E-05	++	0.00	1.00E+00		
PF3D7_0702500	14.74	4.25E-06	++	0.00	1.00E+00		
PF3D7_0703500	14.01	2.72E-04	++	17.28	2.89E-04	++	
PF3D7_0706000	17.74	2.48E-05	++	0.00	1.00E+00		
PF3D7_0707800	16.38	1.22E-06	++	0.00	1.00E+00		
PF3D7_0709100	19.89	1.88E-04	++	0.00	1.00E+00		
PF3D7_0711000	17.09	1.50E-06	++	0.00	1.00E+00		
PF3D7_0716300	2.27	1.56E-01		-14.84	1.02E-05	++	
PF3D7_0719400	17.82	5.13E-06	++	0.00	1.00E+00		
PF3D7_0721600	-0.16	9.43E-01		-14.13	1.73E-03	++	
PF3D7_0727800	1.90	4.94E-01		-18.62	1.69E-09	++	
PF3D7_0731100	22.81	9.36E-06	++	0.00	1.00E+00		
PF3D7_0731600	19.85	1.03E-05	++	0.00	1.00E+00		
PF3D7_0801000	2.75	2.22E-01		-21.40	2.47E-05	++	
PF3D7_0802000	16.84	1.87E-05	++	0.00	1.00E+00		
PF3D7_0810600	-4.87	3.99E-02	+	-19.88	1.42E-06	++	
PF3D7_0811200	2.71	3.33E-01		-15.93	5.69E-04	++	
PF3D7_0816600	20.06	6.11E-09	++	0.00	1.00E+00		
PF3D7_0818900	-1.89	5.19E-01		-25.15	1.01E-06	++	
PF3D7_0820500	17.43	7.07E-07	++	0.00	1.00E+00		
PF3D7_0823800	18.85	7.07E-05	++	0.00	1.00E+00		
PF3D7_0827900	1.19	4.12E-01		2.46	1.23E-01	+	
PF3D7_0902800	15.89	2.52E-04	++	0.00	1.00E+00		
PF3D7_0903700	13.26	3.81E-04	++	11.50	1.46E-05	++	
PF3D7_0905400	-2.04	1.86E-01		-13.85	1.37E-04	++	
PF3D7_0910100	16.68	1.84E-04	++	0.00	1.00E+00		
PF3D7_0915400	20.80	1.86E-03	++	0.00	1.00E+00		
PF3D7_0917900	29.08	1.40E-04	++	27.71	3.14E-05	++	
PF3D7_0919100	19.35	1.72E-07	++	0.00	1.00E+00		
PF3D7_0922200	16.20	3.62E-05	++	0.00	1.00E+00		
PF3D7_0935900	20.58	4.68E-06	++	0.00	1.00E+00		
PF3D7_1001400	1.92	4.80E-01		-15.09	6.39E-04	++	
PF3D7_1008700	17.22	5.91E-05	++	0.00	1.00E+00		

PlasmoDB or Uniprot ID	Stevor1-80^{50W}			Stevor1-80^{51E}			Selected candidate number
	Fold change Log2	p-value	Significance group with ++FDR<0.01 +FDR<0.05	Fold change Log2	p-value	Significance group with ++FDR<0.01 +FDR<0.05	
PF3D7_1013300	18.64	3.21E-04	++	0.00	1.00E+00		3
PF3D7_1015900	26.92	1.09E-04	++	0.00	1.00E+00		
PF3D7_1016300	3.27	2.67E-01		6.26	4.80E-02	+	
PF3D7_1016400	21.96	1.93E-03	++	0.00	1.00E+00		
PF3D7_1018300	18.49	8.02E-05	++	0.00	1.00E+00		
PF3D7_1024800	20.58	2.51E-07	++	0.00	1.00E+00		
PF3D7_1025300	17.92	3.02E-07	++	0.00	1.00E+00		
PF3D7_1027800	15.29	1.71E-05	++	0.00	1.00E+00		
PF3D7_1036900	-0.49	7.70E-01		-16.46	1.60E-04	++	
PF3D7_1037100	21.17	1.76E-05	++	0.00	1.00E+00		
PF3D7_1039000	-0.81	6.30E-01		-16.78	3.67E-04	++	
PF3D7_1102500	15.47	3.43E-05	++	16.74	1.89E-04	++	
PF3D7_1105300	16.22	5.41E-05	++	0.00	1.00E+00		4
PF3D7_1105600	16.47	3.12E-04	++	0.00	1.00E+00		
PF3D7_1108700	19.09	5.33E-06	++	0.00	1.00E+00		
PF3D7_1116400	17.96	1.68E-05	++	0.00	1.00E+00		5
PF3D7_1116700	21.52	4.46E-05	++	0.00	1.00E+00		
PF3D7_1116800	19.87	2.16E-05	++	18.78	6.26E-05	++	6
PF3D7_1123500	-1.54	5.16E-03	++	0.26	6.96E-01		7
PF3D7_1129100	3.08	1.35E-01		2.19	7.88E-02	+	
PF3D7_1133900	3.54	4.50E-02	+	3.69	2.19E-02	++	
PF3D7_1137300	14.37	1.95E-04	++	0.00	1.00E+00		
PF3D7_1201000	3.16	2.70E-01		-16.91	1.96E-04	++	8
PF3D7_1215900	16.32	1.67E-05	++	0.00	1.00E+00		
PF3D7_1222300	3.05	6.38E-03	++	1.77	7.33E-03	++	
PF3D7_1232100	20.00	8.25E-06	++	0.00	1.00E+00		
PF3D7_1239700	18.81	1.22E-05	++	0.00	1.00E+00		
PF3D7_1240600	14.39	3.68E-04	++	0.00	1.00E+00		
PF3D7_1311800	-3.21	2.26E-01		-19.69	9.28E-04	++	
PF3D7_1311900	18.98	5.87E-04	++	0.00	1.00E+00		
PF3D7_1320000	18.67	6.13E-08	++	0.00	1.00E+00		
PF3D7_1323500	16.77	3.80E-06	++	0.00	1.00E+00		9
PF3D7_1324900	12.20	2.23E-04	++	0.00	1.00E+00		
PF3D7_1337200	15.93	1.56E-03	++	0.00	1.00E+00		

PlasmoDB or Uniprot ID	**Stevor1-80^{50W}**			**Stevor1-80^{51E}**			**Selected candidate number**
	Fold change Log2	**p-value**	**Significance group with ++FDR<0.01 +FDR<0.05**	**Fold change Log2**	**p-value**	**Significance group with ++FDR<0.01 +FDR<0.05**	
PF3D7_1344200	20.63	2.07E-06	++	0.00	1.00E+00		
PF3D7_1350500	18.08	6.88E-05	++	0.00	1.00E+00		10
PF3D7_1357000	0.77	4.41E-01		2.08	7.10E-02	+	
PF3D7_1360800	3.36	1.29E-01		-14.23	4.27E-07	++	
PF3D7_1365900	17.96	1.15E-06	++	0.00	1.00E+00		
PF3D7_1404900	1.49	3.14E-01		-17.30	9.39E-06	++	
PF3D7_1406600	17.17	3.36E-05	++	0.00	1.00E+00		
PF3D7_1407800	17.53	5.64E-06	++	0.00	1.00E+00		
PF3D7_1407900	1.62	4.31E-01		-15.46	4.75E-04	++	
PF3D7_1420700	26.78	9.67E-06	++	0.00	1.00E+00		
PF3D7_1423700	1.57	3.66E-01		-14.74	3.83E-04	++	
PF3D7_1432800	19.52	4.20E-05	++	0.00	1.00E+00		
PF3D7_1439300	18.63	7.35E-06	++	0.00	1.00E+00		
PF3D7_1443900	4.18	1.97E-02	+	-15.62	1.40E-04	++	
PF3D7_1451100	18.42	1.49E-04	++	0.00	1.00E+00		
PF3D7_1451800	22.36	6.69E-04	++	0.00	1.00E+00		
PF3D7_1454400	0.60	6.06E-01		-19.76	2.05E-05	++	
PF3D7_1460300	-1.00	3.41E-01		-18.05	6.33E-06	++	
PF3D7_1462800	17.28	1.54E-06	++	0.00	1.00E+00		
PF3D7_1464600	-1.74	5.97E-01		-18.73	1.93E-03	++	
PF3D7_1465900	19.03	2.16E-11	++	0.00	1.00E+00		
PF3D7_1468700	14.43	2.77E-05	++	0.00	1.00E+00		
PF3D7_1478600	16.16	8.64E-04	++	0.00	1.00E+00		
O75342	-0.27	8.67E-01		-21.30	2.10E-05	++	
P01037	15.14	1.65E-03	++	0.00	1.00E+00		
P01040	-4.33	1.45E-01		-5.14	7.60E-02	+	
P01833	17.87	4.66E-03	++	0.00	1.00E+00		
P01834	-2.63	5.55E-01		-18.32	9.92E-03	++	
P01857	18.76	3.13E-04	++	0.00	1.00E+00		
P01876	-2.80	1.29E-01		-16.08	1.10E-04	++	
P02545	1.61	4.98E-01		-17.39	1.78E-05	++	
P02549	19.05	1.17E-04	++	0.00	1.00E+00		
P02730	0.06	9.85E-01		-21.64	1.37E-04	++	
P02788	1.08	6.07E-01		-13.54	5.42E-04	++	

PlasmoDB or Uniprot ID	Stevor1-80^{50W}			Stevor1-80^{51E}			Selected candidate number
	Fold change Log2	p-value	Significance group with ++FDR<0.01 +FDR<0.05	Fold change Log2	p-value	Significance group with ++FDR<0.01 +FDR<0.05	
P04083	-3.13	9.15E-02		-21.14	5.46E-05	++	
P05089	-0.22	9.20E-01		-22.62	1.77E-04	++	
P05109	-3.99	1.37E-01		-23.88	3.05E-04	++	
P06702	-5.23	1.79E-01		-23.37	5.45E-04	++	
P06733	14.76	6.20E-04	++	0.00	1.00E+00		
P06753	-1.16	2.58E-01		-16.18	2.19E-06	++	
P07339	-1.69	1.03E-01		-3.13	1.28E-02	++	
P07384	-0.95	6.73E-01		-17.00	7.54E-04	++	
P07900	-2.15	3.26E-01		-17.35	1.91E-05	++	
P08238	0.45	7.98E-01		-18.84	3.00E-04	++	
P09211	14.70	4.42E-06	++	0.00	1.00E+00		
P0DPH8	15.81	7.19E-04	++	0.00	1.00E+00		
P11021	0.58	5.84E-01		-17.03	5.83E-06	++	
P11142	6.12	2.34E-03	++	-1.37	4.05E-01		
P11171	0.13	8.99E-01		3.17	2.13E-02	++	
P11277	2.88	3.91E-01		-16.47	1.28E-04	++	
P11940	13.85	7.74E-05	++	0.00	1.00E+00		
P12273	-3.45	3.73E-01		-20.62	2.36E-03	++	
P14618	-1.47	3.08E-01		-19.59	7.48E-05	++	
P16157	21.51	1.28E-06	++	0.00	1.00E+00		
P16402	-19.02	6.78E-05	++	-19.02	6.78E-05	++	
P16402	-19.02	6.78E-05	++	-19.02	6.78E-05	++	
P16435	-17.57	8.24E-07	++	-17.57	8.24E-07	++	
P22531	-0.42	7.17E-01		-14.24	1.86E-04	++	
P22532	18.83	6.73E-05	++	17.53	9.97E-06	++	
P23490	-0.52	8.54E-01		-20.74	6.26E-04	++	
P25311	-0.62	3.14E-01		-1.47	1.57E-03	++	
P30613	17.63	1.03E-05	++	0.00	1.00E+00		
P31944	-4.73	1.97E-01		-23.23	7.17E-04	++	
P32119	-3.54	1.94E-01		-21.81	7.53E-05	++	
P37840	20.00	6.51E-05	++	0.00	1.00E+00		
P38646	15.93	2.84E-05	++	0.00	1.00E+00		
P42357	-1.09	7.04E-01		-20.20	9.24E-04	++	
P50990	-6.19	2.01E-01		-24.01	7.59E-04	++	

PlasmoDB or Uniprot ID	Stevor1-80^{50W}			Stevor1-80^{51E}			Selected candidate number
	Fold change Log2	p-value	Significance group with ++FDR<0.01 +FDR<0.05	Fold change Log2	p-value	Significance group with ++FDR<0.01 +FDR<0.05	
P52272	15.06	7.79E-04	++	0.00	1.00E+00		
P61626	18.56	2.59E-05	++	19.98	1.13E-05	++	
P62805	20.81	1.14E-04	++	0.00	1.00E+00		
P63104	-0.83	3.14E-01		-15.96	1.33E-07	++	
P68104	-1.13	4.02E-01		-17.33	6.62E-05	++	
Q01469	-2.31	3.91E-01		-22.47	9.55E-05	++	
Q02413	1.48	9.14E-02		2.99	6.99E-02	+	
Q06830	-20.25	1.37E-05	++	-20.25	1.37E-05	++	
Q08188	-23.15	1.07E-03	++	-23.15	1.07E-03	++	
Q16777	-1.07	6.21E-01		-4.84	1.16E-01	+	
Q16778	0.48	8.86E-01		-15.01	1.96E-03	++	
Q5T750	24.51	2.59E-03	++	0.00	1.00E+00		
Q6UWP8	14.12	4.80E-05	++	0.00	1.00E+00		
Q6ZVX7	-0.51	8.24E-01		-21.19	3.63E-04	++	
Q71U36	16.64	3.32E-04	++	0.00	1.00E+00		
Q92945	11.50	3.95E-04	++	0.00	1.00E+00		
Q96DA0	17.97	5.76E-05	++	0.00	1.00E+00		
Q96FQ6	13.86	3.16E-04	++	0.00	1.00E+00		
Q96P63	22.41	1.52E-05	++	0.00	1.00E+00		
Q96QA5	-0.90	7.19E-01		-21.99	9.30E-06	++	
Q99798	16.92	1.05E-03	++	0.00	1.00E+00		
Q9BYJ1	-1.87	3.25E-01		-19.01	1.02E-04	++	
Q9HCY8	-0.98	6.07E-01		-17.21	8.39E-06	++	

3.2.2 Confirmation of interaction using split-GFP

To confirm the interaction between the PEXEL motif and selected MSHs, I used a split-GFP approach, where stevor1-80 mutants were expressed in fusion with GFP beta sheets 1-10 (GFP1-10), while MSHs were expressed in fusion with GFP beta sheet 11 (GFP11) (Figure 20B). One of the stevor baits was expressed in the parasite simultaneously with one of the MSHs from two episomal plasmids, each providing a different resistance marker for parasite survival under the WR99210 and blasticidin drug pressure. When MSH interacts with the PEXEL element of the fusion protein, parts of GFP are brought together, allowing them to self-assemble and reproduce the GFP signal (Figure 20C).

To clone MSHs, I extracted RNA from *Plasmodium falciparum* 3D7 line, reverse-transcribed RNA using oligo (dt) primers to a single-strand DNA, and amplified genes composed of only exons using forward primers P 37 to P 47, and reverse primers P 48 to P 58 respectively. Amplified inserts were digested with XhoI and AvrII restriction enzymes and ligated into a pre-existing, digested pARL1 vector with GFP11 encoded following MCS. This way, I successfully cloned seven out of ten selected MSH genes, including the controls *HSP101*, *PMV*, and *PTEX150*. All inserts were sequenced to confirm the correct insert sequence and in-frame positioning using primers P 35 and P 36. Inserts of MSH4, 6, 8, and 12 needed additional primers to sequence the entire gene due to the large gene size (P 59 to P 62). Full plasmid sequencing was performed for plasmid containing MSH 1.

To replace miniTurbo with GFP1-10 in stevor1-80^{50W}, stevor1-80^{51E,} and stevor1-80 containing plasmids, I amplified GFP1-10 using primers P 63 and P 64, digested insert and miniTurbo plasmids

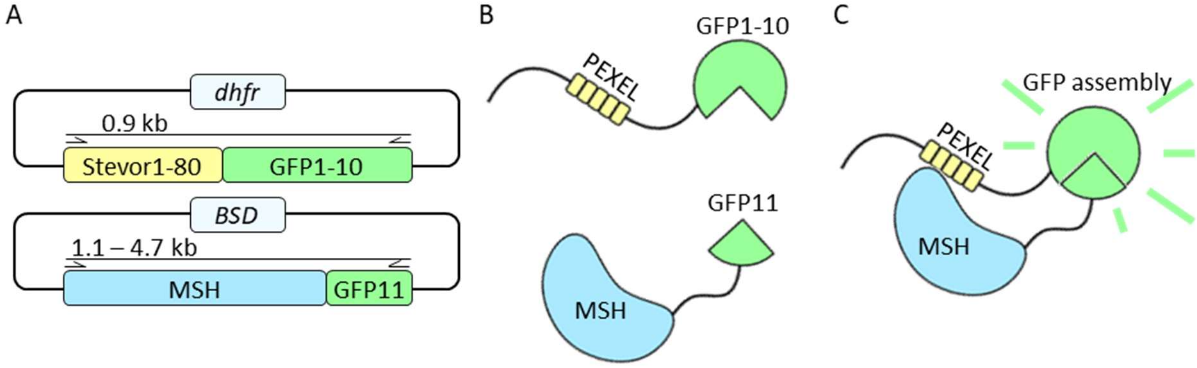

Figure 20 . Schematic representation of split GFP cloning and mode of action.
(A) Schematic representation of plasmid pair transfected. Arrows indicate primers used for genotyping purposes, insert length in MSH plasmid depends on the size of the MSH gene. (B) When mass spectrometry hit (MSH) does not interact with the PEXEL motif, GFP1-10 and GFP11 do not interact due to the distance between two GFP parts. (C) Upon interaction of the PEXEL motif with MSH, two GFP parts are in close proximity, allowing GFP self-assembly and a fluorescent signal.

Table 2. Interactions confirmed by split-GFP experiment.

Nr	PlasmoDB ID	Gene name	Localization of GFP signal			Protein localization	Connection to export pathway	Resource
			Stevor1-80^{50W}	Stevor1-80^{51E}	Stevor1-80			
1	PF3D7_0220000	Liver stage antigen 3	-	-	PV	-		
2	PF3D7_0422100	Transmembrane emp24 domain-containing protein, putative	-	-	-	Apicoplast, ER, GC		
3	PF3D7_1013300	Nicalin domain-containing protein	-	na	-	ER membrane		
5	PF3D7_1116400	Guanine nucleotide-exchange factor SEC12	na	na	ER	ER membrane		
6	PF3D7_1116800	Heat shock protein 101	na	PV	PV	PV	translocon component	Beck et al., 2014; Ho et al., 2018
8	PF3D7_1201000	*Plasmodium* exported protein (PHISTb)	na	na	PV, RBC	PV, RBC		
9	PF3D7_1323500	Plasmepsin V	na	na	na	ER	Recognizes and cleaves PEXEL motif in ER	Matthews et al., 2019
11	PF3D7_1436300	Translocon component PTEX150	na	na	PV	PV	translocon component	Ho et al., 2018; Nessel et al., 2020; Polino, 2021

"-" indicates no signal observed, "na" – non-applicable due to unsuccessful transfection, "PV" – parasitophorous vacuole, "ER" – endoplasmic reticulum.

with BssHII and XmaI, and performed T4 ligation to assemble new plasmid. The correct sequence was confirmed by sequencing using primers P 35 and P 36, which are complimentary to MCS flanking sequences.

All plasmids were transfected in pairs of one stevor1-80, stevor1-80^{50W}, or stevor1-80^{51E} bait carrying a WR99210 resistance marker *dhfr*, with a plasmid expressing one of the MSHs or PTEX150 in fusion with GFP11 and a blasticidin S deaminase (*BSD*) to confer resistance to blasticidin, 24 plasmid pairs were transfected (Figure 20A). Of 24 transfections, 13 were successful, with parasites reappearing in culture under drug pressure. All 13 transfectants were genotyped by PCRs. I extracted DNA from transfectants and performed PCRs using two primer pairs: (1) amplifying one of stevor1-80 mutants fused to GFP1-10 sequence using primers P 65 and P 64, and (2) amplifying MSH fused to GFP11 sequence using forward primers P 37 to P 47 with a reverse primer P 66 (Figure 20A). I prepared the plasmid combinations for transfection, while Dr. Jessica Kehrer performed the transfection and subsequent microscopic analysis of the parasites.

A conclusive GFP signal was observed in 6 transfectants. Five MSHs showed interaction with stevor1-80. One additional interaction was observed between stevor1-80^{51E} and HSP101 (Figure 21, Figure 22, and Figure 23, summary in Table 2). The liver stage antigen, previously not described in terms of its localization, showed a GFP signal interacting with stevor1-80 in the PV compartment. Stevor1-80^{50W} and Stevor1-80^{51E}, combined with liver stage antigen, showed a weak signal that could suggest unspecific GFP self-assembly (Figure 21A).

The transmembrane emp24 domain-containing protein emitted a weak signal, with the maximum in the stevor1-80^{51E} bait transfectant. In all three transfectants, the signal was too weak to determine a specific compartment, and I concluded that it was a sign of unspecific GFP self-assembly (Figure 21B). I made similar observations about the uncharacterized protein PF3D7_1013300. PF3D7_1013300 transfected with Stevor1-80^{50W} or stevor1-80 presented only background signal, while transfectant of PF3D7_1013300 with stevor1-80^{51E} did not grow under the drug pressure and, therefore, could not be characterized (Figure 22A).

Guanine nucleotide-exchange factor SEC12 interacted with stevor1-80 in the ER, where Guanine nucleotide exchange factor SEC12 was localized before (Lee et al., 2008). Transfectants of guanine nucleotide-exchange factor SEC12 combined with other baits did not recover after transfection (Figure 22B). Similarly, I observed an interaction between *Plasmodium* exported protein (PHISTb) and stevor1-80 with localization in PV and RBC compartments where it was described to localize before (Figure 23A, Davies et al., 2016).

As expected, two control proteins, HSP101 and PETEX150, also interacted with stevor1-80, resulting in a GFP signal in the PV compartment. In addition, HSP101 interaction with stevor1-80^{51E} was observed in PV (Figure 22C and Figure 23B). Plasmepsin V control transfectants did not reappear in the culture regardless of bait.

With the split GFP system, I could confirm the interaction between the WT PEXEL element and five proteins of interest. Two of these proteins had never been reported to be involved in protein export. Interaction with liver stage antigen 3 was detected in PV, while the interaction with guanine nucleotide-exchange factor SEC12 was detected in ER. Mutant stevor1-80^{51E} interacted only with HSP101, while stevor1-80^{50W} showed no interaction with selected proteins.

A 1 PF3D7_0220000 Liver stage antigen 3

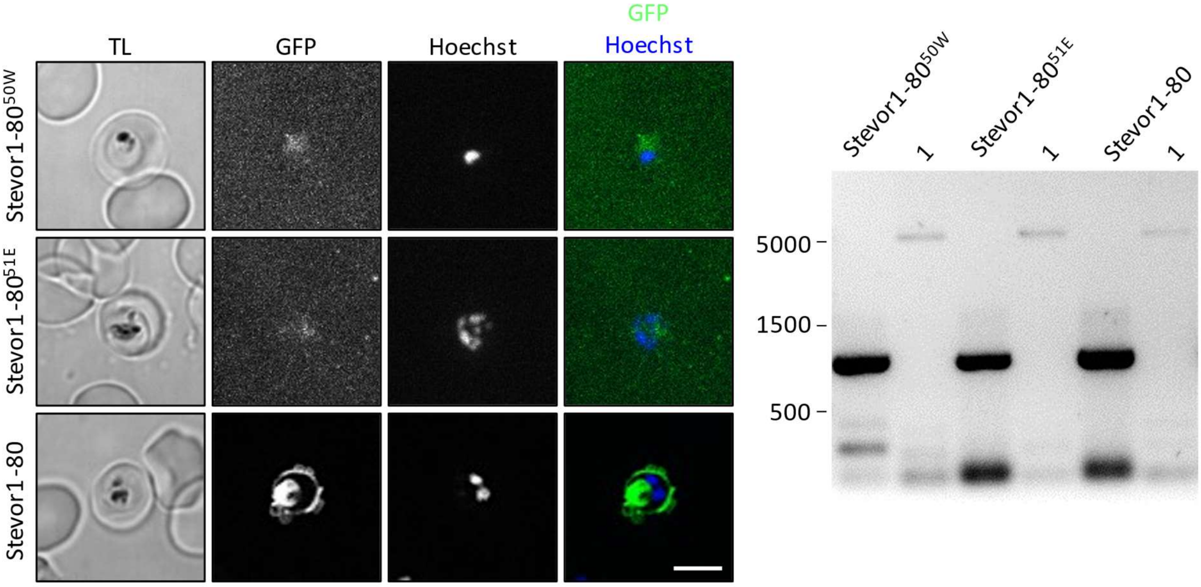

B 2 PF3D7_0422100 Transmembrane emp24 domain-containing protein, putative

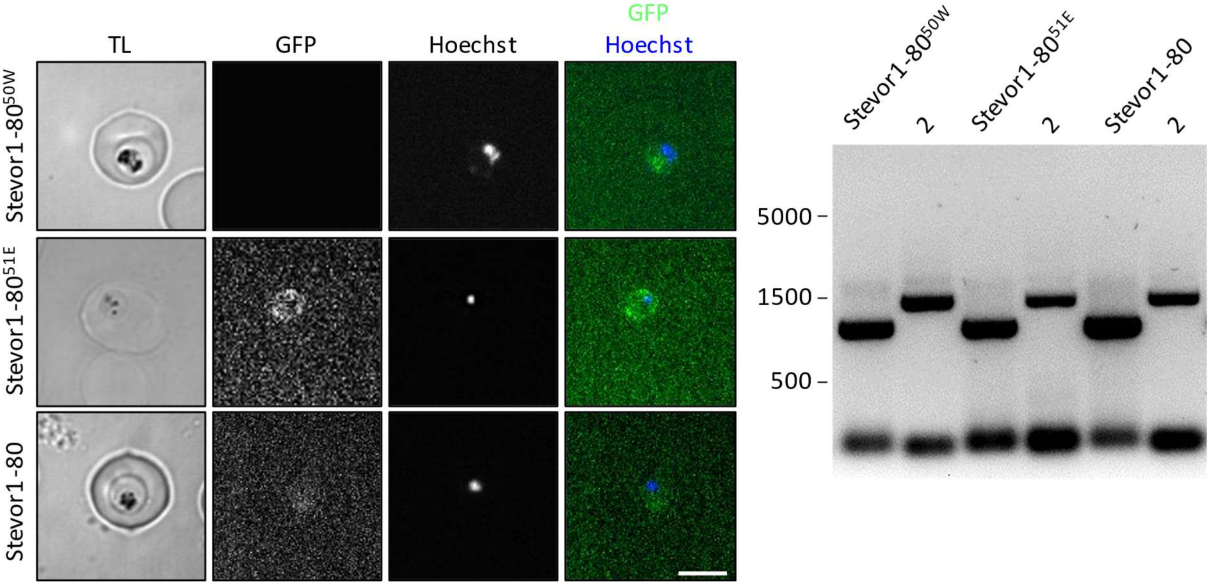

Figure 21. Split GFP transfectant analysis, part one.
(A) Fluorescence microscopy pictures of stevor1-80^{50W}, stevor1-80^{51E}, and stevor1-80 baits interacting with liver stage antigen and respective genotyping PCRs. (B) Fluorescence microscopy analysis of bait proteins interacting with Transmembrane emp24 domain-containing protein and respective genotyping PCRs. The scale bar represents 3 µm.

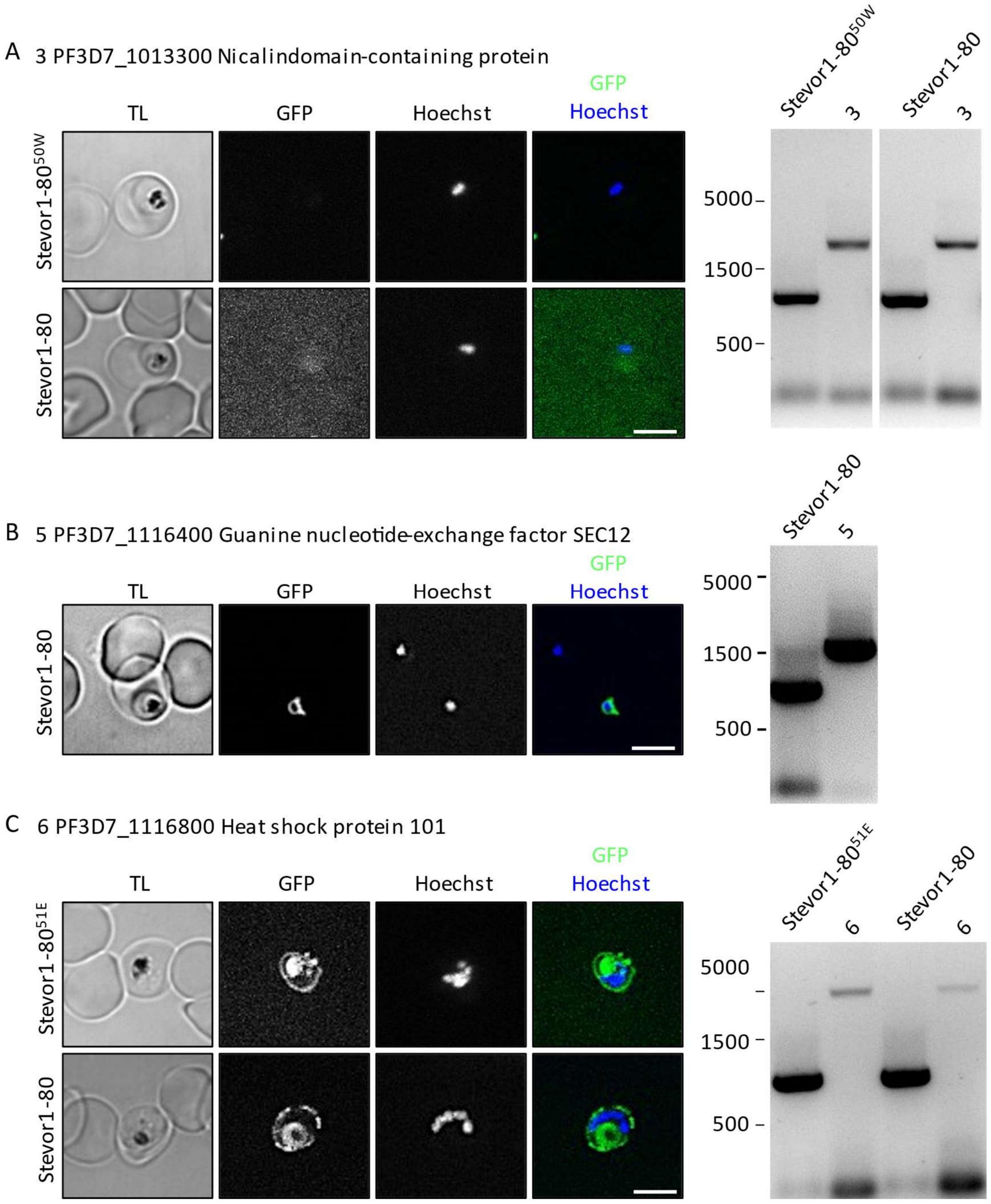

Figure 22. Split GFP transfectant analysis, part two.
(A) Images of bait proteins interacting with an uncharacterized protein (PF3D7_1013300) and respective genotyping PCRs. (B) Fluorescence imaging of Guanidine nucleotide exchange factor SEC12 interaction with stevor1-80 bait protein. The agarose gel shows the presence of the stevor1-80-GFP1-10 and the SEC12-GFP11 gene expressing plasmids. (C) Fluorescence imaging of Heat shock protein 101 (HSP101) interaction with stevor1-80^{51E} and stevor1-80. Agarose gel shows PCRs confirming the presence of both genes to be expressed in the parasite culture. The scale bar represents 3 µm.

A 8 PF3D7_1201000 Plasmodium exported protein (PHISTb)

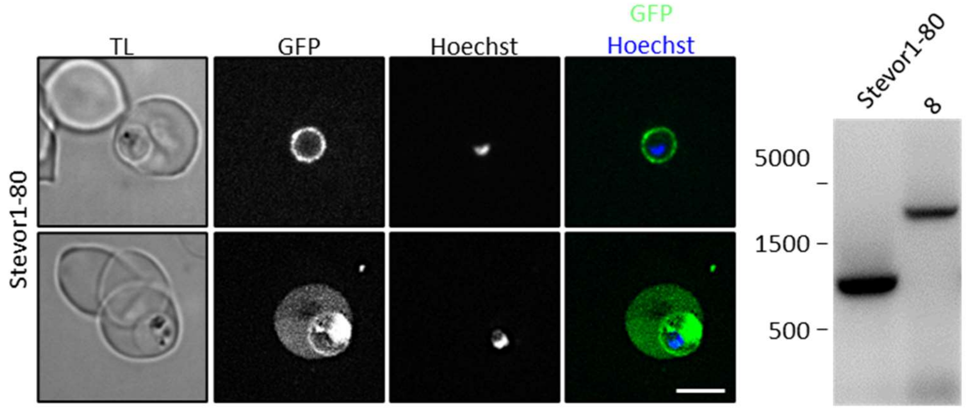

B 11 PF3D7_1436300 Translocon component PTEX150

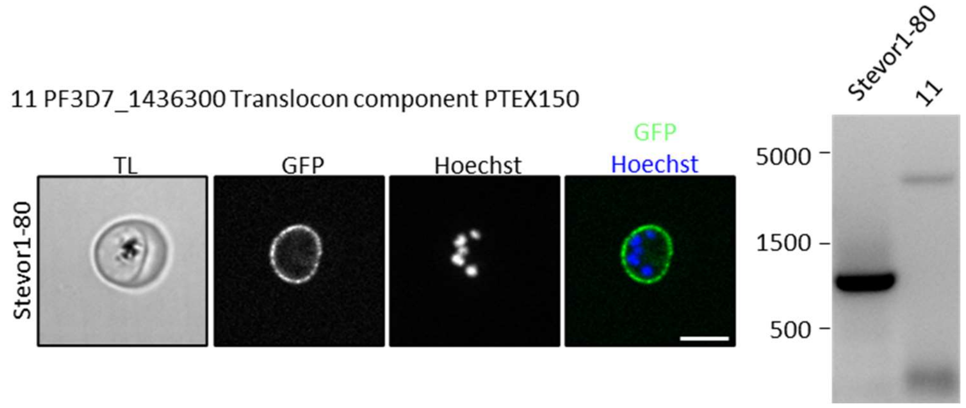

Figure 23. Split GFP transfectant analysis, part three.

(A) Fluorescent imaging of *Plasmodium* exported protein (PHISTb) interaction with stevor1-80, two phenotypes were observed with signal in PV and RBC compartments. Agarose gel displays PCRs confirming the presence of both expression plasmids in the culture. (B) Fluorescent microscopy images of Translocon component PTEX150 interacting with stevor1-80. Agarose gel shows PCR confirmation of both expression plasmids in the culture. The scale bar represents 3 µm.

4. Discussion

4.1 Functional analysis of the HRR and beta-sheet region in KAHRP

4.1.1 Exploring the multifunctional role of the KAHRP histidine-rich region

The HRR of KAHRP has been identified as a critical component of knob formation, with both the HRR and the 5′ repeat region known to interact with PfEMP1 (Waller et al., 2002). However, the substantial discrepancy between the approximately 60 KAHRP molecules and only three PfEMP1 molecules per knob suggests that the HRR may have additional functions in knob assembly beyond its interaction with PfEMP1 (Sanchez et al., 2021). The conserved nature of the HRR hints at an evolutionary advantage for its retention, potentially contributing to protein-protein interactions, signaling processes, or interactions with the RBC membrane.

My attempts to introduce mutations in the HRR proved challenging, often resulting in unstable parasite lines and developing subpopulations. This instability could stem from the disruption in the chromosome 2 end or complete plasmid integration during parasite-mediated double-strand break repair. Despite these challenges, the alanine scanning mutagenesis of the HRR I performed did not reveal any changes in knob appearance or density. It is possible that mutating a single histidine stretch is insufficient to determine the overall impact of the HRR on knob assembly, as the other two stretches remain functional. To address this limitation, future studies could investigate mutants with complete HRR substitutions to better understand its role.

Further exploration of the potential roles of the HRR draws insights from studies on HRG. Research has demonstrated that the HRG's histidine-rich domain is essential for binding to bacterial and fungal cells, destabilizing their membranes, and releasing intracellular contents. This activity is facilitated by the presence of Zn^{2+} ions or under acidic conditions, both of which induce a positive charge on histidine residues (Poon et al., 2011; Rydengård et al., 2008, 2007). Moreover, the oligomerization state of HRG is influenced by pH and Zn^{2+} concentration. At acidic pH levels, such as 6.0 or 5.5, and in the presence of 50 µM Zn^{2+}, HRG predominantly exists in a monomeric form. In contrast, at physiological pH 7.4, a mixture of monomers and dimers is observed, reflecting its pH-dependent behavior (Priebatsch et al., 2017).

The isoelectric point (pKa) of histidine is approximately 6.0, which is close to the pH of 6.8 found in iRBCs (Friedman et al., 1979; Voigt et al., 2000). Under these conditions, a portion of histidine residues will be protonated, while the majority—over 90%—will remain neutral in their deprotonated state (Deplazes et al., 2008). The aromatic imidazole ring of histidine has a unique structure that allows it to attract positively charged metal ions. This property arises from the delocalized electron cloud above and below the plane of the ring. Through these electrons, histidine can form coordinate covalent bonds with metal ions, effectively acting as a ligand. When multiple histidines occur in sequence, they can function as a chelator, stabilizing the interaction by creating several covalent bonds with the metal ion.

Building on the potential roles of the HRR discussed earlier, including its ability to bind metal ions and influence interactions with membranes under varying pH conditions, we focused our research on two specific hypotheses: the HRR's potential interaction with membranes and its involvement with bivalent cations, such as Zn^{2+}. Studies on the HRG have demonstrated that its HRR can interact with bacterial membranes in the presence of Zn^{2+} ions. This mechanism provides a potential explanation for the electron-dense appearance of knobs observed in electron microscopy (EM) images, suggesting that similar interactions might contribute to knob assembly and function.

During the synthesis of the HRR peptide, I observed an unexpected migration pattern in SDS-PAGE. In the *E. coli* lysate, the peptide migrated at a molecular weight higher than predicted. After purification, the apparent molecular weight decreased but remained above the expected value. Further concentration of the purified peptide led to a slightly lower apparent molecular weight, yet it still did not match the theoretical mass. Since the observed migration pattern consistently showed a mass shift above the predicted value, it can be concluded that this effect is not due to degradation.

A plausible explanation for this phenomenon lies in the well-documented ability of histidine residues to chelate metal ions such as Zn^{2+}, Cu^{2+}, or Ni^{2+}. Metal ion binding could increase the peptide's apparent molecular weight during electrophoresis. As purification or concentration removes these metal ions, the peptide may display a reduced apparent mass. Supporting this hypothesis, a recent study using inductively coupled plasma mass spectrometry (ICP-MS) demonstrated that Lysogeny Broth (LB) medium, commonly used for bacterial culture, contains trace amounts of heavy metals. The study quantified metal concentrations in LB Lennox, finding Zn^{2+} at approximately 0.89 mg/L, Cu^{2+} at 16.62 mg/L, and Ni^{2+} at 1.77 mg/L, with copper present at a notably higher concentration (Ng, 2020). These trace metals in the growth medium could chelate with the histidine residues in HRR, altering the peptide’s migration behavior.

My findings indicate that the HRR of KAHRP does not bind to common lipids of iRBCs, regardless of the presence or absence of Zn^{2+} ions. However, Zn^{2+} interaction with the HRR proved strong enough to displace it from the positive control spot on the membrane. While the Zn^{2+} interaction with HRR was not unexpected, it reinforces the idea that Zn^{2+} may play a functional role in modulating HRR activity within the KAHRP protein, albeit not through lipid binding. Interestingly, another bivalent cation, Fe^{2+}, which is less commonly associated with histidine interactions, may also contribute to KAHRP function in iRBCs, warranting further investigation into its potential role.

The parasite relies on hemoglobin as a primary source of amino acids during its development. As hemoglobin is broken down, heme is released, which contributes to oxidative stress within the infected cell. To mitigate this, heme is polymerized into hemozoin crystals within the food vacuole. Each hemozoin crystal consists of five heme molecules and includes Fe^{3+} iron species (Baptista et al., 2022). During the trophozoite stage, approximately 60% of the total iron within the iRBC is sequestered by the parasite, correlating with the digestion of around 62% of hemoglobin at this stage. By the schizont stage, the parasite's iron content increases to approximately 75%, reflecting its continued dependence on hemoglobin catabolism (Egan et al., 2002).

While the oxidative stress resulting from hemoglobin degradation primarily occurs in the food vacuole, the red blood cell (RBC) membrane also experiences oxidative damage as the parasite develops. This is evidenced by an increase in monohydroxy derivatives of polyenoic fatty acids, indicative of lipid peroxidation caused by the release of heme and iron (Percário et al., 2012). However, RBCs possess an intrinsic mechanism to counteract oxidative stress from free heme. Heme oxygenase plays a key role in this process by degrading heme, producing carbon monoxide and releasing free Fe^{2+} ions (Kumar and Bandyopadhyay, 2005).

While interactions with iron are less commonly associated with histidine, as the trivalent form Fe^{3+} is more stable, the intracellular environment of iRBCs presents unique conditions. During heme degradation, Fe^{2+} ions are released, particularly under the increasing oxidative stress associated with parasite development. These free Fe^{2+} ions could potentially interact with KAHRP, altering its oligomerization properties and modulating its interaction with the RBC membrane. This observation opens intriguing possibilities for further research into the diverse roles of the histidine-rich region in KAHRP functionality.

4.1.2 Structured region integrity and its impact on KAHRP-mediated knob formation

KAHRP is known to interact with multiple components of the red blood cell membrane skeleton, including spectrin, actin, and ankyrin. Recent studies reveal that during the ring stage, KAHRP is distributed among these cytoskeletal elements but undergoes a dynamic relocalization in the trophozoite stage, moving toward remodeled actin junctions and away from ankyrin. This redistribution has been proposed to result from post-translational modifications, such as phosphorylation, which may alter KAHRP's binding affinities. Among the phosphorylation sites identified in KAHRP, we focused on a specific tyrosine residue predicted to be phosphorylated, investigating its potential role in regulating KAHRP function and knob assembly.

Tyrosine phosphorylation in *Plasmodium falciparum* plays a significant regulatory role, particularly in protein interactions and signal transduction pathways. While post-translational modifications such as phosphorylation are abundant, tyrosine phosphorylation is relatively rare, constituting only 4–5% of phosphorylation events during the blood stage of infection, comparable to the 1–4% observed in other organisms (Huttlin et al., 2010; Tan et al., 2009). Interestingly, the peak level of tyrosine phosphorylation, exceeding 25%, occurs during the schizont stage, coinciding with the highest detection of phosphopeptides. This level decreases to below 15% during the ring stage and drops further to just 2% in the trophozoite stage (Pease et al., 2013).

In the context of KAHRP, experimental data annotate one tyrosine phosphorylation site at position 343 (Ganter et al., 2017; Lasonder et al., 2012), with an additional site predicted at position 193. These modifications are hypothesized to influence KAHRP's dynamic interactions with the host cytoskeleton during knob formation. The presence of tyrosine kinase activity within *Plasmodium falciparum* provides further context for these findings. For instance, Pfnek3, a dual-specificity kinase, exhibits both serine/threonine and tyrosine kinase activity, underscoring the parasite's capability to mediate tyrosine phosphorylation (Low et al., 2012). Similarly, PfTKL2, a tyrosine kinase-like enzyme related to the IRAK/RLK/Pelle family, demonstrates kinase activity *in vitro* and is exported into the host erythrocyte, potentially contributing to phosphorylation events on host or parasite proteins (Abdi et al., 2013).

Although the presence of parasite-derived tyrosine kinases is limited, human erythrocytes contain at least eight tyrosine kinases that may participate in phosphorylation events during *Plasmodium falciparum* infection (Bryk and Wiśniewski, 2017). The interplay between parasite and host-derived kinases likely shapes tyrosine phosphorylation patterns, potentially regulating KAHRP function and its relocalization during the parasite's intraerythrocytic stages.

In this study, we demonstrated that substituting tyrosine at position 193 with phenylalanine, a non-phosphorylatable analog with a similar structure, did not affect knob shape or density on the iRBC membrane. This tyrosine residue is located immediately following the third β\betaβ-strand within the structured region of KAHRP targeted in this work, overlapping with the site of the alanine screening mutation ga18. Importantly, the knobless phenotype observed with alanine screening mutants ga16, ga17, and ga18 cannot be attributed to the loss of a post-translationally modified residue, as no modifications other than a reported acetylated lysine at position 166, which is unaffected by these alanine substitutions, have been identified in this region.

These findings suggest that disrupting the β-sheet structure in this core region is sufficient to impair knob assembly. Whether this disruption interferes with a specific protein interaction or compromises the structural integrity of KAHRP required for its function remains unclear. Further studies will be needed to determine if the structured core serves as a critical scaffold for binding partners or plays a broader role in maintaining the protein's overall conformation and stability.

4.2 Exploring novel players in *Plasmodium* protein export pathways

4.2.1 Contextualizing proteomic data within known export mechanisms

When analyzing the interaction partners of arrested export proteins, mass spectrometry revealed both expected and unexpected findings. For Stevor1-80$^{50\mathrm{W}}$, whose export is arrested in the ER, significantly higher labeling of Plasmepsin V was observed compared to other baits, consistent with its expected localization in the PfSec61-PfSPC25-PMV complex (Marapana et al., 2018). This finding aligns with previous descriptions of Plasmepsin V as critical for PEXEL motif cleavage during ER entry. Both Stevor1-80^{50W} and Stevor1-80^{51E} baits displayed significantly higher interactions with HSP101 and HSP70, corroborating their roles in engaging exported proteins prior to translocation across the PVM (Elsworth et al., 2016; Gabriela et al., 2022; Russo et al., 2010). These chaperones, known to reside in the ER and PV, facilitate protein stabilization and unfolding, with HSP101 functioning as a molecular motor that threads unfolded proteins through the PTEX translocon (Gabriela et al., 2022; Ho et al., 2018). Importantly, HSP101 is also known to bind PEXEL proteins, such as our bait proteins, in the ER even prior to PEXEL cleavage. This makes it expected that ER-arrested Stevor1-80^{50W} would interact with HSP101, as part of the early export process where the chaperone engages exported proteins before their secretion into the PV (Gabriela et al., 2022).

Notably, Stevor1-80^{51E}, arrested later in the export pathway, in the PV, showed significantly higher interaction with PV1, a component of the EPIC complex, which is implicated in protein trafficking in the PV (Beck and Ho, 2021). This observation suggests that Stevor1-80^{51E} interacts with HSP101 and EPIC machinery prior to PTEX-mediated translocation. Intriguingly, there was no significant change in the abundance of detected PTEX150 between the groups, and EXP2, a core component of PTEX, was not identified in these experiments. This could indicate that bait proteins reach these interaction partners in an unfolded state, rendering the miniTurbo tag inactive when reaching these components.

Unexpectedly, several proteins exhibited significantly higher interactions specifically with Stevor1-80^{50W}, including Exp3, PTEX88, and Pf113—proteins typically associated with the PV—and PfEMP1-trafficking protein, which is exported to Maurer’s clefts (Beck and Ho, 2021; Elsworth et al., 2016). These interactions may reflect transient contacts within the secretory pathway, particularly in the ER, rather than functional roles specific to Stevor1-80^{50W} export. While these findings add complexity to our understanding of the export pathway, further studies will be required to disentangle functional interactions from incidental associations within the trafficking machinery.

4.2.2 Challenges and improvements in capturing *Plasmodium* protein networks

The biotinylation assay used in this study, employing miniTurbo biotin ligase to identify interaction partners of exported proteins arrested at different stages, was instrumental in mapping potential networks involved in *Plasmodium* protein export. However, the approach posed challenges related to the variability in mass spectrometry background observed across different experimental groups. This variability is likely attributable to the long labeling period of 16–18 hours, during which the bait proteins reside in distinct cellular compartments: the parasite ER, PV, and erythrocyte cytosol. Each compartment exhibits a unique protein composition, and the prolonged biotinylation may have resulted in non-specific labeling, complicating the identification of direct interaction partners.

The extended duration of the assay increases the risk of capturing adventitious interactions, particularly in dynamic environments like the ER or PV, where high protein turnover and protein trafficking may introduce noise into the dataset. Additionally, the variability in protein compositions across compartments may result in distinct background profiles in mass spectrometry, potentially masking or diluting true interaction signals.

To address these challenges, improvements to the assay design could enhance the specificity and relevance of identified interactions. Shortening the biotinylation period to approximately 2 hours could limit non-specific labeling and focus the assay on capturing proteins more directly interacting with the bait. This approach would need to be combined with a controlled start of bait export to ensure that the arrested proteins are actively engaging with the export machinery during the labeling window. Techniques like the glmS ribozyme system could be employed to synchronize the bait export, improving the temporal resolution of interaction capture.

An alternative approach to refine interaction identification involves using crosslinkers, such as DSP. Crosslinking directly captures proteins in close physical proximity to the bait, followed by immunoprecipitation and mass spectrometry analysis to identify interaction partners. This method is particularly suited to dynamic systems like *Plasmodium*-infected erythrocytes, where transient interactions are critical. Unlike biotinylation, DSP-based crosslinking could minimize the confounding effects of prolonged labeling, providing a more focused and compartment-specific dataset.

While each method has limitations—shorter biotinylation durations may miss weaker or less abundant interactions, and crosslinking may fail to capture transient or indirect interactions—a hybrid strategy could combine the strengths of both approaches. Parallel experiments using biotinylation and DSP crosslinking could provide complementary datasets, offering insights into both transient and stable interactions of arrested baits.

4.2.3 Novel interactions in the *Plasmodium* exportome

4.2.3.1 Split-GFP assay validation

Split GFP assay was used to confirm the identified interaction partners of the bait protein, which contains the first 80 amino acids of the stevor protein, including the signal peptide and PEXEL motif. The proteins interacting with PEXEL motif must come in close proximity to the bait, which allows split-GFP self-assembly and restoration of it's fluorescence function. Two control proteins HSP101 and PTEX150 were successfully expressed in fusion with GFP11 in *Plasmodium falciparum* 3D7 line. The analyzed parasite presented fluorescent signal in the PV compartment, where the interaction was expected.

PMV was used as the third control for interaction in ER, however, the parasites never recovered after the transfection. This indicates the possibility of negative effects of GFP11 on the parasite when fused to PMV, which potentially competed with the parasite's original PMV and was fatal to the parasite.

4.2.3.2 Key ER mediators and emerging mechanisms in *Plasmodium falciparum* protein export

We identified SEC12 protein among the PEXEL interaction partners. The SEC12 protein in *Plasmodium falciparum* is a guanine nucleotide exchange factor critical for COPII vesicle formation at the ER. It catalyzes the activation of Sar1, a GTPase required for vesicle budding, by facilitating the exchange of GDP for GTP. Unlike in many eukaryotes where SEC12 is localized to distinct transitional ER (tER) sites, *Plasmodium falciparum* SEC12 is distributed throughout the ER (Lee et al., 2008). The interaction of SEC12 with Stevor1-80 in ER was confirmed by split-GFP assay, indicating the possibility of exported protein traversing the Golgi complex before being exported to PV.

The mass spectrometric analysis revealed the putative Transmembrane emp24 domain-containing protein (PF3D7_0422100) as a potential PEXEL interaction partner of stevor fusion protein, the relative abundance in interaction with stevor1-80^{50W} was significantly higher, while with stevor1-80^{51E} PEXEL mutant was significantly lower than with WT PEXEL motif. This interaction could not be confirmed by split-GFP assay due to only a weak signal being present in PF3D7_0422100 interaction with both PEXEL mutants and WT PEXEL protein. This result could be due to the temporary shortness of the interaction as the self-assembled GFP remains flexible, as demonstrated by the interaction with PF3D7_1201000 PHISTb protein.

Emp24 domain proteins typically function as cargo receptors or components of COPII vesicle coats, facilitating vesicular trafficking between the ER and the Golgi apparatus. A putative transmembrane emp24 domain-containing protein (PF3D7_0526900) was identified as an interaction partner of PF3D7_0422100, suggesting an Emp24 complex activity (Knöckel et al., 2021). PF3D7_0422100 protein also interacts with *Plasmodium* exported protein (PF3D7_1148800) that belongs to HYP11 conserved family (Sargeant et al., 2006). This protein is exported but does not contain the PEXEL element. Another membrane-bound PNEP SURFIN4.1 used to analyze PTEX-mediated translocation identified PF3D7_0422100 as an interaction partner in a proximity biotinylation assay (Miyazaki et al., 2021). The interaction partners of PF3D7_0422100 protein indicate that it acts in the part of protein export between ER and Golgi complex, where the pathways of PEXEL and PNEP export may be linked.

In addition to the putative transmembrane emp24 domain-containing protein, two more proteins showed a similar pattern of interaction: (PF3D7_0505700) and HSP90 (PF3D7_1443900). These two proteins are slightly more abundant in interaction with the stevor1-80^{50W} bait and have a 15-18 fold reduction in abundance when interacting with the stevor1-80^{51E} bait, as compared with the WT PEXEL interactome. These results suggest the possibility of the three proteins performing a shared function and losing the ability to interact with exported proteins bearing the 51E mutation (PEXEL motif RLLEQ). While

HSP90 was described to reside in the parasite cytosol, PF3D7_0505700 is described to localize to the ER and to play a role in male gametocyte egress from iRBCs in *P. berghei* and *P. falciparum* (Kehrer et al., 2024; Tabassum et al., 2022). Proteins with certain non-canonical PEXEL motif alterations are naturally directed to intermediate steps of the export pathway rather than completing full export. The three identified proteins may mediate this redirection or its absence.

It has been assumed that there is no gamma secretase complex in *Plasmodium* due to the absence of homologs for complex components identified through sequence similarity. Additionally, inhibitors of the human gamma-secretase complex have proven ineffective in *Plasmodium falciparum* (Li et al., 2009). However, the PF3D7_1013300 Nicalin domain-containing protein shows similarity to both domains of the nicastrin protein, which in other organisms make a part of the gamma secretase protein complex (Behrens and Spielmann, 2023; Xie et al., 2014). In other organisms, the gamma-secretase complex is responsible for the proteolytic cleavage of membrane-integral proteins within the intermembrane space (Tomita et al., 2006). PF3D7_1013300 Nicalin domain-containing protein in fusion with GFP was found to localize in the ER (Khosh-Naucke et al., 2018). This protein was identified as a mass spectrometry hit with significantly higher abundance in the stevor1-80^{50W} bait group compared to stevor1-80 with the WT PEXEL motif. However, the split-GFP assay could not confirm this interaction, suggesting that the interaction conditions were suboptimal for GFP self-assembly, or it may be an unrelated background protein. However, the detection of this protein in the initial analysis provides valuable insight into its expression and localization. Specifically, my findings support that the protein is likely expressed during the blood stages of *Plasmodium falciparum* and localizes to the endoplasmic reticulum, providing a basis for future studies to explore its potential role.

4.2.3.3 LSA-3 interactions in protein export pathways

The *Plasmodium falciparum* protein gene PF3D7_0220000 encodes a ~175 kDa protein called liver stage antigen-3 (LSA-3). LSA-3 is highly expressed during the parasite’s liver and blood stages. In pre-erythrocytic stages, LSA-3 is expressed on the surface of sporozoites, and in the PV (Daubersies et al., 2000; Prieur and Druilhe, 2009), making it an attractive antigen candidate for immune targeting in humans. Furthermore, LSA-3 is highly conserved across diverse *Plasmodium falciparum* isolates, and its conservation is structurally constrained (Prieur and Druilhe, 2009). The protein consists of three non-repeat regions and three repeat regions consisting of motif E-E-X-hydrophobic amino acid-E-E, that create α-helix structures. These repeats are also found in antigens RESA, Pf11.1, and Ag332 (Mattei et al., 1989). However, LSA-3 appears to be the only Glu-rich antigen described in the pre-erythrocytic stage (Daubersies et al., 2000).

Although LSA-3 is exported to the PV, it possesses neither a PEXEL motif nor signal peptide; it is, therefore, unlikely that the interaction detected in PV is due to both proteins being exported in the same pathway. Yeast two-hybrid (Y2H) screening and ELISA experiments show an interaction between LSA-

3 and *Plasmodium falciparum* Ser/Thr Protein Phosphatase type 1 (PP1), essential for parasite development in asexual cycle (Hollin et al., 2016).

While LSA-3 has been mostly studied due to its availability on the interface between parasite and host immune response, the active role of LSA-3 protein remains unclear. Here, we show its potential to interact with the *Plasmodium* protein export pathway. I isolated LSA-3 and identified it by mass spectrometry; the proximity labeling showed it significantly upregulated in the stevor1-80^{50W} group, where bait localizes at the ER, compared to the stevor1-80 group. The interaction between LSA-3-GFP11 and Stevor1-80-GFP-1-10 with WT PEXEL motif was further confirmed and localized in PV. Stevor constructs with mutated PEXEL motif did not yield GFP self-assembly when co-expressed with LSA-3-GFP11, indicating the necessity of an intact PEXEL motif for the interaction.

4.2.3.4 PF3D7_1201000 interaction highlights split-GFP trafficking into the RBC cytosol

At the time of initiating this research, PF3D7_1201000 was not clearly associated with the *Plasmodium* export pathway. However, a recent publication (Yang et al., 2023) has since demonstrated its use of this pathway. This evidence suggests that the protein may not fit within the scope of our original target criteria, which focused on proteins not directly linked to export mechanisms.

Plasmodium exported protein PF3D7_1201000 is a member of the *Plasmodium* helical interspersed subtelomeric (PHIST) protein family, classified explicitly within the PHISTb subgroup. It contains PEXEL motif RILSS and is exported to the iRBC cytoplasm (Sargeant et al., 2006). PF3D7_1201000 has been identified as interacting with components of the RhopH complex—namely RhopH2, RhopH3, and CLAG3—which are implicated in forming new permeability pathways (NPPs) in the host cell membrane (Jonsdottir et al., 2021). This interaction suggests that PF3D7_1201000 may contribute to the trafficking or function of the RhopH complex, thereby facilitating nutrient uptake essential for parasite survival. PF3D7_1201000 shows colocalization with Stevor1-80 in PV and RBC cytoplasm, indicating GFP self-assembly of proteins and confirming the successful export of functional proteins in fusion with partial GFP sequence. The signal distribution between PV and RBC suggests that a self-assembled GFP can disassemble to translocate from PV to RBC compartment, signifying the flexibility of the split-GFP complex.

4.2.4 Methodological limitations in split-GFP interaction analysis

Split-GFP assay proved to be effective in all compartments of interest within the scope of this study as we could identify self-assembled GFP signal in ER, PV and RBC compartments. Although, both positive and negative interactions have been identified, it remains to be questioned, whether the interaction conditions were optimal for each MSH. Some interactions could have been missed due to insufficient linker length between the protein of interest and the GFP11 or GFP11 positioning in suboptimal part of the fusion protein for GFP self-assembly. A potentially false-positive interaction was observed between the bait and a PHISTb group protein (PF3D7_1201000) that contains PEXEL motif and is therefore exported via the same pathway. While this method does not show the mode of interaction, it remains specific enough to identify proteins in near proximity, as opposed to those residing in the same compartment and resulting in a weak background GFP signal.

To confirm the interaction between the MSHs and PEXEL motif further experiments are required, which depend on the assumed function of the interaction partner. For example, a protein complex could be immunoprecipitated and the structural interaction between two proteins could be analysed by cryo-electron microscopy. Förster Resonance Energy Transfer (FRET) system could be used to test potential enzymatic activity. Surface Plasmon Resonance can be used to identify binding interactions between proteins, providing data on binding affinity and kinetics.

4.2.5 Exploring Golgi's role in *Plasmodium* protein export

In my experiments, mass spectrometry identified several Golgi complex proteins, including GP1, GP2, emp24, and COPII-associated vesicular transport proteins such as SEC12. Notably, SEC12 showed the strongest interaction with the Stevor1-80^{50W} bait, consistent with its known localization in the ER, where Stevor1-80^{50W} is arrested. Meanwhile, emp24 interacted with both Stevor1-80^{50W} but not with Stevor1-80^{51E} bait, aligning with its proposed short-term interaction as a cargo receptor, facilitating the recruitment of proteins into vesicles (Kaiser, 2000). This observation is supported by previous studies demonstrating that blocking COPII vesicular transport using brefeldin A results in the accumulation of exported proteins in the ER and halts protein export (Wickham et al., 2001). Despite these findings, the Golgi complex in *Plasmodium falciparum* remains poorly characterized, leaving significant gaps in our understanding of its role in the parasite’s protein trafficking pathways.

The Golgi apparatus in *Plasmodium falciparum* is notably rudimentary compared to other eukaryotic cells, consisting of dispersed, unstacked cis- and trans-cisternae. Despite this simplicity, it plays a central role in the parasite's secretory pathway, ensuring the proper trafficking of proteins critical for survival and development (Hallée et al., 2018). Golgi-associated proteins such as GP1, GP2, emp24, and components of the COPII vesicular transport system, including SEC12, are vital for these processes.

GP1 and GP2, two recently identified proteins, form a complex that localizes to the cis-Golgi throughout the erythrocytic cycle and potentially during mosquito stages. GP1, a Golgi-resident protein, has been shown to be essential for parasite survival, as attempts to knock out its gene were unsuccessful. Meanwhile, GP2, a transmembrane protein, is not essential but plays an important role in optimal asexual development during the blood stages. Conditional repression of GP1 or deletion of GP2 impaired parasite growth, indicating their significance in maintaining Golgi function and the secretory pathway (Hallée et al., 2018).

Emp24, a member of the p24 protein family, plays a role in maintaining the fidelity of COPII vesicle trafficking. In other eukaryotic systems, deletion of EMP24 results in a reduction in small vesicle production and slowed export of certain cargo proteins, suggesting its role as a cargo receptor or indirect facilitator of vesicle assembly (Kaiser, 2000). Although its precise role in *Plasmodium falciparum* remains to be elucidated, similar mechanisms are likely at play given its identification in mass spectrometry datasets of exported protein interaction partners (Kaiser, 2000). PfSEC12 is distributed throughout the ER, while PfSec24 is concentrated at tER sites near the cis-Golgi. These tER sites are marked by the close apposition of PfSec24 and PfGRASP, a Golgi marker, suggesting a spatially coordinated process for ER-to-Golgi trafficking (Lee et al., 2008).

Golgi apparatus is among the least studied organelles of *Plasmodium falciparum*, despite their role in protein secretion and export. Components of COPII vesicular system like Emp24 and SEC12 have a central function in ER-to-Golgi transport. Further, my data shows, that GP1 and GP2 may interact with

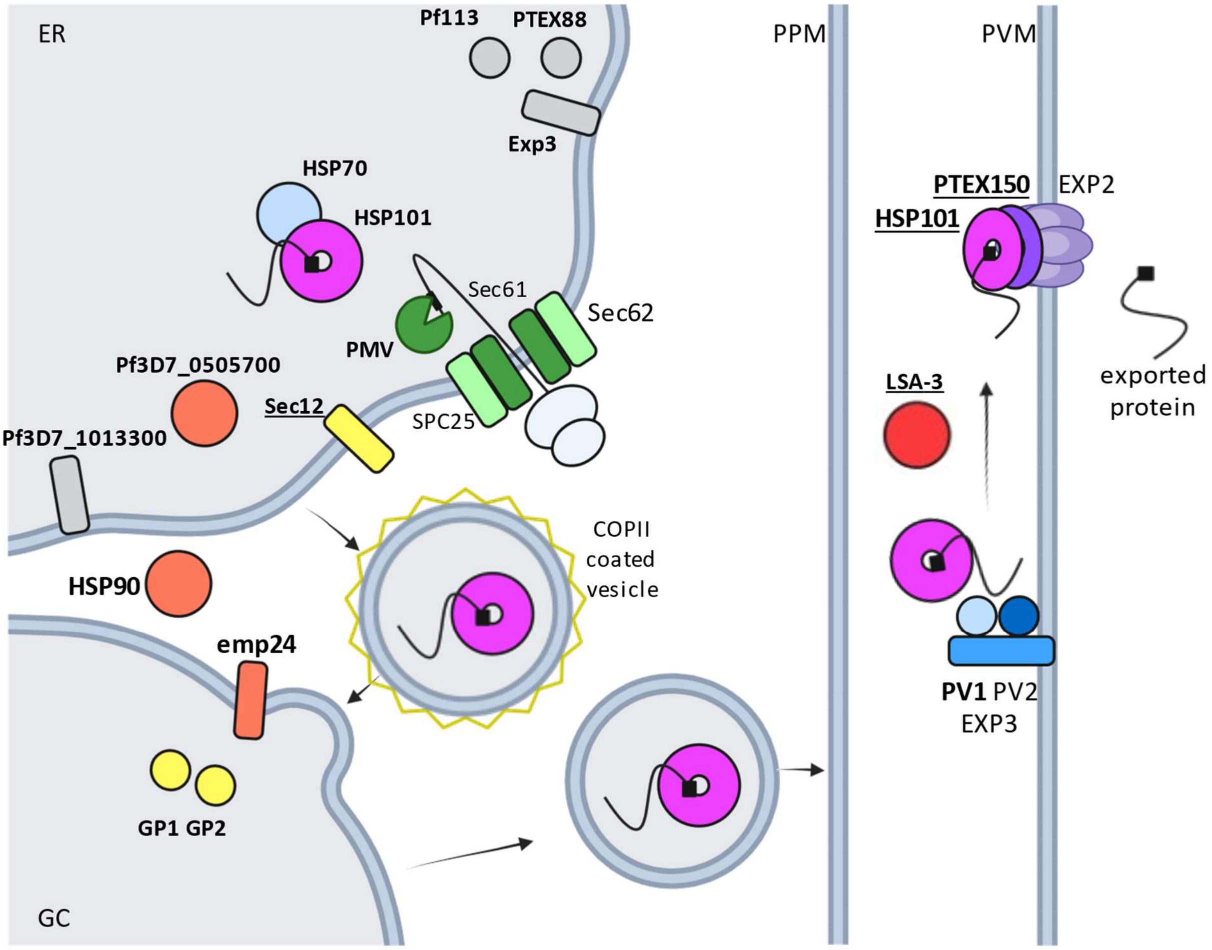

Figure 24. Overview of the *Plasmodium falciparum* protein export pathway highlighting proteins identified in this study.
Proteins detected by mass spectrometry in this project are shown in bold, while interactions confirmed through split-GFP assay are underlined. ER – endoplasmic reticulum, GC – Golgi complex, PPM – parasite plasma membrane, PVM – Parasitophorous vacuole membrane. Figure created with BioRender.com.

the exported protein cargo in Golgi cisternae. Given the Golgi's pivotal position in protein trafficking, it is plausible that some missing steps in our understanding of export pathways, such as the acetylation of PEXEL protein N-termini following cleavage, could occur there. Further exploration of Golgi-mediated processes is essential to unravel the complexities of *Plasmodium* protein export.

4.2.6 Mapping protein interactions in *Plasmodium* export

This section provides an overview of my findings on protein export mechanisms, highlighting key interactions and pathways uncovered during the study (Figure 24). Sec61, Sec62, and SPC25 mediate the translocation of exported proteins into the ER, where the PEXEL motif is cleaved by PMV. In this study, I identified HSP101 interactions with the bait protein in the ER via mass spectrometry and in the PV through split-GFP, consistent with earlier findings that HSP101 engages with PEXEL proteins even before PMV cleavage, ccompanying them to the PTEX translocon. Among ER interactors, mass spectrometry also detected chaperone HSP70 and the Niacin domain-containing protein (PF3D7_1013300). Additionally, interactions with components of the PTEX and EPIC complexes, including Pf113, PTEX88, and Exp3, were identified in the ER.

An unusual interaction pattern emerged with three proteins: a conserved *Plasmodium* membrane protein of unknown function (PF3D7_0505700), HSP90, and a putative transmembrane emp24 domain-containing protein. These proteins showed higher interaction with the stevor1-80^{50W} mutant but significantly reduced abundance in the stevor1-80^{51E} bait group, compared with the WT PEXEL motif group, suggesting a shared function that is dependent on the PEXEL sequence.

I identified multiple Golgi-associated and COPII vesicular transport-related proteins. Split-GFP confirmed the interaction of the bait with SEC12 in the ER, while mass spectrometry suggested Golgi proteins GP1, GP2, and the putative transmembrane emp24 domain-containing protein as interaction partners. These findings are supported by previous studies showing that protein export is ablated by Brefeldin A, emphasizing the necessity of secretory transport in the export process.

Further along the export pathway, multiple interactions were identified in the PV. Mass spectrometry suggested bait interaction with PV1, a component of the EPIC complex previously shown to associate with PTEX-exported proteins. Split-GFP experiments also confirmed an interaction between the bait and LSA-3 in the PV. Control experiments validated the split-GFP assay by confirming the interactions between the bait and two core PTEX components, HSP101 and PTEX150.

5. Bibliography

Abdi, A.I., Carvalho, T.G., Wilkes, J.M., Doerig, C., 2013. A secreted *Plasmodium falciparum* kinase reveals a signature motif for classification of tyrosine kinase-like kinases. Microbiology 159, 2533–2547. https://doi.org/10.1099/mic.0.070409-0

Adams, Y., Olsen, R.W., Bengtsson, A., Dalgaard, N., Zdioruk, M., Satpathi, S., Behera, P.K., Sahu, P.K., Lawler, S.E., Qvortrup, K., Wassmer, S.C., Jensen, A.T.R., 2021. *Plasmodium falciparum* erythrocyte membrane protein 1 variants induce cell swelling and disrupt the blood–brain barrier in cerebral malaria. J Exp Med 218, e20201266. https://doi.org/10.1084/jem.20201266

Amato, R., Lim, P., Miotto, O., Amaratunga, C., Dek, D., Pearson, R.D., Almagro-Garcia, J., Neal, A.T., Sreng, S., Suon, S., Drury, E., Jyothi, D., Stalker, J., Kwiatkowski, D.P., Fairhurst, R.M., 2017. Genetic markers associated with dihydroartemisinin-piperaquine failure in *Plasmodium falciparum* malaria in Cambodia: a genotype-phenotype association study. Lancet Infect Dis 17, 164–173. https://doi.org/10.1016/S1473-3099(16)30409-1

Anand, A.C., Puri, P., 2005. Jaundice in malaria. Journal of Gastroenterology and Hepatology 20, 1322–1332. https://doi.org/10.1111/j.1440-1746.2005.03884.x

Angchaisuksiri, P., 2014. Coagulopathy in malaria. Thrombosis Research 133, 5–9. https://doi.org/10.1016/j.thromres.2013.09.030

Aravind, L., Iyer, L.M., Wellems, T.E., Miller, L.H., 2003. *Plasmodium* Biology: Genomic Gleanings. Cell 115, 771–785. https://doi.org/10.1016/S0092-8674(03)01023-7

Arese, P., Turrini, F., Schwarzer, E., 2005. Band 3/Complement-mediated Recognition and Removal of Normally Senescent and Pathological Human Erythrocytes. Cellular Physiology and Biochemistry 16, 133–146. https://doi.org/10.1159/000089839

Arnot, D.E., Ronander, E., Bengtsson, D.C., 2011. The progression of the intra-erythrocytic cell cycle of *Plasmodium falciparum* and the role of the centriolar plaques in asynchronous mitotic division during schizogony. International Journal for Parasitology 41, 71–80. https://doi.org/10.1016/j.ijpara.2010.07.012

Bachmann, A., Scholz, J.A.M., Janßen, M., Klinkert, M.-Q., Tannich, E., Bruchhaus, I., Petter, M., 2015. A comparative study of the localization and membrane topology of members of the RIFIN, STEVOR and PfMC-2TM protein families in *Plasmodium falciparum*-infected erythrocytes. Malaria Journal 14, 274. https://doi.org/10.1186/s12936-015-0784-2

Badior, K.E., Casey, J.R., 2018. Molecular mechanism for the red blood cell senescence clock. IUBMB Life 70, 32–40. https://doi.org/10.1002/iub.1703

Baer, K., Roosevelt, M., Clarkson Jr, A.B., Van Rooijen, N., Schnieder, T., Frevert, U., 2007. Kupffer cells are obligatory for *Plasmodium* yoelii sporozoite infection of the liver. Cellular Microbiology 9, 397–412. https://doi.org/10.1111/j.1462-5822.2006.00798.x

Baptista, V., Peng, W.K., Minas, G., Veiga, M.I., Catarino, S.O., 2022. Review of Microdevices for Hemozoin-Based Malaria Detection. Biosensors 12, 110. https://doi.org/10.3390/bios12020110

Batinovic, S., McHugh, E., Chisholm, S.A., Matthews, K., Liu, B., Dumont, L., Charnaud, S.C., Schneider, M.P., Gilson, P.R., de Koning-Ward, T.F., Dixon, M.W.A., Tilley, L., 2017. An exported protein-interacting complex involved in the trafficking of virulence determinants in *Plasmodium*-infected erythrocytes. Nat Commun 8, 16044. https://doi.org/10.1038/ncomms16044

Bayili, K., N'do, S., Namountougou, M., Sanou, R., Ouattara, A., Dabiré, R.K., Ouédraogo, A.G., Malone, D., Diabaté, A., 2017. Evaluation of efficacy of Interceptor® G2, a long-lasting insecticide net coated with a mixture of chlorfenapyr and alpha-cypermethrin, against pyrethroid resistant Anopheles gambiae s.l. in Burkina Faso. Malar J 16, 190. https://doi.org/10.1186/s12936-017-1846-4

Beck, J.R., Ho, C.-M., 2021. Transport mechanisms at the malaria parasite-host cell interface. PLOS Pathogens 17, e1009394. https://doi.org/10.1371/journal.ppat.1009394

Beck, J.R., Muralidharan, V., Oksman, A., Goldberg, D.E., 2014. PTEX component HSP101 mediates export of diverse malaria effectors into host erythrocytes. Nature 511, 592–595. https://doi.org/10.1038/nature13574

Beeson, J.G., Brown, G.V., Molyneux, M.E., Mhango, C., Dzinjalamala, F., Rogerson, S.J., 1999. *Plasmodium falciparum* Isolates from Infected Pregnant Women and Children Are Associated with Distinct Adhesive and Antigenic Properties. The Journal of Infectious Diseases 180, 464–472. https://doi.org/10.1086/314899

Behrens, H.M., Spielmann, T., 2023. Identification of domains in *Plasmodium falciparum* proteins of unknown function using DALI search on Alphafold predictions. https://doi.org/10.1101/2023.06.05.543710

Bhattacharyya, M.K., Bhattacharyya nee Deb, S., Jayabalasingham, B., Kumar, N., 2005. Characterization of kinetics of DNA strand-exchange and ATP hydrolysis activities of recombinant PfRad51, a *Plasmodium falciparum* recombinase. Molecular and Biochemical Parasitology 139, 33–39. https://doi.org/10.1016/j.molbiopara.2004.09.007

Blasco, B., Leroy, D., Fidock, D.A., 2017. Antimalarial drug resistance: linking *Plasmodium falciparum* parasite biology to the clinic. Nat Med 23, 917–928. https://doi.org/10.1038/nm.4381

Blisnick, T., Morales Betoulle, M.E., Barale, J.-C., Uzureau, P., Berry, L., Desroses, S., Fujioka, H., Mattei, D., Braun Breton, C., 2000. *Pfsbp*1, a Maurer's cleft *Plasmodium falciparum* protein, is associated with the erythrocyte skeleton. Molecular and Biochemical Parasitology 111, 107–121. https://doi.org/10.1016/S0166-6851(00)00301-7

Boal, D.H., 1994. Computer simulation of a model network for the erythrocyte cytoskeleton. Biophys J 67, 521–529. https://doi.org/10.1016/S0006-3495(94)80511-9

Boddey, J.A., Hodder, A.N., Günther, S., Gilson, P.R., Patsiouras, H., Kapp, E.A., Pearce, J.A., de Koning-Ward, T.F., Simpson, R.J., Crabb, B.S., Cowman, A.F., 2010. An aspartyl protease directs malaria effector proteins to the host cell. Nature 463, 627–631. https://doi.org/10.1038/nature08728

Brown, J.W., Bullitt, E., Sriswasdi, S., Harper, S., Speicher, D.W., McKnight, C.J., 2015. The Physiological Molecular Shape of Spectrin: A Compact Supercoil Resembling a Chinese Finger Trap. PLOS Computational Biology 11, e1004302. https://doi.org/10.1371/journal.pcbi.1004302

Bryk, A.H., Wiśniewski, J.R., 2017. Quantitative Analysis of Human Red Blood Cell Proteome. J. Proteome Res. 16, 2752–2761. https://doi.org/10.1021/acs.jproteome.7b00025

Buffet, P.A., Safeukui, I., Deplaine, G., Brousse, V., Prendki, V., Thellier, M., Turner, G.D., Mercereau-Puijalon, O., 2011. The pathogenesis of *Plasmodium falciparum* malaria in humans: insights from splenic physiology. Blood 117, 381–392. https://doi.org/10.1182/blood-2010-04-202911

Bullen, H.E., Charnaud, S.C., Kalanon, M., Riglar, D.T., Dekiwadia, C., Kangwanrangsan, N., Torii, M., Tsuboi, T., Baum, J., Ralph, S.A., Cowman, A.F., Koning-Ward, T.F. de, Crabb, B.S., Gilson, P.R., 2012. Biosynthesis, Localization, and Macromolecular Arrangement of the *Plasmodium falciparum* Translocon of Exported Proteins (PTEX) *. Journal of Biological Chemistry 287, 7871–7884. https://doi.org/10.1074/jbc.M111.328591

Bultrini, E., Brick, K., Mukherjee, S., Zhang, Y., Silvestrini, F., Alano, P., Pizzi, E., 2009. Revisiting the *Plasmodium falciparum* RIFIN family: from comparative genomics to 3D-model prediction. BMC Genomics 10, 445. https://doi.org/10.1186/1471-2164-10-445

Calhoun, S.F., Reed, J., Alexander, N., Mason, C.E., Deitsch, K.W., Kirkman, L.A., 2017. Chromosome End Repair and Genome Stability in *Plasmodium falciparum*. mBio 8, e00547-17. https://doi.org/10.1128/mBio.00547-17

Callaghan, P.S., Hassett, M.R., Roepe, P.D., 2015. Functional Comparison of 45 Naturally Occurring Isoforms of the *Plasmodium falciparum* Chloroquine Resistance Transporter (PfCRT). Biochemistry 54, 5083–5094. https://doi.org/10.1021/acs.biochem.5b00412

Camara, S., Ahoua Alou, L.P., Koffi, A.A., Clegban, Y.C.M., Kabran, J.-P., Koffi, F.M., Koffi, K., Pennetier, C., 2018. Efficacy of Interceptor® G2, a new long-lasting insecticidal net against wild pyrethroid-resistant Anopheles gambiae s.s. from Côte d'Ivoire: a semi-field trial. Parasite 25, 42. https://doi.org/10.1051/parasite/2018042

Cejka, P., Cannavo, E., Polaczek, P., Masuda-Sasa, T., Pokharel, S., Campbell, J.L., Kowalczykowski, S.C., 2010. DNA end resection by Dna2–Sgs1–RPA and its stimulation by Top3–Rmi1 and Mre11–Rad50–Xrs2. Nature 467, 112–116. https://doi.org/10.1038/nature09355

Chang, H.H., Falick, A.M., Carlton, P.M., Sedat, J.W., DeRisi, J.L., Marletta, M.A., 2008. N-terminal processing of proteins exported by malaria parasites. Molecular and Biochemical Parasitology 160, 107–115. https://doi.org/10.1016/j.molbiopara.2008.04.011

Chisholm, S.A., McHugh, E., Lundie, R., Dixon, M.W.A., Ghosh, S., O'Keefe, M., Tilley, L., Kalanon, M., Koning-Ward, T.F. de, 2016. Contrasting Inducible Knockdown of the Auxiliary PTEX Component PTEX88 in *P. falciparum* and P. berghei Unmasks a Role in Parasite Virulence. PLOS ONE 11, e0149296. https://doi.org/10.1371/journal.pone.0149296

Church, L.W., Le, T.P., Bryan, J.P., Gordon, D.M., Edelman, R., Fries, L., Davis, J.R., Herrington, D.A., Clyde, D.F., Shmuklarsky, M.J., Schneider, I., McGovern, T.W., Chulay, J.D., Ballou, W.R., Hoffman, S.L., 1997. Clinical manifestations of *Plasmodium falciparum* malaria experimentally induced by mosquito challenge. J Infect Dis 175, 915–920. https://doi.org/10.1086/513990

Coppel, R.L., Lustigman, S., Murray, L., Anders, R.F., 1988. MESA is a *Plasmodium falciparum* phosphoprotein associated with the erythrocyte membrane skeleton. Molecular and Biochemical Parasitology 31, 223–231. https://doi.org/10.1016/0166-6851(88)90152-1

Cowman, A.F., Healer, J., Marapana, D., Marsh, K., 2016. Malaria: Biology and Disease. Cell 167, 610–624. https://doi.org/10.1016/j.cell.2016.07.055

Crabb, B.S., Cooke, B.M., Reeder, J.C., Waller, R.F., Caruana, S.R., Davern, K.M., Wickham, M.E., Brown, G.V., Coppel, R.L., Cowman, A.F., 1997. Targeted Gene Disruption Shows That Knobs Enable Malaria-Infected Red Cells to Cytoadhere under Physiological Shear Stress. Cell 89, 287–296. https://doi.org/10.1016/S0092-8674(00)80207-X

Culvenor, J.G., Langford, C.J., Crewther, P.E., Saint, R.B., Coppel, R.L., Kemp, D.J., Anders, R.F., Brown, G.V., 1987. *Plasmodium falciparum:* Identification and localization of a knob protein antigen expressed by a cDNA clone. Experimental Parasitology 63, 58–67. https://doi.org/10.1016/0014-4894(87)90078-6

Cutts, E.E., Laasch, N., Reiter, D.M., Trenker, R., Slater, L.M., Stansfeld, P.J., Vakonakis, I., 2017. Structural analysis of *P. falciparum* KAHRP and PfEMP1 complexes with host erythrocyte spectrin suggests a model for cytoadherent knob protrusions. PLOS Pathogens 13, e1006552. https://doi.org/10.1371/journal.ppat.1006552

Cyrklaff, M., Sanchez, C.P., Kilian, N., Bisseye, C., Simpore, J., Frischknecht, F., Lanzer, M., 2011. Hemoglobins S and C Interfere with Actin Remodeling in *Plasmodium falciparum*–Infected Erythrocytes. Science 334, 1283–1286. https://doi.org/10.1126/science.1213775

Daubersies, P., Thomas, A.W., Millet, P., Brahimi, K., Langermans, J.A.M., Ollomo, B., BenMohamed, L., Slierendregt, B., Eling, W., Van Belkum, A., Dubreuil, G., Meis, J.F.G.M., Guérin-Marchand, C., Cayphas, S., Cohen, J., Gras-Masse, H., Druilhe, P., 2000. Protection against *Plasmodium falciparum* malaria in chimpanzees by immunization with the conserved pre-erythrocytic liver-stage antigen 3. Nat Med 6, 1258–1263. https://doi.org/10.1038/81366

Davies, H.M., Thalassinos, K., Osborne, A.R., 2016. Expansion of Lysine-rich Repeats in *Plasmodium* Proteins Generates Novel Localization Sequences That Target the Periphery of the Host Erythrocyte*. Journal of Biological Chemistry 291, 26188–26207. https://doi.org/10.1074/jbc.M116.761213

de Koning-Ward, T.F., Dixon, M.W.A., Tilley, L., Gilson, P.R., 2016. *Plasmodium* species: master renovators of their host cells. Nat Rev Microbiol 14, 494–507. https://doi.org/10.1038/nrmicro.2016.79

de Koning-Ward, T.F., Gilson, P.R., Boddey, J.A., Rug, M., Smith, B.J., Papenfuss, A.T., Sanders, P.R., Lundie, R.J., Maier, A.G., Cowman, A.F., Crabb, B.S., 2009. A newly discovered protein export machine in malaria parasites. Nature 459, 945–949. https://doi.org/10.1038/nature08104

Deil, S., 2014. New insights into PEXEL-mediated protein export in *Plasmodium falciparum*: The role of N-terminal acetylation.

Deplaine, G., Safeukui, I., Jeddi, F., Lacoste, F., Brousse, V., Perrot, S., Biligui, S., Guillotte, M., Guitton, C., Dokmak, S., Aussilhou, B., Sauvanet, A., Cazals Hatem, D., Paye, F., Thellier, M., Mazier, D., Milon, G., Mohandas, N., Mercereau-Puijalon, O., David, P.H., Buffet, P.A., 2011. The sensing of poorly deformable red blood cells by the human spleen can be mimicked in vitro. Blood 117, e88–e95. https://doi.org/10.1182/blood-2010-10-312801

Deplazes, E., van Bronswijk, W., Zhu, F., Barron, L.D., Ma, S., Nafie, L.A., Jalkanen, K.J., 2008. A combined theoretical and experimental study of the structure and vibrational absorption, vibrational circular dichroism, Raman and Raman optical activity spectra of the L-histidine zwitterion. Theor Chem Account 119, 155–176. https://doi.org/10.1007/s00214-007-0276-8

Dimasuay, K.G., Gong, L., Rosario, F., McBryde, E., Spelman, T., Glazier, J., Rogerson, S.J., Beeson, J.G., Jansson, T., Devenish, R.J., Boeuf, P., 2017. Impaired placental autophagy in placental malaria. PLOS ONE 12, e0187291. https://doi.org/10.1371/journal.pone.0187291

Dondorp, A.M., Nosten, F., Yi, P., Das, D., Phyo, A.P., Tarning, J., Lwin, K.M., Ariey, F., Hanpithakpong, W., Lee, S.J., Ringwald, P., Silamut, K., Imwong, M., Chotivanich, K., Lim, P., Herdman, T., An, S.S., Yeung, S., Singhasivanon, P., Day, N.P.J., Lindegardh, N., Socheat, D., White, N.J., 2009. Artemisinin resistance in *Plasmodium falciparum* malaria. N Engl J Med 361, 455–467. https://doi.org/10.1056/NEJMoa0808859

Doudna, J.A., Charpentier, E., 2014. The new frontier of genome engineering with CRISPR-Cas9. Science 346, 1258096. https://doi.org/10.1126/science.1258096

Dueva, R., Iliakis, G., 2013. Alternative pathways of non-homologous end joining (NHEJ) in genomic instability and cancer. Translational Cancer Research 2. https://doi.org/10.3978/j.issn.2218-676X.2013.05.02

Duffy, M.F., Caragounis, A., Noviyanti, R., Kyriacou, H.M., Choong, E.K., Boysen, K., Healer, J., Rowe, J.A., Molyneux, M.E., Brown, G.V., Rogerson, S.J., 2006. Transcribed var Genes Associated with Placental Malaria in Malawian Women. Infect Immun 74, 4875–4883. https://doi.org/10.1128/IAI.01978-05

Ecker, A., Lehane, A.M., Clain, J., Fidock, D.A., 2012. PfCRT and its role in antimalarial drug resistance. Trends Parasitol 28, 504–514. https://doi.org/10.1016/j.pt.2012.08.002

Eder, P.S., Soong, C.J., Tao, M., 1986. Phosphorylation reduces the affinity of protein 4.1 for spectrin. Biochemistry 25, 1764–1770. https://doi.org/10.1021/bi00355a047

Egan, T.J., Combrinck, J.M., Egan, J., Hearne, G.R., Marques, H.M., Ntenteni, S., Sewell, B.T., Smith, P.J., Taylor, D., van Schalkwyk, D.A., Walden, J.C., 2002. Fate of haem iron in the malaria parasite *Plasmodium falciparum*. Biochem J 365, 343–347. https://doi.org/10.1042/BJ20020793

Elsworth, B., Matthews, K., Nie, C.Q., Kalanon, M., Charnaud, S.C., Sanders, P.R., Chisholm, S.A., Counihan, N.A., Shaw, P.J., Pino, P., Chan, J.-A., Azevedo, M.F., Rogerson, S.J., Beeson, J.G., Crabb, B.S., Gilson, P.R., de Koning-Ward, T.F., 2014. PTEX is an essential nexus for protein export in malaria parasites. Nature 511, 587–591. https://doi.org/10.1038/nature13555

Elsworth, B., Sanders, P.R., Nebl, T., Batinovic, S., Kalanon, M., Nie, C.Q., Charnaud, S.C., Bullen, H.E., de Koning Ward, T.F., Tilley, L., Crabb, B.S., Gilson, P.R., 2016. Proteomic analysis reveals novel proteins associated with the *Plasmodium* protein exporter PTEX and a loss of complex stability upon truncation of the core PTEX component, PTEX150. Cellular Microbiology 18, 1551–1569. https://doi.org/10.1111/cmi.12596

Fortier, N., Snyder, L.M., Garver, F., Kiefer, C., McKenney, J., Mohandas, N., 1988. The Relationship Between in vivo Generated Hemoglobin Skeletal Protein Complex and Increased Red Cell Membrane Rigidity. Blood 71, 1427–1431. https://doi.org/10.1182/blood.V71.5.1427.1427

Francischetti, I.M.B., Seydel, K.B., Monteiro, R.Q., 2008. Blood Coagulation, Inflammation, and Malaria. Microcirculation 15, 81–107. https://doi.org/10.1080/10739680701451516

Fried, M., Duffy, P.E., 1996. Adherence of *Plasmodium falciparum* to Chondroitin Sulfate A in the Human Placenta. Science 272, 1502–1504. https://doi.org/10.1126/science.272.5267.1502

Fried, M., Nosten, F., Brockman, A., Brabin, B.J., Duffy, P.E., 1998. Maternal antibodies block malaria. Nature 395, 851–852. https://doi.org/10.1038/27570

Friedman, M.J., Roth, E.F., Nagel, R.L., Trager, W., 1979. *Plasmodium falciparum:* Physiological interactions with the human sickle cell. Experimental Parasitology 47, 73–80. https://doi.org/10.1016/0014-4894(79)90009-2

Gabriela, M., Matthews, K.M., Boshoven, C., Kouskousis, B., Jonsdottir, T.K., Bullen, H.E., Modak, J., Steer, D.L., Sleebs, B.E., Crabb, B.S., Koning-Ward, T.F. de, Gilson, P.R., 2022. A revised mechanism for how *Plasmodium falciparum* recruits and exports proteins into its erythrocytic host cell. PLOS Pathogens 18, e1009977. https://doi.org/10.1371/journal.ppat.1009977

Ganter, M., Goldberg, J.M., Dvorin, J.D., Paulo, J.A., King, J.G., Tripathi, A.K., Paul, A.S., Yang, J., Coppens, I., Jiang, R.H.Y., Elsworth, B., Baker, D.A., Dinglasan, R.R., Gygi, S.P., Duraisingh, M.T., 2017. *Plasmodium falciparum* CRK4 directs continuous rounds of DNA replication during schizogony. Nat Microbiol 2, 17017. https://doi.org/10.1038/nmicrobiol.2017.17

Garten, M., Nasamu, A.S., Niles, J.C., Zimmerberg, J., Goldberg, D.E., Beck, J.R., 2018. EXP2 is a nutrient-permeable channel in the vacuolar membrane of *Plasmodium* and is essential for protein export via PTEX. Nat Microbiol 3, 1090–1098. https://doi.org/10.1038/s41564-018-0222-7

Gilson, P.R., Gabriela, M., Barnes, C.B.G., Leong, D., Sleebs, B.E., Schneider, M.P., Littler, D.R., Crabb, B.S., Koning-Ward, T.F. de, 2023. Sequence elements within the PEXEL motif and its downstream region modulate PTEX dependent protein export in *Plasmodium falciparum* .

Glenister, F.K., Coppel, R.L., Cowman, A.F., Mohandas, N., Cooke, B.M., 2002. Contribution of parasite proteins to altered mechanical properties of malaria-infected red blood cells. Blood 99, 1060–1063. https://doi.org/10.1182/blood.V99.3.1060

Goel, S., Palmkvist, M., Moll, K., Joannin, N., Lara, P., R Akhouri, R., Moradi, N., Öjemalm, K., Westman, M., Angeletti, D., Kjellin, H., Lehtiö, J., Blixt, O., Ideström, L., Gahmberg, C.G., Storry, J.R., Hult, A.K., Olsson, M.L., von Heijne, G., Nilsson, I., Wahlgren, M., 2015. RIFINs are adhesins implicated in severe *Plasmodium falciparum* malaria. Nat Med 21, 314–317. https://doi.org/10.1038/nm.3812

Gokhin, D.S., Fowler, V.M., 2016. Feisty filaments: actin dynamics in the red blood cell membrane skeleton. Current Opinion in Hematology 23, 206. https://doi.org/10.1097/MOH.0000000000000227

Gokhin, D.S., Nowak, R.B., Khoory, J.A., Piedra, A. de la, Ghiran, I.C., Fowler, V.M., 2015. Dynamic actin filaments control the mechanical behavior of the human red blood cell membrane. MBoC 26, 1699–1710. https://doi.org/10.1091/mbc.E14-12-1583

Gopalakrishnan, A.M., Kumar, N., 2013. Opposing roles for two molecular forms of replication protein A in Rad51-Rad54-mediated DNA recombination in *Plasmodium falciparum*. mBio 4, e00252-00213. https://doi.org/10.1128/mBio.00252-13

Gruenberg, J., Allred, D.R., Sherman, I.W., 1983. Scanning electron microscope-analysis of the protrusions (knobs) present on the surface of *Plasmodium falciparum*-infected erythrocytes. Journal of Cell Biology 97, 795–802. https://doi.org/10.1083/jcb.97.3.795

Grüring, C., Heiber, A., Kruse, F., Flemming, S., Franci, G., Colombo, S.F., Fasana, E., Schoeler, H., Borgese, N., Stunnenberg, H.G., Przyborski, J.M., Gilberger, T.-W., Spielmann, T., 2012. Uncovering Common Principles in Protein Export of Malaria Parasites. Cell Host & Microbe 12, 717–729. https://doi.org/10.1016/j.chom.2012.09.010

Gulati, S., Ekland, E.H., Ruggles, K.V., Chan, R.B., Jayabalasingham, B., Zhou, B., Mantel, P.-Y., Lee, M.C.S., Spottiswoode, N., Coburn-Flynn, O., Hjelmqvist, D., Worgall, T.S., Marti, M., Di Paolo, G., Fidock, D.A., 2015. Profiling the Essential Nature of Lipid Metabolism in Asexual Blood and Gametocyte Stages of *Plasmodium falciparum*. Cell Host Microbe 18, 371–381. https://doi.org/10.1016/j.chom.2015.08.003

Hadley, T.J., Leech, J.H., Green, T.J., Daniel, W.A., Wahlgren, M., Miller, L.H., Howard, R.J., 1983. A comparison of Knobby (K+) and Knobless (K−) parasites from two strains of *Plasmodium falciparum*. Molecular and Biochemical Parasitology 9, 271–278. https://doi.org/10.1016/0166-6851(83)90102-0

Hallée, S., Thériault, C., Gagnon, D., Kehrer, J., Frischknecht, F., Mair, G.R., Richard, D., 2018. Identification of a Golgi apparatus protein complex important for the asexual erythrocytic cycle of the malaria parasite *Plasmodium falciparum*. Cellular Microbiology 20, e12843. https://doi.org/10.1111/cmi.12843

Hanssen, E., Sougrat, R., Frankland, S., Deed, S., Klonis, N., Lippincott-Schwartz, J., Tilley, L., 2008. Electron tomography of the Maurer's cleft organelles of *Plasmodium falciparum*-infected erythrocytes reveals novel structural features. Molecular Microbiology 67, 703–718. https://doi.org/10.1111/j.1365-2958.2007.06063.x

Hasan, M.M., Polino, A.J., Mukherjee, S., Vaupel, B., Goldberg, D.E., 2023. The mature N-termini of *Plasmodium* effector proteins confer specificity of export. mBio 14, e01215-23. https://doi.org/10.1128/mbio.01215-23

Heiber, A., Kruse, F., Pick, C., Grüring, C., Flemming, S., Oberli, A., Schoeler, H., Retzlaff, S., Mesén-Ramírez, P., Hiss, J.A., Kadekoppala, M., Hecht, L., Holder, A.A., Gilberger, T.-W., Spielmann, T., 2013. Identification of New PNEPs Indicates a Substantial Non-PEXEL Exportome and Underpins Common Features in *Plasmodium falciparum* Protein Export. PLOS Pathogens 9, e1003546. https://doi.org/10.1371/journal.ppat.1003546

Heinrich, V., Ritchie, K., Mohandas, N., Evans, E., 2001. Elastic Thickness Compressibilty of the Red Cell Membrane. Biophysical Journal 81, 1452–1463. https://doi.org/10.1016/S0006-3495(01)75800-6

Helms, J.B., Rothman, J.E., 1992. Inhibition by brefeldin A of a Golgi membrane enzyme that catalyses exchange of guanine nucleotide bound to ARF. Nature 360, 352–354. https://doi.org/10.1038/360352a0

Ho, C.-M., Beck, J.R., Lai, M., Cui, Y., Goldberg, D.E., Egea, P.F., Zhou, Z.H., 2018. Malaria parasite translocon structure and mechanism of effector export. Nature 561, 70–75. https://doi.org/10.1038/s41586-018-0469-4

Hollin, T., De Witte, C., Lenne, A., Pierrot, C., Khalife, J., 2016. Analysis of the interactome of the Ser/Thr Protein Phosphatase type 1 in *Plasmodium falciparum*. BMC Genomics 17, 246. https://doi.org/10.1186/s12864-016-2571-z

Hornig, R., Lutz, H.U., 2000. Band 3 protein clustering on human erythrocytes promotes binding of naturally occurring anti-band 3 and anti-spectrin antibodies. Exp Gerontol 35, 1025–1044. https://doi.org/10.1016/s0531-5565(00)00126-1

Horrocks, P., Pinches, R.A., Chakravorty, S.J., Papakrivos, J., Christodoulou, Z., Kyes, S.A., Urban, B.C., Ferguson, D.J.P., Newbold, C.I., 2005. PfEMP1 expression is reduced on the surface of knobless *Plasmodium falciparum* infected erythrocytes. Journal of Cell Science 118, 2507–2518. https://doi.org/10.1242/jcs.02381

Huttlin, E.L., Jedrychowski, M.P., Elias, J.E., Goswami, T., Rad, R., Beausoleil, S.A., Villén, J., Haas, W., Sowa, M.E., Gygi, S.P., 2010. A Tissue-Specific Atlas of Mouse Protein Phosphorylation and Expression. Cell 143, 1174–1189. https://doi.org/10.1016/j.cell.2010.12.001

Imai, T., Ishida, H., Suzue, K., Taniguchi, T., Okada, H., Shimokawa, C., Hisaeda, H., 2015. Cytotoxic activities of CD8+ T cells collaborate with macrophages to protect against blood-stage murine malaria. eLife 4, e04232. https://doi.org/10.7554/eLife.04232

Ipsaro, J.J., Huang, L., Mondragón, A., 2009. Structures of the spectrin-ankyrin interaction binding domains. Blood 113, 5385–5393. https://doi.org/10.1182/blood-2008-10-184358

Ishino, Y., Shinagawa, H., Makino, K., Amemura, M., Nakata, A., 1987. Nucleotide sequence of the iap gene, responsible for alkaline phosphatase isozyme conversion in Escherichia coli, and identification of the gene product. Journal of Bacteriology 169, 5429–5433. https://doi.org/10.1128/jb.169.12.5429-5433.1987

Jäger, J., Patra, P., Sanchez, C.P., Lanzer, M., Schwarz, U.S., 2021. A particle-based computational model to analyse remodelling of the red blood cell cytoskeleton during malaria infections. https://doi.org/10.1101/2021.10.04.462981

Jansen, Ruud., Embden, Jan.D.A. van, Gaastra, Wim., Schouls, Leo.M., 2002. Identification of genes that are associated with DNA repeats in prokaryotes. Molecular Microbiology 43, 1565–1575. https://doi.org/10.1046/j.1365-2958.2002.02839.x

Jespersen, J.S., Wang, C.W., Mkumbaye, S.I., Minja, D.T., Petersen, B., Turner, L., Petersen, J.E., Lusingu, J.P., Theander, T.G., Lavstsen, T., 2016. *Plasmodium falciparum* var genes expressed in children with severe malaria encode CIDRα1 domains. EMBO Molecular Medicine 8, 839–850. https://doi.org/10.15252/emmm.201606188

Jinek, M., Chylinski, K., Fonfara, I., Hauer, M., Doudna, J.A., Charpentier, E., 2012. A Programmable Dual-RNA–Guided DNA Endonuclease in Adaptive Bacterial Immunity. Science 337, 816–821. https://doi.org/10.1126/science.1225829

Jonsdottir, T.K., Counihan, N.A., Modak, J.K., Kouskousis, B., Sanders, P.R., Gabriela, M., Bullen, H.E., Crabb, B.S., de Koning-Ward, T.F., Gilson, P.R., 2021. Characterisation of complexes formed by parasite proteins exported into the host cell compartment of *Plasmodium falciparum* infected red blood cells. Cell Microbiol 23, e13332. https://doi.org/10.1111/cmi.13332

Kaiser, C., 2000. Thinking about p24 proteins and how transport vesicles select their cargo. Proceedings of the National Academy of Sciences 97, 3783–3785. https://doi.org/10.1073/pnas.97.8.3783

Kehrer, J., Pietsch, E., Ricken, D., Strauss, L., Heinze, J.M., Gilberger, T., Frischknecht, F., 2024. APEX-based proximity labeling in *Plasmodium* identifies a membrane protein with dual functions during mosquito infection. PLOS Pathogens 20, e1012788. https://doi.org/10.1371/journal.ppat.1012788

Khosh-Naucke, M., Becker, J., Mesén-Ramírez, P., Kiani, P., Birnbaum, J., Fröhlke, U., Jonscher, E., Schlüter, H., Spielmann, T., 2018. Identification of novel parasitophorous vacuole proteins in *P. falciparum* parasites using BioID. International Journal of Medical Microbiology, Intracellular Compartments as Places of Pathogen-Host Interaction 308, 13–24. https://doi.org/10.1016/j.ijmm.2017.07.007

Kilejian, A., 1979. Characterization of a protein correlated with the production of knob-like protrusions on membranes of erythrocytes infected with *Plasmodium falciparum*. Proc Natl Acad Sci U S A 76, 4650–4653. https://doi.org/10.1073/pnas.76.9.4650

Kilejian, A., Rashid, M.A., Aikawa, M., Aji, T., Yang, Y.-F., 1991. Selective association of a fragment of the knob protein with spectrin, actin and the red cell membrane. Molecular and Biochemical Parasitology 44, 175–181. https://doi.org/10.1016/0166-6851(91)90003-O

Kilili, G.K., LaCount, D.J., 2011. An Erythrocyte Cytoskeleton-Binding Motif in Exported *Plasmodium falciparum* Proteins. Eukaryotic Cell 10, 1439–1447. https://doi.org/10.1128/ec.05180-11

Kirkman, L.A., Lawrence, E.A., Deitsch, K.W., 2014. Malaria parasites utilize both homologous recombination and alternative end joining pathways to maintain genome integrity. Nucleic Acids Research 42, 370–379. https://doi.org/10.1093/nar/gkt881

Klei, T.R.L., Dalimot, J., Nota, B., Veldthuis, M., Mul, F.P.J., Rademakers, T., Hoogenboezem, M., Nagelkerke, S.Q., van IJcken, W.F.J., Oole, E., Svendsen, P., Moestrup, S.K., van Alphen, F.P.J., Meijer, A.B., Kuijpers, T.W., van Zwieten, R., van Bruggen, R., 2020. Hemolysis in the spleen drives erythrocyte turnover. Blood 136, 1579–1589. https://doi.org/10.1182/blood.2020005351

Knöckel, J., Dundas, K., Yang, A.S.P., Galaway, F., Metcalf, T., Gemert, G.-J. van, Sauerwein, R.W., Rayner, J.C., Billker, O., Wright, G.J., 2021. Systematic Identification of *Plasmodium* Falciparum Sporozoite Membrane Protein Interactions Reveals an Essential Role for the p24 Complex in Host Infection. Molecular & Cellular Proteomics 20. https://doi.org/10.1074/mcp.RA120.002432

Knuepfer, E., Rug, M., Klonis, N., Tilley, L., Cowman, A.F., 2005a. Trafficking of the major virulence factor to the surface of transfected P falciparum–infected erythrocytes. Blood 105, 4078–4087. https://doi.org/10.1182/blood-2004-12-4666

Knuepfer, E., Rug, M., Klonis, N., Tilley, L., Cowman, A.F., 2005b. Trafficking determinants for PfEMP3 export and assembly under the *Plasmodium falciparum*-infected red blood cell membrane. Molecular Microbiology 58, 1039–1053. https://doi.org/10.1111/j.1365-2958.2005.04895.x

Koopmans, L.C., van Wolfswinkel, M.E., Hesselink, D.A., Hoorn, E.J., Koelewijn, R., van Hellemond, J.J., van Genderen, P.J.J., 2015. Acute kidney injury in imported *Plasmodium falciparum* malaria. Malar J 14, 523. https://doi.org/10.1186/s12936-015-1057-9

Külzer, S., Charnaud, S., Dagan, T., Riedel, J., Mandal, P., Pesce, E.R., Blatch, G.L., Crabb, B.S., Gilson, P.R., Przyborski, J.M., 2012. lasmodium falciparum-encoded exported hsp70/hsp40 chaperone/co-chaperone complexes within the host erythrocyte. Cellular Microbiology 14, 1784–1795. https://doi.org/10.1111/j.1462-5822.2012.01840.x

Külzer, S., Rug, M., Brinkmann, K., Cannon, P., Cowman, A., Lingelbach, K., Blatch, G.L., Maier, A.G., Przyborski, J.M., 2010. Parasite-encoded Hsp40 proteins define novel mobile structures in the cytosol of the *P. falciparum*-infected erythrocyte. Cellular Microbiology 12, 1398–1420. https://doi.org/10.1111/j.1462-5822.2010.01477.x

Kumar, S., Bandyopadhyay, U., 2005. Free heme toxicity and its detoxification systems in human. Toxicol Lett 157, 175–188. https://doi.org/10.1016/j.toxlet.2005.03.004

Kyes, S.A., Rowe, J.A., Kriek, N., Newbold, C.I., 1999. Rifins: A second family of clonally variant proteins expressed on the surface of red cells infected with *Plasmodium falciparum*. Proceedings of the National Academy of Sciences 96, 9333–9338. https://doi.org/10.1073/pnas.96.16.9333

Lasonder, E., Green, J.L., Camarda, G., Talabani, H., Holder, A.A., Langsley, G., Alano, P., 2012. The *Plasmodium falciparum* schizont phosphoproteome reveals extensive phosphatidylinositol and cAMP-protein kinase A signaling. J Proteome Res 11, 5323–5337. https://doi.org/10.1021/pr300557m

Lee, A.H., Symington, L.S., Fidock, D.A., 2014. DNA Repair Mechanisms and Their Biological Roles in the Malaria Parasite *Plasmodium falciparum*. Microbiology and Molecular Biology Reviews 78, 469–486. https://doi.org/10.1128/mmbr.00059-13

Lee, M.C.S., Moura, P.A., Miller, E.A., Fidock, D.A., 2008. *Plasmodium falciparum* Sec24 marks transitional ER that exports a model cargo via a diacidic motif. Molecular Microbiology 68, 1535–1546. https://doi.org/10.1111/j.1365-2958.2008.06250.x

Leech, J.H., Barnwell, J.W., Aikawa, M., Miller, L.H., Howard, R.J., 1984. *Plasmodium falciparum* malaria: association of knobs on the surface of infected erythrocytes with a histidine-rich protein and the erythrocyte skeleton. J Cell Biol 98, 1256–1264. https://doi.org/10.1083/jcb.98.4.1256

Lennartz, F., Adams, Y., Bengtsson, A., Olsen, R.W., Turner, L., Ndam, N.T., Ecklu-Mensah, G., Moussiliou, A., Ofori, M.F., Gamain, B., Lusingu, J.P., Petersen, J.E.V., Wang, C.W., Nunes-Silva, S., Jespersen, J.S., Lau, C.K.Y., Theander, T.G., Lavstsen, T., Hviid, L., Higgins, M.K., Jensen, A.T.R., 2017. Structure-Guided Identification of a Family of Dual Receptor-Binding PfEMP1 that Is Associated with Cerebral Malaria. Cell Host & Microbe 21, 403–414. https://doi.org/10.1016/j.chom.2017.02.009

Li, H., Qiang, Y., Li, X., Brugnara, C., Buffet, P.A., Dao, M., Karniadakis, G.E., Suresh, S., 2024. Biomechanics of phagocytosis of red blood cells by macrophages in the human spleen. Proceedings of the National Academy of Sciences 121, e2414437121. https://doi.org/10.1073/pnas.2414437121

Li, X., Chen, H., Bahamontes-Rosa, N., Kun, J.F.J., Traore, B., Crompton, P.D., Chishti, A.H., 2009. *Plasmodium falciparum* signal peptide peptidase is a promising drug target against blood stage malaria. Biochemical and Biophysical Research Communications 380, 454–459. https://doi.org/10.1016/j.bbrc.2009.01.083

Lim H. W., G., Wortis, M., Mukhopadhyay, R., 2002. Stomatocyte–discocyte–echinocyte sequence of the human red blood cell: Evidence for the bilayer– couple hypothesis from membrane mechanics. Proceedings of the National Academy of Sciences 99, 16766–16769. https://doi.org/10.1073/pnas.202617299

Liu, Y., Nie, X., Yao, X., Shou, H., Yuan, Y., Ge, Y., Tong, X., Lee, H.-Y., Gao, X., 2024. Developing an erythrocyte–MHC-I conjugate for cancer treatment. Cell Discov 10, 1–14. https://doi.org/10.1038/s41421-024-00713-9

Low, H., Chua, C.S., Sim, T.-S., 2012. *Plasmodium falciparum* possesses a unique dual-specificity serine/threonine and tyrosine kinase, Pfnek3. Cell. Mol. Life Sci. 69, 1523–1535. https://doi.org/10.1007/s00018-011-0888-y

Lucchi, N.W., Peterson, D.S., Moore, J.M., 2008. Immunologic activation of human syncytiotrophoblast by *Plasmodium falciparum*. Malaria Journal 7, 42. https://doi.org/10.1186/1475-2875-7-42

Lustigman, S., Anders, R.F., Brown, G.V., Coppel, R.L., 1990. The mature-parasite-infected erythrocyte surface antigen (MESA) of *Plasmodium falciparum* associates with the erythrocyte membrane skeletal protein, band 4.1. Molecular and Biochemical Parasitology 38, 261–270. https://doi.org/10.1016/0166-6851(90)90029-L

Lux, S.E., IV, 2016. Anatomy of the red cell membrane skeleton: unanswered questions. Blood 127, 187–199. https://doi.org/10.1182/blood-2014-12-512772

Machnicka, B., Czogalla, A., Hryniewicz-Jankowska, A., Bogusławska, D.M., Grochowalska, R., Heger, E., Sikorski, A.F., 2014. Spectrins: A structural platform for stabilization and activation of membrane channels, receptors and transporters. Biochimica et Biophysica Acta (BBA) - Biomembranes, Reciprocal influences between cell cytoskeleton and membrane channels, receptors and transporters 1838, 620–634. https://doi.org/10.1016/j.bbamem.2013.05.002

Magowan, C., Coppel, R., Lau, A., Moronne, M., Tchernia, G., Mohandas, N., 1995. Role of the *Plasmodium falciparum* mature-parasite-infected erythrocyte surface antigen (MESA/PfEMP-2) in malarial infection of erythrocytes. Blood 86, 3196–3204. https://doi.org/10.1182/blood.V86.8.3196.3196

Maiga, H., Lasry, E., Diarra, M., Sagara, I., Bamadio, A., Traore, A., Coumare, S., Bahonan, S., Sangare, B., Dicko, Y., Diallo, N., Tembely, A., Traore, D., Niangaly, H., Dao, F., Haidara, A., Dicko, A., Doumbo, O.K., Djimde, A.A., 2016. Seasonal Malaria Chemoprevention with Sulphadoxine-Pyrimethamine and Amodiaquine Selects Pfdhfr-dhps Quintuple Mutant Genotype in Mali. PLOS ONE 11, e0162718. https://doi.org/10.1371/journal.pone.0162718

Marapana, D.S., Dagley, L.F., Sandow, J.J., Nebl, T., Triglia, T., Pasternak, M., Dickerman, B.K., Crabb, B.S., Gilson, P.R., Webb, A.I., Boddey, J.A., Cowman, A.F., 2018. Plasmepsin V cleaves malaria effector proteins in a distinct endoplasmic reticulum translocation interactome for export to the erythrocyte. Nat Microbiol 3, 1010–1022. https://doi.org/10.1038/s41564-018-0219-2

Matsuoka, Y., Li, X., Bennett, V., 2000. Adducin: structure, function and regulation. CMLS, Cell. Mol. Life Sci. 57, 884–895. https://doi.org/10.1007/PL00000731

Mattei, D., Berzins, K., Wahlgren, M., Udomsangpetch, R., Perlmann, P., Griesser, H.W., Scherf, A., Müjller–Hill, B., Bonnefoy, S., Guillotte, M., Langsley, G., Silva, L.P.D., Mercereau–Puijalon, O., 1989. Cross–reactive antigenic determinants present on different *Plasmodium falciparum* blood–stage antigens. Parasite Immunology 11, 15–29. https://doi.org/10.1111/j.1365-3024.1989.tb00645.x

Matthews, K., Kalanon, M., Chisholm, S.A., Sturm, A., Goodman, C.D., Dixon, M.W.A., Sanders, P.R., Nebl, T., Fraser, F., Haase, S., McFadden, G.I., Gilson, P.R., Crabb, B.S., de Koning-Ward, T.F., 2013. The *Plasmodium* translocon of exported proteins (PTEX) component thioredoxin-2 is important for maintaining normal blood-stage growth. Molecular Microbiology 89, 1167–1186. https://doi.org/10.1111/mmi.12334

Matthews, K.M., Pitman, E.L., Koning-Ward, T.F. de, 2019. Illuminating how malaria parasites export proteins into host erythrocytes. Cellular Microbiology 21, e13009. https://doi.org/10.1111/cmi.13009

Matz, J.M., Ingmundson, A., Costa Nunes, J., Stenzel, W., Matuschewski, K., Kooij, T.W.A., 2015. In Vivo Function of PTEX88 in Malaria Parasite Sequestration and Virulence. Eukaryotic Cell 14, 528–534. https://doi.org/10.1128/ec.00276-14

Matz, J.M., Matuschewski, K., Kooij, T.W.A., 2013. Two putative protein export regulators promote *Plasmodium* blood stage development in vivo. Molecular and Biochemical Parasitology 191, 44–52. https://doi.org/10.1016/j.molbiopara.2013.09.003

Maubert, B., Fievet, N., Tami, G., Cot, M., Boudin, C., Deloron, P., 1999. Development of Antibodies against Chondroitin Sulfate A-Adherent *Plasmodium falciparum* in Pregnant Women. Infection and Immunity 67, 5367–5371. https://doi.org/10.1128/iai.67.10.5367-5371.1999

Mauritz, J.M.A., Esposito, A., Ginsburg, H., Kaminski, C.F., Tiffert, T., Lew, V.L., 2009. The homeostasis of *Plasmodium falciparum*-infected red blood cells. PLoS Comput Biol 5, e1000339. https://doi.org/10.1371/journal.pcbi.1000339

McMillan, P.J., Millet, C., Batinovic, S., Maiorca, M., Hanssen, E., Kenny, S., Muhle, R.A., Melcher, M., Fidock, D.A., Smith, J.D., Dixon, M.W.A., Tilley, L., 2013. Spatial and temporal mapping of the PfEMP1 export pathway in lasmodium falciparum. Cellular Microbiology 15, 1401–1418. https://doi.org/10.1111/cmi.12125

McNamara, C.W., Lee, M.C.S., Lim, C.S., Lim, S.H., Roland, J., Nagle, A., Simon, O., Yeung, B.K.S., Chatterjee, A.K., McCormack, S.L., Manary, M.J., Zeeman, A.-M., Dechering, K.J., Kumar, T.R.S., Henrich, P.P., Gagaring, K., Ibanez, M., Kato, N., Kuhen, K.L., Fischli, C., Rottmann, M., Plouffe, D.M., Bursulaya, B., Meister, S., Rameh, L., Trappe, J., Haasen, D., Timmerman, M., Sauerwein, R.W., Suwanarusk, R., Russell, B., Renia, L., Nosten, F., Tully, D.C., Kocken, C.H.M., Glynne, R.J., Bodenreider, C., Fidock, D.A., Diagana, T.T., Winzeler, E.A., 2013. Targeting *Plasmodium* PI(4)K to eliminate malaria. Nature 504, 248–253. https://doi.org/10.1038/nature12782

McQuaid, F., Rowe, J.A., 2020. Rosetting revisited: a critical look at the evidence for host erythrocyte receptors in *Plasmodium falciparum* rosetting. Parasitology 147, 1–11. https://doi.org/10.1017/S0031182019001288

Mesén-Ramírez, P., Reinsch, F., Soares, A.B., Bergmann, B., Ullrich, A.-K., Tenzer, S., Spielmann, T., 2016. Stable Translocation Intermediates Jam Global Protein Export in *Plasmodium falciparum*

Parasites and Link the PTEX Component EXP2 with Translocation Activity. PLOS Pathogens 12, e1005618. https://doi.org/10.1371/journal.ppat.1005618

Mimitou, E.P., Symington, L.S., 2008. Sae2, Exo1 and Sgs1 collaborate in DNA double-strand break processing. Nature 455, 770–774. https://doi.org/10.1038/nature07312

Miyazaki, S., Chitama, B.-Y.A., Kagaya, W., Lucky, A.B., Zhu, X., Yahata, K., Morita, M., Takashima, E., Tsuboi, T., Kaneko, O., 2021. *Plasmodium falciparum* SURFIN4.1 forms an intermediate complex with PTEX components and Pf113 during export to the red blood cell. Parasitology International 83, 102358. https://doi.org/10.1016/j.parint.2021.102358

Mohandas, N., Gallagher, P.G., 2008. Red cell membrane: past, present, and future. Blood 112, 3939–3948. https://doi.org/10.1182/blood-2008-07-161166

Moreau, A., Yaya, F., Lu, H., Surendranath, A., Charrier, A., Dehapiot, B., Helfer, E., Viallat, A., Peng, Z., 2023. Physical mechanisms of red blood cell splenic filtration. Proc Natl Acad Sci U S A 120, e2300095120. https://doi.org/10.1073/pnas.2300095120

Mosha, J.F., Kulkarni, M.A., Lukole, E., Matowo, N.S., Pitt, C., Messenger, L.A., Mallya, E., Jumanne, M., Aziz, T., Kaaya, R., Shirima, B.A., Isaya, G., Taljaard, M., Martin, J., Hashim, R., Thickstun, C., Manjurano, A., Kleinschmidt, I., Mosha, F.W., Rowland, M., Protopopoff, N., 2022. Effectiveness and cost-effectiveness against malaria of three types of dual-active-ingredient long-lasting insecticidal nets (LLINs) compared with pyrethroid-only LLINs in Tanzania: a four-arm, cluster-randomised trial. The Lancet 399, 1227–1241. https://doi.org/10.1016/S0140-6736(21)02499-5

Mundwiler-Pachlatko, E., Beck, H.-P., 2013. Maurer's clefts, the enigma of *Plasmodium falciparum*. PNAS 110, 19987–19994.

Nacher, M., Singhasivanon, P., Silachamroon, U., Treeprasertsuk, S., Vannaphan, S., Traore, B., Gay, F., Looareesuwan, S., 2001. Helminth infections are associated with protection from malaria-related acute renal failure and jaundice in Thailand. https://doi.org/10.4269/ajtmh.2001.65.834

Ng, W., 2020. ICP-MS analysis of metal and metalloid concentrations of common microbiological growth media reveals presence of heavy metals. https://doi.org/10.1101/2020.09.25.313221

N'Guessan, R., Odjo, A., Ngufor, C., Malone, D., Rowland, M., 2016. A Chlorfenapyr Mixture Net Interceptor® G2 Shows High Efficacy and Wash Durability against Resistant Mosquitoes in West Africa. PLoS One 11, e0165925. https://doi.org/10.1371/journal.pone.0165925

Ngufor, C., Fagbohoun, J., Critchley, J., N'Guessan, R., Todjinou, D., Malone, D., Akogbeto, M., Rowland, M., 2017. Which intervention is better for malaria vector control: insecticide mixture long-lasting insecticidal nets or standard pyrethroid nets combined with indoor residual spraying? Malar J 16, 340. https://doi.org/10.1186/s12936-017-1987-5

Niang, M., Bei, A.K., Madnani, K.G., Pelly, S., Dankwa, S., Kanjee, U., Gunalan, K., Amaladoss, A., Yeo, K.P., Bob, N.S., Malleret, B., Duraisingh, M.T., Preiser, P.R., 2014. STEVOR Is a *Plasmodium falciparum* Erythrocyte Binding Protein that Mediates Merozoite Invasion and Rosetting. Cell Host & Microbe 16, 81–93. https://doi.org/10.1016/j.chom.2014.06.004

Nowak, R.B., Alimohamadi, H., Pestonjamasp, K., Rangamani, P., Fowler, V.M., 2021. Nanoscale organization of Actin Filaments in the Red Blood Cell Membrane Skeleton. https://doi.org/10.1101/2021.03.07.434292

Oh, S.S., Voigt, S., Fisher, D., Yi, S.J., LeRoy, P.J., Derick, L.H., Liu, S.-C., Chishti, A.H., 2000. *Plasmodium falciparum* erythrocyte membrane protein 1 is anchored to the actin–spectrin junction and knob-associated histidine-rich protein in the erythrocyte skeleton. Molecular and Biochemical Parasitology 108, 237–247. https://doi.org/10.1016/S0166-6851(00)00227-9

Pan, L., Yan, R., Li, W., Xu, K., 2018. Super-Resolution Microscopy Reveals the Native Ultrastructure of the Erythrocyte Cytoskeleton. Cell Reports 22, 1151–1158. https://doi.org/10.1016/j.celrep.2017.12.107

Paradkar, S., Gambhire, P., 2021. The Role of Cytoskeleton of a Red Blood Cell in Its Deformability. J Indian Inst Sci 101, 39–46. https://doi.org/10.1007/s41745-020-00221-1

Pease, B.N., Huttlin, E.L., Jedrychowski, M.P., Talevich, E., Harmon, J., Dillman, T., Kannan, N., Doerig, C., Chakrabarti, R., Gygi, S.P., Chakrabarti, D., 2013. Global analysis of protein expression and phosphorylation of three stages of *Plasmodium falciparum* intraerythrocytic development. J Proteome Res 12, 4028–4045. https://doi.org/10.1021/pr400394g

Pei, X., An, X., Guo, X., Tarnawski, M., Coppel, R., Mohandas, N., 2005. Structural and Functional Studies of Interaction between *Plasmodium falciparum* Knob-associated Histidine-rich Protein (KAHRP) and Erythrocyte Spectrin *. Journal of Biological Chemistry 280, 31166–31171. https://doi.org/10.1074/jbc.M505298200

Pei, X., Guo, X., Coppel, R., Bhattacharjee, S., Haldar, K., Gratzer, W., Mohandas, N., An, X., 2007a. The ring-infected erythrocyte surface antigen (RESA) of *Plasmodium falciparum* stabilizes spectrin tetramers and suppresses further invasion. Blood 110, 1036–1042. https://doi.org/10.1182/blood-2007-02-076919

Pei, X., Guo, X., Coppel, R., Mohandas, N., An, X., 2007b. *Plasmodium falciparum* Erythrocyte Membrane Protein 3 (PfEMP3) Destabilizes Erythrocyte Membrane Skeleton *. Journal of Biological Chemistry 282, 26754–26758. https://doi.org/10.1074/jbc.M701612200

Percário, S., Moreira, D.R., Gomes, B.A.Q., Ferreira, M.E.S., Gonçalves, A.C.M., Laurindo, P.S.O.C., Vilhena, T.C., Dolabela, M.F., Green, M.D., 2012. Oxidative stress in malaria. Int J Mol Sci 13, 16346–16372. https://doi.org/10.3390/ijms131216346

Picart, C., Dalhaimer, P., Discher, D.E., 2000. Actin Protofilament Orientation in Deformation of the Erythrocyte Membrane Skeleton. Biophysical Journal 79, 2987–3000. https://doi.org/10.1016/S0006-3495(00)76535-0

Pologe, L.G., Pavlovec, A., Shio, H., Ravetch, J.V., 1987. Primary structure and subcellular localization of the knob-associated histidine-rich protein of *Plasmodium falciparum*. Proc Natl Acad Sci U S A 84, 7139–7143.

Poon, I.K.H., Patel, K.K., Davis, D.S., Parish, C.R., Hulett, M.D., 2011. Histidine-rich glycoprotein: the Swiss Army knife of mammalian plasma. Blood 117, 2093–2101. https://doi.org/10.1182/blood-2010-09-303842

Porteus, M.H., Carroll, D., 2005. Gene targeting using zinc finger nucleases. Nat Biotechnol 23, 967–973. https://doi.org/10.1038/nbt1125

Priebatsch, K.M., Poon, I.K.H., Patel, K.K., Kvansakul, M., Hulett, M.D., 2017. Divalent metal binding by histidine-rich glycoprotein differentially regulates higher order oligomerisation and proteolytic processing. FEBS Letters 591, 164–176. https://doi.org/10.1002/1873-3468.12520

Prieur, E., Druilhe, P., 2009. The malaria candidate vaccine liver stage antigen-3 is highly conserved in *Plasmodium falciparum* isolates from diverse geographical areas. Malar J 8, 247. https://doi.org/10.1186/1475-2875-8-247

Roepe, P.D., 2009. Molecular and Physiologic Basis of Quinoline Drug Resistance in *Plasmodium* Falciparum malaria. Future Microbiology 4, 441–455. https://doi.org/10.2217/fmb.09.15

Rowe, J.A., Moulds, J.M., Newbold, C.I., Miller, L.H., 1997. *P. falciparum* rosetting mediated by a parasite-variant erythrocyte membrane protein and complement-receptor 1. Nature 388, 292–295. https://doi.org/10.1038/40888

Rug, M., Cyrklaff, M., Mikkonen, A., Lemgruber, L., Kuelzer, S., Sanchez, C.P., Thompson, J., Hanssen, E., O'Neill, M., Langer, C., Lanzer, M., Frischknecht, F., Maier, A.G., Cowman, A.F., 2014. Export of virulence proteins by malaria-infected erythrocytes involves remodeling of host actin cytoskeleton. Blood 124, 3459–3468. https://doi.org/10.1182/blood-2014-06-583054

Rug, M., Prescott, S.W., Fernandez, K.M., Cooke, B.M., Cowman, A.F., 2006. The role of KAHRP domains in knob formation and cytoadherence of P falciparum-infected human erythrocytes. Blood 108, 370–378. https://doi.org/10.1182/blood-2005-11-4624

Russo, I., Babbitt, S., Muralidharan, V., Butler, T., Oksman, A., Goldberg, D.E., 2010. Plasmepsin V licenses *Plasmodium* proteins for export into the host erythrocyte. Nature 463, 632–636. https://doi.org/10.1038/nature08726

Russo, I., Oksman, A., Vaupel, B., Goldberg, D.E., 2009. A calpain unique to alveolates is essential in *Plasmodium falciparum* and its knockdown reveals an involvement in pre-S-phase development. Proceedings of the National Academy of Sciences 106, 1554–1559. https://doi.org/10.1073/pnas.0806926106

Rydengård, V., Olsson, A.-K., Mörgelin, M., Schmidtchen, A., 2007. Histidine-rich glycoprotein exerts antibacterial activity. FEBS J 274, 377–389. https://doi.org/10.1111/j.1742-4658.2006.05586.x

Rydengård, V., Shannon, O., Lundqvist, K., Kacprzyk, L., Chalupka, A., Olsson, A.-K., Mörgelin, M., Jahnen-Dechent, W., Malmsten, M., Schmidtchen, A., 2008. Histidine-Rich Glycoprotein

Protects from Systemic Candida Infection. PLOS Pathogens 4, e1000116. https://doi.org/10.1371/journal.ppat.1000116

Sanchez, C.P., Karathanasis, C., Sanchez, R., Cyrklaff, M., Jäger, J., Buchholz, B., Schwarz, U.S., Heilemann, M., Lanzer, M., 2019. Single-molecule imaging and quantification of the immune-variant adhesin VAR2CSA on knobs of *Plasmodium falciparum*-infected erythrocytes. Commun Biol 2, 1–9. https://doi.org/10.1038/s42003-019-0429-z

Sanchez, C.P., Patra, P., Chang, S.-Y., Karathanasis, C., Hanebutte, L., Kilian, N., Cyrklaff, M., Heilemann, M., Schwarz, U.S., Kudryashev, M., Lanzer, M., 2021. KAHRP dynamically relocalizes to remodeled actin junctions and associates with knob spirals in *P. falciparum*-infected erythrocytes. bioRxiv 2021.05.12.443751. https://doi.org/10.1101/2021.05.12.443751

Sanders, P.R., Gilson, P.R., Cantin, G.T., Greenbaum, D.C., Nebl, T., Carucci, D.J., McConville, M.J., Schofield, L., Hodder, A.N., Yates, J.R., Crabb, B.S., 2005. Distinct Protein Classes Including Novel Merozoite Surface Antigens in Raft-like Membranes of *Plasmodium falciparum**. Journal of Biological Chemistry 280, 40169–40176. https://doi.org/10.1074/jbc.M509631200

Sargeant, T.J., Marti, M., Caler, E., Carlton, J.M., Simpson, K., Speed, T.P., Cowman, A.F., 2006. Lineage-specific expansion of proteins exported to erythrocytes in malaria parasites. Genome Biol 7, R12. https://doi.org/10.1186/gb-2006-7-2-r12

Sayama, N., Yoshida, K., Mori, K., Fukazawa, H., Hori, H., Nakazato, N., Tani, J., Nakagawa, Y., Ito, S., 1998. Measurement of red blood cell zinc concentration with Zn-test kit: discrimination between hyperthyroid Graves' disease and transient thyrotoxicosis. Endocr J 45, 767–772. https://doi.org/10.1507/endocrj.45.767

Scherf, A., Hernandez-Rivas, R., Buffet, P., Bottius, E., Benatar, C., Pouvelle, B., Gysin, J., Lanzer, M., 1998. Antigenic variation in malaria: in situ switching, relaxed and mutually exclusive transcription of var genes during intra-erythrocytic development in *Plasmodium falciparum*. The EMBO Journal 17, 5418–5426. https://doi.org/10.1093/emboj/17.18.5418

Schulze, J., Kwiatkowski, M., Borner, J., Schlüter, H., Bruchhaus, I., Burmester, T., Spielmann, T., Pick, C., 2015. The lasmodium falciparum exportome contains non-canonical PEXEL/HT proteins. Molecular Microbiology 97, 301–314. https://doi.org/10.1111/mmi.13024

Sinka, M.E., Bangs, M.J., Manguin, S., Rubio-Palis, Y., Chareonviriyaphap, T., Coetzee, M., Mbogo, C.M., Hemingway, J., Patil, A.P., Temperley, W.H., Gething, P.W., Kabaria, C.W., Burkot, T.R., Harbach, R.E., Hay, S.I., 2012. A global map of dominant malaria vectors. Parasites Vectors 5, 69. https://doi.org/10.1186/1756-3305-5-69

Smith, J.D., Rowe, J.A., Higgins, M.K., Lavstsen, T., 2013. Malaria's deadly grip: cytoadhesion of lasmodium falciparum-infected erythrocytes. Cellular Microbiology 15, 1976–1983. https://doi.org/10.1111/cmi.12183

Snyder, L.M., Leb, L., Piotrowski, J., Sauberman, N., Liu, S.C., Fortier, N.L., 1983. Irreversible spectrin-haemoglobin crosslinking in vivo: a marker for red cell senescence. British Journal of Haematology 53, 379–384. https://doi.org/10.1111/j.1365-2141.1983.tb02038.x

Stokke, B.T., Mikkelsen, A., Elgsaeter, A., 1985. Human erythrocyte spectrin dimer intrinsic viscosity: Temperature dependence and implications for the molecular basis of the erythrocyte membrane free energy. Biochimica et Biophysica Acta (BBA) - Biomembranes 816, 102–110. https://doi.org/10.1016/0005-2736(85)90398-0

Straimer, J., Gnädig, N.F., Witkowski, B., Amaratunga, C., Duru, V., Ramadani, A.P., Dacheux, M., Khim, N., Zhang, L., Lam, S., Gregory, P.D., Urnov, F.D., Mercereau-Puijalon, O., Benoit-Vical, F., Fairhurst, R.M., Ménard, D., Fidock, D.A., 2015. Drug resistance. K13-propeller mutations confer artemisinin resistance in *Plasmodium falciparum* clinical isolates. Science 347, 428–431. https://doi.org/10.1126/science.1260867

Sturm, A., Amino, R., van de Sand, C., Regen, T., Retzlaff, S., Rennenberg, A., Krueger, A., Pollok, J.-M., Menard, R., Heussler, V.T., 2006. Manipulation of Host Hepatocytes by the Malaria Parasite for Delivery into Liver Sinusoids. Science 313, 1287–1290. https://doi.org/10.1126/science.1129720

Tabassum, W., Bhattacharya, M., Bakshi, S., Bhattacharyya, M.K., 2022. Heat Shock Protein 90 Regulates the Activity of Histone Deacetylase Sir2 in *Plasmodium falciparum*. mSphere 7, e00329-22. https://doi.org/10.1128/msphere.00329-22

Tan, C., Bodenmiller, B., Pasculescu, A., Jovanovic, M., Hengartner, M., Jørgensen, C., Bader, G., Aebersold, R., Pawson, T., Linding, R., 2009. Comparative Analysis Reveals Conserved Protein Phosphorylation Networks Implicated in Multiple Diseases. Science signaling 2, ra39. https://doi.org/10.1126/scisignal.2000316

Taylor, S.M., Cerami, C., Fairhurst, R.M., 2013. Hemoglobinopathies: Slicing the Gordian Knot of *Plasmodium falciparum* Malaria Pathogenesis. PLOS Pathogens 9, e1003327. https://doi.org/10.1371/journal.ppat.1003327

Tilley, L., Sougrat, R., Lithgow, T., Hanssen, E., 2008. The Twists and Turns of Maurer's Cleft Trafficking in *P. falciparum*-Infected Erythrocytes. Traffic 9, 187–197. https://doi.org/10.1111/j.1600-0854.2007.00684.x

Tiono, A.B., Ouédraogo, A., Ouattara, D., Bougouma, E.C., Coulibaly, S., Diarra, A., Faragher, B., Guelbeogo, M.W., Grisales, N., Ouédraogo, I.N., Ouédraogo, Z.A., Pinder, M., Sanon, S., Smith, T., Vanobberghen, F., Sagnon, N., Ranson, H., Lindsay, S.W., 2018. Efficacy of Olyset Duo, a bednet containing pyriproxyfen and permethrin, versus a permethrin-only net against clinical malaria in an area with highly pyrethroid-resistant vectors in rural Burkina Faso: a cluster-randomised controlled trial. The Lancet 392, 569–580. https://doi.org/10.1016/S0140-6736(18)31711-2

Tomita, T., Tanaka, S., Morohashi, Y., Iwatsubo, T., 2006. Presenilin-dependent intramembrane cleavage of ephrin-B1. Molecular Neurodegeneration 1, 2. https://doi.org/10.1186/1750-1326-1-2

Trelka, D.P., Schneider, T.G., Reeder, J.C., Taraschi, T.F., 2000. Evidence for vesicle-mediated trafficking of parasite proteins to the host cell cytosol and erythrocyte surface membrane in *Plasmodium falciparum* infected ertythrocytes. Molecular and Biochemical Parasitology 106, 131–145. https://doi.org/10.1016/S0166-6851(99)00207-8

Tungu, P.K., Michael, E., Sudi, W., Kisinza, W.W., Rowland, M., 2021. Efficacy of interceptor® G2, a long-lasting insecticide mixture net treated with chlorfenapyr and alpha-cypermethrin against Anopheles funestus: experimental hut trials in north-eastern Tanzania. Malaria Journal 20, 180. https://doi.org/10.1186/s12936-021-03716-z

Urnov, F.D., Rebar, E.J., Holmes, M.C., Zhang, H.S., Gregory, P.D., 2010. Genome editing with engineered zinc finger nucleases. Nat Rev Genet 11, 636–646. https://doi.org/10.1038/nrg2842

Videvall, E., 2018. *Plasmodium* parasites of birds have the most AT-rich genes of eukaryotes. Microb Genom 4, e000150. https://doi.org/10.1099/mgen.0.000150

Vigan-Womas, I., Guillotte, M., Juillerat, A., Hessel, A., Raynal, B., England, P., Cohen, J.H., Bertrand, O., Peyrard, T., Bentley, G.A., Lewit-Bentley, A., Mercereau-Puijalon, O., 2012. Structural Basis for the ABO Blood-Group Dependence of *Plasmodium falciparum* Rosetting. PLOS Pathogens 8, e1002781. https://doi.org/10.1371/journal.ppat.1002781

Voigt, S., Hanspal, M., LeRoy, P.J., Zhao, P., Oh, S.S., Chishti, A.H., Liu, S.-C., 2000. The cytoadherence ligand *Plasmodium falciparum* Erythrocyte Membrane Protein 1 (PfEMP1) binds to the *P. falciparum* Knob-associated Histidine-rich Protein (KAHRP) by electrostatic interactions. Molecular and Biochemical Parasitology 110, 423–428. https://doi.org/10.1016/S0166-6851(00)00281-4

Voss, T.S., Mini, T., Jenoe, P., Beck, H.-P., 2002. *Plasmodium falciparum* Possesses a Cell Cycle-regulated Short Type Replication Protein A Large Subunit Encoded by an Unusual Transcript *. Journal of Biological Chemistry 277, 17493–17501. https://doi.org/10.1074/jbc.M200100200

Waller, K.L., Cooke, B.M., Coppel, R.L., Nunomura, W., Mohandas, N., 1999. Mapping the Binding Domains Involved in the Interaction between the *Plasmodium falciparum* Knob-associated Histidine-rich Protein (KAHRP) and the Cytoadherence Ligand *P. falciparum* Erythrocyte Membrane Protein 1 (PfEMP1) *. Journal of Biological Chemistry 274, 23808–23813. https://doi.org/10.1074/jbc.274.34.23808

Waller, K.L., Nunomura, W., An, X., Cooke, B.M., Mohandas, N., Coppel, R.L., 2003. Mature parasite-infected erythrocyte surface antigen (MESA) of *Plasmodium falciparum* binds to the 30-kDa domain of protein 4.1 in malaria-infected red blood cells. Blood 102, 1911–1914. https://doi.org/10.1182/blood-2002-11-3513

Waller, K.L., Nunomura, W., Cooke, B.M., Mohandas, N., Coppel, R.L., 2002. Mapping the domains of the cytoadherence ligand *Plasmodium falciparum* erythrocyte membrane protein 1 (PfEMP1) that bind to the knob-associated histidine-rich protein (KAHRP). Mol Biochem Parasitol 119, 125–129. https://doi.org/10.1016/s0166-6851(01)00395-4

Watermeyer, J.M., Hale, V.L., Hackett, F., Clare, D.K., Cutts, E.E., Vakonakis, I., Fleck, R.A., Blackman, M.J., Saibil, H.R., 2016. A spiral scaffold underlies cytoadherent knobs in *Plasmodium falciparum*–infected erythrocytes. Blood 127, 343–351. https://doi.org/10.1182/blood-2015-10-674002

Weber, J.L., 1987. Analysis of sequences from the extremely A + T-rich genome of *Plasmodium falciparum*. Gene 52, 103–109. https://doi.org/10.1016/0378-1119(87)90399-4

Webi, E., Abkallo, H.M., Obiero, G., Ndegwa, P., Xie, S., Zhao, S., Nene, V., Steinaa, L., 2024. Genome Editing in Apicomplexan Parasites: Current Status, Challenges, and Future Possibilities. The CRISPR Journal. https://doi.org/10.1089/crispr.2024.0032

Weng, H., Guo, X., Papoin, J., Wang, J., Coppel, R., Mohandas, N., An, X., 2014. Interaction of *Plasmodium falciparum* knob-associated histidine-rich protein (KAHRP) with erythrocyte ankyrin R is required for its attachment to the erythrocyte membrane. Biochimica et Biophysica Acta (BBA) - Biomembranes 1838, 185–192. https://doi.org/10.1016/j.bbamem.2013.09.014

White, N.J., Pukrittayakamee, S., Hien, T.T., Faiz, M.A., Mokuolu, O.A., Dondorp, A.M., 2014. Malaria. Lancet 383, 723–735. https://doi.org/10.1016/S0140-6736(13)60024-0

Wichers, J.S., Scholz, J.A.M., Strauss, J., Witt, S., Lill, A., Ehnold, L.-I., Neupert, N., Liffner, B., Lühken, R., Petter, M., Lorenzen, S., Wilson, D.W., Löw, C., Lavazec, C., Bruchhaus, I., Tannich, E., Gilberger, T.W., Bachmann, A., 2019. Dissecting the Gene Expression, Localization, Membrane Topology, and Function of the *Plasmodium falciparum* STEVOR Protein Family. mBio 10, 10.1128/mbio.01500-19. https://doi.org/10.1128/mbio.01500-19

Wickham, M.E., Rug, M., Ralph, S.A., Klonis, N., McFadden, G.I., Tilley, L., Cowman, A.F., 2001. Trafficking and assembly of the cytoadherence complex in *Plasmodium falciparum*-infected human erythrocytes. The EMBO Journal 20, 5636–5649. https://doi.org/10.1093/emboj/20.20.5636

Wiser, M.F., 2023. Knobs, Adhesion, and Severe Falciparum Malaria. Tropical Medicine and Infectious Disease 8, 353. https://doi.org/10.3390/tropicalmed8070353

Witkowski, B., Duru, V., Khim, N., Ross, L.S., Saintpierre, B., Beghain, J., Chy, S., Kim, S., Ke, S., Kloeung, N., Eam, R., Khean, C., Ken, M., Loch, K., Bouillon, A., Domergue, A., Ma, L., Bouchier, C., Leang, R., Huy, R., Nuel, G., Barale, J.-C., Legrand, E., Ringwald, P., Fidock, D.A., Mercereau-Puijalon, O., Ariey, F., Ménard, D., 2017. A surrogate marker of piperaquine-resistant *Plasmodium falciparum* malaria: a phenotype-genotype association study. Lancet Infect Dis 17, 174–183. https://doi.org/10.1016/S1473-3099(16)30415-7

World Health Organization, 2024. World malaria report 2024 [WWW Document]. URL https://www.who.int/publications/i/item/9789240104440 (accessed 1.7.25).

World Health Organization, 2020. Report on antimalarial drug efficacy, resistance and response: 10 years of surveillance (2010–2019). World Health Organization.

Xie, T., Yan, C., Zhou, R., Zhao, Y., Sun, L., Yang, G., Lu, P., Ma, D., Shi, Y., 2014. Crystal structure of the γ-secretase component nicastrin. Proceedings of the National Academy of Sciences 111, 13349–13354. https://doi.org/10.1073/pnas.1414837111

Yang, B., Cheng, Z., Luo, L., Cheng, K., Gan, S., Shi, Y., Liu, C., Wang, D., 2023. Comparative analysis of codon usage patterns of *Plasmodium* helical interspersed subtelomeric (PHIST) proteins. Front. Microbiol. 14. https://doi.org/10.3389/fmicb.2023.1320060

Zhu, Z., Chung, W.-H., Shim, E.Y., Lee, S.E., Ira, G., 2008. Sgs1 Helicase and Two Nucleases Dna2 and Exo1 Resect DNA Double-Strand Break Ends. Cell 134, 981–994. https://doi.org/10.1016/j.cell.2008.08.037

List of Abbreviations

°C	degrees Celsius
A	adenine or alanine
Å	Angstrom
ACT	artemisinin combination therapy
AE1	anion exchanger 1
AmpR	Ampicillin resistance
ANOVA	analysis of variance
APS	ammonium persulfate
ATP	adenosine triphosphate
ATS	Acidic terminal segment
bp	base pair(s)
BSA	bovine serum albumin
C	cytosine or cysteine
Cas9	CRISPR associated protein 9
CQ	chloroquine
CR1	Complement receptor 1
CRISPR	Clustered regularly interspaced short palindromic repeats
crRNA	CRISPR RNA
CRT	chloroquine resistance transporter
cryo-EM	Cryo-electron microscopy
CSA	Chondroitin sulfate A
C-terminus	Carboxyl-terminus
D	aspartic acid
Da	Dalton
dd	double distilled
DHA	Dihydroartemisinin
DHFR	dihydrofolate reductase
dhfr	Dihydrofolate reductase
DHODH	Dihydrofolate reductase
dhps	Dihydropteroate synthase
DMSO	dimethyl sulfoxide
DNA	deoxyribonucleic acid
dNTP	deoxyribonucleoside triphosphate
DSBs	double-stranded breaks
dsDNA	Double stranded DNA
DSP	Dithiobis(succinimidyl propionate)
E	glutamic acid
E. coli	*Escherichia coli*
EDTA	ethylenediaminetetracetate
EDV	Electron-dense vesicles
EMP1	Erythrocyte membrane protein 1
EPCR	Endothelial Protein C Receptor
EPIC	Exported protein-interacting complex
ER	endoplasmic reticulum

et al.	Et alia (and others)
F	phenylalanine
FDR	false discovery rate
for	forward
FRET	Förster Resonance Energy Transfer
g	gram
GA	Glutaraldehyde
GC	Golgi complex
gDNA	Genomic DNA
GFP	green fluorescent protein
GlcN	Glucosamine
glmS	Glucosamine-6-phosphate activated ribozyme
GO	gene ontology
GP1	Golgi protein 1
GP2	Golgi protein 2
gRNA	Guide RNA
h	hour or human
HA	Hemagglutinin
Hb	Hemoglobin
HDR	Homology directed repair
HEPES	(4-(2-hydroxyethyl)-1-piperazineethanesulfonic acid)
hpi	hours post invasion
HR	Homology region
HRG	Histidine-rich glycoprotein
HRP2	histidine-rich protein 2
HRP3	histidine-rich protein 3
HRR	Histidine-rich region
Hsp	heat shock protein
IC50	half of maximal inhibitory concentration
ICAM-1	Intercellular adhesion molecule 1
ICP-MS	Inductively coupled plasma mass spectrometry
IFA	Indirect fluorescence assay
IgG	Immunoglobulin G
iRBC	infected red blood cell(s)
IRS	Indoor residual spraying
ITNs	Insecticide-treated nets
K13	Kelch 13 protein
KAHRP	Knob-associated histidine-rich protein
kb	kilobase pair
KD	Knockdown
kDa	kilodalton
KO	Knockout
L	liter
LB	Luria Bertani, lysogeny broth
LSA-3	liver stage antigen-3
m	milli- or meter

M	molar
m/z	mass to charge ratio
MCS	Multiple cloning site
mDHFR	Murine dihydrofolate reductase
MDR	multi-drug resistance
MDR-1	multi-drug resistance transporter 1
MEC	MESA erythrocyte cytoskeleton-binding motif
MESA, EMP2	Mature Parasite-Infected Erythrocyte Surface Antigen
MHC	Major histocompatibility complex
miniTurbo	miniTurbo biotin ligase
mL	milliliter
mm	millimeter
MQ	mefloquine
MRX	Mre11-Rad50-Xrs2
MS	mass spectrometry
MSH	Mass spectrometry hit
n	nano-
NEB	New England Biolabs
NHEJ	Non-homologous end joining
nm	nanometer
NP-40	Tergitol-type NP-40, nonylphenoxypolyethoxylethanol
NPPs	new permeation pathways
N-terminus	Amino-terminus
OD	optical density
P.	Plsmodium
PAGE	polyacrylamide gel electrophoresis
PAM	Protospacer adjacent motif
Pb	*Plasmodium* berghei
PBS	phosphate buffered saline
PBST	Phosphate buffered saline supplemented with Tween-20
PC	phosphatidylcholine
PCR	polymerase chain reaction
PE	phosphatidylethanolamine
PEXEL	*Plasmodium* export element
Pf	*Plasmodium falciparum*
Pf	*Plasmodium falciparum*
PFA	paraformaldehyde
PfTKL2	tyrosine kinase-like enzyme
pH	potential of hydrogen
PHIST	*Plasmodium* helical interspersed subtelomeric proteins
PlasmoDB	*Plasmodium* database
PMV	Plasmepsin V
PNEP	PEXEL-negative exported protein
PP1	Ser/Thr Protein Phosphatase type 1
PPM	Parasite plasma membrane
ppm	parts per million

PS	phosphatidylserine
PTEX	*Plasmodium* translocon of exported proteins
PV	parasitophorous vacuole
PVM	Parasitophorous vacuolar membrane
QD	quinidine
RBC	red blood cell
RESA	Ring-infected erythrocyte surface antigen
rev	reverse
RIPA	Radioimmunoprecipitation assay buffer
RNA	ribonucleic acid
ROS	reactive oxygen species
RPA	Replication protein A
rpm	revolutions per minute
RPMI	Roswell Park Memorial Institute
RT	room temperature
SB	super broth
SDS	sodium dodecylsulfate
SEM	Scanning electron microscope/ microscopy or standard error of the mean
sgRNA	Single-guide RNA
SILAC	Stable isotope labeling of amino acids in cell culture
SMC	Seasonal malaria chemoprevention
SOC	super optimal broth with catabolite repression
ssDNA	Single strand DNA
STEVOR	Subtelomeric Variable Open Reading frame (protein)
T	thymine or threonine
TAE	Tris-acetate EDTA
TALEN	Transcription activator-like effector nuclease
Taq	Thermus aquaticus
TE	Tris-EDTA
TEM	Transmission electron microscopy
TEMED	tetramethyl ethylenediamine
tER	transitional ER
TFA	trifluoroacetic acid
TM	Transmembrane
U	unit
USA	United States of America
V	volt
v/v	volume to volume
var	Variant antigen gene
VLS	Vesicle-like structures
w/v	weight to volume
WHO	World Health Organization
WT	wild type
X	times
x g	g force (relative centrifugal force)
Y	tyrosine

Y2H	Yeast two-hybrid
ZNF	Zinc finger nuclease

List of Figures

Appendix I – Plasmid maps

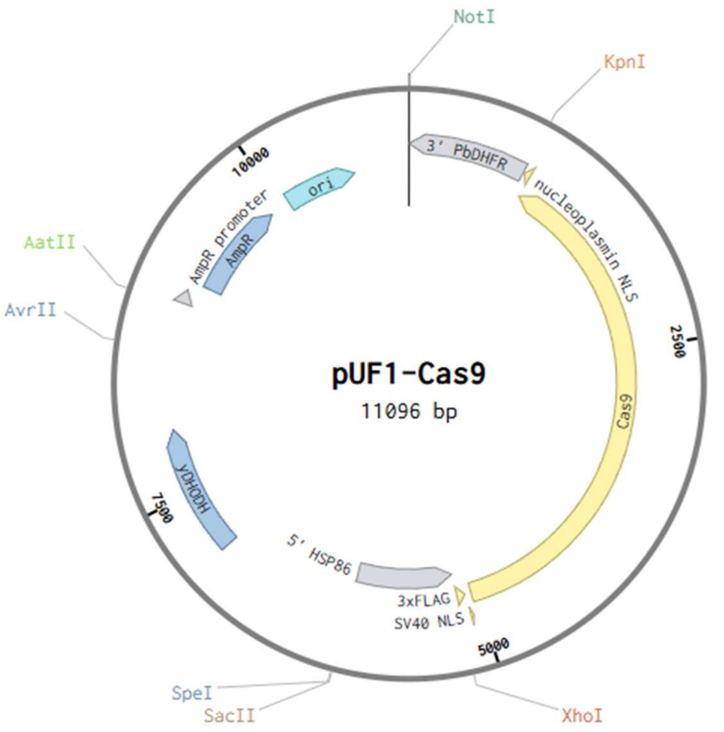

Figure 26. PUF1-Cas9 plasmid map.

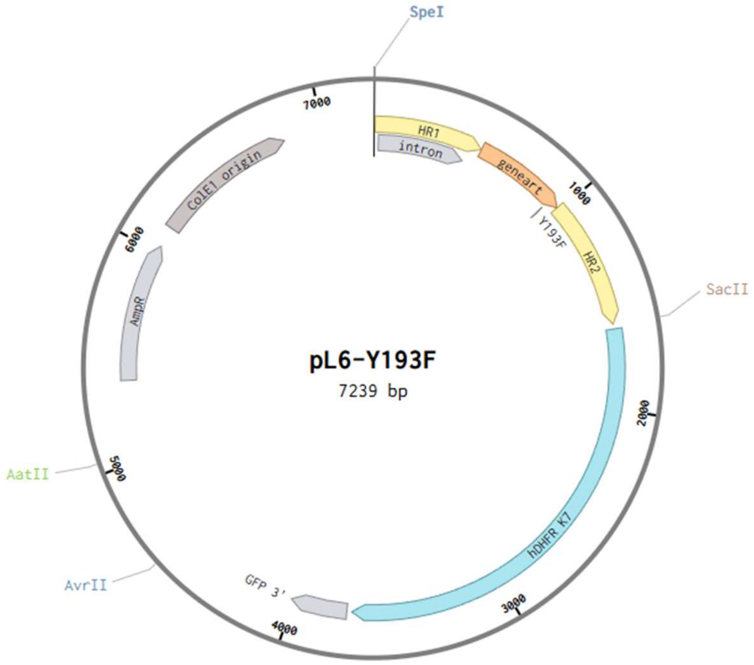

Figure 25. pL6-Y193F plasmid map.

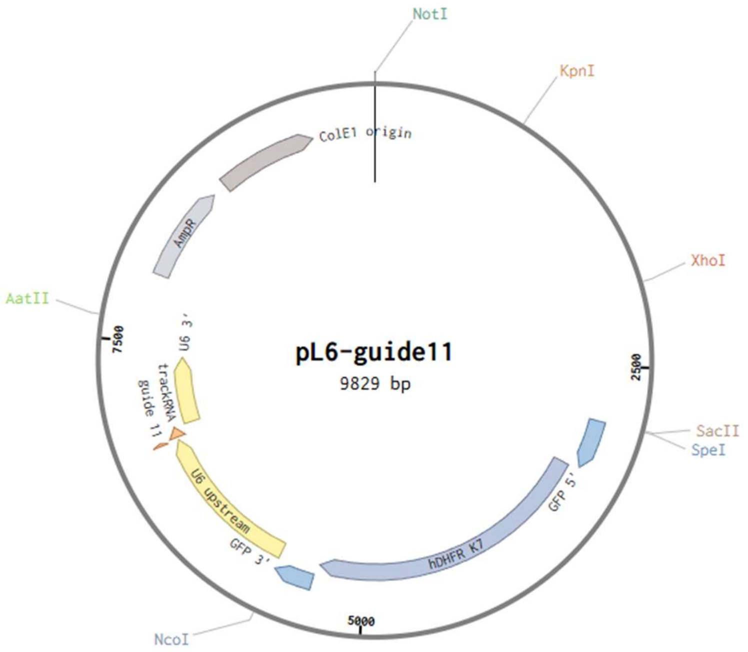

Figure 28. pL6-guide11 plasmid map.

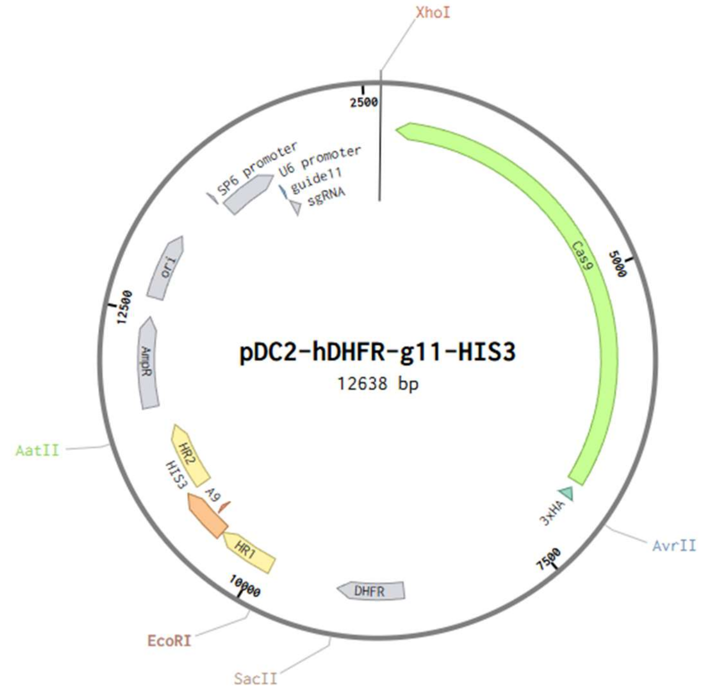

Figure 27. pDC2-hDHFR-g11-HIS3 plasmid map.
Represents the plasmid maps of pDC2 cloned alanine screening plasmids.

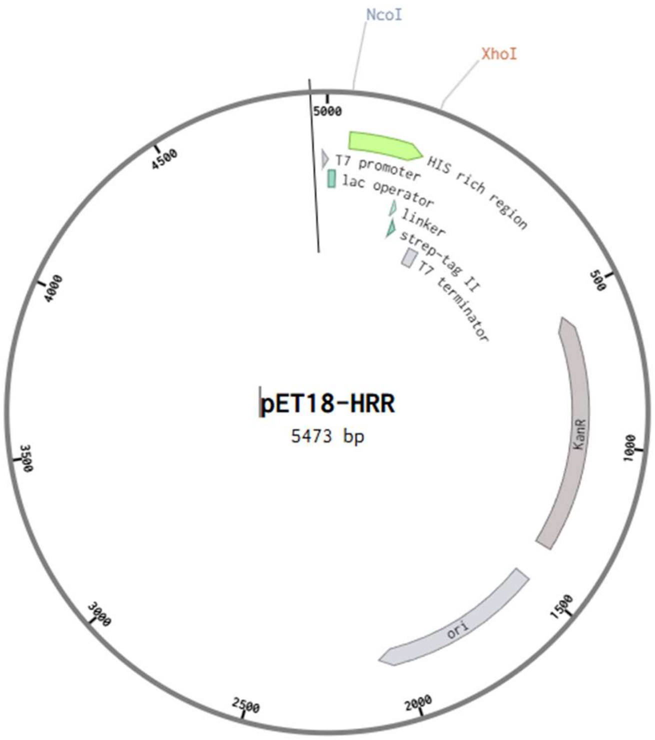

Figure 30. pET18-HRR plasmid map

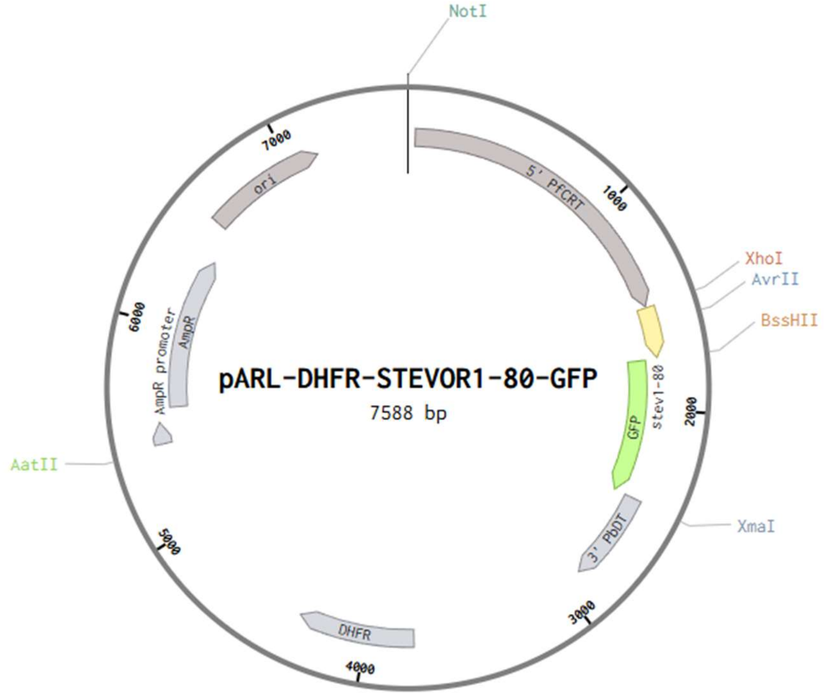

Figure 29. pARL-DHFR-STEVOR1-80-GFP plasmid map.
Represents STEVOR1-80^{50W}-GFP, STEVOR1-80^{51E}-GFP, and STEVOR1-80-GFP expression plasmids.

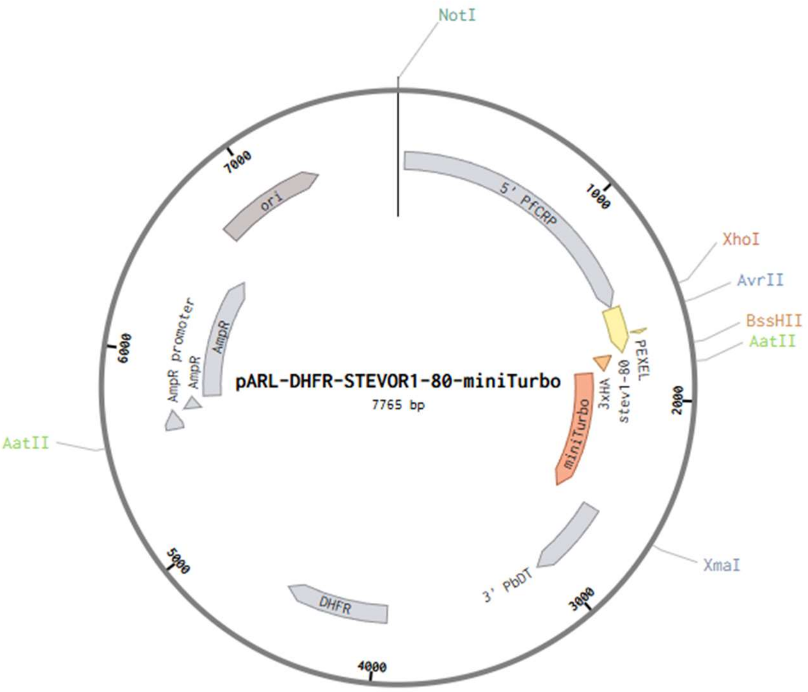

Figure 31. pARL-DHFR-STEVOR1-80-miniTurbo plasmid map.
Represents STEVOR1-80^{50W}-miniTurbo, STEVOR1-80^{51E}-miniTurbo, and STEVOR1-80-miniTurbo expression plasmids.

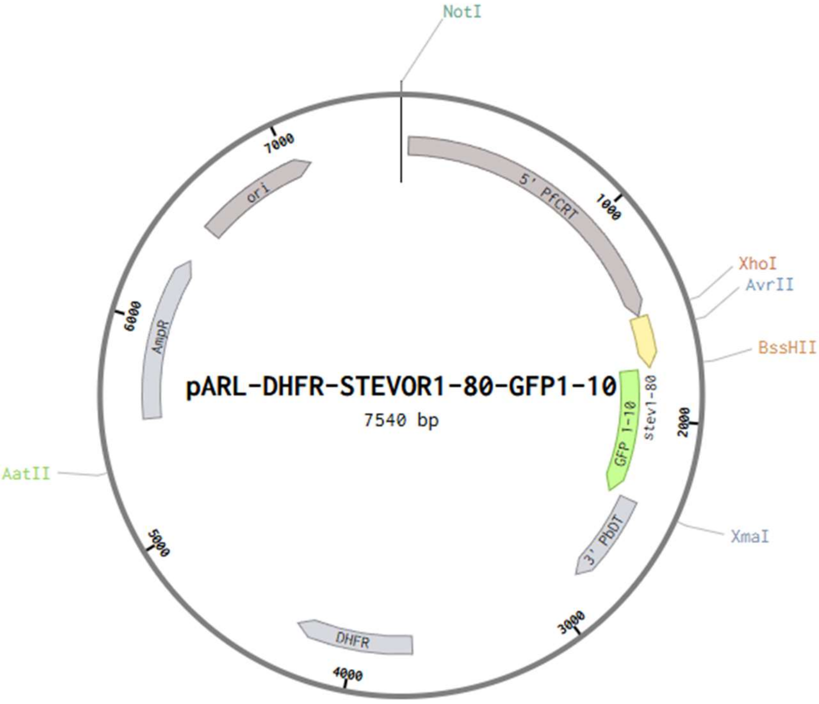

Figure 32. pARL-DHFR-STEVOR1-80-GFP1-10 plasmid map.
Represents STEVOR1-80^{50W}-GFP1-10, STEVOR1-80^{51E}-GFP1-10, and STEVOR1-80-GFP1-10 expression plasmids.

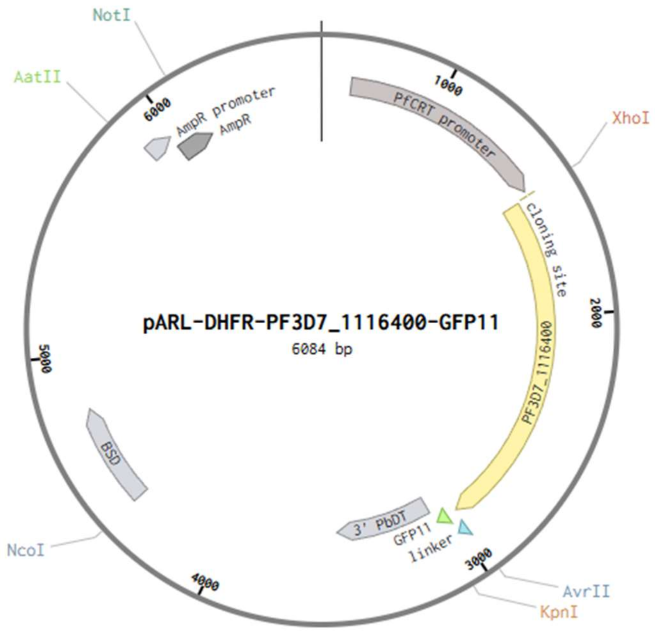

Figure 33. pARL-DHFR-PF3D7_1116400-GFP11 plasmid map.
Represents the expression plasmids of MSH-GFP11 fusion proteins.

Appendix II – Mass spectrometry hit peptide counts

Accession Number	Description	50WTB1 57-04 peptide	50WTB2 72-02 peptide	50WTB3 72-04 peptide	51ETB2 57-08 peptide	51ETB3 72-06 peptide	51ETB4 152-02 peptide	stevTB1 57-12 peptide	stevTB2 72-08 peptide	stevTB3 72-10 peptide	3D71 72-12 peptide	3D72 72-14 peptide	3D73 72-16 peptide	3D7B1 72-18 peptide	3D7B2 72-20 peptide	3D7B3 72-22 peptide
10090	Gene_Symbol=Krt33b keratin complex 1, acidic, gene 3	0	0	0	0	0	0	0	0	0	0	0	0	0	0	13
A0A143ZWL7_PLAF7	Tubulin beta chain OS=*Plasmodium falciparum* (isolate 3D7) OX=36329 GN=PF3D7_1008700 PE=3 SV=1	0	0	2	0	0	0	0	0	0	0	0	0	0	0	0
A0A143ZWU2_PLAF7	GBP130 protein OS=*Plasmodium falciparum* (isolate 3D7) OX=36329 GN=PF3D7_1016300 PE=4 SV=1	6	6	12	14	15	10	1	3	5	0	0	0	0	0	0
A0A143ZZ61_PLAF7	Phosphopyruvate hydratase OS=*Plasmodium falciparum* (isolate 3D7) OX=36329 GN=PF3D7_1015900 PE=3 SV=1	0	3	5	4	5	0	2	0	0	0	0	1	0	0	1
A0A143ZZ61_PLAF7 [3]	Cluster of Phosphopyruvate hydratase OS=*Plasmodium falciparum* (isolate 3D7) OX=36329 GN=PF3D7_1015900 PE=3 SV=1 (A0A143ZZ61_PLAF7)	0	3	5	0	5	0	0	0	0	0	0	2	0	0	1
A0A143ZZV5_PLAF7	Uncharacterized protein OS=*Plasmodium falciparum* (isolate 3D7) OX=36329 GN=PF3D7_0804500 PE=4 SV=1	0	0	0	0	0	0	0	0	0	0	1	0	0	2	0
A0A144A0G8_PLAF7	Prolyl-tRNA synthetase OS=*Plasmodium falciparum* (isolate 3D7) OX=36329 GN=PF3D7_1213800 PE=3 SV=1	0	0	2	0	0	0	0	0	0	0	0	0	0	0	0
A0A144A171_PLAF7	Plasmepsin I OS=*Plasmodium falciparum* (isolate 3D7) OX=36329 GN=PF3D7_1407900 PE=3 SV=1	0	0	4	0	0	0	0	0	0	0	0	0	0	0	0
A0A144A1R5_PLAF7	Actin I OS=*Plasmodium falciparum* (isolate 3D7) OX=36329 GN=PF3D7_1246200 PE=3 SV=1	0	0	4	0	0	0	0	0	0	0	0	0	0	0	0
A0A144A2G5_PLAF7	Dipeptidyl aminopeptidase 1 OS=*Plasmodium falciparum* (isolate 3D7) OX=36329 GN=PF3D7_1116700 PE=3 SV=1	0	7	14	2	6	0	0	0	0	0	0	0	0	0	0
A0A144A2H0_PLAF7	Aminopeptidase P OS=*Plasmodium falciparum* (isolate 3D7) OX=36329 GN=PF3D7_1454400 PE=3 SV=1	0	1	6	0	0	0	0	0	0	0	0	0	0	0	0
A0A5K1K8L5_PLAF7	Uncharacterized protein OS=*Plasmodium falciparum* (isolate 3D7) OX=36329 GN=PF3D7_0520800 PE=4 SV=1	0	1	26	0	0	0	0	0	0	0	0	0	0	0	0
A0A5K1K8Q9_PLAF7	Golgi protein 1 OS=*Plasmodium falciparum* (isolate 3D7) OX=36329 GN=PF3D7_1320000 PE=4 SV=1	0	2	5	0	2	0	0	0	0	0	0	0	0	0	0
ACON_HUMAN	Aconitate hydratase, mitochondrial OS=Homo sapiens OX=9606 GN=ACO2 PE=1 SV=2	0	0	0	0	0	0	0	0	0	2	0	0	0	0	0
ACTB_HUMAN	Actin, cytoplasmic 1 OS=Homo sapiens OX=9606 GN=ACTB PE=1 SV=1	0	3	5	0	3	0	0	0	3	3	3	4	0	0	1
ACTBL_HUMAN	Beta-actin-like protein 2 OS=Homo sapiens OX=9606 GN=ACTBL2 PE=1 SV=2	0	0	1	0	0	0	0	0	0	0	0	1	0	0	0
ACTBM_HUMAN	Putative beta-actin-like protein 3 OS=Homo sapiens OX=9606 GN=POTEKP PE=5 SV=1	0	1	1	0	0	0	0	0	0	1	1	1	0	0	0
ACTBM_HUMAN [7]	Cluster of Putative beta-actin-like protein 3 OS=Homo sapiens OX=9606 GN=POTEKP PE=5 SV=1 (ACTBM_HUMAN)	0	3	5	0	3	0	0	0	3	3	3	4	0	0	1
ACTC_HUMAN	Actin, alpha cardiac muscle 1 OS=Homo sapiens OX=9606 GN=ACTC1 PE=1 SV=1	0	0	0	0	0	0	1	0	0	0	0	0	0	0	0
ACTG_HUMAN	Actin, cytoplasmic 2 OS=Homo sapiens OX=9606 GN=ACTG1 PE=1 SV=1	0	3	5	1	3	0	2	0	3	3	3	4	0	0	1
ACTG_HUMAN [6]	Cluster of Actin, cytoplasmic 2 OS=Homo sapiens OX=9606 GN=ACTG1 PE=1 SV=1 (ACTG_HUMAN)	0	0	0	1	0	0	2	0	0	0	0	0	0	0	0
ACTS_HUMAN	Actin, alpha skeletal muscle OS=Homo sapiens OX=9606 GN=ACTA1 PE=1 SV=1	0	1	3	0	1	0	0	0	2	2	2	2	0	0	0
Alpha-fetoprotein	precursor (Bos taurus)	0	0	0	0	0	0	0	0	0	4	0	0	0	0	0

Accession Number	Description	50WTB1 57-04 peptide	50WTB2 72-02 peptide	50WTB3 72-04 peptide	51ETB2 57-08 peptide	51ETB3 72-06 peptide	51ETB4 152-02 peptide	stevTB1 57-12 peptide	stevTB2 72-08 peptide	stevTB3 72-10 peptide	3D71 72-12 peptide	3D72 72-14 peptide	3D73 72-16 peptide	3D7B1 72-18 peptide	3D7B2 72-20 peptide	3D7B3 72-22 peptide
Alpha-S1-casein	- Bos taurus (Bovine).	0	0	2	0	0	0	0	0	1	1	0	1	1	0	1
ANK1_HUMAN	Ankyrin-1 OS=Homo sapiens OX=9606 GN=ANK1 PE=1 SV=3	0	1	19	4	16	0	0	0	0	0	0	0	0	0	0
ANK1_HUMAN [3]	Cluster of Ankyrin-1 OS=Homo sapiens OX=9606 GN=ANK1 PE=1 SV=3 (ANK1_HUMAN)	0	1	19	0	16	0	0	0	0	0	0	0	0	0	0
ANK2_HUMAN	Ankyrin-2 OS=Homo sapiens OX=9606 GN=ANK2 PE=1 SV=4	0	0	0	0	0	0	0	0	0	0	0	0	0	0	0
ANK3_HUMAN	Ankyrin-3 OS=Homo sapiens OX=9606 GN=ANK3 PE=1 SV=3	0	0	0	0	0	0	0	0	0	0	0	0	0	0	0
ANXA1_HUMAN	Annexin A1 OS=Homo sapiens OX=9606 GN=ANXA1 PE=1 SV=2	0	2	5	0	0	0	0	0	1	0	2	6	0	0	1
ANXA2_HUMAN	Annexin A2 OS=Homo sapiens OX=9606 GN=ANXA2 PE=1 SV=2	0	4	6	2	2	0	2	0	3	2	2	7	1	0	3
ARGI1_HUMAN	Arginase-1 OS=Homo sapiens OX=9606 GN=ARG1 PE=1 SV=2	0	3	3	0	0	0	4	0	5	0	1	3	0	1	0
ATPB_HUMAN	ATP synthase subunit beta, mitochondrial OS=Homo sapiens OX=9606 GN=ATP5F1B PE=1 SV=3	0	0	0	0	2	0	0	0	0	0	0	0	0	0	0
B3AT_HUMAN	Band 3 anion transport protein OS=Homo sapiens OX=9606 GN=SLC4A1 PE=1 SV=3	0	4	21	5	5	2	2	0	2	0	0	2	0	1	0
Beta-lactoglobulin	- Bos taurus (Bovine).	0	0	0	0	0	0	3	0	0	0	0	0	0	0	0
Biognosys|iRT|iRT-Kit_WR_fusion	Biognosys|iRT|iRT-Kit_WR_fusion	11	11	11	11	11	11	10	11	11	11	11	11	11	11	11
BIP_HUMAN	Endoplasmic reticulum chaperone BiP OS=Homo sapiens OX=9606 GN=HSPA5 PE=1 SV=2	0	2	2	0	2	1	0	0	0	18	0	0	0	0	1
BLMH_HUMAN	Bleomycin hydrolase OS=Homo sapiens OX=9606 GN=BLMH PE=1 SV=1	0	2	0	0	0	0	0	0	1	0	0	0	0	0	0
Bovine	serum albumin precursor (Bos taurus)	7	8	11	5	9	3	23	1	7	27	7	7	2	14	4
C0H4Y6_PLAF7	Protein disulfide-isomerase OS=*Plasmodium falciparum* (isolate 3D7) OX=36329 GN=PF3D7_0827900 PE=3 SV=1	0	1	3	3	5	2	0	0	0	0	0	0	0	0	0
C0H530_PLAF7	Exportin-7, putative OS=*Plasmodium falciparum* (isolate 3D7) OX=36329 GN=PF3D7_0910100 PE=4 SV=1	0	0	2	0	0	0	0	0	0	0	0	0	0	0	0
C0H571_PLAF7	High molecular weight rhoptry protein 2 OS=*Plasmodium falciparum* (isolate 3D7) OX=36329 GN=PF3D7_0929400 PE=4 SV=1	0	0	20	0	0	0	0	0	0	0	0	0	0	0	0
C0H5H0_PLAF7	Endoplasmic reticulum chaperone GRP170 OS=*Plasmodium falciparum* (isolate 3D7) OX=36329 GN=PF3D7_1344200 PE=4 SV=1	0	3	14	0	2	0	0	0	0	0	0	0	0	0	0
C6KST5_PLAF7	T-complex protein 1 subunit zeta OS=*Plasmodium falciparum* (isolate 3D7) OX=36329 GN=PF3D7_0608700 PE=3 SV=1	0	0	2	0	0	0	0	0	0	0	0	0	0	0	0
C6KT76_PLAF7	Phosphotransferase OS=*Plasmodium falciparum* (isolate 3D7) OX=36329 GN=PF3D7_0624000 PE=3 SV=1	0	0	3	0	0	0	0	0	0	0	0	0	0	0	0
C6KT90_PLAF7	Uncharacterized protein OS=*Plasmodium falciparum* (isolate 3D7) OX=36329 GN=PF3D7_0625400 PE=4 SV=1	1	3	4	5	3	0	0	0	1	0	0	0	0	0	0
C6KTA4_PLAF7	Pyruvate kinase OS=*Plasmodium falciparum* (isolate 3D7) OX=36329 GN=PF3D7_0626800 PE=1 SV=1	0	2	11	0	5	0	0	0	0	0	0	0	0	0	0
C6KTB8_PLAF7	Protein kinase PK4 OS=*Plasmodium falciparum* (isolate 3D7) OX=36329 GN=PF3D7_0628200 PE=4 SV=1	0	5	19	0	5	0	0	0	0	0	0	0	0	0	0
C6KTC7_PLAF7	DnaJ protein, putative OS=*Plasmodium falciparum* (isolate 3D7) OX=36329 GN=PF3D7_0629200 PE=4 SV=1	0	2	4	0	1	0	0	0	0	0	0	0	0	0	0
C6S3D0_PLAF7	Peptidase, putative OS=*Plasmodium falciparum* (isolate 3D7) OX=36329 GN=PF3D7_1018300 PE=4 SV=1	0	0	6	0	0	0	0	0	0	0	0	0	0	0	0
CAH1_HUMAN	Carbonic anhydrase 1 OS=Homo sapiens OX=9606 GN=CA1 PE=1 SV=2	2	6	2	2	1	2	0	0	2	2	2	2	2	2	2

Accession Number	Description	50WTB1 57-04 peptide	50WTB2 72-02 peptide	50WTB3 72-04 peptide	51ETB2 57-08 peptide	51ETB3 72-06 peptide	51ETB4 152-02 peptide	stevTB1 57-12 peptide	stevTB2 72-08 peptide	stevTB3 72-10 peptide	3D71 72-12 peptide	3D72 72-14 peptide	3D73 72-16 peptide	3D7B1 72-18 peptide	3D7B2 72-20 peptide	3D7B3 72-22 peptide
CAH2_HUMAN	Carbonic anhydrase 2 OS=Homo sapiens OX=9606 GN=CA2 PE=1 SV=2	2	4	3	1	1	2	0	1	1	2	3	2	2	2	1
CAN1_HUMAN	Calpain-1 catalytic subunit OS=Homo sapiens OX=9606 GN=CAPN1 PE=1 SV=1	0	0	2	0	0	0	0	0	0	0	0	0	0	0	0
CAND1_HUMAN	Cullin-associated NEDD8-dissociated protein 1 OS=Homo sapiens OX=9606 GN=CAND1 PE=1 SV=2	0	0	2	0	0	0	0	0	0	0	0	0	0	0	0
CASPE_HUMAN	Caspase-14 OS=Homo sapiens OX=9606 GN=CASP14 PE=1 SV=2	0	1	1	0	0	0	4	0	3	0	0	0	0	0	0
CATA_HUMAN	Catalase OS=Homo sapiens OX=9606 GN=CAT PE=1 SV=3	0	2	0	6	7	0	4	0	1	0	1	0	0	0	0
CCD30_HUMAN-DECOY	Coiled-coil domain-containing protein 30 OS=Homo sapiens OX=9606 GN=CCDC30 PE=2 SV=1	0	0	0	0	0	0	0	0	1	2	1	0	0	0	1
CDAT_PLAF7	Putative cell division cycle ATPase OS=*Plasmodium falciparum* (isolate 3D7) OX=36329 GN=PF07_0047 PE=3 SV=2	0	0	5	0	2	0	0	0	0	0	0	0	0	0	0
CTNB1_HUMAN	Catenin beta-1 OS=Homo sapiens OX=9606 GN=CTNNB1 PE=1 SV=1	0	0	1	0	0	0	0	0	0	0	0	1	0	0	2
CYTN_HUMAN	Cystatin-SN OS=Homo sapiens OX=9606 GN=CST1 PE=1 SV=3	0	0	0	0	0	0	0	0	0	0	0	2	0	0	0
DCD_HUMAN	Dermcidin OS=Homo sapiens OX=9606 GN=DCD PE=1 SV=2	1	3	3	3	1	0	4	1	4	3	3	3	2	3	2
DDX3X_HUMAN	ATP-dependent RNA helicase DDX3X OS=Homo sapiens OX=9606 GN=DDX3X PE=1 SV=3	0	0	0	0	0	0	0	0	0	3	0	0	0	0	0
DESP_HUMAN	Desmoplakin OS=Homo sapiens OX=9606 GN=DSP PE=1 SV=3	0	15	21	7	5	1	11	1	11	11	14	26	6	5	15
DSC1_HUMAN	Desmocollin-1 OS=Homo sapiens OX=9606 GN=DSC1 PE=1 SV=2	0	4	2	0	0	0	0	0	1	2	2	4	1	0	2
DSG1_HUMAN	Desmoglein-1 OS=Homo sapiens OX=9606 GN=DSG1 PE=1 SV=2	0	11	11	5	3	0	8	0	8	9	11	13	8	9	9
E41L1_HUMAN	Band 4.1-like protein 1 OS=Homo sapiens OX=9606 GN=EPB41L1 PE=1 SV=2	0	0	0	0	0	0	0	0	0	0	0	0	0	0	0
E41L3_HUMAN	Band 4.1-like protein 3 OS=Homo sapiens OX=9606 GN=EPB41L3 PE=1 SV=2	0	0	0	1	0	0	0	0	0	0	0	0	0	0	0
EF1A1_HUMAN (+1)	Elongation factor 1-alpha 1 OS=Homo sapiens OX=9606 GN=EEF1A1 PE=1 SV=1	0	0	1	0	0	0	0	0	0	3	0	0	0	0	1
ENOA_HUMAN	Alpha-enolase OS=Homo sapiens OX=9606 GN=ENO1 PE=1 SV=2	0	0	0	0	0	0	0	0	0	0	0	2	0	0	0
ENOB_HUMAN	Beta-enolase OS=Homo sapiens OX=9606 GN=ENO3 PE=1 SV=5	0	0	0	0	0	0	0	0	0	0	0	0	0	0	1
ENPL_HUMAN	Endoplasmin OS=Homo sapiens OX=9606 GN=HSP90B1 PE=1 SV=1	0	0	0	0	1	0	0	0	0	2	0	0	0	0	0
ENSEMBL:|ENSBTAP00000038253|	(Bos taurus) 63 kDa protein	0	12	12	9	8	0	7	0	10	10	11	12	0	10	12
EPB41_HUMAN	Protein 4.1 OS=Homo sapiens OX=9606 GN=EPB41 PE=1 SV=4	0	0	3	5	11	2	0	0	1	0	0	0	0	0	0
EPB41_HUMAN [2]	Cluster of Protein 4.1 OS=Homo sapiens OX=9606 GN=EPB41 PE=1 SV=4 (EPB41_HUMAN)	0	0	3	5	11	2	0	0	1	0	0	0	0	0	0
EZRI_HUMAN	Ezrin OS=Homo sapiens OX=9606 GN=EZR PE=1 SV=4	0	0	0	0	0	0	0	0	0	2	0	0	0	0	0
FABP5_HUMAN	Fatty acid-binding protein 5 OS=Homo sapiens OX=9606 GN=FABP5 PE=1 SV=3	0	2	1	0	1	0	0	0	1	1	1	2	1	1	0
G3P_HUMAN	Glyceraldehyde-3-phosphate dehydrogenase OS=Homo sapiens OX=9606 GN=GAPDH PE=1 SV=3	0	6	5	1	0	1	4	0	5	2	3	5	1	0	1
Gene_Symbol=5430421N21Rik	Keratin type II	0	0	0	0	0	0	0	0	0	2	1	0	0	0	22
Gene_Symbol=Krt10	Isoform 1 of Keratin, type I cytoskeletal 10	0	7	0	0	0	0	7	0	0	7	7	8	0	7	7
Gene_Symbol=Krt13	Isoform 1 of Keratin, type I cytoskeletal 13	0	0	0	4	0	0	6	0	0	0	0	0	0	0	0
Gene_Symbol=Krt16	Keratin intermediate filament 16a;Keratin, type I cytoskeletal 16	0	6	11	0	5	0	0	0	6	10	6	11	7	4	5
Gene_Symbol=Krt17	Keratin, type I cytoskeletal 17	0	0	0	0	0	0	0	0	0	0	0	0	0	0	0
Gene_Symbol=Krt17-DECOY	Keratin, type I cytoskeletal 17	0	0	0	0	0	0	0	0	0	0	0	0	0	0	0
Gene_Symbol=Krt18	Keratin, type I cytoskeletal 18	0	0	0	0	0	0	0	0	0	0	0	0	0	0	0

Accession Number	Description	50WTB1 57-04 peptide	50WTB2 72-02 peptide	50WTB3 72-04 peptide	51ETB2 57-08 peptide	51ETB3 72-06 peptide	51ETB4 152-02 peptide	stevTB1 57-12 peptide	stevTB2 72-08 peptide	stevTB3 72-10 peptide	3D71 72-12 peptide	3D72 72-14 peptide	3D73 72-16 peptide	3D7B1 72-18 peptide	3D7B2 72-20 peptide	3D7B3 72-22 peptide
Gene_Symbol=Krt2	Keratin, type II cytoskeletal 2 epidermal	9	0	0	0	0	0	0	0	9	0	0	0	0	0	0
Gene_Symbol=Krt20	Keratin, type I cytoskeletal 20	0	2	0	2	0	0	3	0	2	0	0	3	0	0	0
Gene_Symbol=Krt34	10 days neonate skin cDNA, RIKEN full-length enriched library, clone:4733401E01 product:keratin complex 1, acidic, gene 4, full insert sequence	0	0	0	0	2	0	5	0	1	2	1	1	0	0	11
Gene_Symbol=Krt35	Krt35 protein	0	0	0	0	0	0	0	0	0	1	1	1	1	0	17
Gene_Symbol=Krt4	Keratin, type II cytoskeletal 4	0	0	9	0	0	0	4	0	3	4	5	5	5	0	7
Gene_Symbol=Krt42	Keratin, type I cytoskeletal 42	0	0	0	0	0	0	0	0	0	0	0	0	0	0	10
Gene_Symbol=Krt5	Keratin, type II cytoskeletal 5	0	22	26	0	14	0	0	7	18	22	20	19	21	16	22
Gene_Symbol=Krt6a	Keratin, type II cytoskeletal 6A	0	15	19	0	0	0	0	0	13	17	0	17	14	0	15
Gene_Symbol=Krt7	Keratin, type II cytoskeletal 7	0	0	0	0	0	0	2	0	0	0	0	0	0	0	0
Gene_Symbol=Krt71	Keratin, type II cytoskeletal 6G	0	0	0	0	2	0	0	0	0	3	0	0	0	0	0
Gene_Symbol=Krt72	Type-II keratin Kb35	0	0	2	1	0	0	0	0	0	4	0	4	0	0	4
Gene_Symbol=Krt77	Keratin, type II cytoskeletal 1b	0	10	11	7	4	5	0	3	8	7	9	9	9	8	9
Gene_Symbol=Krt79	Keratin 79	0	7	10	0	0	3	0	0	7	8	7	7	8	0	7
Gene_Symbol=Krt80	Keratin 80	0	0	0	0	0	0	0	0	0	0	0	0	0	0	0
GFAP_HUMAN	Glial fibrillary acidic protein OS=Homo sapiens OX=9606 GN=GFAP PE=1 SV=1	1	0	0	0	0	0	0	0	0	0	0	0	0	0	0
GRP75_HUMAN	Stress-70 protein, mitochondrial OS=Homo sapiens OX=9606 GN=HSPA9 PE=1 SV=2	0	1	1	0	1	0	0	0	1	8	0	0	0	1	0
H4_HUMAN	Histone H4 OS=Homo sapiens OX=9606 GN=H4-16 PE=1 SV=2	0	0	0	0	0	0	0	0	0	0	1	0	0	0	6
H90B2_HUMAN	Putative heat shock protein HSP 90-beta 2 OS=Homo sapiens OX=9606 GN=HSP90AB2P PE=1 SV=2	0	0	0	0	0	0	0	0	0	0	0	0	0	0	0
HBA_HUMAN	Hemoglobin subunit alpha OS=Homo sapiens OX=9606 GN=HBA2 PE=1 SV=2	6	7	8	9	7	0	6	2	6	7	5	8	1	6	6
HBA_HUMAN [2]	Cluster of Hemoglobin subunit alpha OS=Homo sapiens OX=9606 GN=HBA2 PE=1 SV=2 (HBA_HUMAN)	7	0	0	10	0	0	6	0	0	0	0	0	0	0	0
HBB_HUMAN	Hemoglobin subunit beta OS=Homo sapiens OX=9606 GN=HBB PE=1 SV=2	7	12	13	11	11	4	6	9	12	9	9	12	4	9	8
HBB_HUMAN [2]	Cluster of Hemoglobin subunit beta OS=Homo sapiens OX=9606 GN=HBB PE=1 SV=2 (HBB_HUMAN)	7	0	0	12	0	0	6	0	0	0	0	0	0	0	0
HBB_HUMAN [5]	Cluster of Hemoglobin subunit beta OS=Homo sapiens OX=9606 GN=HBB PE=1 SV=2 (HBB_HUMAN)	0	21	23	0	19	5	0	11	19	16	15	23	6	18	14
HBD_HUMAN	Hemoglobin subunit delta OS=Homo sapiens OX=9606 GN=HBD PE=1 SV=2	5	6	7	7	6	2	3	5	7	5	5	7	3	6	5
HBE_HUMAN	Hemoglobin subunit epsilon OS=Homo sapiens OX=9606 GN=HBE1 PE=1 SV=2	0	0	0	0	0	0	0	0	0	0	0	0	0	0	0
Hemoglobin	subunit alpha (Bos taurus)	4	5	5	4	4	2	2	1	4	4	5	6	3	6	4
H-INV:|HIT000292931|	human Gene_Symbol=- Similar to Keratin, type II cytoskeletal 8	0	0	0	0	0	0	0	0	0	0	0	0	0	0	1
HS71L_HUMAN	Heat shock 70 kDa protein 1-like OS=Homo sapiens OX=9606 GN=HSPA1L PE=1 SV=2	0	0	3	0	0	0	0	0	0	0	0	0	0	0	0
HS902_HUMAN	Heat shock protein HSP 90-alpha A2 OS=Homo sapiens OX=9606 GN=HSP90AA2P PE=1 SV=2	0	0	0	0	0	0	0	0	0	2	0	0	0	0	0
HS904_HUMAN	Putative heat shock protein HSP 90-alpha A4 OS=Homo sapiens OX=9606 GN=HSP90AA4P PE=5 SV=1	0	0	0	0	0	0	0	0	0	1	1	0	0	0	0
HS90A_HUMAN	Heat shock protein HSP 90-alpha OS=Homo sapiens OX=9606 GN=HSP90AA1 PE=1 SV=5	0	1	2	0	0	0	0	0	0	10	0	0	0	0	0
HS90B_HUMAN	Heat shock protein HSP 90-beta OS=Homo sapiens OX=9606 GN=HSP90AB1 PE=1 SV=4	0	1	4	0	1	0	0	0	0	19	1	1	0	1	1
HSP72_HUMAN	Heat shock-related 70 kDa protein 2 OS=Homo sapiens OX=9606 GN=HSPA2 PE=1 SV=1	0	0	4	0	0	0	0	0	0	9	0	0	0	0	0
HSP76_HUMAN	Heat shock 70 kDa protein 6 OS=Homo sapiens OX=9606 GN=HSPA6 PE=1 SV=2	0	3	3	0	0	0	0	0	0	3	0	1	0	0	0
HSP77_HUMAN	Putative heat shock 70 kDa protein 7 OS=Homo sapiens OX=9606 GN=HSPA7 PE=5 SV=2	0	0	0	0	0	0	0	0	0	0	0	0	0	0	1

Accession Number	Description	50WTB1 57-04 peptide	50WTB2 72-02 peptide	50WTB3 72-04 peptide	51ETB2 57-08 peptide	51ETB3 72-06 peptide	51ETB4 152-02 peptide	stevTB1 57-12 peptide	stevTB2 72-08 peptide	stevTB3 72-10 peptide	3D71 72-12 peptide	3D72 72-14 peptide	3D73 72-16 peptide	3D7B1 72-18 peptide	3D7B2 72-20 peptide	3D7B3 72-22 peptide
HSP7C_HUMAN	Heat shock cognate 71 kDa protein OS=Homo sapiens OX=9606 GN=HSPA8 PE=1 SV=1	3	3	3	3	3	2	0	1	2	21	1	2	0	1	2
human	Gene_Symbol=HRNR Hornerin;Gene_Symbol=KRT10 Keratin, type I cytoskeletal 10	137	192	188	205	130	122	202	92	179	161	159	177	159	142	181
human [45]	Cluster of Gene_Symbol=HRNR Hornerin (human)	146	0	0	233	0	0	273	0	0	0	0	0	0	0	0
human [62]	Cluster of Gene_Symbol=KRT10 Keratin, type I cytoskeletal 10 (human)	0	262	270	0	177	136	0	117	245	250	221	265	218	182	327
human-DECOY	Gene_Symbol=KRT1 Keratin, type II cytoskeletal 1	2	2	3	0	0	2	0	0	0	2	0	2	2	0	3
human-DECOY [5]	Cluster of Gene_Symbol=KRT1 Keratin, type II cytoskeletal 1 (human-DECOY)	0	3	4	0	0	3	0	0	1	3	0	3	3	0	4
HUTH_HUMAN	Histidine ammonia-lyase OS=Homo sapiens OX=9606 GN=HAL PE=1 SV=1	0	0	0	0	0	0	2	0	0	0	0	0	0	0	0
Hypothetical	protein MGC139876 (Bos taurus)	0	0	0	0	2	0	0	0	0	0	0	0	0	0	0
IGHA1_HUMAN	Immunoglobulin heavy constant alpha 1 OS=Homo sapiens OX=9606 GN=IGHA1 PE=1 SV=2	0	0	0	0	0	0	0	0	0	0	1	3	0	0	0
K1C17_HUMAN	Keratin, type I cytoskeletal 17 OS=Homo sapiens OX=9606 GN=KRT17 PE=1 SV=2	4	14	14	9	7	4	12	3	11	23	9	14	11	5	13
K1C18_HUMAN	Keratin, type I cytoskeletal 18 OS=Homo sapiens OX=9606 GN=KRT18 PE=1 SV=2	0	0	0	0	0	0	0	0	0	1	0	0	0	0	0
K1C24_HUMAN	Keratin, type I cytoskeletal 24 OS=Homo sapiens OX=9606 GN=KRT24 PE=1 SV=1	0	0	0	0	0	0	0	0	0	0	0	1	0	0	1
K1C27_HUMAN	Keratin, type I cytoskeletal 27 OS=Homo sapiens OX=9606 GN=KRT27 PE=1 SV=2	0	0	0	0	2	0	0	0	0	0	0	0	0	0	0
K1C28_HUMAN	Keratin, type I cytoskeletal 28 OS=Homo sapiens OX=9606 GN=KRT28 PE=1 SV=2	0	0	0	0	0	0	3	0	0	0	0	0	0	0	0
K1C9_HUMAN	Keratin, type I cytoskeletal 9 OS=Homo sapiens OX=9606 GN=KRT9 PE=1 SV=3	18	38	40	35	35	25	32	27	38	34	31	37	31	27	38
K1H2_HUMAN	Keratin, type I cuticular Ha2 OS=Homo sapiens OX=9606 GN=KRT32 PE=1 SV=3	0	0	0	0	0	0	0	0	0	0	0	0	0	0	0
K22E_HUMAN	Keratin, type II cytoskeletal 2 epidermal OS=Homo sapiens OX=9606 GN=KRT2 PE=1 SV=2	38	54	50	52	35	32	44	23	55	44	40	43	41	45	55
K22E_HUMAN-DECOY	Keratin, type II cytoskeletal 2 epidermal OS=Homo sapiens OX=9606 GN=KRT2 PE=1 SV=2	0	1	2	0	0	1	0	0	1	1	0	1	1	0	1
K2C1_HUMAN	Keratin, type II cytoskeletal 1 OS=Homo sapiens OX=9606 GN=KRT1 PE=1 SV=6	44	57	60	51	49	48	41	33	58	52	55	55	57	53	56
K2C1B_HUMAN	Keratin, type II cytoskeletal 1b OS=Homo sapiens OX=9606 GN=KRT77 PE=1 SV=3	0	0	0	0	0	0	0	0	0	0	0	8	0	0	0
K2C4_HUMAN	Keratin, type II cytoskeletal 4 OS=Homo sapiens OX=9606 GN=KRT4 PE=1 SV=5	0	6	19	0	0	0	0	0	5	6	7	17	0	0	2
K2C4_HUMAN (+1)	Keratin, type II cytoskeletal 4 OS=Homo sapiens OX=9606 GN=KRT4 PE=1 SV=5	0	0	0	0	0	0	2	0	0	0	0	0	0	0	0
K2C6B_HUMAN	Keratin, type II cytoskeletal 6B OS=Homo sapiens OX=9606 GN=KRT6B PE=1 SV=5	0	29	38	29	19	9	16	12	24	32	25	32	27	19	24
K2C75_HUMAN	Keratin, type II cytoskeletal 75 OS=Homo sapiens OX=9606 GN=KRT75 PE=1 SV=2	0	11	13	0	7	3	7	3	10	10	8	9	10	7	14
K2C78_HUMAN	Keratin, type II cytoskeletal 78 OS=Homo sapiens OX=9606 GN=KRT78 PE=1 SV=2	0	9	9	0	2	1	0	1	2	5	5	4	2	4	3
K7NTP5_PLAF7	Heat shock protein 70 OS=*Plasmodium falciparum* (isolate 3D7) OX=36329 GN=PF3D7_0831700 PE=1 SV=1	8	22	32	10	18	5	0	2	4	5	1	2	0	3	2
Keratin,	type II cytoskeletal 5 (Bos taurus)	11	27	34	20	22	10	46	8	27	36	31	33	27	22	94
KPRP_HUMAN	Keratinocyte proline-rich protein OS=Homo sapiens OX=9606 GN=KPRP PE=1 SV=1	3	11	9	4	4	1	3	0	7	8	9	12	7	7	8
KR87P_HUMAN	Putative keratin-87 protein OS=Homo sapiens OX=9606 GN=KRT87P PE=5 SV=4	0	0	0	0	0	0	0	0	0	3	2	1	0	0	18
KRT34_HUMAN	Keratin, type I cuticular Ha4 OS=Homo sapiens OX=9606 GN=KRT34 PE=1 SV=2	0	0	0	0	2	0	0	0	1	1	1	3	0	0	8
KRT36_HUMAN	Keratin, type I cuticular Ha6 OS=Homo sapiens OX=9606 GN=KRT36 PE=1 SV=1	0	0	0	0	0	0	0	0	0	0	0	0	0	0	10

Accession Number	Description	50WTB1 57-04 peptide	50WTB2 72-02 peptide	50WTB3 72-04 peptide	51ETB2 57-08 peptide	51ETB3 72-06 peptide	51ETB4 152-02 peptide	stevTB1 57-12 peptide	stevTB2 72-08 peptide	stevTB3 72-10 peptide	3D71 72-12 peptide	3D72 72-14 peptide	3D73 72-16 peptide	3D7B1 72-18 peptide	3D7B2 72-20 peptide	3D7B3 72-22 peptide
KRT37_HUMAN	Keratin, type I cuticular Ha7 OS=Homo sapiens OX=9606 GN=KRT37 PE=1 SV=3	0	0	0	0	0	0	0	0	0	0	0	0	0	0	0
KRT38_HUMAN	Keratin, type I cuticular Ha8 OS=Homo sapiens OX=9606 GN=KRT38 PE=1 SV=3	0	0	0	0	0	0	0	0	0	0	0	0	0	0	0
KRT4	human Gene_Symbol=KRT4 keratin 4	0	6	19	0	2	0	0	0	5	6	7	17	0	0	2
KRT4 [2]	Cluster of human Gene_Symbol=KRT4 keratin 4 (KRT4)	0	6	19	0	2	0	0	0	5	6	7	17	0	0	2
KRT85_HUMAN	Keratin, type II cuticular Hb5 OS=Homo sapiens OX=9606 GN=KRT85 PE=1 SV=1	0	0	0	0	0	0	17	0	0	3	2	4	0	0	30
KRT86_HUMAN	Keratin, type II cuticular Hb6 OS=Homo sapiens OX=9606 GN=KRT86 PE=1 SV=1	0	0	0	0	0	0	19	0	0	4	4	3	0	0	27
LEG7_HUMAN	Galectin-7 OS=Homo sapiens OX=9606 GN=LGALS7B PE=1 SV=2	0	0	0	0	0	0	3	0	0	0	0	0	0	0	0
LMNA_HUMAN	Prelamin-A/C OS=Homo sapiens OX=9606 GN=LMNA PE=1 SV=1	0	0	0	0	0	0	0	0	0	11	0	0	0	0	0
LORI_HUMAN	Loricrin OS=Homo sapiens OX=9606 GN=LORICRIN PE=1 SV=2	0	1	0	0	0	0	0	0	0	1	2	0	0	0	0
LOXE3_HUMAN	Hydroperoxide isomerase ALOXE3 OS=Homo sapiens OX=9606 GN=ALOXE3 PE=1 SV=1	0	2	0	0	0	0	0	0	0	0	0	1	0	0	0
LYSC_HUMAN	Lysozyme C OS=Homo sapiens OX=9606 GN=LYZ PE=1 SV=1	0	1	2	0	1	0	0	0	1	1	1	3	1	1	3
MOES_HUMAN	Moesin OS=Homo sapiens OX=9606 GN=MSN PE=1 SV=3	0	0	0	0	0	0	0	0	0	6	0	0	0	0	0
MOES_HUMAN [3]	Cluster of Moesin OS=Homo sapiens OX=9606 GN=MSN PE=1 SV=3 (MOES_HUMAN)	0	0	0	0	0	0	0	0	0	6	0	0	0	0	0
NFH_HUMAN	Neurofilament heavy polypeptide OS=Homo sapiens OX=9606 GN=NEFH PE=1 SV=4	0	0	0	0	0	0	0	0	0	0	0	0	0	0	0
O77351_PLAF7	Dolichyl-diphosphooligosaccharide--protein glycosyltransferase subunit 1 OS=*Plasmodium falciparum* (isolate 3D7) OX=36329 GN=PF3D7_0311600 PE=3 SV=2	0	2	5	0	0	0	0	0	0	0	0	0	0	0	0
O77361_PLAF7	TVN-junction protein 1 OS=*Plasmodium falciparum* (isolate 3D7) OX=36329 GN=PF3D7_0310400 PE=4 SV=1	0	1	27	0	1	0	0	0	0	0	0	0	0	0	0
O77391_PLAF7	CS domain-containing protein OS=*Plasmodium falciparum* (isolate 3D7) OX=36329 GN=PF3D7_0316400 PE=4 SV=1	0	0	4	0	0	0	0	0	0	0	0	0	0	0	0
O96275_PLAF7	Liver stage antigen 3 OS=*Plasmodium falciparum* (isolate 3D7) OX=36329 GN=PF3D7_0220000 PE=4 SV=1	0	0	3	0	3	0	0	0	0	0	0	0	0	0	0
OAT_PLAF7	Ornithine aminotransferase OS=*Plasmodium falciparum* (isolate 3D7) OX=36329 GN=OAT PE=1 SV=1	0	0	4	0	0	0	0	0	0	0	0	0	0	0	0
P113_PLAF7	Surface protein P113 OS=*Plasmodium falciparum* (isolate 3D7) OX=36329 GN=P113 PE=1 SV=1	2	5	22	0	0	0	0	0	0	0	0	0	0	0	0
P5CS_HUMAN	Delta-1-pyrroline-5-carboxylate synthase OS=Homo sapiens OX=9606 GN=ALDH18A1 PE=1 SV=2	0	0	0	0	0	0	0	0	0	2	0	0	0	0	0
PABP1_HUMAN	Polyadenylate-binding protein 1 OS=Homo sapiens OX=9606 GN=PABPC1 PE=1 SV=2	0	0	0	0	0	0	0	0	0	2	0	0	0	0	0
PABP1_HUMAN [2]	Cluster of Polyadenylate-binding protein 1 OS=Homo sapiens OX=9606 GN=PABPC1 PE=1 SV=2 (PABP1_HUMAN)	0	0	0	0	0	0	0	0	0	2	0	0	0	0	0
PABP4_HUMAN	Polyadenylate-binding protein 4 OS=Homo sapiens OX=9606 GN=PABPC4 PE=1 SV=1	0	0	0	0	0	0	0	0	0	1	0	0	0	0	0
PF07_PLAF7	Uncharacterized protein PFC0810c OS=*Plasmodium falciparum* (isolate 3D7) OX=36329 GN=PFC0810c PE=1 SV=1	0	0	3	0	0	0	0	0	0	0	0	0	0	0	0
PGK_PLAF7	Phosphoglycerate kinase OS=*Plasmodium falciparum* (isolate 3D7) OX=36329 GN=PGK PE=1 SV=1	0	0	2	0	0	0	0	0	0	0	0	0	0	0	0
PIP_HUMAN	Prolactin-inducible protein OS=Homo sapiens OX=9606 GN=PIP PE=1 SV=1	0	1	3	0	0	0	0	0	1	0	1	2	0	0	1

Accession Number	Description	50WTB1 57-04 peptide	50WTB2 72-02 peptide	50WTB3 72-04 peptide	51ETB2 57-08 peptide	51ETB3 72-06 peptide	51ETB4 152-02 peptide	stevTB1 57-12 peptide	stevTB2 72-08 peptide	stevTB3 72-10 peptide	3D71 72-12 peptide	3D72 72-14 peptide	3D73 72-16 peptide	3D7B1 72-18 peptide	3D7B2 72-20 peptide	3D7B3 72-22 peptide
PKP1_HUMAN	Plakophilin-1 OS=Homo sapiens OX=9606 GN=PKP1 PE=1 SV=2	0	2	2	0	0	0	0	0	1	1	1	1	1	0	1
PLAK_HUMAN	Junction plakoglobin OS=Homo sapiens OX=9606 GN=JUP PE=1 SV=3	0	8	12	5	4	0	5	0	6	10	12	15	10	7	11
PLAK_HUMAN [2]	Cluster of Junction plakoglobin OS=Homo sapiens OX=9606 GN=JUP PE=1 SV=3 (PLAK_HUMAN)	0	8	12	0	4	0	0	0	6	10	12	15	10	7	11
POTEE_HUMAN	POTE ankyrin domain family member E OS=Homo sapiens OX=9606 GN=POTEE PE=2 SV=3	0	1	3	0	1	0	0	0	2	2	2	2	0	0	0
POTEE_HUMAN (+1)	POTE ankyrin domain family member E OS=Homo sapiens OX=9606 GN=POTEE PE=2 SV=3	0	0	0	0	0	0	0	0	0	0	0	0	0	0	0
POTEF_HUMAN	POTE ankyrin domain family member F OS=Homo sapiens OX=9606 GN=POTEF PE=1 SV=2	0	0	3	0	1	0	0	0	2	2	2	2	0	0	0
Q76NL8_PLAF7	Falcilysin OS=*Plasmodium falciparum* (isolate 3D7) OX=36329 GN=PF3D7_1360800 PE=1 SV=1	0	1	15	0	1	0	0	0	0	0	0	0	0	0	0
Q76NM3_PLAF7	L-lactate dehydrogenase OS=*Plasmodium falciparum* (isolate 3D7) OX=36329 GN=PF3D7_1324900 PE=1 SV=1	0	0	5	0	0	0	0	0	0	0	0	0	0	0	0
Q7K6A4_PLAF7	S-adenosylmethionine synthase OS=*Plasmodium falciparum* (isolate 3D7) OX=36329 GN=PF3D7_0922200 PE=3 SV=1	0	0	3	0	0	0	0	0	0	0	0	0	0	0	0
Q8I0P6_PLAF7	Elongation factor 1-alpha OS=*Plasmodium falciparum* (isolate 3D7) OX=36329 GN=PF3D7_1357000 PE=3 SV=1	0	0	9	3	0	0	0	0	0	1	0	0	0	0	1
Q8I0U8_PLAF7	Merozoite surface antigens OS=*Plasmodium falciparum* (isolate 3D7) OX=36329 GN=PF3D7_0930300 PE=4 SV=1	0	0	3	0	0	0	0	0	0	0	0	0	0	0	0
Q8I0V3_PLAF7	60 kDa chaperonin OS=*Plasmodium falciparum* (isolate 3D7) OX=36329 GN=PF3D7_1232100 PE=3 SV=2	0	2	16	0	0	0	0	0	0	0	0	0	0	0	0
Q8I0V4_PLAF7	Endoplasmin, putative OS=*Plasmodium falciparum* (isolate 3D7) OX=36329 GN=PF3D7_1222300 PE=1 SV=1	9	30	48	7	19	6	0	2	2	0	0	0	0	0	0
Q8I207_PLAF7	PRESAN domain-containing protein OS=*Plasmodium falciparum* (isolate 3D7) OX=36329 GN=PF3D7_0401800 PE=4 SV=1	0	1	2	3	2	1	0	0	1	0	0	0	0	0	0
Q8I255_PLAF7	Secreted ookinete protein, putative OS=*Plasmodium falciparum* (isolate 3D7) OX=36329 GN=PF3D7_0108700 PE=4 SV=2	0	3	15	0	1	0	0	0	0	0	0	0	0	0	0
Q8I259_PLAF7	Uncharacterized protein OS=*Plasmodium falciparum* (isolate 3D7) OX=36329 GN=PF3D7_0108300 PE=4 SV=2	0	0	1	0	5	0	0	0	0	0	0	0	0	0	0
Q8I266_PLAF7	Niemann-Pick type C1-related protein OS=*Plasmodium falciparum* (isolate 3D7) OX=36329 GN=PF3D7_0107500 PE=4 SV=1	0	1	7	0	0	0	0	0	0	0	0	0	0	0	0
Q8I2A1_PLAF7	Parasite-infected erythrocyte surface protein OS=*Plasmodium falciparum* (isolate 3D7) OX=36329 GN=PF3D7_0103900 PE=4 SV=1	0	3	11	0	2	0	0	0	0	0	0	0	0	0	0
Q8I2B2_PLAF7	Seipin domain-containing protein, putative OS=*Plasmodium falciparum* (isolate 3D7) OX=36329 GN=PF3D7_0102800 PE=4 SV=2	0	0	2	0	0	0	0	0	0	0	0	0	0	0	0
Q8I2G1_PLAF7	Ring-exported protein 1 OS=*Plasmodium falciparum* (isolate 3D7) OX=36329 GN=PF3D7_0935900 PE=4 SV=1	0	0	2	0	4	1	0	0	0	0	0	0	0	0	0
Q8I2W2_PLAF7	DnaJ protein, putative OS=*Plasmodium falciparum* (isolate 3D7) OX=36329 GN=PF3D7_0919100 PE=4 SV=1	0	0	2	0	0	0	0	0	0	0	0	0	0	0	0
Q8I2X4_PLAF7	Heat shock protein 70 OS=*Plasmodium falciparum* (isolate 3D7) OX=36329 GN=PF3D7_0917900 PE=3 SV=1	20	31	47	16	24	12	4	2	2	4	0	1	0	0	1
Q8I2Z8_PLAF7	Probable ATP-dependent 6-phosphofructokinase OS=*Plasmodium*	0	0	2	0	3	0	0	0	0	0	0	0	0	0	0

Accession Number	Description	50WTB1 57-04 peptide	50WTB2 72-02 peptide	50WTB3 72-04 peptide	51ETB2 57-08 peptide	51ETB3 72-06 peptide	51ETB4 152-02 peptide	stevTB1 57-12 peptide	stevTB2 72-08 peptide	stevTB3 72-10 peptide	3D71 72-12 peptide	3D72 72-14 peptide	3D73 72-16 peptide	3D7B1 72-18 peptide	3D7B2 72-20 peptide	3D7B3 72-22 peptide
	falciparum (isolate 3D7) OX=36329 GN=PF3D7_0915400 PE=3 SV=1															
Q8I3C0_PLAF7	Serine repeat antigen 9 OS=*Plasmodium falciparum* (isolate 3D7) OX=36329 GN=PF3D7_0902800 PE=3 SV=1	0	1	6	0	0	0	0	0	0	0	0	0	0	0	0
Q8I3F1_PLAF7	PRESAN domain-containing protein OS=*Plasmodium falciparum* (isolate 3D7) OX=36329 GN=PF3D7_0532300 PE=4 SV=1	1	4	5	12	12	9	2	0	0	0	0	0	0	0	0
Q8I3J8_PLAF7	Uncharacterized protein OS=*Plasmodium falciparum* (isolate 3D7) OX=36329 GN=PF3D7_0526700 PE=4 SV=1	0	0	7	0	0	0	0	0	0	0	0	0	0	0	0
Q8I3M5_PLAF7	Karyopherin beta OS=*Plasmodium falciparum* (isolate 3D7) OX=36329 GN=PF3D7_0524000 PE=4 SV=1	0	1	12	0	1	0	0	0	0	0	0	0	0	0	0
Q8I431_PLAF7	60S ribosomal protein L4 OS=*Plasmodium falciparum* (isolate 3D7) OX=36329 GN=PF3D7_0507100 PE=1 SV=1	0	2	4	0	2	0	0	0	0	0	0	0	0	0	0
Q8I445_PLAF7	Uncharacterized protein OS=*Plasmodium falciparum* (isolate 3D7) OX=36329 GN=PF3D7_0505700 PE=4 SV=1	0	1	9	0	0	0	0	0	0	0	0	0	0	0	0
Q8I488_PLAF7	Parasite-infected erythrocyte surface protein OS=*Plasmodium falciparum* (isolate 3D7) OX=36329 GN=PF3D7_0501200 PE=4 SV=1	0	1	1	0	3	2	0	0	0	0	0	0	0	0	0
Q8I492_PLAF7	Mature parasite-infected erythrocyte surface antigen OS=*Plasmodium falciparum* (isolate 3D7) OX=36329 GN=PF3D7_0500800 PE=4 SV=1	1	16	50	7	47	3	0	0	6	0	0	0	0	0	0
Q8I526_PLAF7	ATP-dependent zinc metalloprotease FTSH 1 OS=*Plasmodium falciparum* (isolate 3D7) OX=36329 GN=PF3D7_1239700 PE=3 SV=1	0	0	2	0	0	0	0	0	0	0	0	0	0	0	0
Q8I5P3_PLAF7	Uncharacterized protein OS=*Plasmodium falciparum* (isolate 3D7) OX=36329 GN=PF3D7_1216400 PE=4 SV=2	0	0	4	0	0	0	0	0	0	0	0	0	0	0	0
Q8I5P8_PLAF7	Serpentine receptor, putative OS=*Plasmodium falciparum* (isolate 3D7) OX=36329 GN=PF3D7_1215900 PE=4 SV=1	0	0	2	0	0	0	0	0	0	0	0	0	0	0	0
Q8I5Q5_PLAF7	SUN domain-containing protein, putative OS=*Plasmodium falciparum* (isolate 3D7) OX=36329 GN=PF3D7_1215100 PE=4 SV=1	0	0	12	0	0	0	0	0	0	0	0	0	0	0	0
Q8I635_PLAF7	Uncharacterized protein OS=*Plasmodium falciparum* (isolate 3D7) OX=36329 GN=PF3D7_1201000 PE=4 SV=1	0	3	6	2	6	0	0	0	0	0	0	0	0	0	0
Q8I6Z1_PLAF7	Acyl-CoA synthetase OS=*Plasmodium falciparum* (isolate 3D7) OX=36329 GN=PF3D7_0731600 PE=4 SV=1	0	0	3	0	0	0	0	0	0	0	0	0	0	0	0
Q8I6Z5_PLAF7	Plasmepsin V OS=*Plasmodium falciparum* (isolate 3D7) OX=36329 GN=PF3D7_1323500 PE=3 SV=1	0	2	1	0	2	0	0	0	0	0	0	0	0	0	0
Q8IAK9_PLAF7	PRESAN domain-containing protein OS=*Plasmodium falciparum* (isolate 3D7) OX=36329 GN=PF3D7_0801000 PE=4 SV=1	1	2	23	9	19	1	0	0	0	0	0	0	0	0	0
Q8IAM0_PLAF7	Glutamate dehydrogenase, putative OS=*Plasmodium falciparum* (isolate 3D7) OX=36329 GN=PF3D7_0802000 PE=3 SV=1	0	0	3	0	0	0	0	0	0	0	0	0	0	0	0
Q8IAU7_PLAF7	ER membrane protein complex subunit 1 OS=*Plasmodium falciparum* (isolate 3D7) OX=36329 GN=PF3D7_0811200 PE=3 SV=1	0	5	22	0	4	0	0	0	0	0	0	0	0	0	0
Q8IAV1_PLAF7	Uncharacterized protein OS=*Plasmodium falciparum* (isolate 3D7) OX=36329 GN=PF3D7_0811600 PE=4 SV=1	0	6	26	0	4	0	0	0	0	0	0	0	0	0	0
Q8IB03_PLAF7	Chaperone protein ClpB1 OS=*Plasmodium falciparum* (isolate 3D7) OX=36329 GN=PF3D7_0816600 PE=1 SV=1	0	2	8	0	0	0	0	0	0	0	0	0	0	0	0
Q8IB24_PLAF7	Heat shock protein 70 OS=*Plasmodium falciparum* (isolate 3D7) OX=36329 GN=PF3D7_0818900 PE=3 SV=1	2	12	29	15	18	8	0	3	8	4	2	2	0	5	1

Accession Number	Description	50WTB1 57-04 peptide	50WTB2 72-02 peptide	50WTB3 72-04 peptide	51ETB2 57-08 peptide	51ETB3 72-06 peptide	51ETB4 152-02 peptide	stevTB1 57-12 peptide	stevTB2 72-08 peptide	stevTB3 72-10 peptide	3D71 72-12 peptide	3D72 72-14 peptide	3D73 72-16 peptide	3D7B1 72-18 peptide	3D7B2 72-20 peptide	3D7B3 72-22 peptide
Q8IB24_PLAF7 [7]	Cluster of Heat shock protein 70 OS=*Plasmodium falciparum* (isolate 3D7) OX=36329 GN=PF3D7_0818900 PE=3 SV=1 (Q8IB24_PLAF7)	0	15	33	0	21	10	0	3	9	25	2	3	0	5	2
Q8IB24_PLAF7 [8]	Cluster of Heat shock protein 70 OS=*Plasmodium falciparum* (isolate 3D7) OX=36329 GN=PF3D7_0818900 PE=3 SV=1 (Q8IB24_PLAF7)	8	0	0	21	0	0	0	0	0	0	0	0	0	0	0
Q8IB72_PLAF7	DnaJ protein, putative OS=*Plasmodium falciparum* (isolate 3D7) OX=36329 GN=PF3D7_0823800 PE=4 SV=1	0	2	7	0	0	0	0	0	0	0	0	0	0	0	0
Q8IBF1_PLAF7	EMP1-trafficking protein OS=*Plasmodium falciparum* (isolate 3D7) OX=36329 GN=PF3D7_0731100 PE=4 SV=1	0	0	6	4	9	0	0	0	0	0	0	0	0	1	0
Q8IBF2_PLAF7	EMP1-trafficking protein OS=*Plasmodium falciparum* (isolate 3D7) OX=36329 GN=PF3D7_0730900 PE=4 SV=1	2	8	20	21	25	10	2	1	6	0	0	0	0	0	0
Q8IBH9_PLAF7	Cation transporting ATPase, putative OS=*Plasmodium falciparum* (isolate 3D7) OX=36329 GN=PF3D7_0727800 PE=4 SV=1	0	0	13	0	0	0	0	0	0	0	0	0	0	0	0
Q8IBN5_PLAF7	40S ribosomal protein S5, putative OS=*Plasmodium falciparum* (isolate 3D7) OX=36329 GN=PF3D7_0721600 PE=1 SV=1	0	0	3	0	0	0	0	0	0	0	0	0	0	0	0
Q8IBN5_PLAF7 [2]	Cluster of 40S ribosomal protein S5, putative OS=*Plasmodium falciparum* (isolate 3D7) OX=36329 GN=PF3D7_0721600 PE=1 SV=1 (Q8IBN5_PLAF7)	0	0	3	0	0	0	0	0	0	0	0	0	0	0	0
Q8IBT7_PLAF7	Uncharacterized protein OS=*Plasmodium falciparum* (isolate 3D7) OX=36329 GN=PF3D7_0716300 PE=4 SV=1	0	2	4	0	1	0	0	0	0	0	0	0	0	0	0
Q8IBW9_PLAF7	Erythrocyte membrane protein 1, PfEMP1 OS=*Plasmodium falciparum* (isolate 3D7) OX=36329 GN=PF3D7_0712600 PE=4 SV=1	0	0	1	0	0	0	0	0	0	0	0	0	0	0	0
Q8IBZ8_PLAF7	Cg1 protein OS=*Plasmodium falciparum* (isolate 3D7) OX=36329 GN=PF3D7_0709100 PE=4 SV=1	0	1	6	0	0	0	0	0	0	0	0	0	0	0	0
Q8IC05_PLAF7	Heat shock protein 90 OS=*Plasmodium falciparum* (isolate 3D7) OX=36329 GN=PF3D7_0708400 PE=1 SV=1	0	4	20	0	1	0	0	0	1	4	0	2	0	2	1
Q8IC05_PLAF7 [7]	Cluster of Heat shock protein 90 OS=*Plasmodium falciparum* (isolate 3D7) OX=36329 GN=PF3D7_0708400 PE=1 SV=1 (Q8IC05_PLAF7)	0	5	21	0	2	0	0	0	1	23	2	2	0	2	1
Q8IC11_PLAF7	RAP protein, putative OS=*Plasmodium falciparum* (isolate 3D7) OX=36329 GN=PF3D7_0707800 PE=4 SV=1	0	0	3	0	0	0	0	0	0	0	0	0	0	0	0
Q8IC35_PLAF7	Erythrocyte membrane-associated antigen OS=*Plasmodium falciparum* (isolate 3D7) OX=36329 GN=PF3D7_0703500 PE=3 SV=2	0	0	1	0	3	0	0	0	0	0	0	0	0	0	0
Q8ID50_PLAF7	Ubiquitin OS=*Plasmodium falciparum* (isolate 3D7) OX=36329 GN=PF3D7_1365900 PE=1 SV=1	0	1	3	0	1	0	0	0	1	0	0	0	0	0	0
Q8IDW0_PLAF7	1-deoxy-D-xylulose-5-phosphate synthase OS=*Plasmodium falciparum* (isolate 3D7) OX=36329 GN=PF3D7_1337200 PE=3 SV=1	0	1	11	0	0	0	0	0	0	0	0	0	0	0	0
Q8IEJ5_PLAF7	Uncharacterized protein OS=*Plasmodium falciparum* (isolate 3D7) OX=36329 GN=PF3D7_1312700 PE=4 SV=1	0	4	8	2	2	0	0	0	0	0	0	0	0	0	0
Q8IEK1_PLAF7	M1-family alanyl aminopeptidase OS=*Plasmodium falciparum* (isolate 3D7) OX=36329 GN=PF3D7_1311800 PE=1 SV=1	0	0	6	0	2	0	0	0	0	0	0	0	0	0	0
Q8IFP5_PLAF7	Transmembrane emp24 domain-containing protein, putative OS=*Plasmodium falciparum* (isolate 3D7) OX=36329 GN=PF3D7_0422100 PE=3 SV=1	1	1	4	2	1	0	0	0	0	0	0	0	0	0	0

Accession Number	Description	50WTB1 57-04 peptide	50WTB2 72-02 peptide	50WTB3 72-04 peptide	51ETB2 57-08 peptide	51ETB3 72-06 peptide	51ETB4 152-02 peptide	stevTB1 57-12 peptide	stevTB2 72-08 peptide	stevTB3 72-10 peptide	3D71 72-12 peptide	3D72 72-14 peptide	3D73 72-16 peptide	3D7B1 72-18 peptide	3D7B2 72-20 peptide	3D7B3 72-22 peptide
Q8IHN4_PLAF7	Antigen 332, DBL-like protein OS=*Plasmodium falciparum* (isolate 3D7) OX=36329 GN=PF3D7_1149000 PE=4 SV=2	0	17	82	4	101	1	0	2	2	0	0	0	0	0	0
Q8IHZ2_PLAF7	CLPTM1 domain-containing protein, putative OS=*Plasmodium falciparum* (isolate 3D7) OX=36329 GN=PF3D7_1137300 PE=3 SV=1	0	1	3	0	0	0	0	0	0	0	0	0	0	0	0
Q8II26_PLAF7	Uncharacterized protein OS=*Plasmodium falciparum* (isolate 3D7) OX=36329 GN=PF3D7_1133900 PE=4 SV=2	0	10	34	0	10	1	0	0	0	0	0	0	0	0	0
Q8II72_PLAF7	Parasitophorous vacuolar protein 1 OS=*Plasmodium falciparum* (isolate 3D7) OX=36329 GN=PF3D7_1129100 PE=4 SV=1	0	0	0	2	0	0	0	0	0	0	0	0	0	0	0
Q8IIC8_PLAF7	Golgi protein 2 OS=*Plasmodium falciparum* (isolate 3D7) OX=36329 GN=PF3D7_1123500 PE=4 SV=1	0	11	33	2	14	4	0	0	0	0	0	0	0	0	0
Q8IIJ8_PLAF7	Heat shock protein 101 OS=*Plasmodium falciparum* (isolate 3D7) OX=36329 GN=PF3D7_1116800 PE=1 SV=1	0	0	9	0	0	0	0	0	0	0	0	0	0	0	0
Q8IIR6_PLAF7	DnaJ homolog subfamily C member 16 OS=*Plasmodium falciparum* (isolate 3D7) OX=36329 GN=PF3D7_1108700 PE=4 SV=1	0	0	2	0	0	0	0	0	0	0	0	0	0	0	0
Q8IIR7_PLAF7	Endoplasmic reticulum-resident calcium binding protein OS=*Plasmodium falciparum* (isolate 3D7) OX=36329 GN=PF3D7_1108600 PE=4 SV=1	0	2	2	0	2	0	0	0	0	0	0	0	0	0	0
Q8IIU7_PLAF7	Translocon component PTEX88 OS=*Plasmodium falciparum* (isolate 3D7) OX=36329 GN=PF3D7_1105600 PE=4 SV=2	0	0	2	0	0	0	0	0	0	0	0	0	0	0	0
Q8IIU9_PLAF7	Uncharacterized protein OS=*Plasmodium falciparum* (isolate 3D7) OX=36329 GN=PF3D7_1105300 PE=4 SV=2	0	2	1	0	0	0	0	0	0	0	0	0	0	0	0
Q8IIX5_PLAF7	PRESAN domain-containing protein OS=*Plasmodium falciparum* (isolate 3D7) OX=36329 GN=PF3D7_1102500 PE=4 SV=1	0	0	2	0	0	0	0	0	0	0	0	0	0	0	0
Q8IJ21_PLAF7	Serine/threonine protein kinase, FIKK family OS=*Plasmodium falciparum* (isolate 3D7) OX=36329 GN=PF3D7_1039000 PE=4 SV=1	0	1	7	0	3	0	0	0	0	0	0	0	0	0	0
Q8IJ37_PLAF7	Pyruvate kinase OS=*Plasmodium falciparum* (isolate 3D7) OX=36329 GN=PF3D7_1037100 PE=3 SV=1	0	1	13	0	0	0	0	0	0	0	0	0	0	0	0
Q8IJC6_PLAF7	60S ribosomal protein L3 OS=*Plasmodium falciparum* (isolate 3D7) OX=36329 GN=PF3D7_1027800 PE=1 SV=1	0	0	3	0	0	0	0	0	0	0	0	0	0	0	0
Q8IJC6_PLAF7 [2]	Cluster of 60S ribosomal protein L3 OS=*Plasmodium falciparum* (isolate 3D7) OX=36329 GN=PF3D7_1027800 PE=1 SV=1 (Q8IJC6_PLAF7)	0	0	3	0	0	0	0	0	0	0	0	0	0	0	0
Q8IJF6_PLAF7	Exported protein 3 OS=*Plasmodium falciparum* (isolate 3D7) OX=36329 GN=PF3D7_1024800 PE=4 SV=2	0	0	4	0	1	0	0	0	0	0	0	0	0	0	0
Q8IJN3_PLAF7	Serine/threonine protein kinase, FIKK family OS=*Plasmodium falciparum* (isolate 3D7) OX=36329 GN=PF3D7_1016400 PE=4 SV=2	1	2	4	2	6	0	0	0	0	0	0	0	0	0	0
Q8IJR2_PLAF7	Uncharacterized protein OS=*Plasmodium falciparum* (isolate 3D7) OX=36329 GN=PF3D7_1013300 PE=4 SV=1	0	1	2	0	0	0	0	0	0	0	0	0	0	0	0
Q8IK22_PLAF7	Exported lipase 1 OS=*Plasmodium falciparum* (isolate 3D7) OX=36329 GN=PF3D7_1001400 PE=4 SV=1	0	0	4	0	3	0	0	0	0	0	0	0	0	0	0
Q8IKF0_PLAF7	Eukaryotic initiation factor 4A OS=*Plasmodium falciparum* (isolate 3D7) OX=36329 GN=PF3D7_1468700 PE=3 SV=1	0	0	2	0	0	0	0	0	0	0	0	0	0	0	0
Q8IKJ1_PLAF7	Serine/threonine protein phosphatase UIS2, putative OS=*Plasmodium falciparum* (isolate 3D7) OX=36329 GN=PF3D7_1464600 PE=4 SV=2	0	6	25	0	1	0	0	0	0	0	0	0	0	0	0

Accession Number	Description	50WTB1 57-04 peptide	50WTB2 72-02 peptide	50WTB3 72-04 peptide	51ETB2 57-08 peptide	51ETB3 72-06 peptide	51ETB4 152-02 peptide	stevTB1 57-12 peptide	stevTB2 72-08 peptide	stevTB3 72-10 peptide	3D71 72-12 peptide	3D72 72-14 peptide	3D73 72-16 peptide	3D7B1 72-18 peptide	3D7B2 72-20 peptide	3D7B3 72-22 peptide
Q8IKL1_PLAF7	GTP-binding protein, putative OS=*Plasmodium falciparum* (isolate 3D7) OX=36329 GN=PF3D7_1462300 PE=4 SV=1	5	25	53	3	8	1	0	0	1	0	0	0	0	0	0
Q8IKN7_PLAF7	Uncharacterized protein OS=*Plasmodium falciparum* (isolate 3D7) OX=36329 GN=PF3D7_1459400 PE=4 SV=1	0	0	4	0	0	0	0	0	0	0	0	0	0	0	0
Q8IKQ7_PLAF7	MA3 domain-containing protein, putative OS=*Plasmodium falciparum* (isolate 3D7) OX=36329 GN=PF3D7_1457300 PE=3 SV=1	0	0	3	0	0	0	0	0	0	0	0	0	0	0	0
Q8IKV8_PLAF7	Sortilin OS=*Plasmodium falciparum* (isolate 3D7) OX=36329 GN=PF3D7_1451800 PE=3 SV=1	0	0	5	0	0	0	0	0	0	0	0	0	0	0	0
Q8IKW5_PLAF7	Elongation factor 2 OS=*Plasmodium falciparum* (isolate 3D7) OX=36329 GN=PF3D7_1451100 PE=3 SV=1	0	0	2	0	0	0	0	0	0	0	0	0	0	0	0
Q8IL32_PLAF7	Heat shock protein 90, putative OS=*Plasmodium falciparum* (isolate 3D7) OX=36329 GN=PF3D7_1443900 PE=1 SV=1	0	1	8	0	0	0	0	0	0	0	0	0	0	0	0
Q8IL76_PLAF7	Sad1/UNC domain-containing protein, putative OS=*Plasmodium falciparum* (isolate 3D7) OX=36329 GN=PF3D7_1439300 PE=4 SV=2	0	1	3	0	0	0	0	0	0	0	0	0	0	1	0
Q8ILA1_PLAF7	Translocon component PTEX150 OS=*Plasmodium falciparum* (isolate 3D7) OX=36329 GN=PF3D7_1436300 PE=1 SV=1	1	5	14	4	13	1	0	0	0	0	0	0	0	0	0
Q8ILD4_PLAF7	HP12 protein homolog, putative OS=*Plasmodium falciparum* (isolate 3D7) OX=36329 GN=PF3D7_1432800 PE=4 SV=1	0	0	3	0	0	0	0	0	0	0	0	0	0	0	0
Q8IM28_PLAF7	ATP-dependent Clp protease regulatory subunit ClpC OS=*Plasmodium falciparum* (isolate 3D7) OX=36329 GN=PF3D7_1406600 PE=4 SV=1	0	0	4	0	0	0	0	0	0	0	0	0	0	0	0
Q8IM45_PLAF7	Uncharacterized protein OS=*Plasmodium falciparum* (isolate 3D7) OX=36329 GN=PF3D7_1404900 PE=4 SV=1	0	2	4	0	2	0	0	0	0	0	0	0	0	0	0
Q9U0G6_PLAF7	Erythrocyte membrane protein 1, PfEMP1 OS=*Plasmodium falciparum* (isolate 3D7) OX=36329 GN=PF3D7_0412400 PE=4 SV=1	0	0	1	0	0	0	0	0	2	0	0	0	0	0	0
Q9U0G6_PLAF7 [2]	Cluster of Erythrocyte membrane protein 1, PfEMP1 OS=*Plasmodium falciparum* (isolate 3D7) OX=36329 GN=PF3D7_0412400 PE=4 SV=1 (Q9U0G6_PLAF7)	0	0	1	0	0	0	0	0	2	0	0	0	0	0	0
RADI_HUMAN	Radixin OS=Homo sapiens OX=9606 GN=RDX PE=1 SV=1	0	0	0	0	0	0	0	0	0	2	0	0	0	0	0
REFSEQ:|XP_932229|	human Gene_Symbol=KRT126P similar to Keratin, type II cytoskeletal 2 oral	0	0	0	0	0	0	0	0	0	0	0	0	0	0	0
RL3_HUMAN	60S ribosomal protein L3 OS=Homo sapiens OX=9606 GN=RPL3 PE=1 SV=2	0	0	1	0	0	0	0	0	0	0	0	0	0	0	0
RS27A_HUMAN	Ubiquitin-40S ribosomal protein S27a OS=Homo sapiens OX=9606 GN=RPS27A PE=1 SV=2	0	2	3	0	2	1	0	0	2	1	0	0	0	0	1
RS27A_HUMAN [2]	Cluster of Ubiquitin-40S ribosomal protein S27a OS=Homo sapiens OX=9606 GN=RPS27A PE=1 SV=2 (RS27A_HUMAN)	0	2	4	0	2	1	0	0	2	1	0	0	0	0	1
RS5_HUMAN	40S ribosomal protein S5 OS=Homo sapiens OX=9606 GN=RPS5 PE=1 SV=4	0	0	0	0	0	0	0	0	0	0	0	0	0	0	0
S10A8_HUMAN	Protein S100-A8 OS=Homo sapiens OX=9606 GN=S100A8 PE=1 SV=1	0	1	2	0	0	0	0	0	1	1	1	2	0	1	0
S10A9_HUMAN	Protein S100-A9 OS=Homo sapiens OX=9606 GN=S100A9 PE=1 SV=1	0	2	2	1	0	0	3	0	1	1	1	2	0	0	1
SBSN_HUMAN	Suprabasin OS=Homo sapiens OX=9606 GN=SBSN PE=1 SV=2	0	0	0	0	0	0	0	0	2	0	0	1	0	0	1
SERA5_PLAF7	Serine-repeat antigen protein 5 OS=*Plasmodium falciparum* (isolate 3D7) OX=36329 GN=SERA5 PE=1 SV=1	0	0	2	0	0	0	0	0	0	0	0	0	0	0	0

Accession Number	Description	50WTB1 57-04 peptide	50WTB2 72-02 peptide	50WTB3 72-04 peptide	51ETB2 57-08 peptide	51ETB3 72-06 peptide	51ETB4 152-02 peptide	stevTB1 57-12 peptide	stevTB2 72-08 peptide	stevTB3 72-10 peptide	3D71 72-12 peptide	3D72 72-14 peptide	3D73 72-16 peptide	3D7B1 72-18 peptide	3D7B2 72-20 peptide	3D7B3 72-22 peptide
SERA6_PLAF7	Serine-repeat antigen protein 6 OS=*Plasmodium falciparum* (isolate 3D7) OX=36329 GN=SERA6 PE=1 SV=3	0	0	2	0	0	0	0	0	0	0	0	0	0	0	0
sp|P02538|human	Gene_Symbol=KRT6A Keratin, type II cytoskeletal 6A	0	30	39	0	21	9	0	14	28	32	27	34	29	21	28
sp|P02768-1|human	Gene_Symbol=ALB Isoform 1 of Serum albumin precursor	0	2	4	0	2	0	0	0	2	6	1	4	4	2	1
sp|P05787|human	Gene_Symbol=KRT8 Keratin, type II cytoskeletal 8	0	0	0	0	0	0	0	0	0	5	0	0	0	0	6
sp|P08779|KRT16 humanGene_Symbol=KRT16 Keratin, type I cytoskeletal 16	human Gene_Symbol=KRT16 Keratin, type I cytoskeletal 16;sp|P08779|KRT16 human Gene_Symbol=KRT16 Keratin, type I cytoskeletal 16	9	27	30	29	22	8	24	13	24	27	25	30	25	18	17
sp|P08779|KRT16 humanGene_Symbol=KRT16 Keratin, type I cytoskeletal 16-DECOY	sp|P08779|KRT16 human Gene_Symbol=KRT16 Keratin, type I cytoskeletal 16	0	0	0	0	0	0	0	0	0	0	0	0	0	0	0
sp|P0DMV9|HS71B_HUMANHeat shock 70 kDa protein 1B OS=Homo sapiens OX=9606 GN=HSPA1B PE=1 SV=1	sp|P0DMV9|HS71B_HUMAN Heat shock 70 kDa protein 1B OS=Homo sapiens OX=9606 GN=HSPA1B PE=1 SV=1	0	0	0	0	2	0	0	0	0	0	0	1	0	0	0
sp|P0DUB6|AMY1A_HUMAN Alpha-amylase 1A OS=Homo sapiens OX=9606 GN=AMY1A PE=1 SV=1	sp|P0DUB6|AMY1A_HUMAN Alpha-amylase 1A OS=Homo sapiens OX=9606 GN=AMY1A PE=1 SV=1	0	0	0	0	0	0	0	0	0	0	0	4	0	0	0
sp|P13647|human	Gene_Symbol=KRT5 Keratin, type II cytoskeletal 5	0	32	38	0	20	13	0	13	31	34	32	34	31	25	34
sp|P20930|human	Gene_Symbol=FLG Filaggrin	0	1	0	0	0	0	0	0	2	0	1	0	0	0	0
sp|P35900|human	Gene_Symbol=KRT20 Keratin, type I cytoskeletal 20	0	0	0	0	0	0	0	0	0	2	0	0	0	0	0
sp|P48668|human	Gene_Symbol=KRT6C Keratin, type II cytoskeletal 6C	0	30	38	0	21	9	0	14	27	31	27	32	29	21	27
sp|Q14525|Keratin,	type I cuticular HA3-II (Hair keratin, type I HA3-II)	0	0	0	0	2	0	0	0	2	1	1	4	0	0	12
sp|Q14CN4-1|human	Gene_Symbol=KRT72 Isoform 1 of Keratin, type II cytoskeletal 72	0	0	0	0	0	0	0	0	0	4	0	0	0	0	0
sp|Q3KNV1|human	Gene_Symbol=KRT7 keratin 7	0	0	0	0	0	0	0	0	0	0	0	0	0	0	0
sp|Q3KNV1|human Gene_Symbol=KRT7 keratin 7-DECOY	sp|Q3KNV1|human Gene_Symbol=KRT7 keratin 7	0	0	0	0	0	0	0	0	0	0	0	0	0	0	0
sp|Q5D862|human	Gene_Symbol=FLG2 Filaggrin-2	0	6	3	0	1	1	0	1	3	2	2	3	2	2	3
sp|Q6IFU5|keratin KA3Type I hair keratin - Homo sapiens (Human).	sp|Q6IFU5|keratin KA3 Type I hair keratin - Homo sapiens (Human).	0	0	0	0	0	0	0	0	0	0	0	0	0	0	1
sp|Q6ISB0|Keratin,	hair, basic, 4 - Homo sapiens (Human).	0	1	0	0	0	0	0	0	0	0	0	0	0	0	0
sp|Q6KB66-1|human	Gene_Symbol=KRT80 Isoform 1 of Keratin, type II cytoskeletal 80	0	4	3	0	1	1	0	1	4	1	1	3	0	0	1
sp|Q6NT21|Keratin,	hair, basic, 3 - Homo sapiens (Human).	0	0	0	0	0	0	0	0	0	4	0	1	0	0	27
sp|Q7RTS7|human	Gene_Symbol=KRT74 Keratin, type II cytoskeletal 74	0	0	5	0	0	0	0	0	0	0	0	4	0	0	4
sp|Q7Z3Y9|human	Gene_Symbol=KRT26 Keratin, type I cytoskeletal 26	0	0	0	0	0	0	0	0	0	0	0	0	0	0	0
sp|Q7Z3Z0|human	Gene_Symbol=KRT25 Keratin, type I cytoskeletal 25	0	0	0	0	0	0	0	0	0	0	0	2	0	0	0
sp|Q86Y46|KRT73 humanGene_Symbol=KRT73 Keratin-73	human Gene_Symbol=KRT73 Keratin-73;sp|Q86Y46|KRT73 human Gene_Symbol=KRT73 Keratin-73	0	5	6	0	0	0	0	0	4	5	0	5	0	0	4
sp|Q86YZ3|human	Gene_Symbol=HRNR Hornerin	0	16	17	0	11	1	0	0	14	13	7	10	8	12	12
sp|Q8N1A0|human	Gene_Symbol=KRT222P truncated type I keratin KA21	0	0	0	0	1	0	0	0	0	1	0	0	0	0	0
sp|Q99456|human	Gene_Symbol=KRT12 Keratin, type I cytoskeletal 12	0	0	0	0	0	0	0	0	0	0	0	0	0	0	0
sp|Q9C075|human	Gene_Symbol=KRT23 Keratin, type I cytoskeletal 23	0	1	0	0	0	0	0	0	0	1	0	0	0	0	0
SPB12_HUMAN	Serpin B12 OS=Homo sapiens OX=9606 GN=SERPINB12 PE=1 SV=1	0	3	1	0	0	0	2	0	1	1	1	2	0	0	0

Accession Number	Description	50WTB1 57-04 peptide	50WTB2 72-02 peptide	50WTB3 72-04 peptide	51ETB2 57-08 peptide	51ETB3 72-06 peptide	51ETB4 152-02 peptide	stevTB1 57-12 peptide	stevTB2 72-08 peptide	stevTB3 72-10 peptide	3D71 72-12 peptide	3D72 72-14 peptide	3D73 72-16 peptide	3D7B1 72-18 peptide	3D7B2 72-20 peptide	3D7B3 72-22 peptide
SPR2B_HUMAN	Small proline-rich protein 2B OS=Homo sapiens OX=9606 GN=SPRR2B PE=2 SV=1	0	0	1	0	0	0	0	0	1	2	2	2	0	1	1
SPR2E_HUMAN	Small proline-rich protein 2E OS=Homo sapiens OX=9606 GN=SPRR2E PE=2 SV=2	0	0	1	0	0	0	0	0	1	2	2	2	0	1	1
SPR2E_HUMAN [3]	Cluster of Small proline-rich protein 2E OS=Homo sapiens OX=9606 GN=SPRR2E PE=2 SV=2 (SPR2E_HUMAN)	0	0	1	0	0	0	0	0	1	2	2	2	0	1	1
SPR2G_HUMAN	Small proline-rich protein 2G OS=Homo sapiens OX=9606 GN=SPRR2G PE=3 SV=1	0	0	1	0	0	0	0	0	1	2	2	2	0	1	1
SPTA1_HUMAN	Spectrin alpha chain, erythrocytic 1 OS=Homo sapiens OX=9606 GN=SPTA1 PE=1 SV=5	0	0	2	4	14	1	0	0	0	0	0	0	0	0	0
SPTB1_HUMAN	Spectrin beta chain, erythrocytic OS=Homo sapiens OX=9606 GN=SPTB PE=1 SV=5	0	0	2	0	1	0	0	0	0	0	0	0	0	0	0
Streptavidin	(S.avidinii)	5	6	5	9	6	9	5	5	6	4	5	5	5	6	7
SYUA_HUMAN	Alpha-synuclein OS=Homo sapiens OX=9606 GN=SNCA PE=1 SV=1	0	0	0	0	5	0	0	0	0	0	0	0	0	0	0
TBA1A_HUMAN (+1)	Tubulin alpha-1A chain OS=Homo sapiens OX=9606 GN=TUBA1A PE=1 SV=1	0	0	0	0	0	0	0	0	0	1	0	0	0	0	1
TBA1A_HUMAN [5]	Cluster of Tubulin alpha-1A chain OS=Homo sapiens OX=9606 GN=TUBA1A PE=1 SV=1 (TBA1A_HUMAN)	0	0	0	0	0	0	0	0	0	2	0	0	0	0	2
TBA1B_HUMAN (+1)	Tubulin alpha-1B chain OS=Homo sapiens OX=9606 GN=TUBA1B PE=1 SV=1	0	0	0	0	0	0	2	0	0	0	0	0	0	0	0
TBA1B_HUMAN [3]	Cluster of Tubulin alpha-1B chain OS=Homo sapiens OX=9606 GN=TUBA1B PE=1 SV=1 (TBA1B_HUMAN)	0	0	0	0	0	0	2	0	0	0	0	0	0	0	0
TBA3E_HUMAN (+1)	Tubulin alpha-3E chain OS=Homo sapiens OX=9606 GN=TUBA3E PE=1 SV=2	0	0	0	0	0	0	0	0	0	2	0	0	0	0	0
TBA4A_HUMAN	Tubulin alpha-4A chain OS=Homo sapiens OX=9606 GN=TUBA4A PE=1 SV=1	0	0	0	0	0	0	1	0	0	0	0	0	0	0	1
TCHP_HUMAN	Trichoplein keratin filament-binding protein OS=Homo sapiens OX=9606 GN=TCHP PE=1 SV=1	0	0	0	0	0	0	14	0	0	0	0	0	0	0	0
TCPQ_HUMAN	T-complex protein 1 subunit theta OS=Homo sapiens OX=9606 GN=CCT8 PE=1 SV=4	0	0	0	13	15	5	0	1	0	0	0	0	0	0	0
TGM1_HUMAN	Protein-glutamine gamma-glutamyltransferase K OS=Homo sapiens OX=9606 GN=TGM1 PE=1 SV=4	0	8	1	0	0	0	4	0	1	0	1	2	0	0	0
TGM3_HUMAN	Protein-glutamine gamma-glutamyltransferase E OS=Homo sapiens OX=9606 GN=TGM3 PE=1 SV=4	0	4	1	0	0	0	3	0	2	0	0	1	1	1	2
TPM1_HUMAN	Tropomyosin alpha-1 chain OS=Homo sapiens OX=9606 GN=TPM1 PE=1 SV=2	0	0	0	0	0	0	0	0	0	0	0	3	0	0	0
TPM3_HUMAN	Tropomyosin alpha-3 chain OS=Homo sapiens OX=9606 GN=TPM3 PE=1 SV=2	0	0	0	0	0	0	0	0	0	0	0	3	0	0	0
TPM3_HUMAN [2]	Cluster of Tropomyosin alpha-3 chain OS=Homo sapiens OX=9606 GN=TPM3 PE=1 SV=2 (TPM3_HUMAN)	0	0	0	0	0	0	0	0	0	0	0	4	0	0	0
TRFE_HUMAN	Serotransferrin OS=Homo sapiens OX=9606 GN=TF PE=1 SV=3	0	0	0	0	0	0	0	0	0	17	0	0	0	0	0
TRFL_HUMAN	Lactotransferrin OS=Homo sapiens OX=9606 GN=LTF PE=1 SV=6	0	0	0	0	0	0	0	0	0	2	0	5	0	0	0
TRYP_PIG	Trypsin - Sus scrofa (Pig).	2	3	4	1	2	2	0	1	2	2	2	2	2	2	1
Type	I hair keratin 3A - Homo sapiens (Human).	0	0	0	0	0	0	7	0	0	0	0	0	0	0	0
XP32_HUMAN	Skin-specific protein 32 OS=Homo sapiens OX=9606 GN=XP32 PE=1 SV=1	0	2	1	0	1	0	0	0	0	1	3	1	1	3	0
ZA2G_HUMAN	Zinc-alpha-2-glycoprotein OS=Homo sapiens OX=9606 GN=AZGP1 PE=1 SV=2	0	3	3	0	0	0	2	0	2	1	1	3	0	1	3
ZG16B_HUMAN	Zymogen granule protein 16 homolog B OS=Homo sapiens OX=9606 GN=ZG16B PE=1 SV=3	0	0	1	0	0	0	0	0	0	0	0	2	0	0	0